



**HAL**  
open science

## Structural fatigue of superelastic NiTi wires

Eduardo Augusto Alarcon Tarquino

► **To cite this version:**

Eduardo Augusto Alarcon Tarquino. Structural fatigue of superelastic NiTi wires. Mechanics of materials [physics.class-ph]. Université de Bretagne occidentale - Brest, 2018. English. NNT : 2018BRES0019 . tel-01871232

**HAL Id: tel-01871232**

**<https://theses.hal.science/tel-01871232>**

Submitted on 10 Sep 2018

**HAL** is a multi-disciplinary open access archive for the deposit and dissemination of scientific research documents, whether they are published or not. The documents may come from teaching and research institutions in France or abroad, or from public or private research centers.

L'archive ouverte pluridisciplinaire **HAL**, est destinée au dépôt et à la diffusion de documents scientifiques de niveau recherche, publiés ou non, émanant des établissements d'enseignement et de recherche français ou étrangers, des laboratoires publics ou privés.

**THÈSE / UNIVERSITÉ DE BRETAGNE OCCIDENTALE**

*sous le sceau de l'Université Bretagne Loire*

pour obtenir le titre de

**DOCTEUR DE L'UNIVERSITÉ DE BRETAGNE OCCIDENTALE**

*Spécialité: Mécanique des solides, des matériaux, des structures et  
des surfaces*

**École Doctorale Science pour l'Ingénieur [ED 602]**

présentée par

**Eduardo ALARCON**

Préparée à l'IRD (CNRS FRE3744)  
Institut de Recherche Dupuy de Lôme  
et au FZU

Institute of Physics of the Czech Academy of  
Sciences

# Structural Fatigue of Superelastic NiTi Wires

**Thèse soutenue le 30 Janvier 2018**

devant le jury composé de :

**Xavier BALANDRAUD**

Professeur, SIGMA, Clermont-Ferrand, France / *Rapporteur*

**Michal LANDA**

Docteur, Institute of Thermodynamics of the CAS, Prague,  
République Tchèque / *Rapporteur*

**Tarak BEN ZINEB**

Professeur, Polytech Nancy (ex ESSTIN), Nancy, France /  
*Examineur*

**Sylvain CALLOCH**

Professeur, ENSTA Bretagne, Brest, France / *Examineur*

**Petr SITNER**

Dir. Rech. FZU, Institute of Physics of the CAS, Prague,  
République Tchèque / *Examineur*

**Shabnam ARBAB CHIRANI**

Professeur, ENIB, Brest, France / *Directrice de Thèse*

**Miroslav KARLIK**

Professeur, Czech Technical University in Prague, Prague / *Co-  
directeur de Thèse*

**Ludek HELLER**

Chargé de Recherche, Institute of Physics of the CAS, Prague,  
République Tchèque / *Co-encadrant de thèse*

**Luc SAINT-SULPICE**

Maître de Conférences, ENIB, Brest, France / *Co-encadrant de  
thèse*





# Acknowledgements

A new stage on my professional career has come to its end. It would not have been possible without the contributions of a very valuable group of people and institutions, who encouraged and supported me in many different ways to untangle the complexities of this co-supervised Ph.D. program carried out between France and the Czech Republic.

First, I would like to thank my supervisors' team. I start by thanking my co-supervisor Ludek Heller in the *Fyzikální Ústav* (FZU) in Prague, for his expert advice and constant encouragement. His passion for knowledge, combined with his patient guidance skills during the last three years, contributed significantly to my development as a researcher. I am also indebted to my co-supervisors in the *Institut de Recherche Dupuy de Lôme* (IRDL) in Brest, Professor Shabnam Arbab Chirani and Luc Saint Sulpice, for their guidance and fruitful discussions. I would like to thank especially Professor Shabnam Arbab Chirani for all the organization effort and administration procedures she carried out in order to lead to a good ending this Ph.D. work. In a similar way, I would like to thank Professor Miroslav Karlík, who was always at disposal for academic consultations and suggestions concerning my Ph.D. study program and administrative procedures in the *Czech Technical University*.

In addition, I would like to express my sincere gratitude to Professor Michal Landa and Professor Xavier Balaundraud, who reviewed my thesis dissertation. Their invaluable comments, remarks, and questions concerning my research work will certainly contribute to its future development. Similarly, I would like to thank the other members of my thesis jury: Professor Sylvain Calloch, Petr Sittner, and especially to Professor Tarak Ben Zineb who presided the thesis jury. Their interventions made my Ph.D. defense a much more enjoyable and rich experience than I could have expected.

Many, many thanks as well to the researchers, engineers, and technicians that helped me out with my sometime overwhelming experimental setups. Particularly I would like to thank Thierry (Titi) at the ENI-Brest, Younes at the ENSTA-Bretagne, and Martin and Lukas at the FZU. In addition, I would like to acknowledge the 'backstage' work carried out by Marcela at the FZU, and Jean-Luc at the ENI-Brest with respect to all the administrative procedures that my Ph.D. study entailed.

During my Ph.D., I had the fortune to work with instruments at the cutting edge of measurement technology. That was the case of crystallographic phase quantification via synchrotron source X-ray diffraction experiments, which I performed on beamline ID11 at the European Synchrotron Radiation Facility (ESRF), Grenoble, France. I am grateful to Nicholas Harker at the ESRF for providing assistance in using beamline ID11.

I would not leave this opportunity without thanking all my dear colleagues at the ENI-Brest and ENSTA-Bretagne in France, and those in the FZU in the Czech Republic. I especially thank to the ‘*Hey Cara*’ group of ENI-Brest. Although the time we shared was somehow short, I really enjoyed the distressful moments I spent with you guys, like the ‘*guitarrinha*’ of Henriquinho or the French pronunciation lessons from Guillaumesinho. From the Czech side, I would like to thank David and Lukas, with whom I shared office during my first stay in Prague. Apart from the interesting NiTi discussions we had, I thank you guys for introducing me to climbing and to the beauty of Czech language slang.

Finally, this project would have been impossible to achieve without the financial support of the city of Brest (*Brest Métropole*) and the Ecole Nationale d’Ingénieurs de Brest (ENI-Brest), a city and an education institution that welcomed me with opened arms since I first arrived in France in 2011, and which had a vast contribution to my personal and professional development.

*To my parents, my sister Karen,  
Simona and little Alex*





# Table of Contents

List of Figures	v
List of Tables	xv
<b>Chapter 1. Introduction</b>	<b>1</b>
1.1. Introduction.....	1
1.2. Generalities of Shape Memory Alloys .....	2
1.3. Historical Background and Overview .....	4
1.4. Statement of the Problem .....	6
1.5. Purpose of the study.....	7
1.6. Procedures .....	7
1.7. Organization of the dissertation .....	8
<b>Chapter 2. State of the Art</b>	<b>9</b>
<b>2.1. Physical Metallurgy of NiTi Alloys .....</b>	<b>11</b>
2.1.1. Binary Phase Diagram .....	11
2.1.2. Martensitic Phase Transformations in NiTi Alloys.....	13
<b>2.2. Thermodynamic aspects of phase transformations in NiTi .....</b>	<b>16</b>
2.2.1. Thermal hysteresis .....	16
2.2.2. Heat release/absorption .....	20
2.2.3. Effects of externally applied stresses – Clausius-Clapeyron relation .....	21
<b>2.3. Mechanical Properties of NiTi alloys .....</b>	<b>22</b>
2.3.1. Detwinning of B19' and R-phase.....	22
2.3.2. Elasticity.....	24
2.3.3. Stress-induced phase transformations & superelasticity .....	25
2.3.4. Plastic deformation through dislocation slip .....	27
<b>2.4. Applications of NiTi .....</b>	<b>29</b>
2.4.1. Constrained-recovery .....	29
2.4.2. Actuation .....	30
2.4.3. Superelastic .....	30
<b>2.5. Fatigue of NiTi Alloys .....</b>	<b>33</b>
2.5.1. Functional fatigue.....	34

---

2.5.2. Structural fatigue.....	36
<b>2.6. Summary.....</b>	<b>43</b>
<b>Chapter 3. Tensile Behavior of Hourglass-Shaped NiTi Samples</b>	<b>45</b>
<b>3.1. The hourglass shape.....</b>	<b>47</b>
3.1.1. Linear-Elastic Response .....	47
3.1.2. Non-linear material behavior.....	56
<b>3.2. Material of the study .....</b>	<b>57</b>
3.2.1. Cold-drawn NiTi wires.....	58
3.2.2. Preparation of hourglass-shaped samples .....	60
3.2.3. Effects of annealing temperatures .....	62
<b>3.3. Thermomechanical behavior of 500°C-annealed NiTi.....</b>	<b>72</b>
3.3.1. Stress-strain response .....	72
3.3.2. Microstructure evolution resolved via X-ray diffraction.....	78
3.3.3. Simulation of the tensile response using 3D finite element analysis .....	83
<b>3.4. Summary.....</b>	<b>102</b>
<b>Chapter 4. Fatigue of NiTi hourglass-shaped samples</b>	<b>105</b>
<b>4.1. Experimental protocol .....</b>	<b>107</b>
<b>4.2. S-N curves.....</b>	<b>109</b>
4.2.1. Effects of the mean stress .....	112
4.2.2. Hints for superelastic NiTi fatigue modeling.....	118
<b>4.3. Stress-Strain-N representation .....</b>	<b>119</b>
<b>4.4. Fatigue crack characterization.....</b>	<b>122</b>
4.4.1. Fracture surfaces.....	122
4.4.2. Characterization of the crack’s size.....	127
4.4.3. Tensile response evolution.....	130
<b>4.5. Microstructure evolution evaluated via high resolution x-ray diffraction .....</b>	<b>136</b>
<b>4.6. Summary.....</b>	<b>137</b>
<b>Chapter 5. Fatigue Assessment of NiTi Wires through the Self-Heating Method</b>	<b>141</b>
<b>5.1. Description of the self-heating method.....</b>	<b>143</b>
5.1.1. Background .....	143
5.1.2. Thermodynamic framework .....	149
<b>5.2. Experimental protocol .....</b>	<b>153</b>
5.2.1. Experimental setup .....	153
5.2.2. Post-processing of temperature data .....	155
<b>5.3. Experimental results .....</b>	<b>158</b>

---

5.3.1. Self-heating curves .....	158
5.3.2. Effects of the loading frequency .....	160
5.3.3. Evolution of the temperature harmonics.....	162
5.3.4. Influence of the shape of the sample .....	165
5.3.5. Temperature evolution during monotonic tensile tests.....	167
<b>5.4. Modeling of the thermomechanical behavior of NiTi.....</b>	<b>172</b>
5.4.1. 1D diffusion problem in hourglass-shaped samples.....	172
5.4.2. Identification of the heat exchange coefficients.....	178
5.4.3. Cyclic thermoelastic effect .....	181
5.4.4. Cyclic phase transformation latent heat .....	182
5.4.5. Interaction between the thermoelastic effect and the transformation latent heats .....	184
<b>5.5. Summary.....</b>	<b>186</b>
<b>Conclusions</b>	<b>189</b>
<b>References</b>	<b>192</b>



# List of Figures

Figure 1-1 Schematic representation of the temperature domains of austenite and martensite phases upon cooling (a) and upon heating (b).....	3
Figure 1-2 a) Schematic representation of the shape memory effect. b) Actuation cycle or two-way shape memory effect. c) Superelasticity. Note that, since stress is applied, the transformation temperatures $M_f'$ , $M_s'$ , $A_s'$ , and $A_f'$ in (b) are higher than their stress-free counterparts $M_f$ , $M_s$ , $A_s$ , and $A_f$ introduced back in Figure 1-1. ....	4
Figure 2-1 Binary phase diagram of NiTi alloys.....	12
Figure 2-2 Transformation-Time-Temperature (TTT) diagram of a 52 at. %Ni alloy by Nishida et al. [17].	13
Figure 2-3 Crystallographic phases observed in near equiatomic NiTi: (a) B2 cubic austenite, (b) B19' monoclinic martensite, (c) R-phase (shown here simply as a distortion of the B2 phase in the $\langle 111 \rangle_{B2}$ direction), and (d) $Ti_3Ni_4$ , which we complement here with a TEM bright field image and an schematic representation of the lenticular-shape precipitates that this phase forms. ....	14
Figure 2-4 Schematic representation of the B2 to B19' transformation. The axis i, j, k correspond to the reference axis system of the B2 lattice, while the axis i', j' k' correspond to the reference axis system of B19' lattice. a) Tetragonal lattice depicted within four cubic lattices.....	15
Figure 2-5 Schematic representation of self-accommodated wedge of B19' twinned variants.....	16
Figure 2-6 Schematic representation of the coexistence of B2, R-phase and B19' according to Zhang et al.[19]. The individual variants of B19' are denoted as $CV_M$ and those from R phase are denoted as $CV_R$ . ....	17
Figure 2-7 Schematic representation of the free chemical potentials of austenite and martensite. a)Hypothetical phase-temperature domains in the absence of elastic and irreversible energies opposing the propagation of the transformation. b)Phase-temperature domains considering elastic and irreversible energies. ....	18
Figure 2-8 Effect of the Gibbs free energy terms on the transformation kinetics of solid-state phase transformations in SMA. a)Chemical energy only. b)Chemical and elastic energies. c)Chemical and irreversible energies. d)Chemical, elastic and irreversible energies.....	19
Figure 2-9 a) DSC results carried out on a Ti-50.9at%Ni, heat-treated at 800°C (upper graph) and 300°C (lower graph)[31].....	20
Figure 2-10 Schematic representation of the stress-temperature-phase diagram of a NiTi alloy showing the stress-temperature domains of B2, R and B19' phases.....	22
Figure 2-11Tensile stress responses showing the detwinning of B19'(a)[35] and R-phase (b)[36]. ....	23
Figure 2-12 Characterization of the elastic modulus of austenite and martensite of a polycrystalline NiTi wire/bar upon tension/compression loading (extracted from Sittner et al. [37]). ....	24
Figure 2-13 Superelastic tensile responses of NiTi. a) $B2 \rightarrow R \rightarrow B2$ , b) $B2 \rightarrow R \rightarrow B19' \rightarrow B2$ [38], c) $R \rightarrow B19' \rightarrow R$ , and d) $B2 \rightarrow B19' \rightarrow B2$ [39]. ....	25
Figure 2-14 Stress state of grains in the vicinity of a localization band upon stretching a 0.1mm NiTi wire [42]. ....	26

Figure 2-15 Transmission electron microscopy images showing the presence of dislocations produced after phase transformations in NiTi. The left-hand side shows dislocations in the austenite domains [48]–[53]. The right-hand side shows dislocations appearing in the martensite domains [54], [55]. This figure was extracted from the review paper of Chowdhury et al. [56].	28
Figure 2-16 Stress-temperature-phase diagram for NiTi including B19' detwinning and plasticity boundaries.	29
Figure 2-17 NiTi tube couplings [58].	30
Figure 2-18 NiTi self-expanding stents. a)Stent shrinking inside a sheath previous to placement procedure. b)Deployment of a stent inside a blood vessel. c)Schematic representation of the loading path of a self-expanding stent during installation and operation.	31
Figure 2-19 a) Endodontic file for tooth root canalization.	31
Figure 2-20 Prototype of a superelastic damper for stay-cable bridges using NiTi wires [65].	32
Figure 2-21 Operation of a prototype of elastocaloric device made of superelastic NiTi plates [72].	33
Figure 2-22 Functional fatigue exhibited by NiTi alloys upon thermal cycles [73].	34
Figure 2-23 Functional fatigue of NiTi upon tensile stress cycles [77].	35
Figure 2-24 Definition of the low cycle (LCF) and high cycle (HCF) regimes for superelastic NiTi.	36
Figure 2-25 Experimental setups used for evaluating the fatigue of NiTi. a)Rotary bending system. b)Diamond shaped samples using for evaluating the fatigue of NiTi stents [81]. c)Reduced cross-section samples. d)Snubbing gripping device used for fatigue testing of thin wires. In this example the red zone of the wire was trained before the fatigue testing introducing a “virtual cross-section reduction” [82].	37
Figure 2-26 Fatigue curves of NiTi wires showing the effects of the temperature. a)Stress-life approach [88]. b)Strain-life approach[89].	38
Figure 2-27 Influence of the mean strain on the fatigue performance of NiTi. a)Elastic and transformation regimes (replotted from [93]). b) Biphasic regime (replotted from [94]).	40
Figure 2-28 Special features of S-N and Strain-N curves in NiTi. a)C-shaped S-N curve obtained in NiTi flat samples [97]. b)Z-shaped Strain-N curve obtained upon rotary bending fatigue of NiTi wires [98]. c) Constant life time upon deformation in the strain plateau [82].	41
Figure 2-29 HCF failure mechanisms in NiTi [99].	43
Figure 3-1 a) Geometry of hourglass-shaped samples. b) Experimental boundary conditions used during characterization and fatigue tests of hourglass-shaped samples. c) Boundary conditions and geometry used for carrying out an analytical solution for stresses and strains in the gauge length $L_G$ .	48
Figure 3-2 a) Axial stress distribution in hourglass-shaped samples of different wire diameters and radius reductions. The axial stress across the cross-section was normalized with respect to the stress in the straight part of the samples. The maximum stress increase at the mid cross-section is plotted in terms of the radius reduction in (b). Figures in (c) show the effect of the wire radius on the axial stress gradient in the groove zone of hourglass shaped samples.	49
Figure 3-3 a) Evolution of term $C$ with respect to the radius reduction ratio ( $r_n / r_w$ ). The evolution of $C$ was approximated by a cubic polynomial, the constants of which evolve quadratically with respect to $1/r_w$ as shown in (b-e).	50
Figure 3-4 Mesh convergence study for elastic simulations of tensile loaded hourglass-shaped samples. a) Boundary conditions used for the simulation. b) Meshes used for comparison. c) Nominal stress vs displacement results showing the very small differences between the analytical and the different meshed finite element solutions. d) Axial stress distribution at the mid cross-section evaluated using the meshes presented in (a).	51

Figure 3-5 Axisymmetric simulation of an hourglass-shaped sample using a isotropic elastic constitutive law. We show contour plots of the stress tensor components in the studied plane of hourglass-shaped samples of $rw = 0.5\text{mm}$ and radius reductions between 0.5-0.9. Upon the simulations, the samples were subjected to a nominal axial stress of 100MPa. a) Axial stress. b) Radial stress. c) Transverse stress. d) Shear stress. e) Triaxiality ratio. ....	53
Figure 3-6 Axial stress (a) and triaxiality ratio (b) distributions at the mid cross-section of hourglass shaped samples ( $rw = 0.5\text{mm}$ , $rt = 10\text{mm}$ , and $rn/rw = 0.5 - 0.9$ ) obtained from finite element simulations of a tensile loading up to $\sigma_{nom} = 100\text{MPa}$ . The radius in the abscissa of both curves was normalized to $rn$ . ....	54
Figure 3-7 Stress concentration factor (a) and maximum triaxiality ratio (b) at the mid cross-section of hourglass shape samples with $rw$ between 0.5-1mm, $rt$ equal to 10mm and $rn/rw$ between 0.5-0.9. ....	55
Figure 3-8 Perfect plasticity constitutive law. ....	56
Figure 3-9 Simulation of the tensile response of a perfect-plastic hourglass shaped sample. a) Force-displacement macroscopic response. b) Evolution of the yielding zone. c-g) Stress tensor components distribution in the groove zone. h) Triaxiality ratio distribution. ....	56
Figure 3-10 200x strain scaled contour plots of the stress tensor components upon plastic deformation (stage 2). The color maps are kept the same as previously in Figure 3-9. ....	57
Figure 3-11. Tensile responses of cold-drawn NiTi#1 wires at 40°C(a), 60°C(b), and 80°C(c). ....	58
Figure 3-12 Evolution of the mechanical properties of cold-drawn NiTi wires with temperature: a) tensile responses, b) Young's Modulus, c) residual strain after different maximal strain loadings, and d) yield stress identified using the 0.2% offset yield criterion for elastoplastic materials. ....	59
Figure 3-13 NiTi hourglass shaped samples used in this fatigue study. ....	60
Figure 3-14 Dimensions of a group of 70 hourglass-shaped NiTi samples. a) Diameter at the mid cross-section. b) Wire diameter outside the reduced cross-section zone. ....	61
Figure 3-15 Surface roughness of grinded and electropolished hourglass NiTi samples. a) Example of a depth-composed 3D surface image taken at 1000x magnification in the middle of hourglass-shaped NiTi samples. b) Surface profiles of 5 hourglass-shaped NiTi samples. ....	62
Figure 3-16 Straightening device for annealing of hourglass-shaped samples. ....	63
Figure 3-17 HDR optical microscope images from hourglass-shaped samples annealed during 30 minutes in an air furnace at temperatures between 400 and 500°C. ....	64
Figure 3-18 Geometry of samples used for DSC tests. ....	64
Figure 3-19 DSC curves for a NiTi annealed at 400°C (a) and 500°C (b) for 30 minutes. ....	65
Figure 3-20 Experimental setup used for infrared thermal image acquisition upon tensile tests. ....	67
Figure 3-21 Tensile responses of NiTi hourglass-shaped samples issued from annealing treatments between 400 and 500°C. ....	68
Figure 3-22 Onsets of phase transformations of NiTi#1 with respect to the annealing temperature: a) R/B2→B19'. b) B2→R. ....	69
Figure 3-23 Stress-temperature slopes of phase transformations in NiTi#1 evaluated with respect to the annealing temperatures: a) R/B2→B19'. b) B2→R. ....	69
Figure 3-24. Optical microscope image revealing the grained microstructure of 500°C-annealed NiTi. ....	70
Figure 3-25 2D-DIC technique for strain field measurements upon tensile testing of hourglass-shaped samples: a) experimental setup, b) surface speckle pattern applied to the surface of an hourglass-shaped sample. ....	71

Figure 3-26 Tensile response of hourglass-shaped samples in the B2 $\leftrightarrow$ R phase transformation regime: a) Macroscopic response. b) Axial lagrangian strain fields obtained using 2D-DIC at points highlighted in part (a). c) The local response of the material at the mid cross-section of the sample. d) 3.4mm-length axial strain profiles along the axis of the sample centered at the mid cross-section. The elastic strain profiles, plotted in dotted lines along with the experimental strain ones, were calculated via the Hooke's law using the material Young's modulus (70GPa), the sample's geometry and the nominal stresses at points 1 (dark-blue), 2 (green) and 3 (red). .....	74
Figure 3-27. Tensile response of hourglass-shaped samples in the B2/R $\rightarrow$ B19' phase transformation regime upon loading. The macroscopic response is shown in (a). The lagrangian axial strain fields at the points highlighted in part (a) are shown in (d). The local response at the mid cross-section is plotted in (b) and the 3.4mm-length axial strain profiles along the axis of the sample in (c). .....	75
Figure 3-28 Tensile response of hourglass-shaped samples in the B2/R $\rightarrow$ B19' phase transformation regime upon unloading. The macroscopic (a) and local (b) responses are the same shown in Figure 3-27. The lagrangian axial strain fields at the points highlighted in part (a) are shown in (d), and the 3.4mm-length axial strain profiles along the axis of the sample are shown in (c). .....	76
Figure 3-29 Comparison of the tensile responses of 500 $^{\circ}$ C-annealed NiTi#1 at 32.5 $^{\circ}$ C using a hourglass shaped sample and a straight sample. ....	77
Figure 3-30 Experimental setup for in situ synchrotron source x-ray diffraction experiments in tensile loaded hourglass NiTi samples. ....	79
Figure 3-31 Comparisons of diffraction patterns recorded on a single sample prior (a) and after the stress-induced martensitic transformation (b). Colormaps in (a) and (b) represent diffraction patterns acquired during scans along the axial direction. Diffraction patterns shown in (c) and (d) were recorded approximately in the center of the concave zone of the sample. ....	80
Figure 3-32 Results of spatially resolved quantitative phase analysis performed on a single sample prior (a) and after the martensitic transformation occurred (b). ....	81
Figure 3-33 Comparisons of diffraction patterns recorded on a single sample during straining after the martensitic transformation occurred. Colormaps (a), (b), and (c) correspond to loading stages shown in (e), denoted as MT1, MT2, MT3. Diffraction patterns (d), (e), (f) were taken in the mid cross-section of the sample at loading stages MT1, MT2, MT3 respectively. ....	82
Figure 3-34 Results of spatially resolved quantitative phase analysis performed on a single sample after the martensitic transformation occurred. The results correspond to loading stages MT2 and MT3 shown in Figure 3-33e. ....	83
Figure 3-35 B2 phase Young's Modulus evolution with temperature. ....	88
Figure 3-36 Evolution of the B2 $\rightarrow$ R transformation stress onset with temperature. ....	89
Figure 3-37 Tensile responses of NiTi upon stress-induced B2 $\rightarrow$ R phase transformation at 32.5, 40, 60, and 80 $^{\circ}$ C. The experimental curves are plotted in solid lines while the modeled ones are plotted in dashed lines. The experimental curve at 32.5 $^{\circ}$ C was extracted from the local response of an hourglass-shaped sample, whereas the experimental responses at 40, 60, and 80 $^{\circ}$ C were obtained from tensile tests of straight wires. ....	91
Figure 3-38 Constitutive responses of NiTi at 32.5, 40, and 80 $^{\circ}$ C using the Sedláč model and the parameters identified in Table 3-6. ....	94
Figure 3-39 Superelastic tensile response of hourglass-shaped samples of NiTi#1 heat-treated at 500 $^{\circ}$ C for 30 minutes obtained experimentally and by simulations: a) 32.5 $^{\circ}$ C, b) 40 $^{\circ}$ C, and c) 80 $^{\circ}$ C. The curves are presented in terms of the elongation of a clip-on ( $u_z$ ) attached outside the groove zone of the samples, and the nominal stress ( $\sigma_{nom}$ ), calculated as the force measured by the load cell divided by the initial mid cross-section of the sample. ....	95

Figure 3-40 Tensile response of an hourglass-shaped sample at 32.5°C in the <b>B2→R regime</b> . a) Comparison between experimental and simulated macroscopic responses. b) Comparison between experimental and simulated axial strain profiles centered at the mid cross-section. c) Evolution of the stress tensor components, triaxiality ratio $M$ and volume fraction of R-phase. ....	96
Figure 3-41 Tensile response of an hourglass-shaped sample at 32.5°C in the <b>B2/R→B19' regime upon loading</b> . a) Experimental and simulated macroscopic responses. b) Experimental and simulated axial strain profiles centered at the mid cross-section. c) Stress tensor components, triaxiality ratio $M$ and volume fraction of R-phase and B19'.....	97
Figure 3-42 Scaled deformed stress contour maps upon stress-induced B2→R (a) and B2/R→B19' (b) phase transformations. The color scale for each contour plot was kept the same as in Figure 3-40 and Figure 3-41. ....	98
Figure 3-43 Distribution of the axial stress, triaxiality ratio and crystallographic phases upon stress-induced B2→R transformation (b), and B2/R→B19' transformation (c) at highlighted stages shown in (a). ....	99
Figure 3-44 Inelastic local strain evolution in terms of inelastic macroscopic displacement. ....	102
Figure 4-1 Fatigue tests experimental protocol. a) Experimental setup. b) Clamps alignment verification. c) Three-jaw chucks used for clamping the samples. d) Schematic representation of the load applied to a sample during a fatigue testing. ....	107
Figure 4-2 Nominal stress vs extensometer elongation responses of hourglass-shaped samples tensile tested at 40, 60, and 80°C. The response at 60°C was obtained from finite element simulations. ....	108
Figure 4-3 S-N curves at 40°C (a), 60°C (b), and 80°C (c). ....	110
Figure 4-4 Schematic representation of a constant life diagram.....	113
Figure 4-5 Tensile tests carried out until rupture. The test at 40°C was stopped when the extensometer elongation reached 1mm, then the sample was observed under an optical microscope to measure the diameter of the reduced cross-section (picture on the right). ....	115
Figure 4-6 Infinite-life diagrams. The boundaries between failure and runout are plotted using the constant-life relations (4.6) to (4.8). a) B2→R loading regime (40°C). b) B2 elastic loading regime (60°C and 80°C). ....	116
Figure 4-7 Fatigue predictions. a) Goodman. b) Soderberg. c) Soderberg modified. ....	117
Figure 4-8 Parameters of the Basquin's law using three different constant-life formulations. a) Fatigue strength coefficient. b) Basquin's fatigue exponent. c) Fatigue endurance limit in fully reversed conditions. ....	118
Figure 4-9 Strain-Stress-N representation of fatigue results. ....	120
Figure 4-10 a) Typical fatigue fracture surface as viewed from light 3D microscope and SEM. 3D optical microscopy allowed us to examine the topology of the fracture surfaces. b) Five zones with distinct morphology as identified on the fracture surface. River marks shown in (a) point towards the fracture initiation zone 1, followed by the zone 2 with quasi-cleavage morphology continued with fatigue striation zone 3, ductile fatigue crack zone 4, and ductile overload zone 5. ....	121
Figure 4-11 SEM images of the crack initiation zone are shown in (a). Compared to the overload part of the samples (b) no shear lip was detected near the crack initiation zones. 3D optical microscope allowed us to reconstruct a 3D image of the surface, where we clearly see inclusions and geometric imperfections created after machining. ....	123
Figure 4-12 First crack propagation zone with quasi cleavage morphology. a) SEM images. b) Fracture surface topology. ....	124
Figure 4-13 a) Morphology of the fatigue striations zone Sst. b) Case of accelerated crack propagation due to merge of two well-developed fatigue crack fronts. ....	126

Figure 4-14 Morphology of the transition and overload zones.....	127
Figure 4-15 Size dependence of fatigue crack surfaces on the peak of nominal stress for two testing temperatures 40°C and 80°C. <b>a)</b> Fracture surface with denoted final overload surfaces for samples subjected to three different peaks of nominal stress. <b>b)</b> Dependence of the relative size of overload surfaces on the peak of nominal stress. ....	128
Figure 4-16 Evolutions of crack surface areas with the number of cycles to rupture identified for fatigue testing temperature of 40°C. The total crack area is plotted in green. A part of the crack area including crack initiation, quasi-cleavage, and fatigue striation zones is plotted in blue. ....	129
Figure 4-17 Nominal axial stresses at the final overload evaluated for testing temperatures of 40°C, 60°C, and 80°C. The stress in the y-axis was calculated as the ratio between the force at the instant of rupture and the overload surface identified by microscopy (Sov).....	129
Figure 4-18 The evolution of fatigue loading in terms of peaks of force and extensometer displacement, and force-displacement hysteresis in last 1,000 cycles before failure (a) with a zoom to last 50 cycles (b) where the loading conditions evolve with the highest rate. The results correspond to fatigue cycling at 40°C with the maximum nominal stress of 430 MPa.....	130
Figure 4-19 Evolution of tensile responses of hourglass shaped samples over 100 cycles before failure during fatigue cycling in a force controlled regime with peaks of nominal stresses below the martensitic transformation regime at 40°C a), 80°C b), and within the martensitic transformation regime at 40°C c). Related evolutions of force-displacement hysteresis are shown in d). Note that the cyclic responses and hysteresis do not change over cycling until few tens of cycles before fatigue failure.....	131
Figure 4-20 Observations of fatigue damage of an hourglass sample prior to fatigue failure at the onset of hysteresis increase upon which the fatigue test was arrested <b>a)</b> . The arrested fatigue test was performed at 40°C with R ratio of 0.1, maximum nominal stress at 580 MPa being below the nominal stress for martensitic transformation. <b>b)</b> A large crack was located on the sample and its opening was measured upon quasistatic tensile overloading at room temperature (32°C).....	132
Figure 4-21 The crack opening and local strains near the crack as measured on the sample after a fatigue test arrest prior to failure as described in Fig. 12. The measurement was performed during a force controlled tensile test till failure. Spread of martensitically transforming zone illustrated in <b>a)</b> is based on three virtual extensometers' elongation measurements near the crack tip <b>b)</b> and on the crack opening measurement <b>c)</b> all realized using DIC method. ....	134
Figure 4-22 Evolutions of temperature averaged over the gauge volume as recorded by IR camera during two fatigue tests performed for limited RAM in several interrupted slots; the first test lasting ~20e3 cycles was performed at 40°C, R=0.1, 25 Hz, a maximal nominal stress 585 MPa; the second test lasting ~2e3 cycles was performed at 80°C, R=0.1, 25 Hz, peak of nominal stress 900 MPa. Graphs a) b) show temperature evolutions during complete tests at 40°C and 80°C, respectively. Graphs c) d) show one cycle temperature and stress evolutions in selected cycles of tests at 40°C and 80°C, respectively. ....	135
Figure 4-23 Differential thermographs that evaluate spatially temperature changes with respect to the virgin state recorded in the first fatigue cycle. Thermographs show temperature changes within the gauge volumes of hourglass samples at different cycles of two fatigue tests. The first test, lasting ~20e3 cycles, was performed at 40°C, R=0.1, 25 Hz and a maximal nominal stress of 585 MPa. The second test, lasting ~2e3 cycles, was performed at 80°C, R=0.1, 25 Hz and a maximal nominal stress of 900 MPa. Thermographs in <b>(a)</b> show two localized heat sources as first spotted 6,000 and 3,000 cycles before rupture during the test at 40°C. Thermographs in <b>(b)</b> show localized heat source as first spotted 600 cycles before rupture during the test at 80°C. Thermographs in <b>(c)</b> & <b>(d)</b> show localized heat sources 20 cycles before rupture of both the tests. ...	136
Figure 4-24 Comparisons of diffraction patterns recorded on a virgin sample a) and sample that was subjected to 1000 cycles at 80 °C, R=0.1 and maximum stress of 880 MPa b). Colormaps in a), b) represents diffraction	

patterns acquired during scanning along the axial direction. Diffraction patterns shown in c), d) were recorded approximately in the center of the concave zone of the sample. ....	137
Figure 5-1 Basic experimental protocol for assessing the fatigue properties of materials using the self-heating method. The experimental setup image is shown in (a). The applied loading is presented in (b), and the equivalent temperature elevation in one block of constant amplitude cycles is illustrated in (c). The images were taken from [130].....	143
Figure 5-2 Deterministic approach for determining the endurance limit. Image replotted from [130]. ....	144
Figure 5-3 Lock-in technique used in the fast estimation of the endurance limit of a 7010 aluminum alloy. a)Mean temperature elevation. b)Amplitude of the first Fourier component. c)Difference between the amplitude of the first Fourier component and the linear fit of the first part of the curve shown in (b). d)Amplitude of the second Fourier component. ....	145
Figure 5-4 Validation of the self-heating fatigue prediction method for different materials. a)Dual phase steel [130]. b)Aluminum bronze [138]. c)Short fiber reinforced plastic[140] .....	147
Figure 5-5 Material heterogeneities at the grain scale. a)Cast defects and phase segregation in a copper aluminum alloy [138]. b) Schematic of the representative elementary volume (REV) used for multiscale modeling of the self-heating curves.....	148
Figure 5-6 Examples of common mechanisms of heat dissipation and fatigue damage in structural alloys. b)Persistent slip bands (PBS). b)Dislocation movements: mechanically reversible under low shear stress but yielding plastic deformation when Frank-Read mechanisms are generated.....	149
Figure 5-7 Simplification of the thermal diffusion problem. ....	150
Figure 5-8 Experimental setup used for infrared thermographs acquisition upon self heating measurements. a)Tests performed inside the heat chamber (40° and 80°). b)Tests performed at ambient temperature (~25°C). c)Schematic representation of the position of the sample within the testing machine clamps.....	152
Figure 5-9 Schematic representation of the load sequence applied to one sample during a self-heating test. a) Successive blocks of constant stress amplitude cycles. b) Illustration of the cyclic loading applied in one block of cycles.....	154
Figure 5-10 Infrared emissivity (here denoted as $\epsilon$ ) evolution in terms of the angle of vision of the IR camera with respect to the normal of the sample surface ( $\varphi$ ). Schematic image taken from [147].....	155
Figure 5-11 Post-processing of temperature data acquired during self-heating measurement. a) Evaluation zones for $T$ and $T_s$ . b) Example of the conversion of raw temperature data into temperature elevation data.....	156
Figure 5-12 Example of the frequency spectrum obtained using a discrete Fourier transformation algorithm. ....	157
Figure 5-13 Low pass filtering of the temperature data recorded in the mid cross-section of the sample. ....	157
Figure 5-14 Identification of the steady-state temperature elevation $\theta$ .....	157
Figure 5-15 Self-heating curves.....	159
Figure 5-16 Comparison of the temperature elevations extracted from blocks of cycles at 25°C (a), 40°C(b), and 80°C (c).....	160
Figure 5-17 Effects of the loading frequency on self-heating behavior of NiTi samples. ....	161
Figure 5-18 Harmonic decomposition of the temperature elevation signal.....	161
Figure 5-19 DC value of the temperature elevation signal. a)25°C. b)40°C. c)80°C. ....	162
Figure 5-20 First harmonic amplitude of the temperature elevation signal. a)25°C. b)40°C. c)80°C. ....	163
Figure 5-21 Second harmonic amplitude of the temperature elevation signal. a)25°C. b)40°C. c)80°C.....	164

Figure 5-22 Third harmonic amplitude of the temperature elevation signal. a)25°C. b)40°C. c)80°C.....	164
Figure 5-23 Steel samples. a)Geometry. b)Quasi-static tensile response. ....	165
Figure 5-24 Self-heating of steel samples .....	166
Figure 5-25 Cooling stage after cycling. a) Dog-bone sample. b) Hourglass sample. ....	166
Figure 5-26 Schematic representation of the conversion of 2D thermographs into 1D array of temperature elevation values.....	168
Figure 5-27 Temperature elevations upon high strain rate tests in the B2↔R loading regime at 40°C. a)Load up to 500MPa. b)Unloading down to 10 MPa. c) Nominal stress vs extensometer elongation response. ....	169
Figure 5-28 Temperature elevations upon high strain rate tests in the B2↔R loading regime at 80°C. a)Load up to 800MPa. b)Unloading to 10 MPa. c) Nominal stress vs extensometer elongation response.....	170
Figure 5-29 Temperature elevations upon high strain rate tests in the B2/R↔B19' loading regime at 40°C. a)Load up to 630MPa. b)Unloading down to 10 MPa. c) Nominal stress vs extensometer elongation response. ....	171
Figure 5-30 Temperature elevations upon high strain rate tests in the B2/R↔B19' loading regime at 80°C. a)Load up to 930MPa. b)Unloading down to 10 MPa. c) Nominal stress vs extensometer elongation response. ....	172
Figure 5-31 Fitting of a Gaussian function to the temperature profile obtained at the end of the high strain loading test presented in Figure 5-27a.....	179
Figure 5-32 Results of simulations of the natural cooling/heating after high strain rate tests presented in Figure 5-27a (a) and Figure 5-27b (b). In addition the differences between the experimental temperature elevations and the modeled ones are presented in the form of height-time-temperature diagrams.....	180
Figure 5-33 Simulated temperature response of an isotropic elastic hourglass-shaped sample under cyclic tensile stress. a) Height-time-temperature diagram showing the axial temperature distribution of the total length of the sample in the last 10 cycles of the simulation. b) Temperature elevation evolution in the mid cross-section. ....	181
Figure 5-34 Frequency spectrum of the temperature elevation response in the mid cross-section of an elastic hourglass-shaped sample under cyclic tensile loading.....	182
Figure 5-35 Schematic representation of the loop routine used for simulating the thermomechanical response of cyclic loaded hourglass-shaped NiTi samples. ....	182
Figure 5-36 Simulated stress-strain response of an hourglass-shaped NiTi sample under cyclic tensile stresses, where the thermoelastic effect has been neglected.....	183
Figure 5-37 Simulated temperature response of NiTi hourglass-shaped sample under cyclic tensile stress neglecting the thermoelastic contributions. a) Height-time-temperature diagram showing the axial temperature distribution of the total length of the sample in the last 10 cycles of the simulation. b) Temperature elevation evolution in the mid cross-section.....	183
Figure 5-38 Frequency spectrum of the temperature elevation response in the mid cross-section of NiTi hourglass-shaped sample under cyclic tensile loading, where the thermoelastic effect has been neglected. ...	184
Figure 5-39 Simulated stress-strain response of an hourglass-shaped NiTi sample under cyclic tensile stresses considering both the thermoelastic effect and the transformation latent heats.....	185
Figure 5-40 Simulated temperature response of NiTi hourglass-shaped sample under cyclic tensile stress considering both the transformation latent and the thermoelasticity. a) Height-time-temperature diagram showing the axial temperature distribution of the total length of the sample in the last 10 cycles of the simulation. b) Temperature elevation evolution in the mid cross-section. ....	185

Figure 5-41 Frequency spectrum of the temperature elevation response in the mid cross-section of NiTi hourglass-shaped sample under cyclic tensile loading, considering both the thermoelastic effect and the transformation latent heats.....185



# List of Tables

Table 2-1 Estimates of the lifetime of a NiTi actuator according to its strains and stress outputs. This table was extracted from [59].	30
Table 3-1. Chemical composition of studied NiTi wires certified by FWM, the provider of the wires. The values are expressed in wt.%.	58
Table 3-2. Relation between the thickness of TiO <sub>2</sub> layer and its color according to Velten et al.[103]	63
Table 3-3 Transformation temperatures of 400°C and 500°C annealed NiTi.	65
Table 3-4. Phase transformation thermal hysteresis ( $\delta$ ), specific heat exchange upon transformation ( $\Delta Q$ ) and specific heat capacities ( $Cp$ ) of individual phases of NiTi annealed at 400 and 500°C. The heat capacities obtained upon heating and those obtained upon cooling are marked with $\uparrow$ and $\downarrow$ symbols respectively.	66
Table 3-5 2D-DIC parameters	72
Table 3-6 Model parameters used for simulating the tensile response of the studied material in a range of temperatures between 30-80°C.	93
Table 4-1 Selection of fatigue tests used for the calculation of the endurance limit at 40°C. The tests marked as X represent failure and those marked as O represent runout.	111
Table 4-2 Selection of fatigue tests used for the calculation of the endurance limit at 60°C. The tests marked as X represent failure and those marked as O represent runout.	111
Table 4-3 Selection of fatigue tests used for the calculation of the endurance limit at 80°C. The tests marked as X represent failure and those marked as O represent runout.	111
Table 4-4 Calculation of the mean endurance limit at 40°C.	112
Table 4-5 Calculation of the mean endurance limit at 60°C	112
Table 4-6 Calculation of the mean endurance limit at 80°C	112
Table 4-7 Estimate of the endurance limit in fully-reversed conditions at 40°C. The failure of the tested samples occurred in the mid cross-section.	114
Table 4-8 Estimate of the endurance limit in fully-reversed conditions at 60°C. The failure of the tested samples occurred inside the clamps. The sample 1 failed after 15718 cycles under a stress amplitude of 320MPa, sample 2 did it after 34504 cycles under a stress amplitude of 380MPa, and sample 3 failed after 198310 cycles under a stress amplitude of 460MPa.	114
Table 4-9 Estimate of the endurance limit in fully-reversed conditions at 80°C. The failure of the tested samples occurred inside the clamps. The samples 1 and 2 failed under a stress amplitude of 403MPa. The sample 1 failed after 126204, while sample 2 did it after 234800 cycles.	114
Table 5-1 Main technical characteristics of MWIR detectors used for self-heating measurements.	153
Table 5-2 Thermal material parameters for simulations of tensile loadings on NiTi hourglass-shaped samples	179





# Chapter 1. Introduction

## 1.1. Introduction

This Ph.D. dissertation thesis addresses the conditions and mechanisms that lead superelastic NiTi wires to fail under cyclic mechanical loadings, termed structural fatigue. NiTi is a very particular alloy that exhibits shape memory properties. When subjected to mechanical loading, NiTi can reach up to 10% fully reversible strain; much higher than the maximum elastic strain of traditional metals, which is below 1%. The superelastic behavior of NiTi results from solid-state martensitic phase transformations, which, although very attractive for their associated macroscopic properties, make it more difficult to understand and predict the thermomechanical behavior of these alloys.

The structural fatigue has become one of the main topics in NiTi research since the boom of NiTi biomedical applications in the 1990's. However, despite the refinement of the fabrication process of NiTi alloys and the advances in the characterization of their properties, achieving a stable thermomechanical response and long fatigue lives are still some of the main concerns of the scientific community. The lack of understanding of the sources of fatigue damage in NiTi hinders the development of life prediction models. As a result, engineers and designers tend to use largely conservative models to predict the fatigue life of NiTi-based devices, or simply put them under expensive fatigue testing.

The role of phase transformations in the initiation of cracks and their subsequent propagation remains unanswered. On the one hand, martensitic phase transformations may show full reversibility, without evidence of macroscopic damage. Moreover, they serve as stress relief mechanisms around defects [1], playing a similar shielding role as plastic deformation does in traditional structural alloys. On the other hand, when the material undergoes repetitive mechanical loading involving back and forth phase transformations, it withstands only some thousands of cycles in the best-case scenario. This fatigue performance contrasts with the millions of cycles that one may obtain in the absence of phase transformations. As a result, at first sight, one may blame martensitic phase transformations for the early failure of NiTi structures, although the scientific community lacks fundamental understanding on how the structural damage initiates and proceeds through the material.

In NiTi, the progressive fatigue damage upon loading cycles depends strongly on factors such as stress/strain levels, temperature, alloy composition and thermomechanical history

(to be detailed in Chapter 2). The Low Cycle Fatigue (LCF) regime in NiTi is associated to stress-induced martensitic phase transformations, given that the material barely supports some thousands of cycles under repetitive transformation conditions. In the High Cycle Fatigue (HCF) regime on the other hand, the material does not evidence any macroscopic sign of damage upon cycling. As we will detailed later in Chapter 2, fatigue studies on NiTi have overlooked the HCF regime leading to the idea that non-transforming NiTi has infinite fatigue life.

One of the main difficulties related to the HCF testing of NiTi is the size and shape of the testing samples. The size of the samples used for testing biomedical NiTi oscillates in the order of hundreds of micrometers, making it difficult to machine them into a standard HCF geometry. Consequently, most failures of constant cross-section samples tested in the HCF regime occur within the testing machine grips. This hinders us to draw reliable conclusions about the fatigue of NiTi, as the actual stress/strain state at the failure spot is unmeasurable. To face this difficulty we propose in this study to analyze the tensile fatigue behavior of relatively larger diameter NiTi wires machined into an hourglass shape. In this way, we intend to confine all transformation and fatigue processes into the middle volume of the sample, making it easier to track the material structural and functional properties during application of tensile stress cycles. Moreover, we believe that hourglass shaped samples suppress the undesired effects of strain localization, which, as discussed in the later in Chapter 2, has a huge detrimental impact on the fatigue life of tensile tested NiTi.

In the following sections of this introductory chapter, we present the basic concepts of shape memory alloys. Then, we review the historical development of NiTi since its discovery. After that, we state the purposes of this study and the procedure adopted for addressing them. Finally, the last section of this introductory chapter presents the organization of this document.

## 1.2. Generalities of Shape Memory Alloys

NiTi alloys are classified as Shape Memory Alloys (SMA), as they are capable of displaying large reversible deformations during temperature or stress changes. This behavior is the consequence of solid-state reversible martensitic phase transformations. The crystallographic phases responsible for the deformation processes in SMA are known as Austenite, the hot phase, as it is stable at high temperatures, and Martensite, the cold phase, stable at low temperatures. The structures of both crystallographic phases vary depending on the alloy. In NiTi alloys, the austenite phase has a CsCl-like cubic structure and the martensite B19' has a monoclinic structure. We detail the main characteristics of these phases in the first part Chapter 2. The phase transformations in SMA's are diffusionless, hence they are time-independent processes characterized by the unchanged chemical composition of product phases with respect to the parent phase.

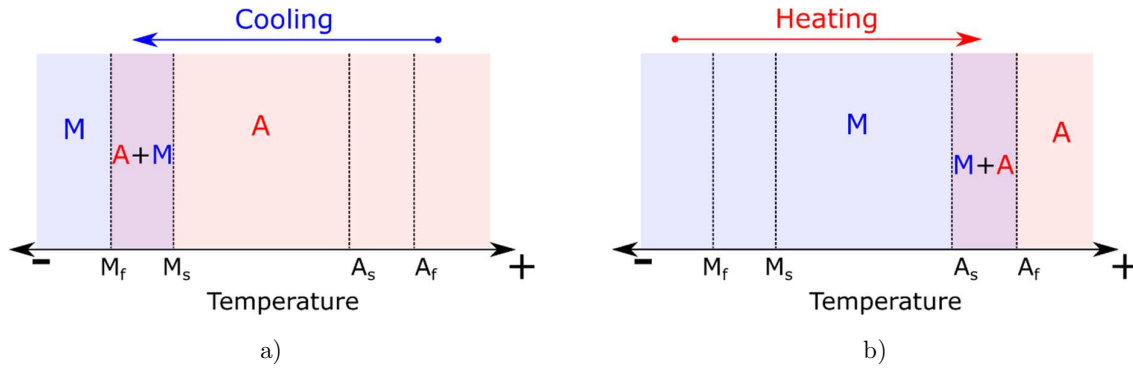


Figure 1-1 Schematic representation of the temperature domains of austenite and martensite phases upon cooling (a) and upon heating (b).

Temperature-induced transformations proceed through nucleation and propagation stages. The nucleation of martensite crystals within the austenite matrix (forward transformation) starts upon cooling at a temperature denoted as  $M_s$ . Upon further cooling, nuclei of martensite expand at the austenite's expense until the entire matrix becomes martensite at a temperature denoted as  $M_f$  (see the schematic representation in Figure 1-1a). During heating, the reverse transformation starts at a temperature denoted as  $A_s$  and finishes at temperature  $A_f$  (Figure 1-1b). Experimental evidence shows that  $M_f < A_s$ , consequently, phase transformations in SMAs exhibit thermal hysteresis.

From a simplified point of view, the structure of martensite is an elongated version of the austenite structure. Since the first martensite nuclei grow at the expense of a group of austenite lattices, it must accommodate itself to the available space left in the matrix. Due to this restriction, different variants of martensite develop in different directions in such a way that their local lattice distortions do not add to macroscopic deformation. Only when stress is applied, the martensite variants orient towards a common direction, producing large macroscopic deformations. The interesting part of this process is that the apparent macroscopic plastic deformation that remains after unloading martensitic sample can be recovered if the material transforms back into austenite (upon heating). This property is known as Shape Memory Effect (Figure 1-2a). If the SMA element is rather heated and cooled under constant stress, there is not only the high-temperature shape that is going to be remembered but also the low temperature one. Since the material produces mechanical work, a thermal cycle like this is considered as an actuation cycle. This property is a variant of the shape memory effect, often denoted as assisted two-way shape memory effect (Figure 1-2b).

Martensitic phase transformations can be also induced by stress under constant temperature conditions. In a similar way to the process described above for temperature-induced transformations, there exist stress thresholds that initiate stress-induced transformations. The process is described as follows. An austenitic element transforms into martensite at a stress threshold denoted as  $\sigma_{mt}$ . Since the produced martensite variants are oriented due to the applied stress, large macroscopic deformations are generated with the transformation (see the low stiffness zone of the curve above  $\sigma_{mt}$  in Figure 1-2c). When the stress is relieved, martensite becomes unstable at the stress threshold  $\sigma_{rev}$  and transforms

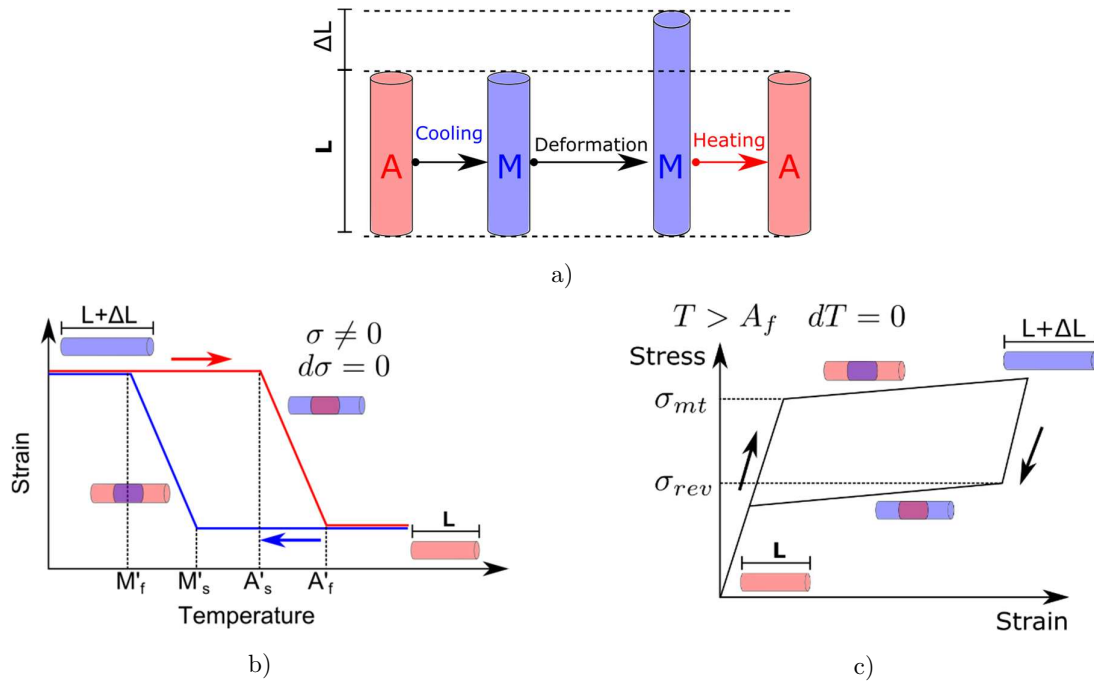


Figure 1-2 a) Schematic representation of the shape memory effect. b) Actuation cycle or two-way shape memory effect. c) Superelasticity. Note that, since stress is applied, the transformation temperatures  $M'_f$ ,  $M'_s$ ,  $A'_s$ , and  $A'_f$  in (b) are higher than their stress-free counterparts  $M_f$ ,  $M_s$ ,  $A_s$ , and  $A_f$  introduced back in Figure 1-1.

back into austenite. Such behavior gives rise to the characteristic superelastic property in SMA's (Figure 1-2c).

The described processes involve exchanges of thermal, chemical and mechanical energy. In an effort to describe these phenomena, Wollants et al. established in 1979 the basis of the thermodynamic framework of martensitic phase transformations [2]. They proposed a minimization of the amount of energy that the material can perform under the effects of external mechanical loading. We describe the basic concepts of this framework later in Chapter 2 (section 2.2).

NiTi is by far the most common SMA used in the industry nowadays, not only because of its outstanding shape memory properties, but also for its good structural properties, corrosion resistance, and biocompatibility. The most successful applications of NiTi are found in biomedicine. Self-expanding stents for the treatment of vascular diseases, endodontic wires for root canal treatment, and orthodontic archwires are some of the most common devices fabricated from NiTi. We detail more about NiTi applications in Chapter 2 (section 2.4).

### 1.3. Historical Background and Overview

The development of Shape Memory Alloys is relatively recent compared to steel or even aluminum alloys. The first observation of shape changes related to metallic solid-state phase transformations was done on an AuCd alloy by Olander in 1932 [3]. Twenty years later, Chang and Read [4] discovered that the shape changes in Au-Cd were reversible, leading to

the concept of Shape Memory effect. Reynolds and Bever [5] did a similar discovery concurrently on Cu-Zn alloys but observed that elastic strains shifted the phase transformation temperatures to higher values. At the end of the 50's, Rachinger [6] introduced the concept of superelasticity after observations made on Cu-Al-Ni subjected to back and forth tensile stresses at a constant temperature. The mathematical description of the phase transformation mechanisms in SMA was first proposed by Wechsler et al. [7] and Bowles & Mackenzie [8] in 1953 and 1954 respectively. They established the so-called "phenomenological theory of martensitic transformations". In 1987, Ball & James [9] proposed an alternative theory known as the "nonlinear theory of martensitic transformations". Both theories permit researchers to predict the crystal phase variants during martensitic transformations in SMA, based on the geometry of the parent and product phases.

In 1963, despite the awareness of the properties of SMA, Buehler, Gilfrich, and Wiley [10] misunderstood the origins of the shape memory effect on NiTi when they discovered it. It was only until 1971 when Wasilewski [11] recognized that reversible solid-state phase transformations were at the origin of shape memory behavior in NiTi.

The shape memory properties of NiTi, together with its good corrosion resistance, biocompatibility, and sound mechanical properties were very attractive for the development of engineering applications right after its discovery. However, difficulties in manufacturing stemmed from melting accuracy, purity, forming and machining, hindered the commercial development of NiTi-based devices. It was only until the early 1980's when the first NiTi devices came to light in form of orthodontic archwires [12] and human implants [13].

In the 1990's, the biomedical industry started producing new products stimulated by the demand for smaller and less invasive devices. In this way, products such as endodontic NiTi files, NiTi hook wires for tumor detection, thermally deployed atrial septal occlusion devices and thermally deployed vena cava filters started to be commercialized [14]. By the same time, stents, devices used to scaffold diseased arteries, were born giving room to the most commercially-important product ever made from NiTi [15].

The growing interest in industrial applications came along with an expansion of the scientific community working on SMA. As a result, in the last thirty years, the research community have made significant advances in terms of characterization of the crystallographic microstructure, description of mechanisms of phase transformations, characterization of material properties, and fabrication of NiTi alloys.

The binary phase diagram of NiTi, as it is known today, was proposed by Massalski et al. in 1991[16]. They included the groundbreaking results from Nishida et al. [17] in 1986, who established the chemical composition of concurrent crystallographic microstructures of near equiatomic NiTi. However, difficulties related to the production of single crystals hindered an early development of the fundamental crystallography theory of phase transformations in NiTi. In 1999, Hane & Shield [18] finally achieved to calculate all the possible twinned variants of martensite produced after phase transformation using the nonlinear theory of Ball & James, already employed in the crystallography description of other SMA. More

recent works, such as the one of Zhang & Sehitoglu [19] contributed with calculations of twin systems of R-phase, an intermediate phase sometimes induced between austenite and martensite in NiTi alloys.

Thermomechanical experimental data obtained since the discovery of NiTi allowed the early characterization of the main phenomenological features of properties such as superelasticity or shape memory effect. Several articles and books have been written in this respect [20]–[22]. As a result, the deformation mechanisms responsible for the particular thermomechanical behavior of NiTi alloys have been identified and documented with respect to temperature, loading type, alloy heat treatment, and alloy composition. However, there are still some unresolved questions especially regarding the relationship between shape memory mechanisms and crystallographic lattice damage. Consequently, the sources of the cyclic degradation of the functional properties of NiTi, as well as their fatal failure, are one of the present topics of debate among the NiTi research community.

The strict requirements of biomedical devices for proving safety and efficacy have pushed researchers to investigate the fatigue of NiTi. From the often cited article of Eggeler et al. [23], researchers approaches the fatigue of NiTi from two different perspectives: functional fatigue, and structural fatigue. Functional fatigue addresses the degradation of the functional properties of NiTi upon thermomechanical cycles, which means the decrease of phase transformation strain, appearance of residual strain, changes in the strain hardening response of the material, and shifting of its characteristic transformation temperatures. Structural fatigue, on the other hand, addresses the number of cycles that the alloy can resist before failure under certain thermomechanical repetitive loading.

The first studies of the structural fatigue of NiTi were carried out in 1979 by Melton & Mercier [24], who produced the first Stress-N curves for polycrystalline NiTi bars tested at different temperatures. However, early in the 1990’s researchers opted rather for strain-life approaches expecting to reproduce better the in-service loading conditions on NiTi devices. In this regard, the development of rotating-bending experiments boosted the number of fatigue data of biomedical wires. In consequence, the majority of the fatigue curves available in the literature corresponds to rotating-bending experiments, although most of the characterization prior to fatigue testing is carried out by tensile tests. In Chapter 2, we detail the most important outcomes of fatigue experiments reported in the literature concerning the mechanisms and thermomechanical conditions leading to fatigue failure in NiTi alloys.

## 1.4. Statement of the Problem

The mechanisms and loading conditions that lead NiTi components to fatigue failure are a current topic of debate. We consider that the roles of martensitic transformations and plastic deformation remain unclear in spite of the growing amount of data concerning the fatigue of NiTi reported in the literature in the last decade. Moreover, due to the complex thermomechanical behavior of NiTi, we recognize difficulties to interpret the effects of stress/strain, temperature, and microstructure initial state on the fatigue performance of NiTi using traditional stress/strain-N curves only. Finally, we encounter that most of the

NiTi fatigue studies focus on its Low Cycle Fatigue behavior, thus, overlooking the assessment of the High Cycle Fatigue aspects of the alloy.

## 1.5. Purpose of the study

The first purpose of this study is to develop a new experimental protocol that will allow us to better assess the fatigue performance of superelastic NiTi wires. We opted for using hourglass-shaped samples subjected to pull-pull tensile stress cycles under controlled temperature conditions. The hourglass geometry allows us to confine all deformation, transformation and fatigue processes in the middle of the sample, hence avoiding the undesired effects of localization during fatigue testing of superelastic NiTi wires. Moreover, this shape is more suitable for evaluating the High Cycle Fatigue of NiTi as it prevents the rupture of the sample inside the grips.

The second purpose of the study is to apply the self-heating method for evaluating the fatigue performance of NiTi wires. The self-heating have proven efficacy as a HCF assessment method of traditional structural alloys such as steel and aluminum alloys. This approach is based on the assumption that local damage occurs through micro plasticity that engenders thermal energy dissipation. By implementing this technique, we intend to contribute to the understanding of the relationship between plasticity, phase transformations and fatigue in NiTi alloys.

## 1.6. Procedures

In this document, we propose different experimental and modeling techniques to determine how the accumulation of damage and microstructure changes proceed in NiTi components subjected to cyclic tensile stresses.

The first part of this work focuses on the characterization of the thermomechanical behavior of superelastic NiTi wires processed into hourglass-shaped samples. There, we combine finite element analysis, with full field strain measurements and X-ray diffraction experiments to obtain the stress-strain and crystallographic phase distribution in the middle part of the samples.

In the second part, we analyze the fatigue performance of hourglass shaped samples subjected to stress-controlled pull-pull fatigue experiments under controlled temperature conditions. This allowed us to evaluate the fatigue behavior of NiTi in different loading scenarios involving different phase transformation paths. We complemented the fatigue analysis by Optical and Scanning Electron microscopy observations, in-situ infrared thermography and ex-situ X-ray diffraction experiments.

Finally, in the last part of this document we analyze the Self-Heating response of NiTi using infrared thermography. We perform the analysis of the recorded thermographs in the time and frequency domains to identify patterns that might serve as indicators of fatigue damage initiation.

## 1.7. Organization of the dissertation

This dissertation is divided into four chapters. In Chapter 2, we present the state of the art of the fatigue of NiTi alloys. For the purpose of illustration, in the beginning of this chapter, we introduce shortly the main properties of NiTi, which position it as the most frequently used SMA for industrial applications. Then, we describe the most important outcomes concerning the fatigue behavior of NiTi alloys.

In Chapter 3, we start by describing the impact of the cross-section reduction in the tensile behavior of cylindrical cross-section samples using linear-elastic and perfect-plastic constitutive laws. After that, we describe the preparation of the NiTi hourglass shaped samples, highlighting the impact of heat treatment on the thermomechanical response of NiTi. Then, we characterize the thermomechanical response of NiTi hourglass shaped samples subjected to a selected heat treatment. We complement the characterization of these samples using finite element simulations, high-resolution x-ray diffraction, and Digital Image Correlation (DIC).

In Chapter 4, we analyze the fatigue behavior of NiTi hourglass-shaped samples at different temperatures with a focus on the HCF regime. There, we complement classic S-N and Strain-N approaches with detailed observations of the fracture surfaces, in-situ detection of crack nucleation and propagation through infrared thermography and ex-situ X-ray diffraction.

Finally, in Chapter 5 we introduce the self-heating method. We start this chapter outlining the study cases that demonstrate the efficacy of the method for predicting the fatigue behavior of different materials, as well as the theoretical framework that supports the method. After that, we detail the experimental protocol and post-processing techniques used for applying the self-heating to our NiTi hourglass-shaped samples. We finish the chapter showing experimental results and their subsequent analysis using one-dimensional thermomechanical simulations.

# Chapter 2. State of the Art

In this chapter, we introduce the main characteristics of NiTi alloys. In section 2.1, we start describing the main physical metallurgy features of this alloy, including the crystallographic aspects of its unique solid-state phase transformations. After that, we present the macroscopic aspects of phase transformations of NiTi, which we describe using the phenomenological framework of martensitic phase transformations. This framework will facilitate the understanding of the thermomechanical model used for simulating the tensile response of NiTi hourglass shaped samples later in Chapter 3. In section 2.3, we detail the mechanical properties of NiTi alloys that makes it an attractive candidate for engineering applications, some of which we introduce in section 2.4. We show how the lifetime requirements of NiTi used for applications motivated a large number of fatigue studies since the 1980's. In section 2.5, we present the most important outcomes of the fatigue studies published in the literature. This chapter concludes by presenting the up-to-date information about the characterization, prevention, and prediction of fatigue failure in NiTi-based devices.

## Contents

<b>2.1. Physical Metallurgy of NiTi Alloys .....</b>	<b>11</b>
2.1.1. Binary Phase Diagram .....	11
2.1.1.1. NiTi or B2 phase .....	12
2.1.1.2. $Ti_3Ni_4$ .....	12
2.1.1.3. B19' phase .....	13
2.1.1.4. R-phase .....	13
2.1.2. Martensitic Phase Transformations in NiTi Alloys .....	13
2.1.2.1. B2→B19' transformation .....	15
2.1.2.1. B2→R and R→B19' transformations .....	16
<b>2.2. Thermodynamic aspects of phase transformations in NiTi .....</b>	<b>16</b>
2.2.1. Thermal hysteresis .....	16
2.2.1.1. Gibbs free energy potential .....	17
2.2.2. Heat release/absorption .....	20
2.2.3. Effects of externally applied stresses – Clausius-Clapeyron relation .....	21
<b>2.3. Mechanical Properties of NiTi alloys .....</b>	<b>22</b>

---

2.3.1. Detwinning of B19' and R-phase.....	22
2.3.2. Elasticity.....	24
2.3.2.1. B2.....	24
2.3.2.2. B19'.....	24
2.3.2.3. R-phase.....	24
2.3.3. Stress-induced phase transformations & superelasticity.....	25
2.3.3.1. Deformation localization.....	27
2.3.4. Plastic deformation through dislocation slip.....	27
<b>2.4. Applications of NiTi .....</b>	<b>29</b>
2.4.1. Constrained-recovery .....	29
2.4.2. Actuation.....	30
2.4.3. Superelastic.....	30
2.4.3.1. Stents.....	30
2.4.3.2. Endodontic files.....	32
2.4.3.3. Dampers for civil engineering structures.....	32
2.4.3.4. Elastocaloric devices.....	33
<b>2.5. Fatigue of NiTi Alloys .....</b>	<b>33</b>
2.5.1. Functional fatigue.....	34
2.5.1.1. Temperature cycles.....	34
2.5.1.2. Stress cycles.....	35
2.5.2. Structural fatigue.....	36
2.5.2.1. Commonly used experimental setups.....	37
2.5.2.2. Classic fatigue approaches.....	39
2.5.2.3. Special features of fatigue life curves.....	41
2.5.2.4. Fatigue damage mechanisms.....	42
<b>2.6. Summary.....</b>	<b>43</b>

## 2.1. Physical Metallurgy of NiTi Alloys

### 2.1.1. Binary Phase Diagram

Figure 2-1 shows the equilibrium phase diagram of the Ti-Ni alloy system according to Massalski et al.[16], taking into account the later modifications made by Otsuka and Ren [20]. The phase diagram has a vital importance in the production of NiTi because the ratio Ni/Ti plays a determinant role in the setup of the alloy functional properties [25]. Binary NiTi Shape Memory Alloys are B2 intermetallic compounds located in the central part of the phase diagram. Their composition lays between  $\sim 49.5$  and 57 at. %Ni [25].

As shown in the phase diagram, the boundary of NiTi B2 phase from the Ti-rich side is practically vertical and close to 50Ni. In the Ni-rich side, at temperatures above 650°C, the boundary on the Ni-rich shows a positive slope, reflecting an increase of the solubility of Ni in the B2 phase with temperature. At temperatures below 650°C, the B2 region becomes very narrow, therefore Nickel-rich B2 compositions often exhibit some precipitation reactions.

The characterization of the crystallographic phases in the near equiatomic NiTi region took some time after its discovery, mainly because of difficulties regarding the production of single crystals of NiTi. It was only until 1986 when Nishida et al. [17] shed light on the evolution of metastable and stable phases of NiTi at different temperatures. They performed diffusion-controlled studies on a 52 at. %Ni alloy with parallel metallography observations, electron microscopy observations, and energy dispersive X-ray spectroscopy (EDS) measurements. As a result, they generated the first reliable time-temperature-transformation (TTT) diagram for NiTi alloys, which we reproduce in Figure 2-2.

The conclusions of this study permitted to define three possible scenarios of the diffusion-controlled phase transformations in near equiatomic NiTi alloys:

- a. for NiTi aged at temperatures below 680°C:-



- b. for NiTi aged at temperatures between 680°C and 750°C:



- c. for NiTi aged at temperatures between 750°C and 800°C:



The *aging* term is replaced by *annealing* when referring to the heat treatment of polycrystalline NiTi, due to recovery and recrystallization processes that occur together with precipitation reactions during the heat treatment.

The most common annealing temperatures for polycrystalline shape memory NiTi are between 400°C-600°C, as higher annealing temperatures result in bigger grain size, which worsens the functional properties of the alloy. For this reason, the most common phases encountered in near equiatomic NiTi SMA are the B2 phase and  $\text{Ti}_3\text{Ni}_4$  phase, which appears in the form of precipitates. Moreover, when lowering the temperature, the B2 phase can transform into metastable monoclinic B19' phase or metastable trigonal R-phase. The

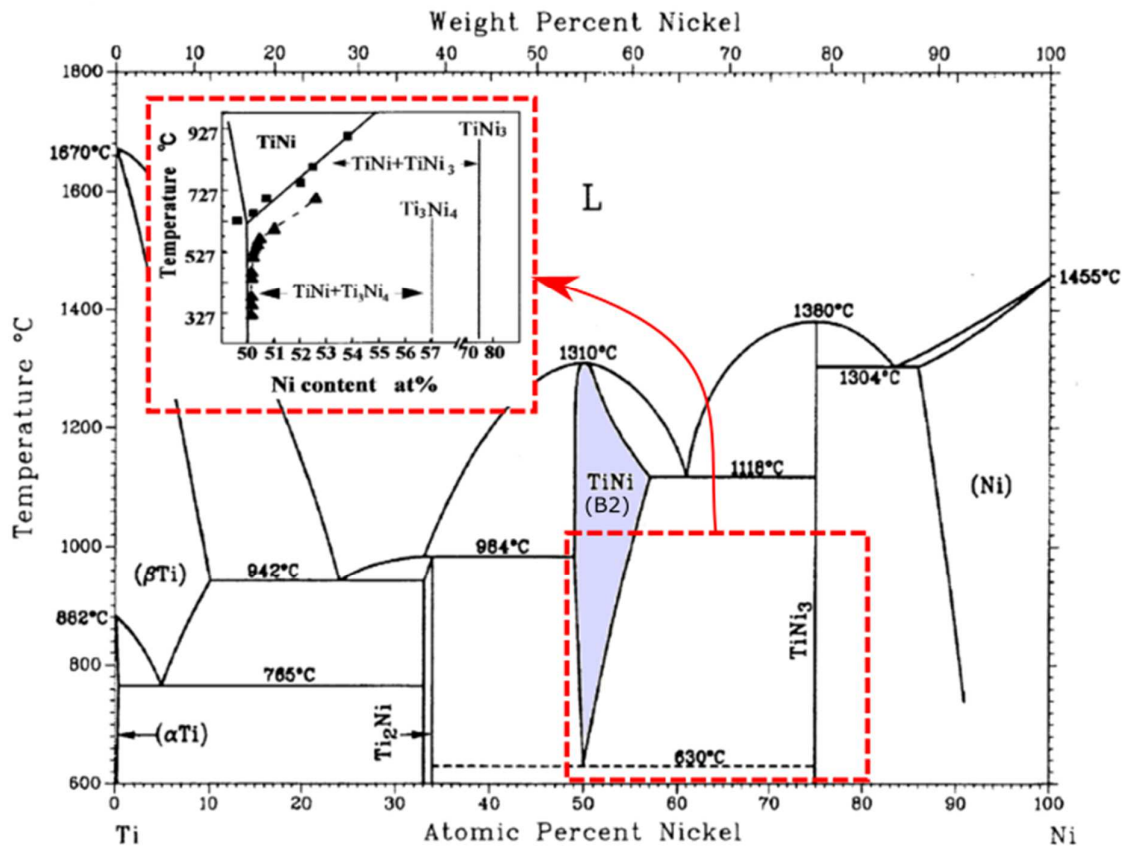


Figure 2-1 Binary phase diagram of NiTi alloys.

characteristics of the crystallographic phases that are present in shape memory NiTi alloys are briefly described next.

#### 2.1.1.1. NiTi or B2 phase

NiTi or B2 phase (Figure 2-3a) has a Cs-Cl-type B2 ordered structure with a lattice constant  $a_0=0.3015\text{nm}$  at room temperature. The B2 structure can be viewed as an ordered BCC lattice formed by two interpenetrated primitive cubic lattices of Ni and Ti atoms. This crystallographic phase is considered as the parent phase when describing phase transformation processes in NiTi, also denoted as austenite.

#### 2.1.1.2. Ti<sub>3</sub>Ni<sub>4</sub>

Ti<sub>3</sub>Ni<sub>4</sub> are coherent precipitates that form lenticular-shaped domains as observed in the electron micrograph in Figure 2-3d. Its lattice microstructure is rhombohedral with parameters  $a=0.670\text{nm}$  and  $\alpha=113.8^\circ$ . The structure of Ti<sub>3</sub>Ni<sub>4</sub> consist of planes ABCDEF shown in Figure 2-3d, stacked in the direction of axis  $\{111\}_{\text{B2}}$  of B2. Ti<sub>3</sub>Ni<sub>4</sub> precipitates introduce distortion inside the B2 matrix, therefore, they induce internal stress and increase the elastic energy stored in the matrix. This increase of elastic energy may lead to a phase transformation from B2 phase into R-phase, as detailed in later sections.

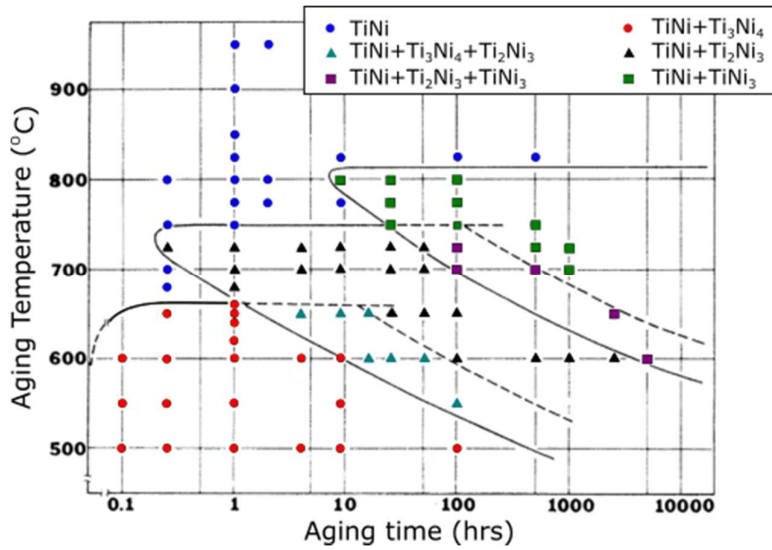


Figure 2-2 Transformation-Time-Temperature (TTT) diagram of a 52 at. %Ni alloy by Nishida et al. [17].

### 2.1.1.3. B19' phase

B19' martensite exhibits an internal twinned structure. Its lattice is monoclinic (Figure 2-3b). Contrarily to the lattice parameter of B2 phase, which is standard for binary NiTi alloys, the lattice parameters of B19' phase depend on the chemical composition of the alloy and temperature. For instance, the lattice parameters reported by Hane and Shield for a Ti-49.75at.%Ni are [18]:

- $a=0.2889\text{nm}$ ,
- $b=0.4120\text{nm}$ ,
- $c=0.4662\text{nm}$ ,
- and  $\beta=96.88^\circ$ .

### 2.1.1.4. R-phase

R-phase has trigonal structure. We can perceive the structure of R-phase as an elongated version of the B2 phase in the  $\langle 111 \rangle$  direction as illustrated in Figure 2-3c. The R-phase shows a deviation of the angle  $\alpha$  from  $90^\circ$  by lowering the temperature [26]. According to Sittner et al. [27], the lattice parameters of R-phase are

- $a=0.73535\text{nm}$ ,
- $c=0.52582\text{-}0.52759\text{ nm}$  (for  $\alpha$  between  $89.57^\circ$ -  $89.32^\circ$ ).

Like the B19' phase, R-phase shows an internal twinned structure.

## 2.1.2. Martensitic Phase Transformations in NiTi Alloys

Depending on the applied thermomechanical heat treatment, the B2 phase can transform in a single step into B19' phase upon cooling or follow a two-step phase transformation passing first through the R-phase. A single step phase transformation is observed in the solution treated NiTi, where precipitation reactions are avoided, while two-step phase

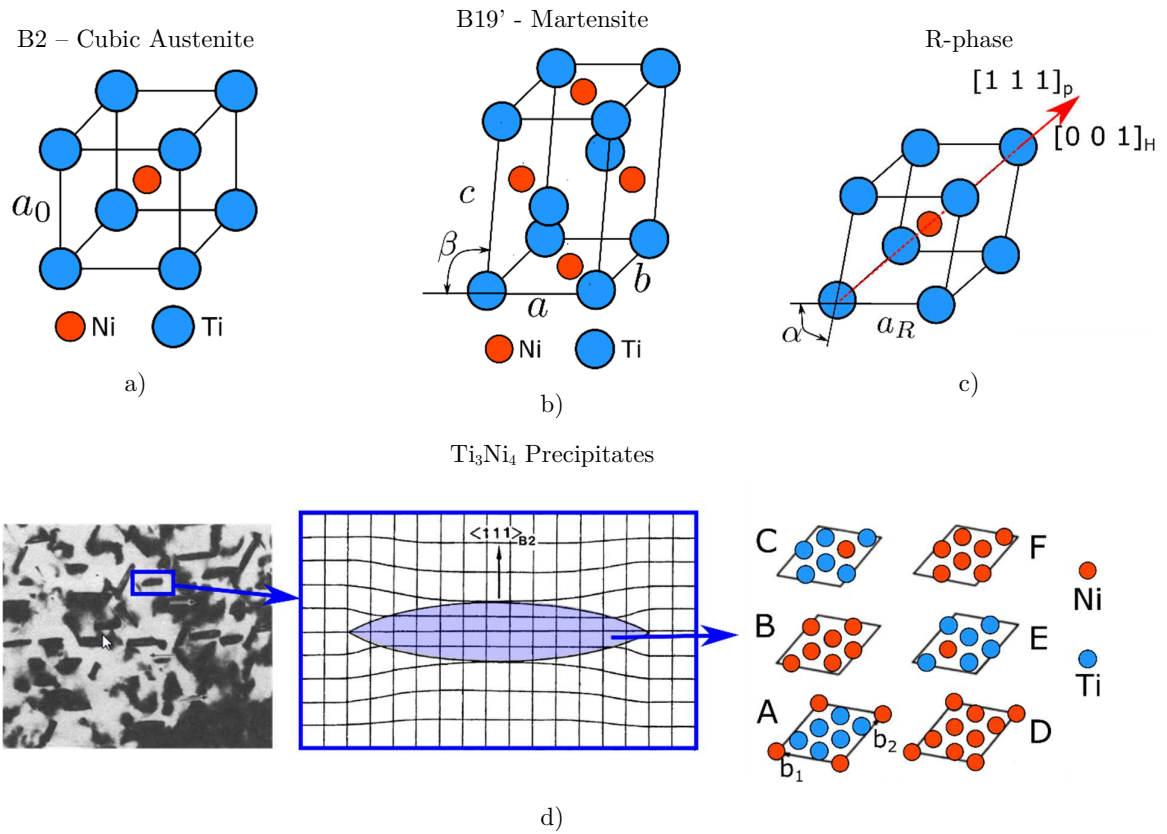


Figure 2-3 Crystallographic phases observed in near equiatomic NiTi: (a) B2 cubic austenite, (b) B19' monoclinic martensite, (c) R-phase (shown here simply as a distortion of the B2 phase in the  $\langle 111 \rangle_{B2}$  direction), and (d) Ti<sub>3</sub>Ni<sub>4</sub>, which we complement here with a TEM bright field image and an schematic representation of the lenticular-shape precipitates that this phase forms.

transformation is observed whenever precipitates or dislocations are introduced into the B2 matrix.

The intermediate phase transformation, from B2 to R-phase, is also a martensitic transformation, which shows superelastic and shape memory properties. However, the resulting amount of reversible deformation after B2 to R is much lower than the B2 to B19' transformation, making it less attractive for applications.

The crystallographic calculations of B2→B19', B2→R and R→B19' have been tackled by several authors in the literature using the different phenomenological theory of martensitic transformations. In this respect, we highlight the works of Matsumoto et al. [28] and Knowles et al. [29], who used the Wechsler et al. theory to calculate the twin variants upon the B2→B19' transformation and compared them to experimental diffraction information obtained in NiTi single crystals. We should also mention the work of Hane and Shield who performed an equivalent work using the Ball and James phenomenological theory [18], as well as the work of Zhang et al. who used the Ball and James theory to calculate twin variants upon B2→R→B19' transformation [19]. We present the main outcome of these studies in the following subsections.

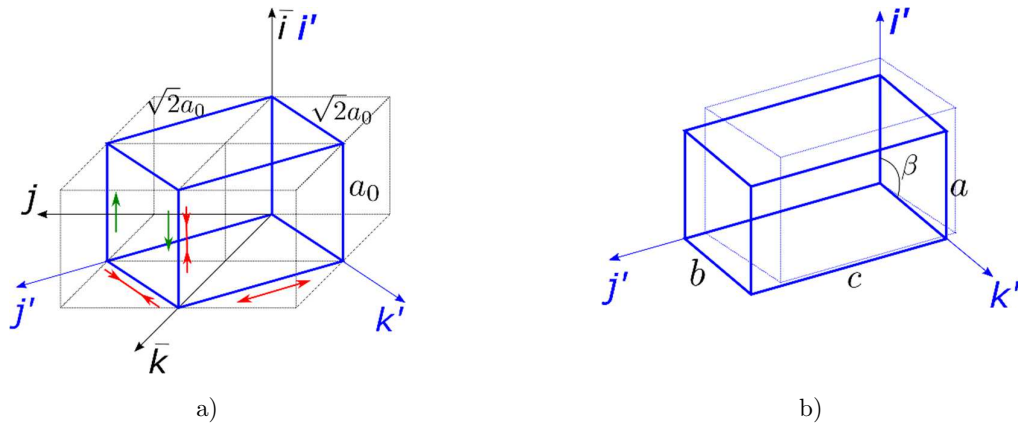


Figure 2-4 Schematic representation of the B2 to B19' transformation. The axis  $i, j, k$  correspond to the reference axis system of the B2 lattice, while the axis  $i', j', k'$  correspond to the reference axis system of B19' lattice. a) Tetragonal lattice depicted within four cubic lattices.

#### 2.1.2.1. B2→B19' transformation

For the purpose of illustration, the B2 to B19' phase transformation is described as a series of deformations applied to a tetragonal unit cell depicted within four cubic unit cells as shown in Figure 2-4a. The deformations steps are:

1. shrinking of vectors  $[\bar{1} 0 0]_{B2}$  from  $a_0$  down to  $a$ ,
2. shrinking of vectors  $[0 1 \bar{1}]_{B2}$  from  $\sqrt{2}a_0$  down to  $b$ ,
3. shrinking of vectors  $[0 \bar{1} \bar{1}]_{B2}$  from  $\sqrt{2}a_0$  up to  $c$ ,
4. shearing of the plane  $(0 1 1)_{B2}$  in the  $[1 0 0]_{B2}$  direction in order to create angle  $\beta$ .

The total number of lattice correspondence variants of martensite (c.v) that can result from B2→B19' are calculated as

$$N = \frac{\text{rotation symmetry order of the parent phase}}{\text{rotation symmetry order of the product phase}}. \quad (2.1)$$

Since B2 has rotation symmetry order 24 and B19' has rotation symmetry order 2, the number of B19' martensite variants in NiTi alloys is 12. However, none of these variants can produce a compatible interface (habit plane solution) with the B2 phase [18][29]. Instead, the B2 lattice forms an interface with a twin arrangement of two B19' variants. This explains the internal twinned structure of B19' often reported in the literature.

By using the nonlinear theory of martensitic transformations of Ball and James [9], Hane & Shield [18] calculated 66 variant pairs of B19' martensite that can form twins, which resulted in a total of 528 habit plane variant solutions (denoted as HPV). However, out of all these habit plane solutions, only 24 have been unambiguously observed in experiments.

During the B2 to B19' transformation, a negligible volume change occurs. Moreover, when no external mechanical forces participate in the transformation process, B19' twinned pairs form wedge arrangements (see Figure 2-5), also known as self-accommodated martensite. In this way, the shear deformation of individual B19' twinned variants is canceled, which

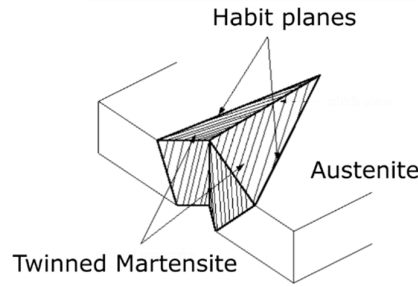


Figure 2-5 Schematic representation of self-accommodated wedge of B19' twinned variants.

explains why the macroscopic shape does not change after temperature-induced transformation.

#### 2.1.2.1. B2→R and R→B19' transformations

Trigonal R-phase results from a rhombohedral distortion of the cubic B2 phase matrix, induced by the presence of precipitates, third alloy elements or dislocations. Thermally induced B2 to R-phase transformation has been reported in NiTi alloyed with a small percentage of Fe or Al, in aged Ni-rich NiTi alloys, and in cold worked NiTi. In near equiatomic NiTi, dislocations and precipitates create an extra energy barrier for transformation into B19', making R-phase a lower energy alternative [30], [31].

R-phase has rotation symmetry order 6. In consequence, there exist four lattice correspondence variants (c.v) of R phases (see equation (2.1)). Like B19' martensite, R-phase produces an internal twinned structure. According to calculations made by Zhang & Sehitoglu [19], 36 habit plane solutions for R-phase can be obtained. Subsequent transformation, R→B19', results in four new B19' habit plane solutions in addition to those found in B2→B19'. A schematic representation of the coexistence of B2, R-phase, and B19' is illustrated in Figure 2-6.

## 2.2. Thermodynamic aspects of phase transformations in NiTi

### 2.2.1. Thermal hysteresis

The martensitic phase transformations in NiTi are considered as thermoelastic first-order phase transformations. From a thermodynamic viewpoint, the driving force that governs the nucleation and propagation of product phases is, as for the forward transformation, a decrease of temperature or an increase of the applied stress. The thermoelastic denomination refers to the reversible nature of phase transformation with temperature. Since phase transformations in SMA's involve structural distortion, reversibility is fulfilled only if no structural damage occurs during the transformation process. This implies that the interface between parent and product phases must be coherent and that the volume change after the transformation are negligible. In this regard,  $B2/R \rightarrow B19'$  martensitic transformations in NiTi, although exhibiting one of the best functional properties among SMA's, presents one

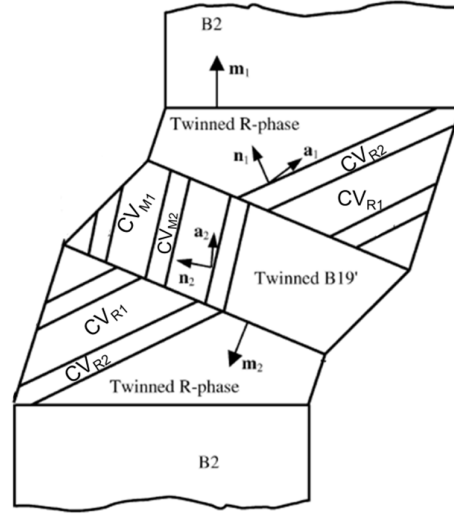


Figure 2-6 Schematic representation of the coexistence of B2, R-phase and B19' according to Zhang et al. [19]. The individual variants of B19' are denoted as  $CV_M$  and those from R phase are denoted as  $CV_R$ .

of the less coherent austenite/martensite interfaces and relatively large volume changes [32]. These interface incoherencies turn out on dissipation of energy and thermal hysteresis.

In order to describe the characteristic thermal hysteresis of NiTi alloys, we refer to the phenomenological thermodynamic framework of phase transformations. This framework is based on the evaluation of the Gibbs free energy potential, which consist of as chemical and mechanical energy terms.

#### 2.2.1.1. Gibbs free energy potential

Diffusionless crystallographic phase transformation results in an atomic rearrangement leading to lattice distortion. Consequently, temperature-induced martensitic transformations in NiTi can be considered as a mechanical-chemical process. This statement allows to establish the following form of the change of mass-specific Gibbs free-energy potential of a transforming system [33]:

$$\Delta G = \Delta H - T\Delta S + \Delta E_{cl} + \Delta E_{ir}, \quad (2.2)$$

The equation (2.2) is valid for temperature-induced phase transformations under constant volume and pressure conditions. The phase transformation part is defined by the local chemical Gibbs free energy potential:  $\Delta G_{chem} = \Delta H - T\Delta S$ , where  $\Delta H$  is the change of the specific enthalpy energy, and  $T\Delta S$  is the temperature-specific entropy change energy. The evolution of the free chemical energy potentials of martensite and austenite with temperature are illustrated in Figure 2-7. Since the specific entropy of austenite is higher than the specific entropy of martensite, the chemical potential of austenite drops faster with temperature, making it the most stable phase at high temperature. In the diagrams illustrated in Figure 2-7, the temperature  $T_0$  denotes the chemical equilibrium temperature, at which the parent and product phases would coexist if the phase transformations were merely chemical process (i.e. no hysteresis nor transformation kinetics would be observed). Under this assumption, the material would be in a martensite state at any temperature below  $T_0$ , and in an austenite

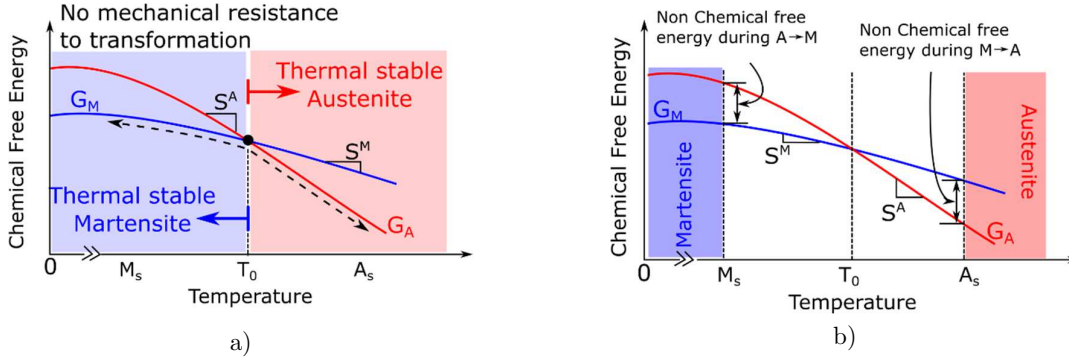


Figure 2-7 Schematic representation of the free chemical potentials of austenite and martensite.

- a) Hypothetical phase-temperature domains in the absence of elastic and irreversible energies opposing the propagation of the transformation. b) Phase-temperature domains considering elastic and irreversible energies.

state at temperatures above  $T_0$  as illustrated in Figure 2-7a. The expression for  $T_0$  is obtained by evaluating the chemical equilibrium condition  $\Delta G_{chem} = 0$ ; therefore

$$T_0 = \frac{\Delta H_{T_0}}{\Delta S_{T_0}}, \quad (2.3)$$

where  $\Delta S_{T_0} = S_{T_0}^A - S_{T_0}^M$ , and  $\Delta H_{T_0} = H_{T_0}^M - H_{T_0}^A$  are the differences between the specific entropies and enthalpies of austenite and martensite phases at  $T_0$  respectively.

The mechanical part of the process is described by two terms,  $\Delta E_{el}$  and  $\Delta E_{ir}$ , which describe the absorption/release of elastic strain energy and the sum of all irreversible energies changes upon phase transformation respectively. Both energies oppose the nucleation and further propagation of the product phase. Consequently, the thermal hysteresis defines the forward and reverse transformations initiation using two different “quasi-equilibrium” conditions:

$$A \rightarrow M: \Delta G^{A \rightarrow M} = \Delta H^{A \rightarrow M} - T \Delta S^{A \rightarrow M} + \Delta E_{el}^{A \rightarrow M} + \Delta E_{ir}^{A \rightarrow M} = 0, \quad (2.4)$$

$$M \rightarrow A: \Delta G^{M \rightarrow A} = \Delta H^{M \rightarrow A} - T \Delta S^{M \rightarrow A} + \Delta E_{el}^{M \rightarrow A} + \Delta E_{ir}^{M \rightarrow A} = 0. \quad (2.5)$$

The elastic strain energy  $\Delta E_{el}^{A \rightarrow M}$  is stored in the system during the forward transformation due to the elastic accommodation of distorted lattices of martensite within the austenite matrix. As the transformation proceeds, the stored elastic energy increases and further transformation is prohibited. Consequently, the elastic energy is a function of the volume fraction of martensite  $f_m$ . This implies that, in order to continue the propagation, an increase of the driving force is required (i.e. a decrease of temperature). The elastic energy accumulated during the forward transformation is fully released during the reverse transformation, hence,

$$\Delta E_{el}^{A \rightarrow M}(f_m) = -\Delta E_{el}^{M \rightarrow A}(f_m). \quad (2.6)$$

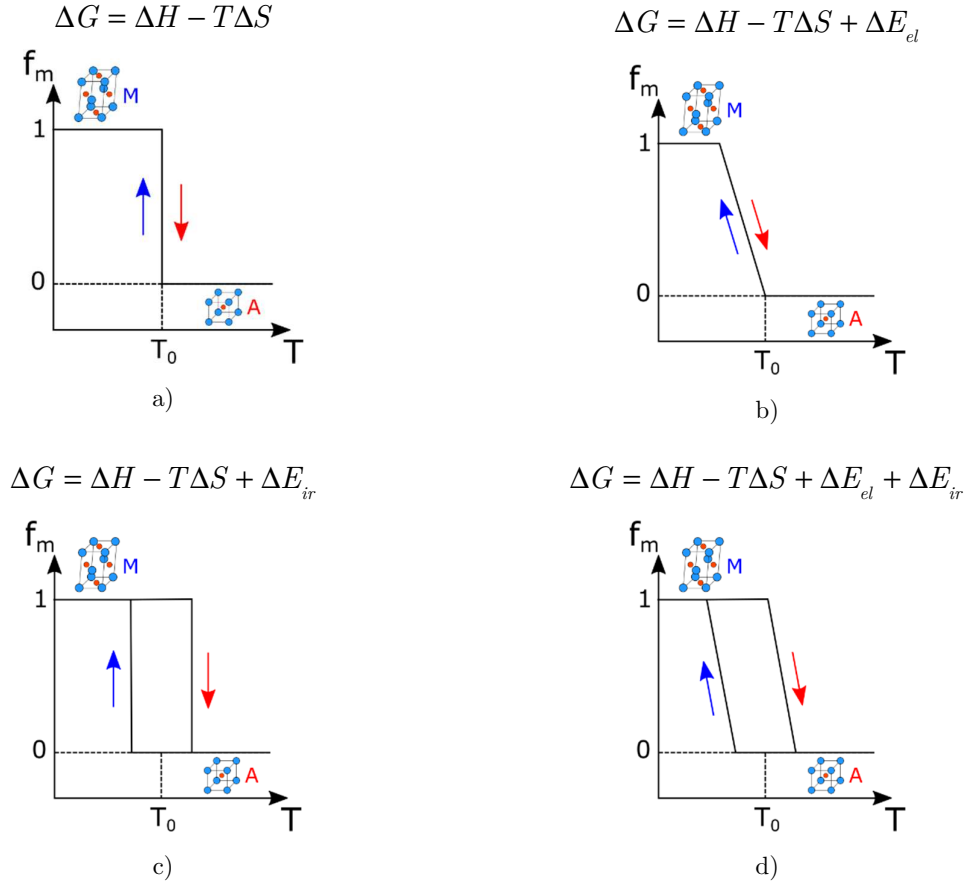


Figure 2-8 Effect of the Gibbs free energy terms on the transformation kinetics of solid-state phase transformations in SMA. a) Chemical energy only. b) Chemical and elastic energies. c) Chemical and irreversible energies. d) Chemical, elastic and irreversible energies.

On the other hand, the irreversible energy losses term  $\Delta E_{ir}$  is related to dissipation processes such as the production of structural defects, friction heat, and acoustic emission. It is defined as positive and often set constant during the entire forward and reverse transformation process:

$$\Delta E_{ir}^{A \rightarrow M} = \Delta E_{ir}^{M \rightarrow A} . \quad (2.7)$$

The terms  $\Delta E_{el}$  and  $\Delta E_{ir}$  shift the transformation temperatures away from  $T_0$ . As a result, the chemical free energy experiences a “jump” when transformation is initiated (Figure 2-7b). According to the phase equilibrium condition, the sudden change of chemical potential equals the sum of the mechanical terms  $\Delta E_{el}$  and  $\Delta E_{ir}$ . A graphical description of the effects of each free energy term in equation (2.2) on the evolution of the volume fraction of martensite  $f_m$  upon a thermally induced phase transformation is illustrated in Figure 2-8.

In the case of NiTi exhibiting R-phase, the phase transformation path upon cooling can be different to the one observed upon heating. Two situations are commonly observed, one where the B2 austenite transforms into R then into B19' upon cooling, and from B19' directly into B2 upon heating, overtaking the intermediate phase R. The other possibility occurs when the intermediate phase transformation occurs upon both heating and cooling. The

preference from one path over the other is caused by the interaction of thermal hysteresis between phases couples.

### 2.2.2. Heat release/absorption

In first-order phase transformations, the state functions of a transforming thermodynamic system, like specific entropy or specific volume, are not continuous at the transformation phase boundary. In NiTi sudden entropy changes turn out into latent heat release/absorption, which explains the endothermic and exothermic peaks observed in differential scanning calorimetry (DSC) experiments. From the DSC experimental results shown in Figure 2-9, we can observe that  $B2 \leftrightarrow R$ ,  $B2 \leftrightarrow B19'$  and  $R \leftrightarrow B19'$  transformations, all release heat when the material experience a high entropy to low entropy change, and absorb heat when the inverted entropy change occurs.

To examine the heat absorption/release of a transforming system, let us describe the specific free energy balance over an infinitesimal step during the transformation as:

$$dG = dH - TdS + dE_{el}(f_m) + dE_{ir}(f_m) . \quad (2.8)$$

The irreversible energy term can be separated in two: irreversible heat  $dE_{ir,q}(f_m)$  and irreversible work other than heat  $dE_{ir,w}(f_m)$ , i.e.

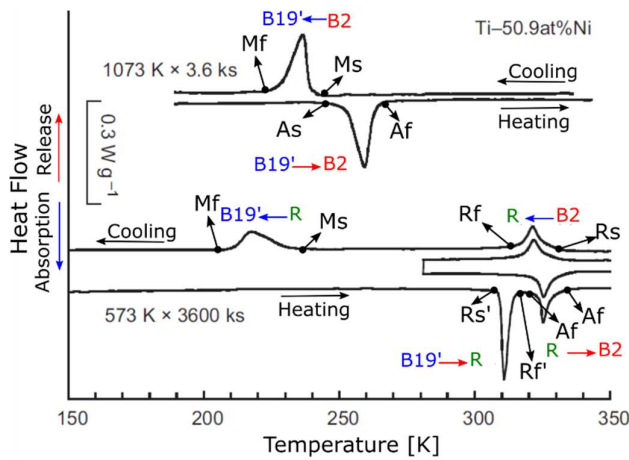
$$dE_{ir}(f_m) = dE_{ir,q}(f_m) + dE_{ir,w}(f_m) . \quad (2.9)$$

Thus, the “quasi-equilibrium” condition  $dG=0$  becomes equivalent to

$$dH - TdS + dE_{el}(f_m) + dE_{ir,q}(f_m) + dE_{ir,w}(f_m) = 0 , \quad (2.10)$$

which allow us to define the heat term

$$dq = TdS - dE_{ir,q}(f_m) = dH + dE_{el}(f_m) + dE_{ir,w}(f_m) . \quad (2.11)$$



a)

**Characteristic temperature thresholds for stress-free thermal-induced transformations:**

- Ms: B2/R  $\rightarrow$  B19' starts
- Mf: B2/R  $\rightarrow$  B19' finishes
- Rs: B2  $\rightarrow$  R starts
- Rf: B2  $\rightarrow$  R finishes
- Rs': B19'  $\rightarrow$  R starts
- Rf': B19'  $\rightarrow$  R finishes
- As: B19'/R  $\rightarrow$  B2 starts
- Af: B19'/R  $\rightarrow$  B2 finishes

Figure 2-9 a) DSC results carried out on a Ti-50.9at%Ni, heat-treated at 800°C (upper graph) and 300°C (lower graph)[31].

Integrating over  $0 \rightarrow f_m$ , we calculate the heat produced during the full transformation of a unit of mass of austenite into martensite:

$$\begin{aligned}
 Q(f_m) &= \int_0^{f_m} dq = \int_0^{f_m} \left[ dH + dE_{el}(f_m) + dE_{ir,w}(f_m) \right] \\
 &= \int_0^{f_m} \Delta H df_m + \int_0^{f_m} \Delta E_{el}(f_m) df_m + \int_0^{f_m} \Delta E_{ir,w}(f_m) df_m \\
 &= \Delta H df_m + \Delta E_{el}(f_m) + \Delta E_{ir,w}(f_m) \quad . \quad (2.12)
 \end{aligned}$$

For a complete transformation, assuming  $\Delta E_{el}(0) = 0$  and  $\Delta E_{ir,w}(0) = 0$ , the total heat produced results in

$$Q(f_m) = \Delta H + \Delta E_{el}(1) + \Delta E_{ir,w}(1). \quad (2.13)$$

The equation (2.13) shows that the heat effect of a martensitic transformation is not only related to the enthalpy change, as commonly defined, but also to the sum of two more energy quantities, the elastic and the irreversible work other than heat.

### 2.2.3. Effects of externally applied stresses – Clausius-Clapeyron relation

Let us consider now that an external force is applied to the system, which produces the equivalent stress  $\sigma$  and the macroscopic deformation  $\varepsilon_T$ , product of a stress-induced phase transformation. Therefore, the free energy balance becomes:

$$\Delta G^{A \rightarrow M} = \Delta H^{A \rightarrow M} - T \Delta S^{A \rightarrow M} + \Delta E_{el}^{A \rightarrow M} + \Delta E_{ir}^{A \rightarrow M} - \frac{1}{\rho} \sigma \varepsilon_T, \quad (2.14)$$

where  $\rho$  is the density of the material. By evaluating the quasi-equilibrium condition  $\Delta G^{A \rightarrow M} = 0$ , we can determine the external stress at the initiation of the phase transformation by:

$$\sigma = \frac{\rho}{\varepsilon_T^{A \rightarrow M}} \left( \Delta H^{A \rightarrow M} - T \Delta S^{A \rightarrow M} + \Delta E_{el}^{A \rightarrow M} + \Delta E_{ir}^{A \rightarrow M} \right). \quad (2.15)$$

As a result, the effect of temperature on the stress needed to initiate the transformation  $\sigma$  is:

$$\frac{\partial \sigma}{\partial T} = -\rho \frac{\Delta S}{\varepsilon_T} = -\rho \frac{\Delta H}{T_0 \varepsilon_T}. \quad (2.16)$$

The equation (2.16) is known as the Clausius-Clapeyron relation. It expresses the transformation temperature dependence on the external stress. The relationship (2.16) becomes constant if we assume that  $\Delta S = S^A - S^M$  and  $\Delta H = H^A - H^M$  are temperature-independent variables, which implies that the heat capacities of martensite and austenite phases are equal. As a result, the relationship between stress and the transformation temperatures is often considered as linear.

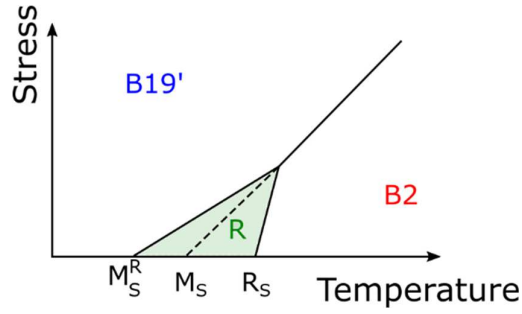


Figure 2-10 Schematic representation of the stress-temperature-phase diagram of a NiTi alloy showing the stress-temperature domains of B2, R and B19' phases.

The phenomenological thermodynamic framework allows us to describe the three phase transformations pairs observed in NiTi alloys:  $B2 \leftrightarrow R$ ,  $B2 \leftrightarrow B19'$  and  $R \leftrightarrow B19'$ . Since the deformation caused by each transformation and the specific entropies and enthalpies of B2, R, and B19' phases are different, the heat quantities and Clausius-Clapeyron slopes for each transformation are unequal. To give an order of magnitude of the Clausius-Clapeyron slopes of the phase transformations in NiTi, we refer to the values reported by Stachowlak & McCormick in [34] for a cold-worked Ti50.2at.%Ni alloy:

$$\left. \frac{d\sigma}{dT} \right|_{B2 \rightarrow B19'} = 6.4 \text{ MPa} / \text{K}, \quad \left. \frac{d\sigma}{dT} \right|_{B2 \rightarrow R} = 15.6 \text{ MPa} / \text{K}, \quad \text{and} \quad \left. \frac{d\sigma}{dT} \right|_{R \rightarrow B19'} = 5.6 \text{ MPa} / \text{K}$$

This kind of characterization allows us to construct stress-temperature-phase diagrams as the one illustrated in Figure 2-10. Since the Clausius-Clapeyron slopes depend on the macroscopic transformation strain  $\varepsilon_T$ , the stress-temperature-phase diagram changes according to the preparation of the alloy. Note that, for a particular alloy, we may avoid the stress-induced B2→R transformation by increasing the temperature, regardless of the identification of R-phase in DSC curves.

## 2.3. Mechanical Properties of NiTi alloys

The mechanical response of NiTi combines stress-induced phase transformations with other deformation mechanisms such as B2, B19' and R-phase elasticity, B19' and R-phase detwinning, and B2 plasticity through dislocation slip. All these mechanisms are stress and temperature dependent, making complex their characterization and modeling. In this section, we show the impact of these mechanisms on the mechanical response of NiTi and describe some of their most relevant characteristics.

### 2.3.1. Detwinning of B19' and R-phase

Detwinning occurs mainly when self-accommodated arrangements of habit plane variants (HPV) of R or B19' phases are subjected to stress at temperatures below  $M_f$  and  $R_f$  respectively. The applied stress causes twin boundary motion and reorientation of HPV's in such a way that the sum of individual crystal distortions, instead of being canceled, contribute to deform the NiTi sample. Consequently, upon removal of the stress, residual

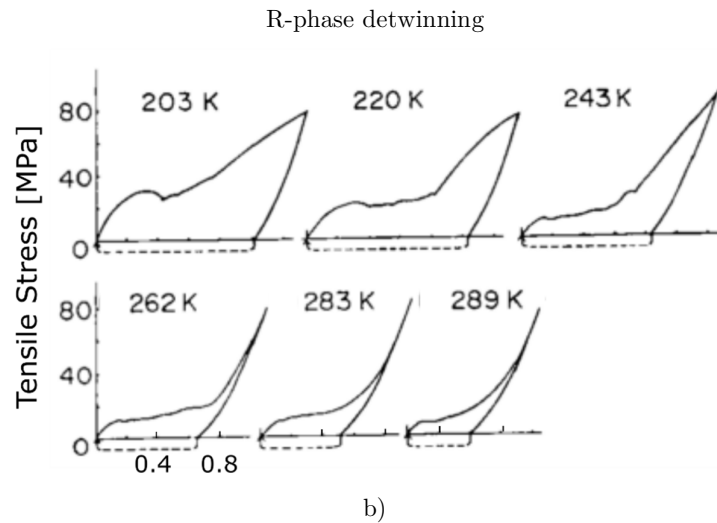
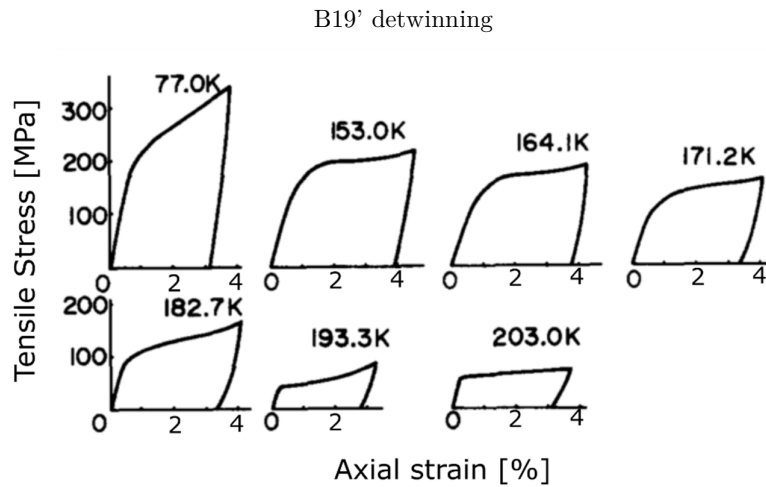


Figure 2-11 Tensile stress responses showing the detwinning of B19'(a)[35] and R-phase (b)[36].

deformation remains on the sample (see Figure 2-11). Only by heating the sample above  $A_f$  then cooling it down, the self-accommodated structures are recreated and the deformation reversed. This phenomenon allows the shape memory effect.

Detwinning is characterized by two stages. In the first stage, we observe a stress plateau, which allows deformations up to  $\sim 3\%$  in the case of  $B2 \rightarrow B19'$  transformation (Figure 2-11a) and  $\sim 0.3\%$  in the case of  $B2 \rightarrow R$  transformations (Figure 2-11b). In the second stage, the material exhibits a more pronounced strain hardening response, as observed clearer in the  $B2 \rightarrow R$  transformation curves shown in Figure 2-11b. Twins boundaries in R-phase are more mobile than those in B19' martensite, hence it is substantially easier to move twins in R than in B19'. The yield stresses (plateau stresses) for R-phase are about 5–25 MPa while in B19' are between 50–250 MPa. Both yield stresses decrease by increasing the temperature as illustrated in Figure 2-11.

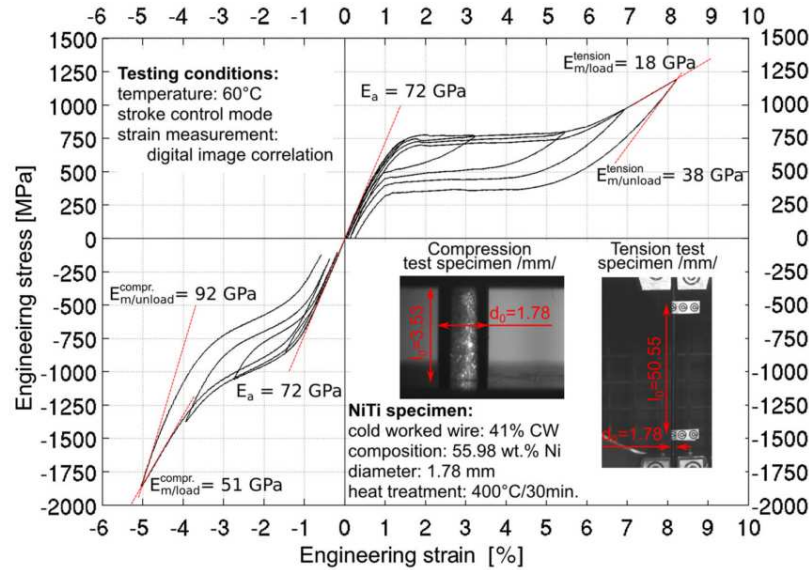


Figure 2-12 Characterization of the elastic modulus of austenite and martensite of a polycrystalline NiTi wire/bar upon tension/compression loading (extracted from Sittner et al. [37]).

## 2.3.2. Elasticity

### 2.3.2.1. B2

At temperatures above  $A_f$ , the mechanical response of NiTi shows a linear-elastic behavior. The elastic properties of B2 phase are considered as isotropic for polycrystalline NiTi, which is explained by the high symmetry of its crystallographic structure. Common values for the elastic modulus of austenite ( $E_a$ ) are about 70-80GPa (see Figure 2-12).

### 2.3.2.2. B19'

The elastic modulus of B19' martensite has been a matter of debate for many years. From a macroscopic point of view, the internal twinned structure that characterizes the B19' phase makes it anisotropic, dependent on the texture of the material. Moreover, the monoclinic structure of B19' itself is highly anisotropic due to its lower symmetry. In textured polycrystalline NiTi, like annealed cold-drawn wires, it is commonly reported that the elastic modulus of B19' upon compressive stresses doubles the elastic modulus upon tensile stress (see for example Figure 2-12). The typical values of the tensile elastic modulus of B19' martensite for polycrystalline cold-drawn NiTi wires are about 20-50GPa [20], [21], [37].

### 2.3.2.3. R-phase

The elastic properties of R-phase are as complicated to extract as B19' martensite. Moreover, the characteristic distortion of the lattice angle of R-phase upon stress or temperature changes, together with detwinning phenomena, makes it difficult to correlate crystal elastic constants with macroscopic values measured by mechanical testing. Sittner et al. [27] have shown that the elastic constants of R-phase evolve with temperature and stress (both in magnitude and direction).

The typical values of the tensile elastic modulus of R-phase ( $E_R$ ) for polycrystalline cold-drawn NiTi wires are about 30-40GPa [38]–[41]. These values are usually measured using

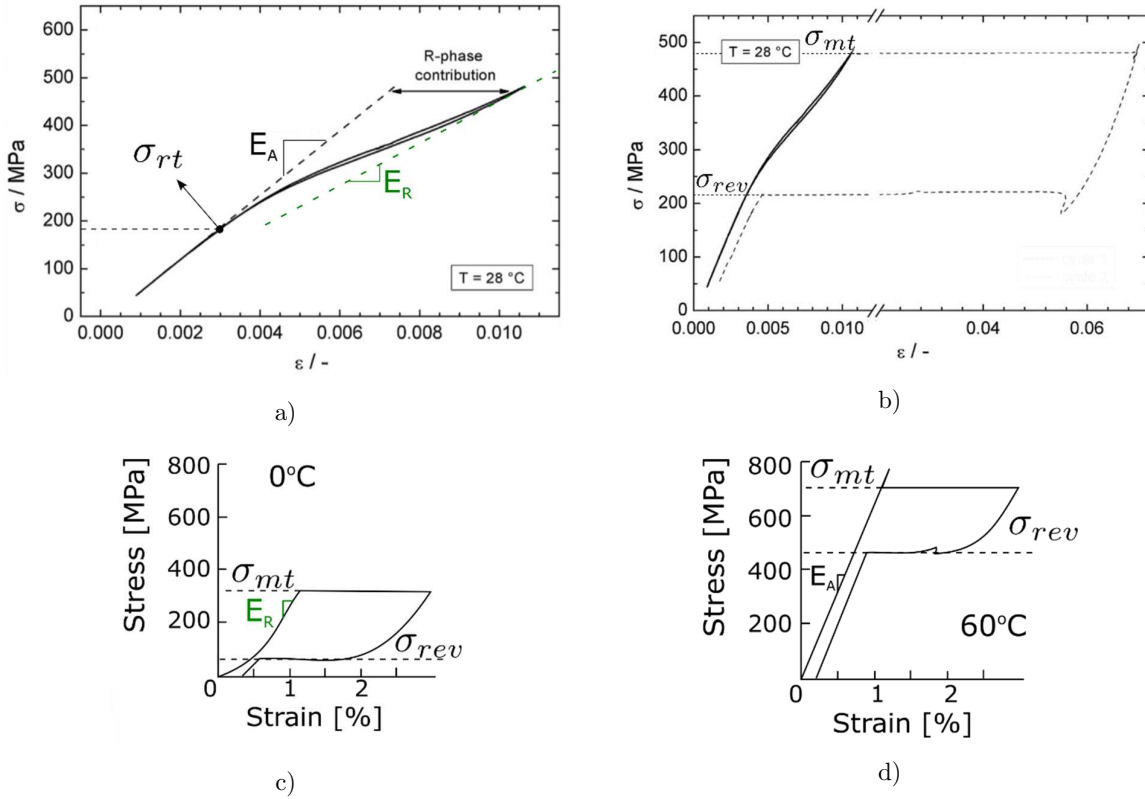


Figure 2-13 Superelastic tensile responses of NiTi. a)  $B2 \rightarrow R \rightarrow B2$ , b)  $B2 \rightarrow R \rightarrow B19' \rightarrow B2$  [38], c)  $R \rightarrow B19' \rightarrow R$ , and d)  $B2 \rightarrow B19' \rightarrow B2$  [39].

Hooke's Law ( $E = \sigma/\varepsilon$ ) on nearly linear elastic parts of tensile curves (see for example Figure 2-13a&c).

### 2.3.3. Stress-induced phase transformations & superelasticity

Unlike detwinning, stress-induced phase transformations allow recovering large deformations by relieving the stress applied to the material (no need for heating up the material after deformation). The stress-induced phase transformations are the base of the superelastic behavior of SMA. The material shows superelastic behavior when loaded under isothermal conditions at temperatures above  $R_f'$  for alloys exhibiting R-phase, and above  $A_f$  for alloys without R-phase.

The deformations associated with the  $B2 \rightarrow R$  transformation can go up to 1%, while the deformations associated with the  $B2/R \rightarrow B19'$  transformation can go up to 10%. The stress-induced transformation paths observed upon superelasticity are:

- $B2 \rightarrow R \rightarrow B2$ ,
- $B2 \rightarrow B19' \rightarrow B2$ ,
- $B2 \rightarrow R \rightarrow B19' \rightarrow R \rightarrow B2$ ,
- $B2 \rightarrow R \rightarrow B19' \rightarrow B2$ ,
- $R \rightarrow B19' \rightarrow R$ .

The stress-strain curve of NiTi exhibiting  $B2 \rightarrow R \rightarrow B2$  is illustrated in Figure 2-13a. In this loading regime, we observe a progressive loss of stiffness upon loading. The forward transformation thresholds  $\sigma_{rt}$  is often defined at the inflection point of the loading curve. After the  $B2 \rightarrow R$  transformation starts, the material experiences a continuous distortion of the R-phase lattice angle  $\alpha$  and R-phase detwinning, which turns out in the transition zone between linear B2 and R elasticities.  $B2 \rightarrow R \rightarrow B2$  transformation exhibit hysteresis of about 5-10MPa, much smaller than the one of the B2/R  $\rightarrow$  B19' transformation.

$B2 \rightarrow B19' \rightarrow B2$ , is observed at temperatures far above  $R_f$  or in alloys without R-phase. The upper stress-plateau, starting at  $\sigma_{mt}$  in Figure 2-13d, depicts the evolution of the forward phase transformation. The reverse transformation, on the other hand, starts at  $\sigma_{rev}$  and proceeds through the lower stress plateau. Since the R-phase transformation is avoided, the material shows linear elasticity of B2 phase prior to the upper transformation plateau and after the lower transformation plateau completion. The hysteresis in the case is much greater than in  $B2 \rightarrow R \rightarrow B2$  transformation, being in the order of 200-250MPa. Unlike  $B2 \rightarrow R \rightarrow B2$  transformation, the forward  $B2 \rightarrow B19'$  and reverse  $B19' \rightarrow B2$  proceeds heterogeneously in constant cross-section tensile testing samples. Large deformation bands are produced instants before the stress plateau, which propagate until the end of the stress plateau. The behavior is similar to localized plastic deformation bands observed in low carbon steels and certain Al-Mg alloys. This phenomenon will be detailed in the next subsection.

$R \rightarrow B19' \rightarrow R$  shows similar characteristics to  $B2 \rightarrow B19' \rightarrow B2$  transformation path: upper and lower constant stress plateaus, similar hysteresis values and deformation localization. However, due to detwinning of R-phase, residual strains remains after unloading (Figure 2-13c).

The two-step transformation paths  $B2 \rightarrow R \rightarrow B19' \rightarrow R \rightarrow B2$  and  $B2 \rightarrow R \rightarrow B19' \rightarrow B2$  combine the three transformation paths described before. However, in most cases, due to the

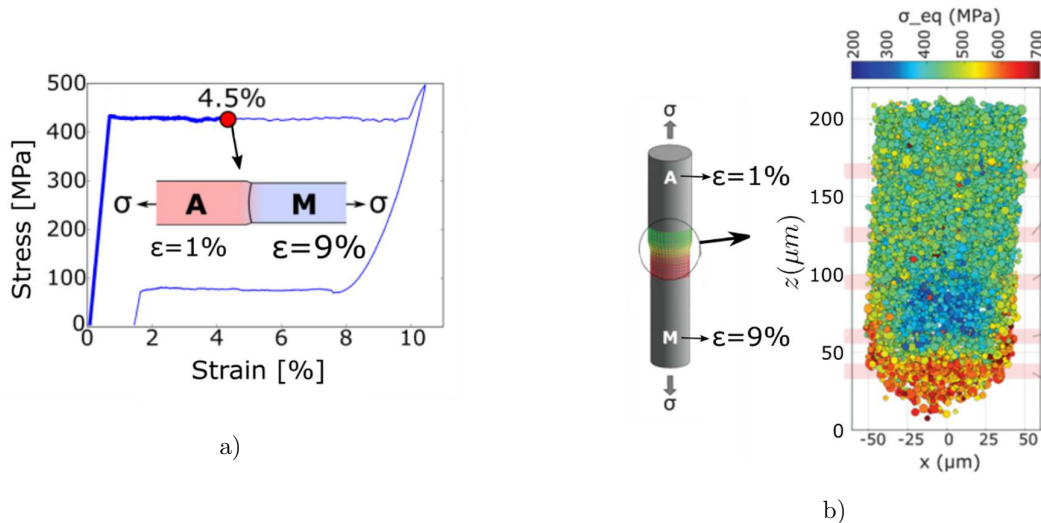


Figure 2-14 Stress state of grains in the vicinity of a localization band upon stretching a 0.1mm NiTi wire [42].

large hysteresis of the B19' transformation, the resulting stress upon the reverse transformation is too low to stabilize the R-phase. Consequently, the  $B2 \rightarrow R \rightarrow B19' \rightarrow B2$  (Figure 2-13b) path is more commonly encountered in experiments.

#### 2.3.3.1. Deformation localization

Localized deformation bands have been reported upon stress-induced phase transformations into B19' martensite in NiTi samples using full-field deformation measurements [43]–[45]. These bands, not only introduce a heterogeneous deformation field but can induce high gradients of temperature in the sample, affecting the superelastic properties of the material [46].

We illustrate the strain localization of a wire tested in tension in Figure 2-14a. Upon the transformation plateau, the material divides into austenite (A) and martensite (M) regions. While the region A sees a deformation equivalent to the deformation at the beginning of the plateau (1%), region M sees a deformation equivalent to the end of it (9%). When the sample is elongated, the martensite region grows at the expense of the austenite region whilst the strain of the two regions remains unchanged until the end of the stress plateau. Consequently, the nominal strain plotted in stress-strain curves is only an average of the deformation of the two regions weighted by their volume fractions of austenite and martensite.

So far, this heterogeneous distribution of strain-phases has been reported in polycrystalline NiTi alloys, and not in any other SMA. They have been observed under tensile and bending stress in NiTi wires, thick bars, ribbons, plates, tubes, and sheets. In each case, the geometry of the martensitic bands changes:  $\sim 55^\circ$  tilted martensitic bands has been reported in tensile tested ribbons and thin sheets [43], helix-like forms in tensile tested tubes [47], straight lines perpendicular to the tensile load axes in wires and bars [45][42], and sawtooth-like forms in bended tubes [44].

More recently, 3D-XRD synchrotron studies carried out on NiTi wires under tension have shown that the  $B2 \rightarrow B19'$  transformation, apart from occurring locally and causing high deformation gradients, also generates considerable stress concentration at the band front [42]. In this study, the authors showed that the equivalent stress in the austenite part of the band front was almost twice the nominal stress (see Figure 2-14b). Moreover, they showed that the stress at the band front is far from uniaxial due to strain compatibility conditions. All these facts may lead to a misinterpretation of the real mechanical state of NiTi components subjected to mechanical loading, which represents a challenge for design of NiTi-based devices and engineering models.

#### **2.3.4. Plastic deformation through dislocation slip**

One of the conditions needed for developing thermoelastic martensitic transformations in a SMA is that the internal stress generated by the transformed martensite lattices does not exceed the slip resistance of the austenite matrix. If the externally applied stress exceeds the slip resistance of austenite, the rate of elastic energy accumulated in the material decreases as the plastic deformation through slip relieves the internal stresses. Moreover, slip

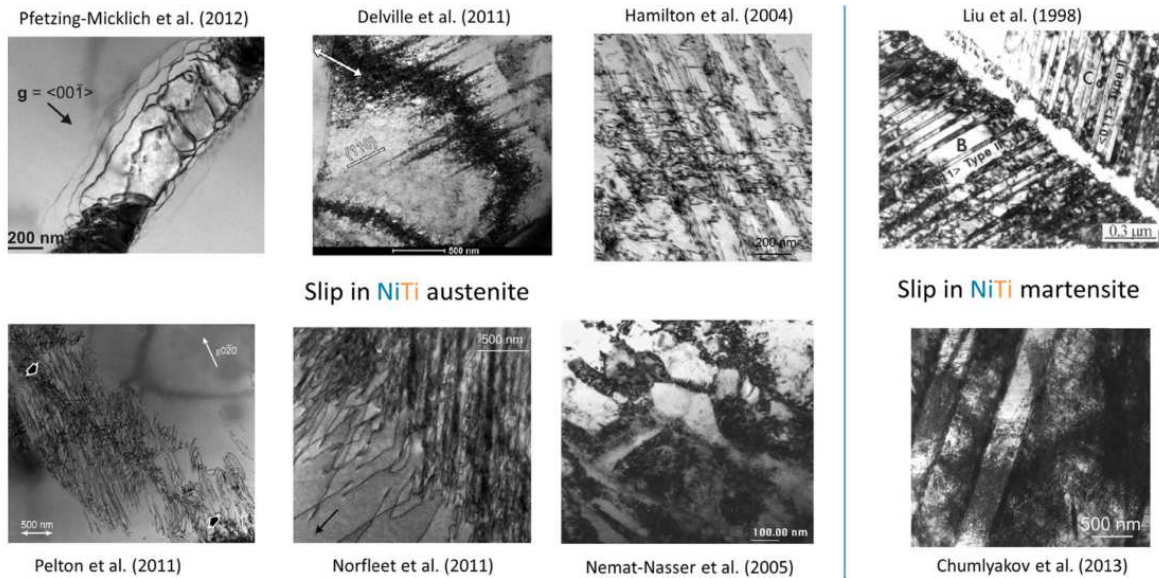


Figure 2-15 Transmission electron microscopy images showing the presence of dislocations produced after phase transformations in NiTi. The left-hand side shows dislocations in the austenite domains [48]–[53].

The right-hand side shows dislocations appearing in the martensite domains [54], [55]. This figure was extracted from the review paper of Chowdhury et al. [56].

dislocations create new interfaces, which may increase the surface energy needed to nucleate new martensite lattices.

Upon the application of stress at high temperatures, the large amount of energy needed for overcoming the phase transformation energetic barrier results impossible to achieve as the external stress applied to the material is relieved through the plastic deformation of austenite. As a result, NiTi shows a temperature threshold above which, upon the application of stress, plastic deformation develops before the stress-induced phase transformation could be initiated. This threshold is commonly denoted in the literature as  $M_d$ .

From the beginning of the 2000s, an increasing amount of research has focused on the interaction between plastic deformation through dislocation slip and phase transformations in NiTi. Chowdhury et al. extensively review the most recent advances made in this matter [56]. In this review paper, the authors highlight the use of transmission electron microscopy and computations at the atomistic scale using density functional theory (DFT) to characterize the dislocation slip systems in different SMA. In Figure 2-15, we reproduce one figure from the Chowdhury et al. article, which shows transmission electron microscopy evidence of the appearance of dislocations upon B2→B19' phase transformation in the austenite and martensite domains. Ezaz et al, using atomistic scale simulations, determined the magnitude of the shear stress needed for activate each of the possible six dislocation systems in NiTi austenite, which results in values larger than 2GPa [57]. The authors associate the appearance of dislocations during the phase transformation to the large strain that the austenite must accommodate upon the evolution of martensite. On the other hand, the slip in martensite has been less often reported in the literature. Quantitative and more detailed qualitative analysis of the dislocation systems in NiTi martensite is still missing.

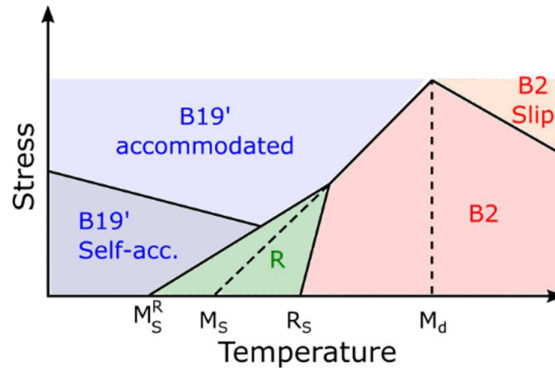


Figure 2-16 Stress-temperature-phase diagram for NiTi including B19' detwinning and plasticity boundaries.

These remarks, together with the Clausius-Clapeyron slopes for phase transformations, allow us to build a complete stress-temperature-phase diagram as the one illustrated in Figure 2-16, which defines the domains of phases and deformation mechanism. This diagram is distinct for each NiTi alloy as it depends on variables such as composition, thermomechanical heat treatment, and loading history.

## 2.4. Applications of NiTi

Soon after the discovery of the shape memory properties of NiTi in the 1960s, there was a great deal of commercial interest in these alloys, mainly because it showed better mechanical properties than previously discovered SMA. However, the applications based on NiTi started to emerge only in the 1990's with the boom of medical devices. Nowadays, applications of NiTi can be found in fields such as robotics, civil engineering, aeronautic and automotive. According to the type of load supported by the alloy, the applications of NiTi are generally divided into three main groups: constrained-recovery, actuation, and superelastic.

### 2.4.1. Constrained-recovery

The constrained-recovery category refers to the applications where force is generated due to a motion constraint of a SMA device upon phase transformations. NiTi-based devices such as heat-recoverable couplings, heat-to-shrink fasteners, and dematable connectors, work under this principle. In Figure 2-17, we illustrate the working mode of a NiTi coupling for tubing. The NiTi coupling is first deformed in martensite state so its internal diameter results slightly larger than the external diameter of the tubes for assembling. Upon warming, the coupling shrinks due to thermal expansion and the reverse transformation into austenite. When the coupling enters in contact with the surface of the tubes, the deformation is constrained and the coupling radial stress increases; thus, sealing the tube connection.

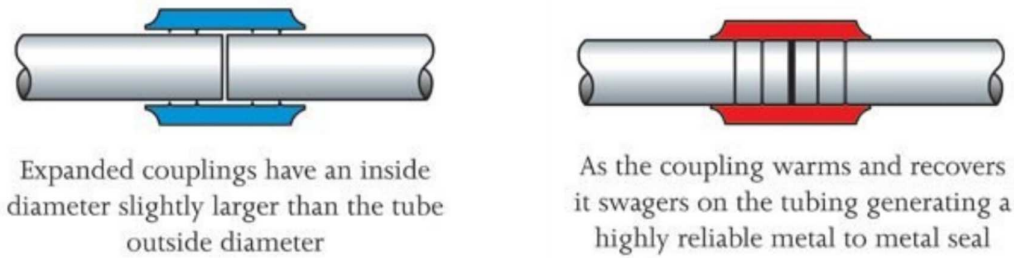


Figure 2-17 NiTi tube couplings [58].

### 2.4.2. Actuation

In the actuation mode, a NiTi device shrinks and expands upon heating and cooling under the application of external forces. In this mode, the chemical/thermal energy of the phase transformation is transformed into mechanical work. For this reason, SMA-based actuators can be considered as thermal actuators. They can be controlled using radiating, conductive, inductive or resistive heating systems. Resistive heating is the most widely used control mode for NiTi devices as it results in more homogeneous and faster responses [59].

Actuators based on SMA show a higher power-to-weight ratio compared to other actuating technologies such as DC motors or gas turbines [59]. Moreover, their motion is carried out without the need for friction mechanisms or vibrating parts, allowing for smaller, cleaner and more silent devices. NiTi actuators are used in applications such as bone lengthening devices [60], soft robotics [61] and heat engines [62].

However, SMA-based actuators are limited by their poor structural fatigue performance. Depending on the maximum actuation stress/strain, temperature, and alloy heat treatment, the lifetime of SMA actuators can change dramatically. Table 2-1 shows an example of the lifetime restrictions for commercial NiTi actuators according to their strain and stress outputs [59].

### 2.4.3. Superelastic

#### 2.4.3.1. Stents

The best example of a superelastic medical device fabricated in NiTi is the *self-expanding stent* (Figure 2-18). Stents are devices used to scaffold or brace the inside circumference of tubular passages inside the body, such as the esophagus, biliary duct, and blood vessels including coronary, carotid, aorta and femoral arteries. Blood vessels self-expanding stents are manufactured at the vessel diameter (or slightly above). They are shrunk into a

Cycles	Maximum Strain [%]	Maximum Stress [MPa]
1	8	500
100	4	275
10 000	2	140
100 000 +	1	70

Table 2-1 Estimates of the lifetime of a NiTi actuator according to its strains and stress outputs. This table was extracted from [59].

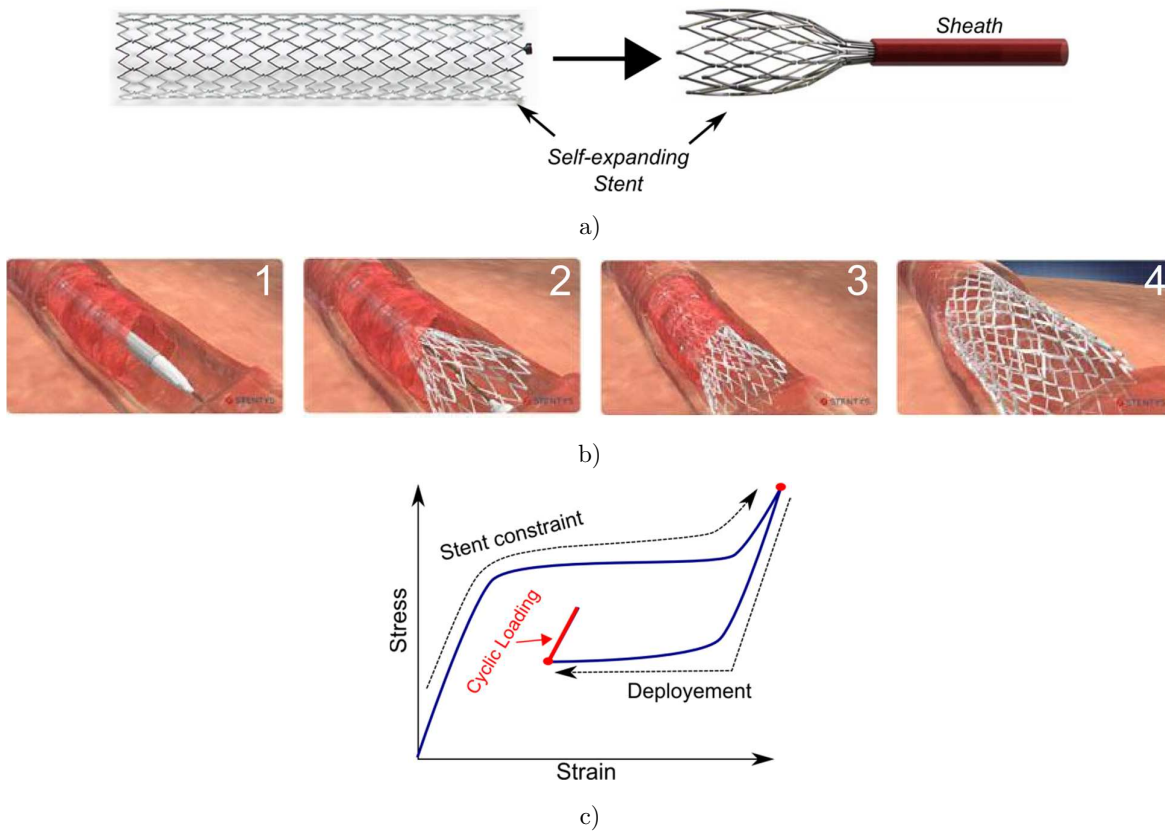


Figure 2-18 NiTi self-expanding stents. a) Stent shrinking inside a sheath previous to placement procedure. b) Deployment of a stent inside a blood vessel. c) Schematic representation of the loading path of a self-expanding stent during installation and operation.



Figure 2-19 a) Endodontic file for tooth root canalization.

retractable sheath, which is mounted on a catheter. Upon the insertion procedure, the surgeon introduces the catheter into the body with the assistance of fluoroscopy or x-ray images to guide the placement of the stent. Once the stent is in place, the surgeon deploys it by removing the cover sheath (images 2 and 3 in Figure 2-18b). As the stent tries to return to its original shape due to its intrinsic superelastic behavior, it applies pressure towards the vessel walls (image 4 in Figure 2-18b). The applied pressure guarantees the overture of the vessel and therefore the correct circulation of blood.

Schematically, the loading path followed by the stent can be viewed as superelastic cycle interrupted at the lower stress plateau (see Figure 2-18c). Once the stent is placed and

deployed, it is subjected to repetitive small amplitude loadings at frequencies varying between 40Hz and 120Hz. Stents, like other medical implants, are designed to sustain at least 600 million of cycles [63].

#### 2.4.3.2. Endodontic files

NiTi alloys are also very popular materials for manufacturing endodontic files. Compared to their stainless steel counterparts, NiTi has the higher torsional strength and can display larger reversible strokes, which is ideal for following the shape of a tooth canal. The popularity of NiTi among dentist and biomedical engineers has grown especially in the last decade due to significant advances in the microstructure control of the alloy and manufacturing techniques [64].

Endodontic files are subjected basically to torsional and cyclic rotary bending stresses, although due to their particular shape, very complex multiaxial stresses can be generated inside the files [66]. The distribution of stresses depends on many factors such as dentist skills, use of engine-driven instrumentation, the shape of teeth canals and material properties. Torsional and fatigue are reported as the most common causes of failure of endodontic files made in both stainless steel and NiTi [67]–[69]. Nevertheless, there is a perception among dentist that fracture incidence with rotary NiTi instruments is more frequent [70]. Moreover, failure in NiTi instruments is usually categorized as “unexpected”, since visible warnings of potential fracture, such as permanent deformation, are hard to detect. For this reason, recent studies on the subject have focused on looking for alternatives to improve the fatigue and torsional resistance of NiTi files. In what respects material properties enhancements, a new range of NiTi instruments showing a more pronounced R-phase region has started to be promoted among dentist. The companies producing R-phase endodontic files claim that these instruments have a better fatigue performance [70]. However, the fundamental role of R-phase in the fatigue behavior of NiTi alloys is not yet understood and barely tackled in the literature.

#### 2.4.3.3. Dampers for civil engineering structures

Due to their high damping capacity, environmental resistance, solid-state actuation and high power density, dampers for civil engineering purposes based on superelastic technologies are one of the most promising non-biomedical applications for NiTi. Conventional dampers, mainly those based on low yield stress elastoplastic materials, are allowed to dissipate energy

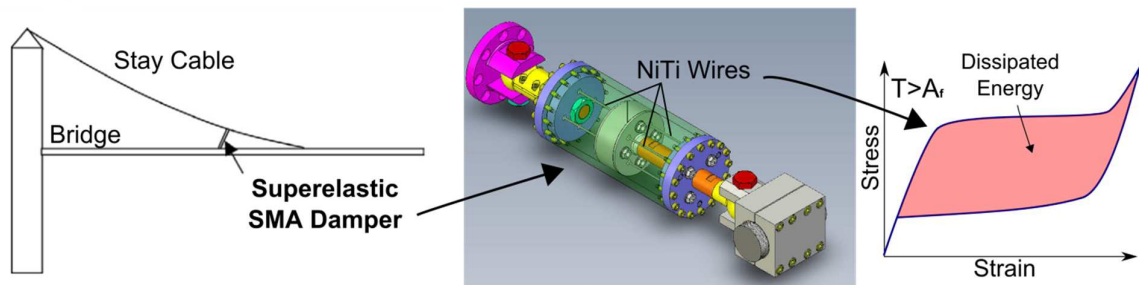


Figure 2-20 Prototype of a superelastic damper for stay-cable bridges using NiTi wires [65].

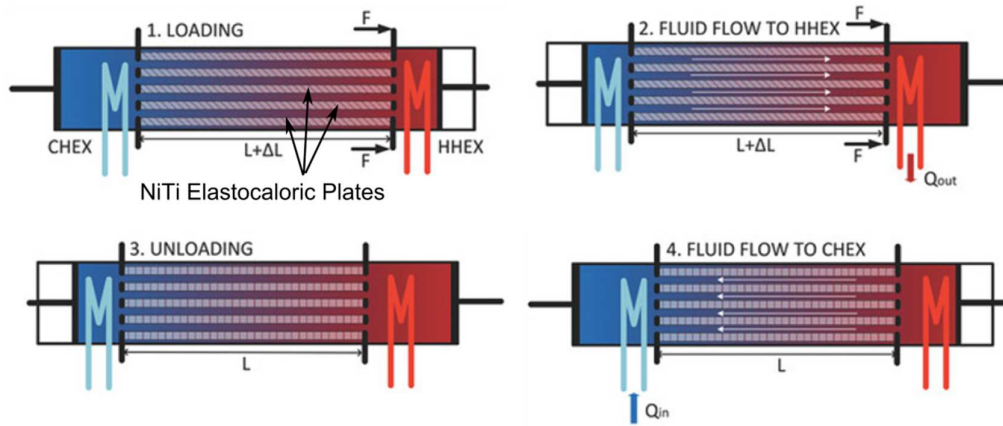


Figure 2-21 Operation of a prototype of elastocaloric device made of superelastic NiTi plates [72].

at the expense of plastic deformation, under the presumption that such deformation can be tolerated by the structure. By using superelastic NiTi instead, plastic deformation can be reduced substantially while keeping a high rate of dissipated energy.

A prototype of a bridge cable damper designed by Peignet et al. [65] is illustrated in Figure 2-20.

#### 2.4.3.4. Elastocaloric devices

Elastocaloric devices are a new cooling technology based on martensitic phase transformations of SMA. Since NiTi alloys show one of the highest latent heat production/absorption upon phase transformations (leading to adiabatic temperature span of more than 20K [71]), it has become an ideal candidate for the task. The schematic of the elastocaloric device prototype proposed by Tusek et al. in [72] is illustrated in Figure 2-21. It consists of parallel elastocaloric plates made of NiTi, a hot heat exchanger (HHEX), a cold heat exchanger (CHEX), a heat-transfer fluid, a fluid displacement system, and an actuator to load and unload the NiTi plates.

The elastocaloric device shown in Figure 2-21 works as follows. First, the actuator load the NiTi elastocaloric plates inducing the forward martensitic transformation. Heat-transfer fluid, flowing to the hot heat exchanger HHEX, evacuates the heat produced by the plates upon the transformation. The cooling action occurs when heat-transfer fluid is pumped towards the cold heat exchanger CHEX at the same time as the plates are unloaded, inducing the reverse transformation. These operational steps are repeated to maintain low the temperature at CHEX.

Like other applications that use NiTi elements subjected to repetitive superelastic cycles, the structural and functional fatigue of NiTi are the main drawbacks that has slowed down the development of solid-state SMA elastocaloric devices.

## 2.5. Fatigue of NiTi Alloys

After the paper of Eggeler et al. [23], researchers has tackled the fatigue of SMA from two different perspectives: functional fatigue and structural fatigue. The former refers to the

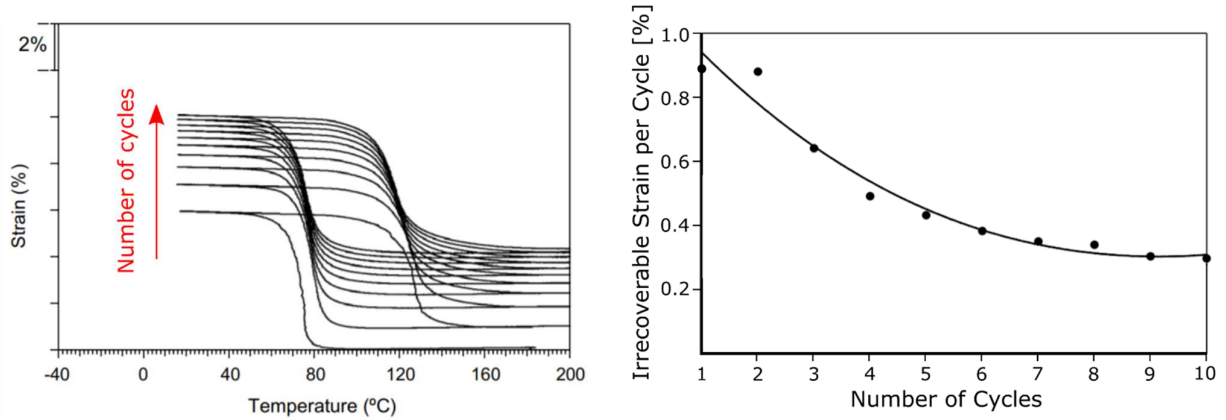


Figure 2-22 Functional fatigue exhibited by NiTi alloys upon thermal cycles [73].

degradation of the functional properties of the material during repetitive thermal or mechanical cycles such as reduction of transformation strain, transformation temperatures shifting, transformation hysteresis reduction, appearance of irrecoverable strain, etc. Structural fatigue, on the other hand, refers to the initiation and propagation of cracks in the material that leads to fatal failure during repetitive mechanical loading. Both approaches are of great interest to the NiTi community as they determine the safety and efficacy of NiTi-based engineering applications. In the following sections, we introduce the main aspects of the functional fatigue of NiTi alloys. Then, we detail the up-to-date findings concerning the structural fatigue of NiTi alloys.

### 2.5.1. Functional fatigue

#### 2.5.1.1. Temperature cycles

The cyclic instability of the shape memory effect upon thermal cycles under constant stress (actuation cycles) is an often problem reported in the literature [73]–[75]. The commonly observed phenomena over cycles are (Figure 2-22):

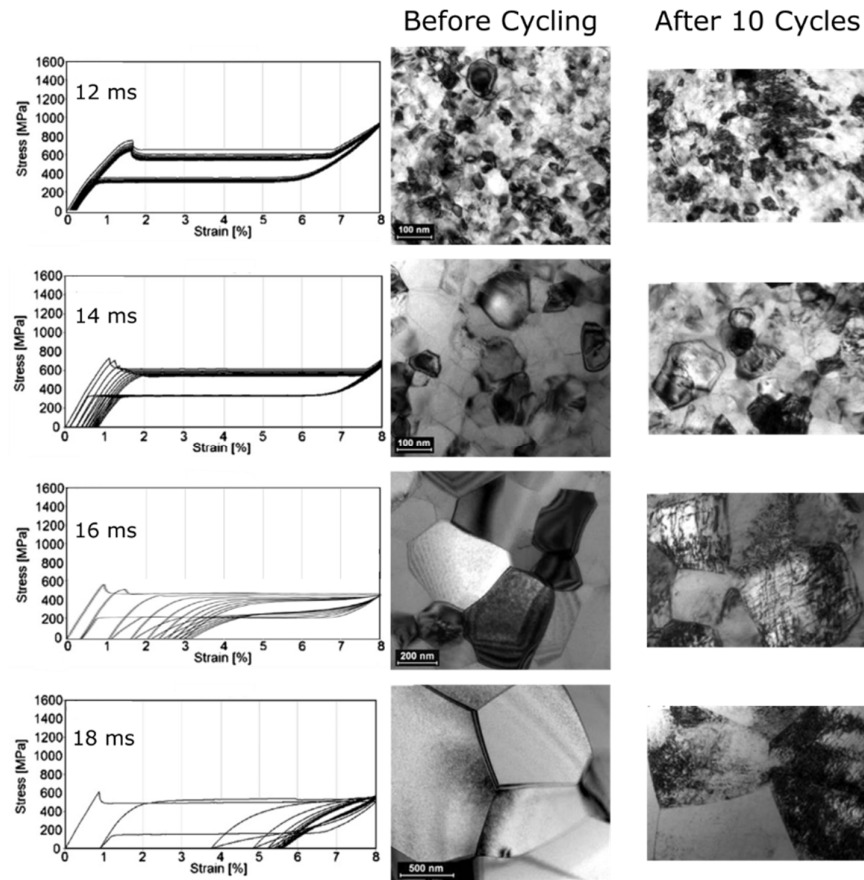
- the decrease of the thermal hysteresis loops,
- the increase of the martensite start temperature ( $M_s$ ),
- the decrease of transformation strain, and
- an irrecoverable (plastic) strain.

The cyclic instability of the shape memory effect in NiTi SMA has been attributed to local plasticity through dislocation slip caused by incompatibility between austenite and martensite phases during transformation [51]. The local plastic deformation modifies the stress in the matrix at the point that residual martensite is retained after heating [76]. Consequently, residual martensite-austenite interfaces lower the driving force needed for the forward transformation in subsequent cycles, justifying the increase of temperature  $M_s$ . Moreover, the reported changes in the strain-temperature response of NiTi are magnified by increasing the applied stress.

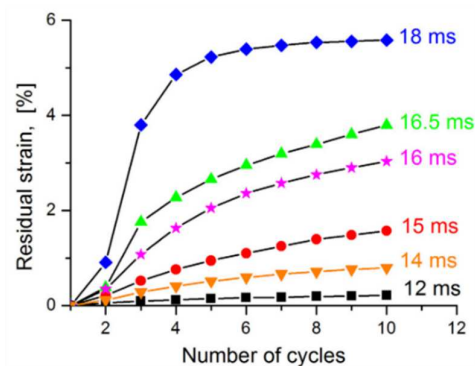
## 2.5.1.2. Stress cycles

Upon repetitive superelastic cycles, the stress-strain response of the material also varies considerably. Similar phenomena to the ones listed for actuation cycles are often reported in the literature [77]–[79]:

- decrease of the mechanical hysteresis,
- decrease of the stress needed for the forward transformation  $\sigma_{mt}$ ,
- irrecoverable (plastic) strain,



a)



b)

Figure 2-23 Functional fatigue of NiTi upon tensile stress cycles [77].

- strain hardening behavior change (distortion of the plateau-like stress-strain response),
- the decrease of the transformation strain.

These changes evolve exponentially with the number of cycles until the stress-strain response is finally stabilized. Moreover, thermomechanical heat treatment, resulting in different grain size and precipitates density, has proven to have a significant impact on the evolution of the superelastic response of NiTi with cycles [49], [78]. To illustrate the impact of grain size in the cyclic response of NiTi, Figure 2-23 shows experimental results obtained on cold-worked 100 $\mu\text{m}$  wires prepared by different electric power pulse heat treatments [77]. As shown, bigger grain sizes resulted in more dramatic functional properties drop, although sooner stress-strain response stabilization (Figure 2-23b). The authors attributed this behavior to high slip dislocation density observed in bigger grain size wires ( $>200\text{nm}$ ) (see TEM bright filed images comparison in Figure 2-23a). Since small grain size provides higher dislocation slip resistance, nanosize grain NiTi components are preferred for applications.

Together with dislocations, residual martensite is often reported upon superelastic cycles. This phenomenon seems to be a consequence of the resultant residual stress generated due to plastic deformation in the austenitic matrix[80]. However, the interaction between phase transformations and plasticity is still one of the main matters of debate nowadays.

### 2.5.2. Structural fatigue

The structural fatigue of NiTi is similar to classic metal fatigue in the sense that the number of cycles until rupture (lifetime) is the most important failure parameter. The mechanical fatigue of traditional metals is divided into low-cycle (LCF) and high-cycle fatigue (HCF), as they show different deformation and cyclic damage mechanisms. The yielding point of the material often defines the transition between these two regimes. Lifetimes of samples loaded above the yielding stress are considered in the LCF regime, as they differ by orders of magnitude with lifetimes of samples loaded below the yielding stress, which belong to the HCF regime. However, applying such definition to NiTi alloys is less straightforward due to its complex thermomechanical behavior.

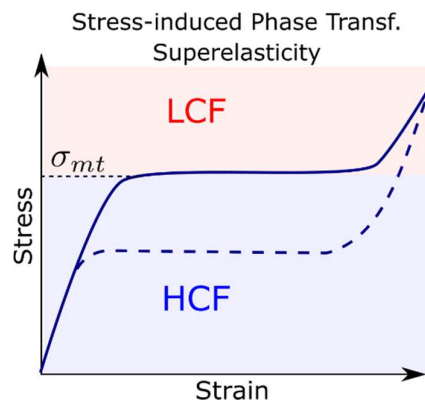


Figure 2-24 Definition of the low cycle (LCF) and high cycle (HCF) regimes for superelastic NiTi.

As we discussed in previous sections, NiTi exhibits several yielding points: martensite detwinning, stress-induced  $B2 \rightarrow R$  and  $B2/R \rightarrow B9'$  transformations, and B2 and B19' slip. All these yielding points and their related deformation mechanisms depend on temperature, alloy composition, loading path, and thermomechanical heat treatment. However, for reasons of simplicity, we decided to define the transition point from HCF and LCF at the phase transformation stress  $\sigma_{mt}$  for superelastic NiTi (Figure 2-22).

Since the most attractive properties of NiTi alloys involve stress-induced phase transformations, less attention has been paid to the characterization of the HCF properties of superelastic NiTi in fatigue studies. Consequently, the mechanisms leading to failure in the “elastic regime” of NiTi are still unknown, and most of the existing failure models proposed in the literature are based on Coffin-Manson fatigue relationship, applicable for large strains only. Moreover, HCF requires large number of testing hours, special sample preparation, and carefully conditioning of experimental setups, which might discourage researchers to address this matter.

#### 2.5.2.1. Commonly used experimental setups

The development of NiTi-based endodontic files for tooth root canalization in the late 1980's motivated the study of the fatigue of NiTi wires using rotary bending tests (Figure

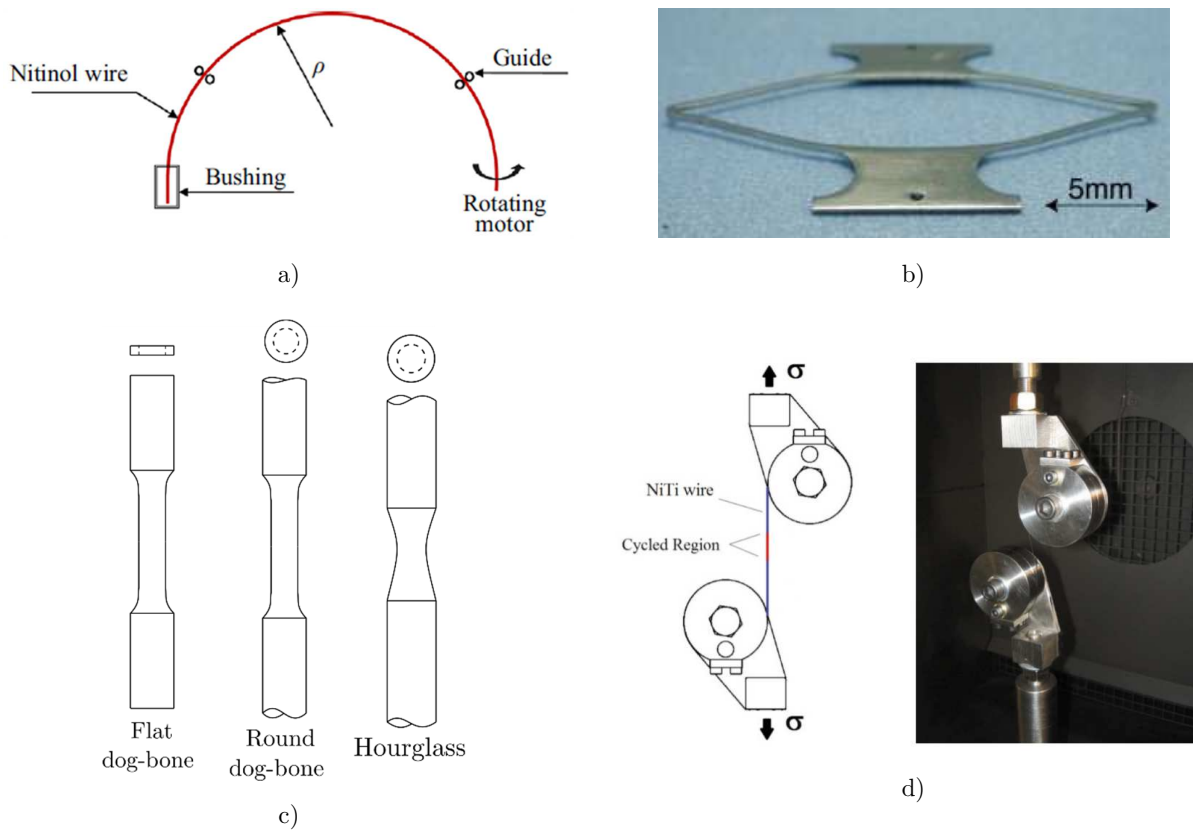


Figure 2-25 Experimental setups used for evaluating the fatigue of NiTi. a) Rotary bending system. b) Diamond shaped samples using for evaluating the fatigue of NiTi stents [81]. c) Reduced cross-section samples. d) Snubbing gripping device used for fatigue testing of thin wires. In this example the red zone of the wire was trained before the fatigue testing introducing a “virtual cross-section reduction” [82].

2-25a). Since then, a good amount of Strain-N curves has been reported in the literature showing the fatigue behavior of straight wire samples [83]–[86] and endodontic instruments [67], [69], [87]. Rotary bending experiments, although allowing a good characterization of endodontic files under nearly operation conditions, underestimate the surface strain in straight wire samples since it is calculated using the theory of pure bending of linear-elastic beams. However, due to the simplicity of the experimental setup and the possibility of applying high loading frequencies, rotary bending is today one of the most common methods used for evaluating the fatigue of NiTi wires.

Another common industrial-aimed fatigue experimental setup is the cyclic bending of laser cut “diamond” shaped samples (Figure 2-25b). This sample shape intends to mimic the cyclic loading conditions of laser cut stents. The calculation of the stresses and strain in the diamond is usually carried out using standard SMAs mechanical models implemented in Finite Element software suites. This type of approach results attractive for evaluating the

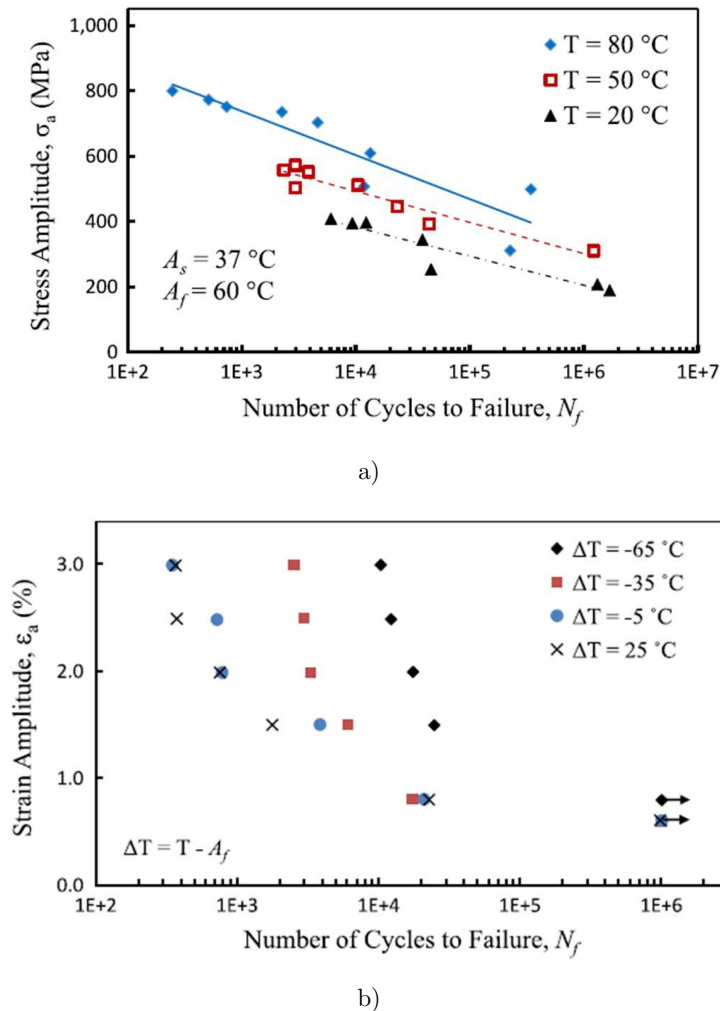


Figure 2-26 Fatigue curves of NiTi wires showing the effects of the temperature. a)Stress-life approach [88]. b)Strain-life approach[89]

lifetime of real devices, but the complexity of the local mechanical state upon loading hinders the understanding of the mechanisms and conditions leading to fatigue failure in NiTi.

The fundamental characterization of the fatigue of NiTi is carried out mostly using cyclic uniaxial tests. One of the main difficulties of tensile cyclic testing of NiTi elements using standard deformation rigs is the localization of the fatigue failure inside the rig clamps. Consequently, cross-section reduction samples are commonly employed for cyclic testing such as flat and cylindrical dog bone samples (Figure 2-25c). In the case of NiTi thin wires, cross-section reduction samples result difficult to manufacture. From our experience, the failure of thin wire samples upon fatigue loading is very often located at the clamping points, which cast doubts on the real stress and strain conditions leading to the fatigue failure. Researchers have tried to overcome this issue by using capillary clamping [90], microstructure gradients obtained through special heat treatments, and local material training (Figure 2-25d) [82]. In this work, we propose to assess the fatigue of  $\varnothing 1.78\text{mm}$  wires carefully manufactured into hourglass-shaped samples, which is the recommended shape for high cycle fatigue testing of metals [91]. This sample geometry was used for fatigue tests of NiTi in the pioneering work of Melton and Mercier back in 1979 [92], however, since then, no more fatigue studies have been conducted using this kind of samples.

#### 2.5.2.2. Classic fatigue approaches

The multiplicity of deformation mechanisms that characterizes the NiTi behavior makes it difficult to compare fatigue performances based on S-N (or Strain-N) fatigue curves only. For example, due to differences in elastic properties and yielding stress, martensitic samples may exhibit better fatigue performance than austenitic samples in terms of the applied strain, but worse in terms of the bearable stress. Of course, for engineering applications, the choice of one criterion over the other depends on the loading conditions of the NiTi device. However, this particular fact leads often to misinterpretations upon analysis of the impact of crystallographic phases, deformation mechanisms, temperature, heat treatments, and stress/strain ratio in the fatigue performance of NiTi. Such is the case of studies that compare the fatigue behavior of samples with different transformation temperatures or samples tested at different temperatures with respect to  $A_f$  [24], [86], [88], [89]. For instance, in Figure 2-26 we show two fatigue studies obtained by stress and strain life approaches using tensile and rotary fatigue testing respectively. In the stress-life approach (Figure 2-26a), the fatigue performance of NiTi at  $80^\circ\text{C}$  outperforms the fatigue performance at lower temperatures. In contrast, the samples tested at lower temperatures using the strain life approach (Figure 2-26b) shows better fatigue performance than the ones tested at higher temperatures. Since the temperature change implies different deformation mechanisms upon loading, we can deduce that samples tested at  $80^\circ\text{C}$  and  $50^\circ\text{C}$  in Figure 2-26a, and  $\Delta T = 25^\circ\text{C}$  samples in Figure 2-26b involved austenite elastic loading and superelasticity, while the rest of the samples might involve martensite detwinning, martensite elasticity and partial superelasticity. In these studies, the lack of information about the thermal history of the samples and the rest of transformation temperatures renders more difficult the analysis.

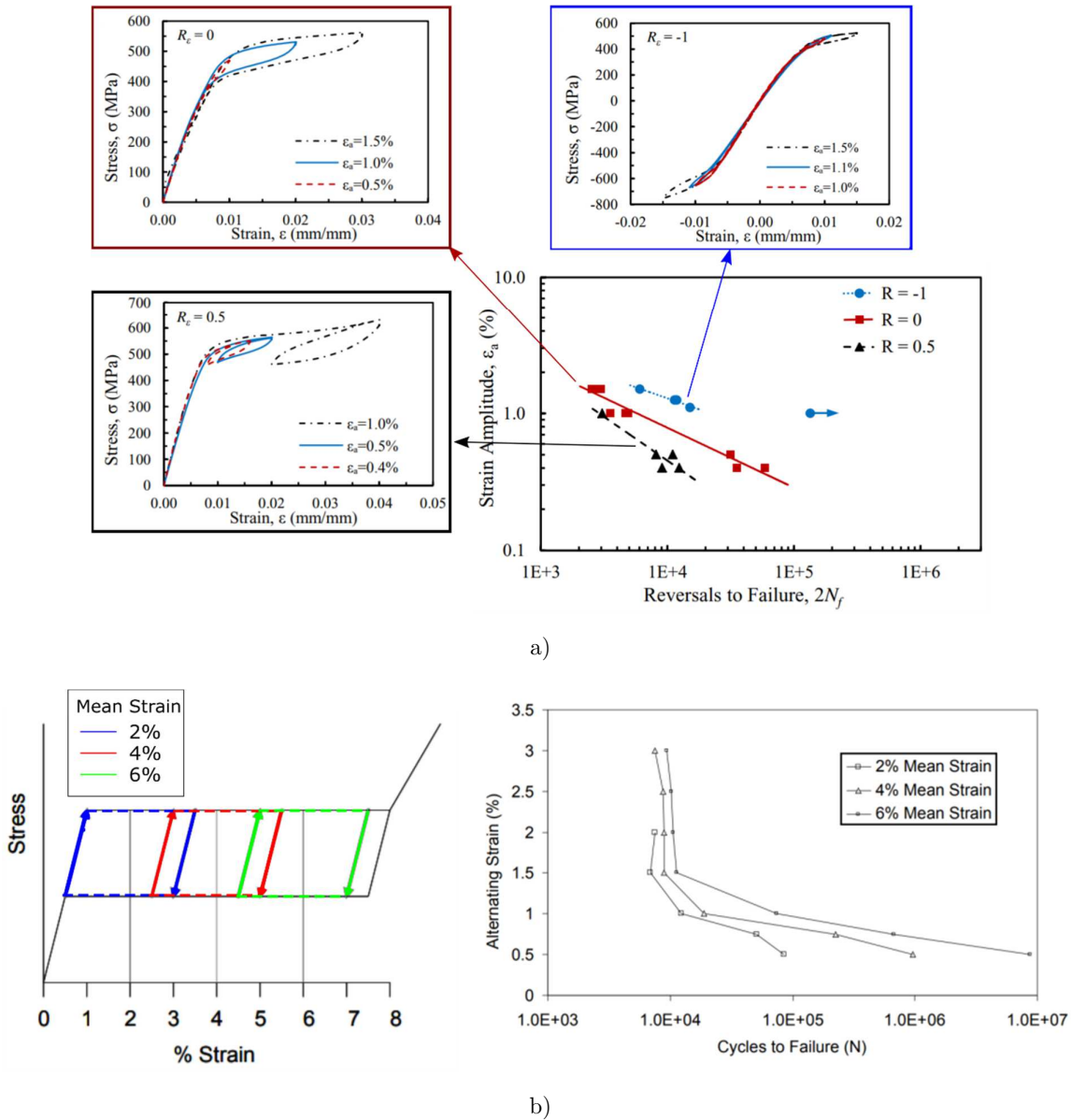


Figure 2-27 Influence of the mean strain on the fatigue performance of NiTi. a) Elastic and transformation regimes (replotted from [93]). b) Biphasic regime (replotted from [94]).

In the superelastic regime, due to the forward and reverse transformation stress plateaus, the impact of the stress amplitude, mean stress, strain amplitude, and mean strain in the lifetime of NiTi is more difficult to evaluate. Some studies like [94], [95] have reported that the tensile mean strain enhances the fatigue resistance of NiTi, contrarily to what happens in traditional alloys. However, other studies have proven differently. For instance, experimental results reported in [93] (Figure 2-27a), show that higher mean strains resulted in worse fatigue performance, whereas results reported in [96] (Figure 2-27b), show better fatigue performances when the mean strain was equal to the strain at the middle of the stress plateau. These discrepancies might be caused by differences in the experimental protocols adopted in each study. While the results reported in [94]–[96] focused on mean strains in the stress plateau (as in Figure 2-27b), with ongoing martensitic transformation, the results in

[93] included austenite elastic loading and martensitic transformation onset (Figure 2-27a). As a result, we may conclude that mean strain has a significant impact on the fatigue of NiTi, but show different trends according to the loading regime under which the material is loaded.

### 2.5.2.3. Special features of fatigue life curves

A more recent study [97] revealed some interesting aspects of the effects of mean-strain and loading scenario in the fatigue of NiTi. In this study, the researchers assessed the tensile structural fatigue of superelastic NiTi in three different strain regimes under same stress conditions: elastic austenite, austenite to martensite transformation, and elastic martensite.

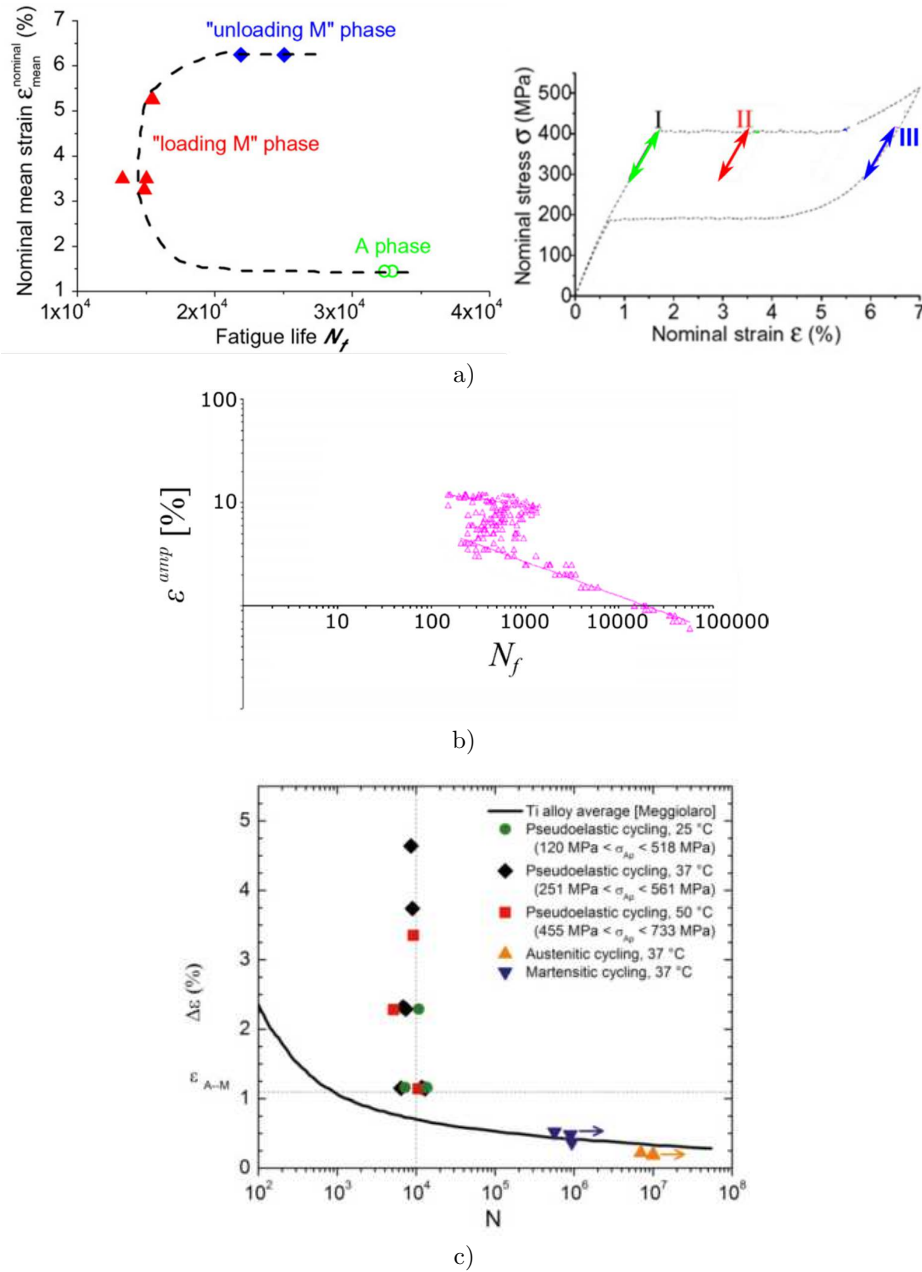


Figure 2-28 Special features of S-N and Strain-N curves in NiTi. a) C-shaped S-N curve obtained in NiTi flat samples [97]. b) Z-shaped Strain-N curve obtained upon rotary bending fatigue of NiTi wires [98]. c) Constant life time upon deformation in the strain plateau [82].

Their results showed that austenite and martensite elastic regimes outperformed the fatigue performance of transforming NiTi samples. Consequently, the resulting Strain-N curve showed a very unusual C-shape (Figure 2-28a). In the case of transforming NiTi, fatal cracks were found in zones where the characteristic localization bands of tensile loaded NiTi appeared. Based on x-ray resolved stress at the band front previously shown in Figure 2-14, we may deduce that the local stress in the case of transforming NiTi was much higher than in the elastically loaded cases, which resulted in earlier fatigue failure.

The localized nature of the deformation of NiTi contrasts with the nominal strain values showed in NiTi Strain-N curves. As a result, the lifetime obtained in the transformation region is apparently independent of the applied strain amplitude. Such is the case of the Strain-N curves of rotary bending and tensile-tensile fatigue tests of wires shown in Figure 2-28b and Figure 2-28c respectively. The peculiar z-shaped trend of the Strain-N curve in Figure 2-28b even shows that in a range of 1-10% strain amplitude, longer lifetimes are obtained by increasing the applied strain. In Figure 2-28c, tensile-tensile fatigue of superelastic NiTi wires (referred as pseudoelastic in the legend of the figure) shows same lifetimes ( $10^4$ ) regardless of the temperature and stress level attained upon cycling. Moreover, results in Figure 2-28c show infinite lifetimes upon elastic loading of austenite and martensite.

The apparent detrimental effects of the martensite transformation on the fatigue life of NiTi as well as its heterogeneous behavior may induce earlier fatigue failure in samples with constant cross-section. These detrimental effects are maximized in the clamping points during cyclic tensile testing. Failure inside the machine clamps might lead to a large underestimation of the fatigue strength of the material, and to an increase of the fatigue data scatter.

#### 2.5.2.4. Fatigue damage mechanisms

The mechanisms responsible for the fatigue failure of NiTi in the LCF regime are commonly related to the mechanisms behind its functional fatigue, i.e. dislocation slip plasticity and retained martensite. On the other hand, we found very little evidence in the literature concerning the failure mechanisms in the HCF regime. We consider that there is a lack of knowledge on how cracks initiate and propagate when the amplitude of the applied loading remains beneath the stress need for B19' martensite phase transformation.

So far, we have found only one study that addressed the material structural damage after a high cycle fatigue loading of superelastic NiTi [99]. In this study, the authors cycled in tension a dog bone 50.8at.%Ni flat sample in strain control conditions reaching a maximal stress of  $\sim 300$ MPa (Figure 2-29a),  $\sim 100$ MPa lower than the martensite stress plateau. The sample was obtained from a cold rolled sheet annealed at  $600^\circ\text{C}$  for 30min. The authors studied the damage of a sample loaded in pull-pull tension (stress ratio  $R=0$ ) at 0.25% strain amplitude at a frequency of 20Hz. The sample was subjected to  $2 \times 10^5$  cycles, then, ex-situ TEM analyses were performed. For comparison purposes, the initial microstructure of an equally prepared sample, observed under TEM, is presented in Figure 2-29c and the TEM

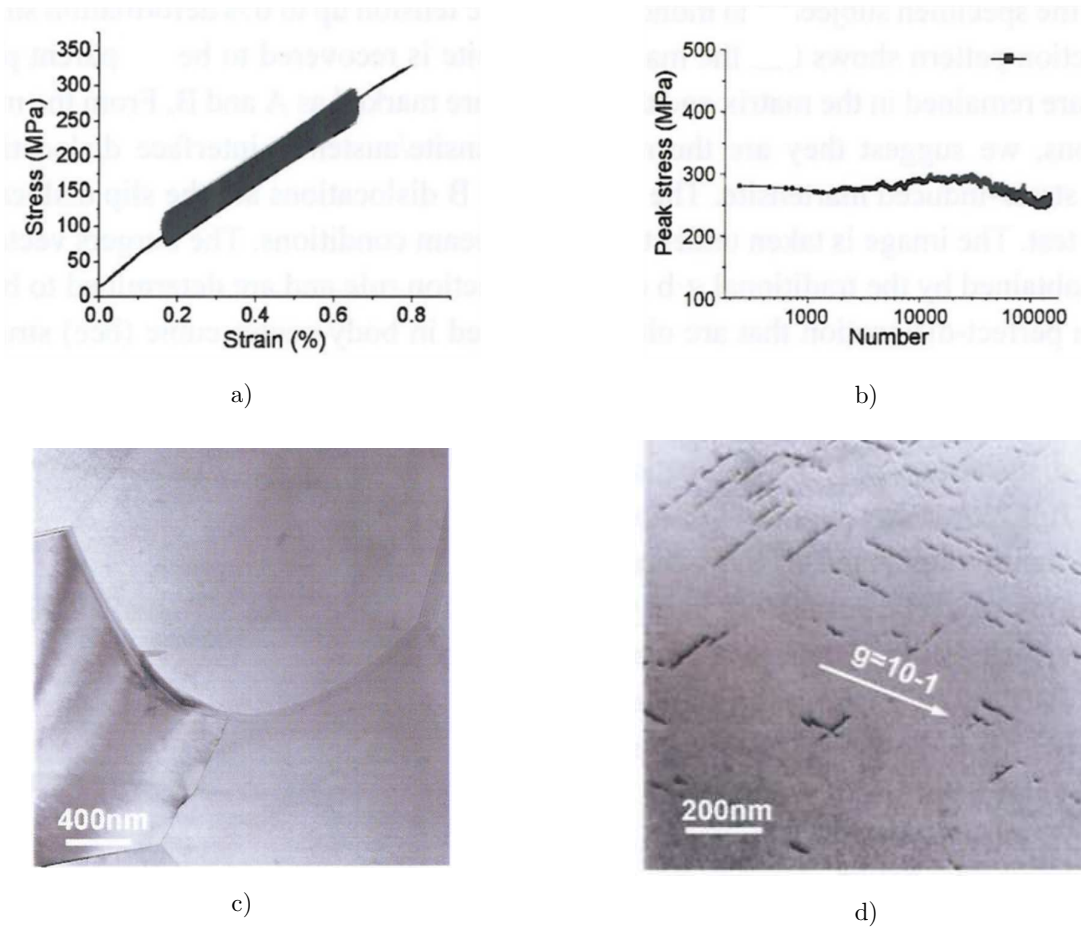


Figure 2-29 HCF failure mechanisms in NiTi [99].

of the cycled sample is shown in Figure 2-29d. The authors evidenced that the elastic austenite loading region produced short slip dislocations, which they related to the subtle material softening observed after  $2 \times 10^4$  cycles (see decrease of the maximal stress attained in b). After the high cycle fatigue, the authors did not evidence residual martensite.

## 2.6. Summary

In this state-of-the-art, we tackled the main properties of NiTi alloys. We pointed out that most commercial NiTi wires as the ones we use for this work, are susceptible to develop R-phase, as they exhibit microstructures with high dislocation density produced upon cold work together with precipitates, which grow upon annealing the alloy at temperatures between  $400^\circ\text{C}$  and  $500^\circ\text{C}$ . As a result, commercial NiTi exhibits a multiplicity of deformation mechanisms, which depend on temperature, thermomechanical heat treatment, and loading history. Such a diverse mechanical behavior renders difficult the assessment of the structural fatigue of NiTi. We consider that the use of classic fatigue approaches for describing the fatigue behavior of NiTi needs to be carried out taking into account factors such as the testing temperature, loading regime, preparation of the alloy, and of course stress and strain values. Based on the presented experimental evidence, we draw the following conclusions and remarks concerning the structural fatigue of NiTi alloys:

- NiTi shows an accelerated fatigue wearing when the stress-induced B19' transformation regime is entered. In contrast, elastic loaded NiTi, either in austenite or martensite state, might exhibit infinite life. Experiments show that even when superelastic NiTi is preloaded at high strain levels into the martensite regime, and then fatigued at small loading amplitudes, the resulting fatigue lives are comparable to elastically loaded austenite.
- The heterogeneous nature of the B19' phase transformation in tensile tested NiTi cast doubts on the strain and stress values reported in S-N and Strain-N fatigue curves. Moreover, the strain localization in superelastic NiTi might be responsible for the well-known, but not often reported, accelerated failure of samples within the clamping system of fatigue machines.
- During superelastic phase transformation, the fatigue damage seems to be concentrated to the interface between austenite and martensite phases.
- The structural fatigue performance of NiTi is temperature dependent. However, there is still no certainty that this is caused by a change of the deformation mechanisms induced by the temperature or an effect of the temperature itself.
- The austenite-to-martensite transformation introduces dislocation slip, which is responsible for the so-called functional fatigue of NiTi. Dislocation slip might be also responsible for structural LCF damage. On the other hand, cyclic elastic loading of austenite might produce short dislocation slip like in other structural metals upon low amplitude repetitive loading. This may explain the rarely reported failure of austenite in the HCF regime.
- The heat treatment affects the fatigue behavior of NiTi alloys either by modifying their transformation temperatures or by affecting their polycrystalline microstructure (grain size, defects, precipitation). As result, the conclusions drawn from HCF studies of NiTi usually mixed the role of the polycrystalline microstructure with the effects of temperature and crystallographic phase transformations.



# Chapter 3. Tensile Behavior of Hourglass-Shaped NiTi Samples

In this chapter, we analyze the thermomechanical behavior of hourglass-shapes used for assessing the fatigue performance of NiTi wires. The chapter is divided into four sections. First, we present an analysis of the stress distribution in the progressively reduced cross-section of the samples. For this purpose, we used an isotropic-elastic and perfect plastic constitutive laws. We emphasize on the impact of the sample shape on the stress concentration and triaxiality ratio in the mid cross-section. In the second part, we present the material used for the fatigue study. We start by showing the material response of as-received cold-drawn wires and the impact of annealing temperatures on the thermomechanical behavior of the samples. According to this evaluation, we chose the heat treatment used for fatigue tests presented later in chapter 4. In the third section, we describe the confined deformation/transformation processes occurring upon tensile loading in the mid cross-section of hourglass-shaped samples using Digital Image Correlation (DIC) and Synchrotron source x-ray diffraction. These experimental results permitted us to fit an SMA-suited thermomechanical model, with which we evaluated the impact of phase transformations on the stress in hourglass-shaped samples. This detailed description of the mechanical and chemical processes that take place during tensile loading of NiTi laid the groundwork for the fatigue analysis presented in the next chapter. The last section summarizes the main aspects to consider when using hourglass shaped samples for fatigue assessment of NiTi wires.

## Contents

<b>3.1. The hourglass shape.....</b>	<b>47</b>
3.1.1. Linear-Elastic Response .....	47
3.1.1.1. Analytical solution.....	47
3.1.1.2. Finite element solution .....	52
3.1.2. Non-linear material behavior.....	56
<b>3.2. Material of the study .....</b>	<b>57</b>
3.2.1. Cold-drawn NiTi wires.....	58
3.2.1.1. Tensile response.....	58
3.2.2. Preparation of hourglass-shaped samples .....	60

3.2.3. Effects of annealing temperatures .....	62
3.2.3.1. Oxide Layer .....	63
3.2.3.2. Differential Calorimetry Scanning measurements .....	64
3.2.3.3. Tensile responses .....	66
3.2.3.4. Heat treatment choice for fatigue testing .....	70
<b>3.3. Thermomechanical behavior of 500°C-annealed NiTi.....</b>	<b>72</b>
3.3.1. Stress-strain response .....	72
3.3.1.1. B2↔R phase transformation regime .....	73
3.3.1.2. R/B2→B19' phase transformation regime .....	76
3.3.2. Microstructure evolution resolved via X-ray diffraction.....	78
3.3.2.1. Experimental setup.....	79
3.3.2.2. Diffraction pattern evolution upon loading.....	81
3.3.3. Simulation of the tensile response using 3D finite element analysis .....	83
3.3.3.1. Description of the model.....	83
3.3.3.2. Model parameters identification .....	88
3.3.3.3. Simulations vs Experiments.....	94
3.3.3.4. Approximation of the local material response of NiTi using the macroscopic response of hourglass-shaped samples.....	101
<b>3.4. Summary .....</b>	<b>102</b>

### 3.1. The hourglass shape

The hourglass-shaped samples used in this study have a progressive circular cross-section reduction introduced by a U-shaped groove of radius  $r_t$ , as illustrated in Figure 3-1a. There, the radius of the original wire is denoted as  $r_w$  and the radius of the mid cross-section is denoted as  $r_n$ . The main experimental setup that we used for evaluating the mechanical and fatigue responses of hourglass-shaped samples consisted of a tensile testing machine allowing force or displacement constraints, and a clip-on extensometer. The experimental boundary conditions upon tensile testing were defined either in terms of the applied tensile force or in terms of the elongation of the extensometer, gauge length of which was delimited within planes A and B, perpendicular to the sample's axis as shown in Figure 3-1b. The initial gauge length  $L_G$  in Figure 3-1b is defined as the initial distance between the arms of a clip-on extensometer attached to the sample, and  $u_{gl}$  as the elongation of the gauge length upon tensile loading.

Next, we evaluate the impact of sample geometry on the distribution of the stress and strain along the reduced cross-section zone. First, we develop an analytic expression for the calculation of nominal stress and strain from the force and extensometer elongation data, assuming an isotropic-elastic material behavior. After that, the analytical solution is contrasted with an equivalent finite element solution. Finally, the changes of the stress distribution upon a strong material nonlinearity are subjected to analysis. For this, we carried out finite element simulations using a perfect-plasticity constitutive law.

The study cases presented next are valid for wire diameters between 1-2mm, radius reductions ( $r_n/r_w$ ) between 0.5-0.9 and a groove radius  $r_t$  equal to 10mm. These geometric conditions cover the range of testing samples used during this research work.

#### 3.1.1. Linear-Elastic Response

##### 3.1.1.1. Analytical solution

Due to the mid-plane symmetry of hourglass shaped samples, we consider only a half of a sample subjected to the tensile force  $F$  as shown in Figure 3-1c. The coordinate  $z$  is introduced at the mid cross-section in the same direction as the axis of the sample. Assuming that the axial stress is uniformly distributed over the cross-section  $A(z)$  at a fixed value of  $z$ , the stress and strain tensors for an isotropic elastic material, with Young Modulus equal to  $E$  and Poisson's ratio  $\nu$ , in cylindrical coordinates simply reads

$$\bar{\sigma} = \begin{bmatrix} 0 & 0 & 0 \\ & \sigma_{zz} & 0 \\ sym & & 0 \end{bmatrix}_{rz\theta}, \quad (3.1)$$

and

$$\bar{\varepsilon} = \begin{bmatrix} -\nu \sigma_{zz}/E & 0 & 0 \\ & \sigma_{zz}/E & 0 \\ sym & & -\nu \sigma_{zz}/E \end{bmatrix} \quad (3.2)$$

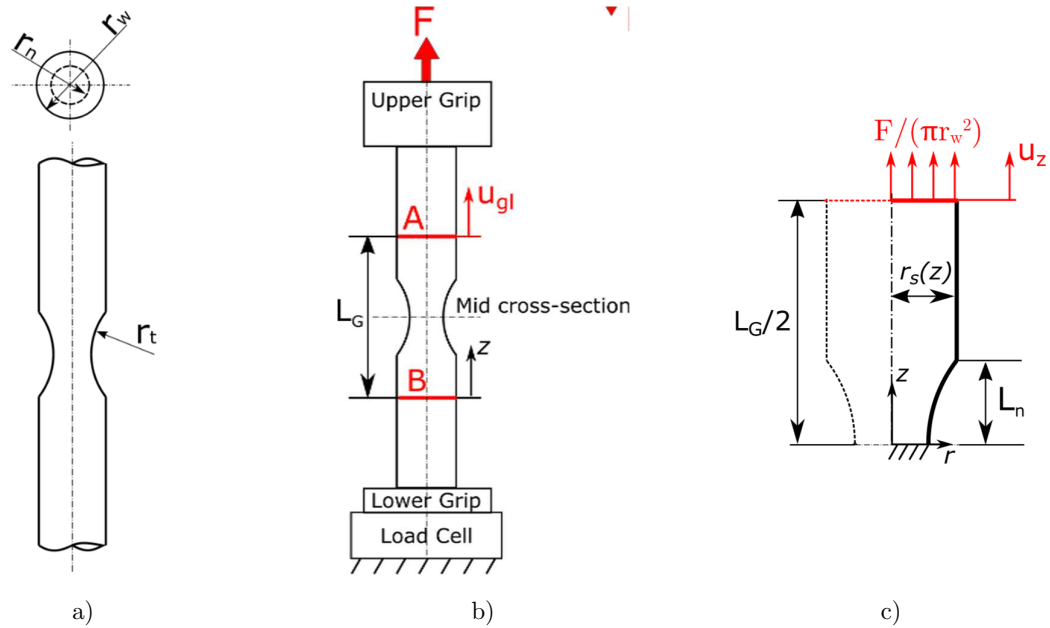


Figure 3-1 a) Geometry of hourglass-shaped samples. b) Experimental boundary conditions used during characterization and fatigue tests of hourglass-shaped samples. c) Boundary conditions and geometry used for carrying out an analytical solution for stresses and strains in the gauge length  $L_G$ .

where

$$\sigma_{zz}(z) = \frac{F}{A(z)} \quad (3.3)$$

The circular cross section  $A(z)$  is equal to  $\pi r_s^2$ , being  $r_s$  the radius of the cross-section along the  $z$  axis. The radius  $r_s$  is a function of  $z$ , which can be written as

$$\begin{aligned} 0 < z < L_n : \quad r_s(z) &= -\sqrt{r_t^2 - z^2} + r_n + r_t \\ L_n < z < L_G : \quad r_s(z) &= r_w \end{aligned} \quad (3.4)$$

As it can be deduced from equations (3.3) and (3.4), the distribution of the axial stress along the axis  $z$  depends on the geometry of the sample, defined by the parameters  $r_n$ ,  $r_w$ , and  $r_t$ . The effect of the radius reduction and wire radius on the axial stress distribution illustrated in Figure 3-2a. Here, the axial stress distribution along the  $z$ -axis is plotted for different combinations of wire diameters between 1-2mm, groove radius equal to 10mm, and radius reductions ( $r_n/r_w$ ) between 0.5 and 0.9.

The axial stress at the mid cross-section is solely determined by the radius  $r_n$ . On the other hand, the wire radius  $r_w$  determines the axial stress gradient in the groove. For same radius reduction, larger wire radius  $r_w$  results in longer groove length, which allows for lower gradients of axial stress along  $z$  axis (Figure 3-2c). From equation (3.2), we can deduce that higher gradient of axial stress produces higher gradient of radial strains as well ( $-\nu\sigma_{zz}$ ). This causes shear stresses in the sample's surface, which are not contemplated by the analytical solution but will be analyzed later using finite element analysis.

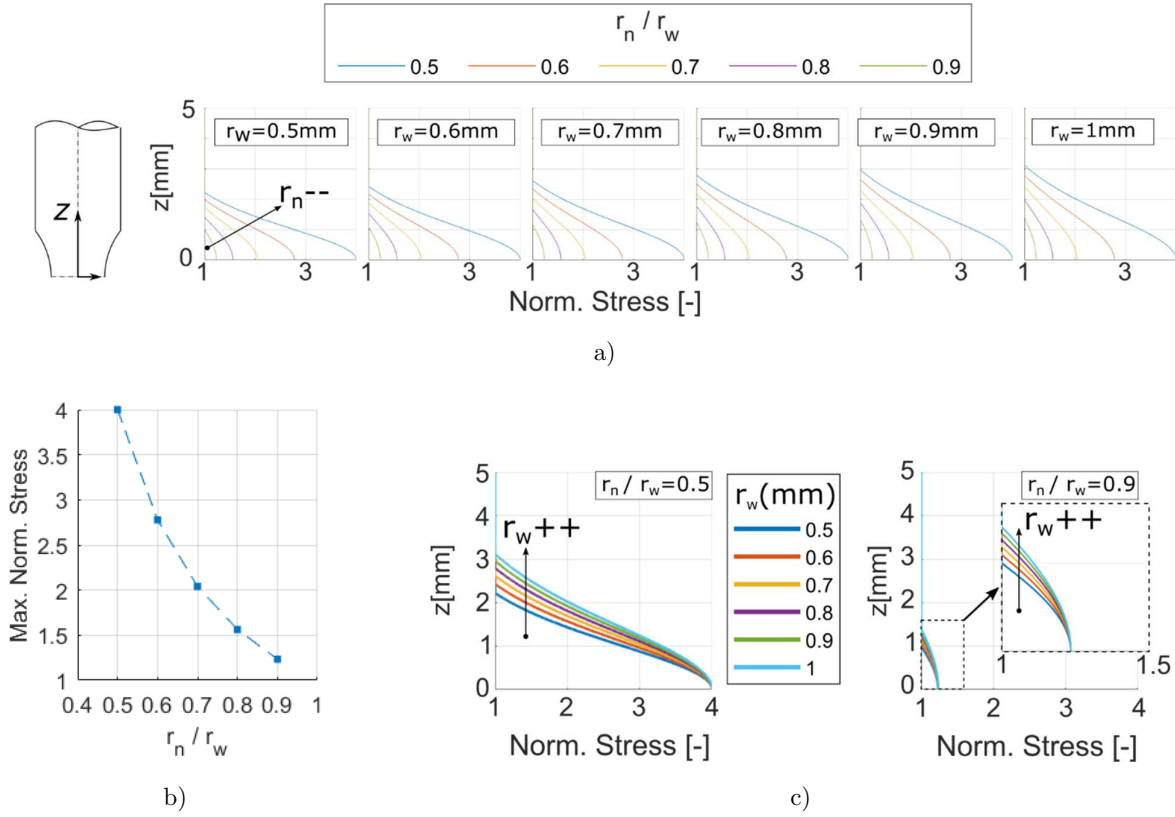


Figure 3-2 a) Axial stress distribution in hourglass-shaped samples of different wire diameters and radius reductions. The axial stress across the cross-section was normalized with respect to the stress in the straight part of the samples. The maximum stress increase at the mid cross-section is plotted in terms of the radius reduction in (b). Figures in (c) show the effect of the wire radius on the axial stress gradient in the groove zone of hourglass shaped samples.

With the definition of the axial stress along the z-axis, a half of the elongation of the gauge length of the samples ( $u_z$ ), in response to the applied force  $F$ , can be calculated by integrating the axial component of the strain (3.2) in the z direction:

$$\begin{aligned}
 u_z(L_G / 2) &= \int_0^{L_G/2} \varepsilon_{zz} dz = \frac{F}{\pi E} \int_0^{L_G/2} \frac{1}{r(z)^2} dz \\
 &= \frac{F}{\pi E} \left[ C + \frac{1}{r_w^2} \left( \frac{L_G}{2} - L_n \right) \right] .
 \end{aligned} \tag{3.5}$$

where

$$C = \int_0^{L_n} \frac{1}{r(z)^2} dz = \int_0^{L_n} \frac{1}{\left( \sqrt{r_t^2 - z^2} + r_n + r_t \right)^2} dz . \tag{3.6}$$

We addressed the resolution of (3.6) numerically using the commercial mathematical computing software MATLAB. For a fixed groove radius  $r_t$ , equal to 10mm, and wire radius  $r_w$  between 1-2mm, the evolution of  $C$  with respect to the radius reduction  $r_n/r_w$  in a range between 0.5-1 is plotted in Figure 3-3a.

Based on this group of solutions, we propose an alternative procedure for calculating  $C$ , consisting in approximating the curves in Figure 3-3a by a cubic polynomial

$$C = A_3 \left( r_n / r_w \right)^3 + A_2 \left( r_n / r_w \right)^2 + A_1 r_n / r_w + A_0. \quad (3.7)$$

The polynomial constants  $A_3$ ,  $A_2$ ,  $A_1$ , and  $A_0$  show a quadratic evolution with  $1/r_w$ , as it is illustrated in Figure 3-3(b-e). Using polynomial fitting, these polynomial constants read

$$\begin{aligned} A_3 &= -17.91 \left( 1/r_w \right)^2 - 51.73/r_w + 12.3 \\ A_2 &= 44.82 \left( 1/r_w \right)^2 + 129.24/r_w - 30.84 \\ A_1 &= -40.76 \left( 1/r_w \right)^2 - 117.38/r_w + 28.14 \\ A_0 &= 13.95 \left( 1/r_w \right)^2 + 40.13/r_w - 9.65. \end{aligned}$$

The polynomial approximation of  $C$  is valid only for  $r_t = 10\text{mm}$ , wire diameters between 1-2mm, and radius reduction  $r_n/r_w$  between 0.5-1.

Finally, the elongation of the entire gauge length resulting from the application of the axial force  $F$  can be written as

$$u_{gl} = 2u_z(L_G / 2) = \frac{2F}{\pi E} \left[ C + \frac{1}{r_w^2} \left( \frac{L_G}{2} - L_n \right) \right]. \quad (3.8)$$

Solving (3.8) for  $F$ , we can also calculate the reaction force resulting from an elongation  $u_{gl}$  as follows:

$$C = A_3 \left( r_n / r_w \right)^3 + A_2 \left( r_n / r_w \right)^2 + A_1 r_n / r_w + A_0$$

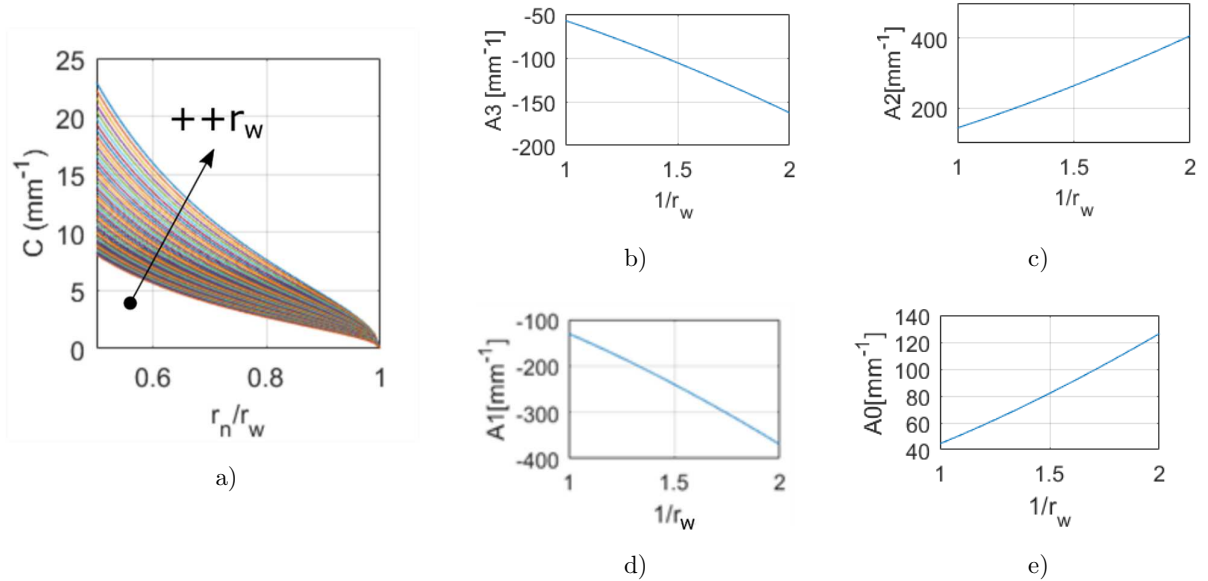


Figure 3-3 a) Evolution of term  $C$  with respect to the radius reduction ratio ( $r_n / r_w$ ). The evolution of  $C$  was approximated by a cubic polynomial, the constants of which evolve quadratically with respect to  $1/r_w$  as shown in (b-e).

$$F = \frac{\pi E u_{gl}}{2 \left[ C + \frac{1}{r_w^2} \left( \frac{L_G}{2} - L_n \right) \right]} \quad (3.9)$$

We can calculate the Young's Modulus  $E$  from a linear load vs extensometer elongation response using the following expression:

$$E = \frac{2F}{\pi u_{gl}} \left[ C + \frac{1}{r_w^2} \left( \frac{L_G}{2} - L_n \right) \right] \quad (3.10)$$

Equations (3.8) and (3.9) allow us to calculate the elastic response of hourglass shaped samples upon a monotonic tensile loading from force or displacement imposed boundary conditions. This solution assumes that the stress is uniform in the cross section  $A(z)$  and did not take into account the section reduction due to the radial and transverse components of the strain tensor.

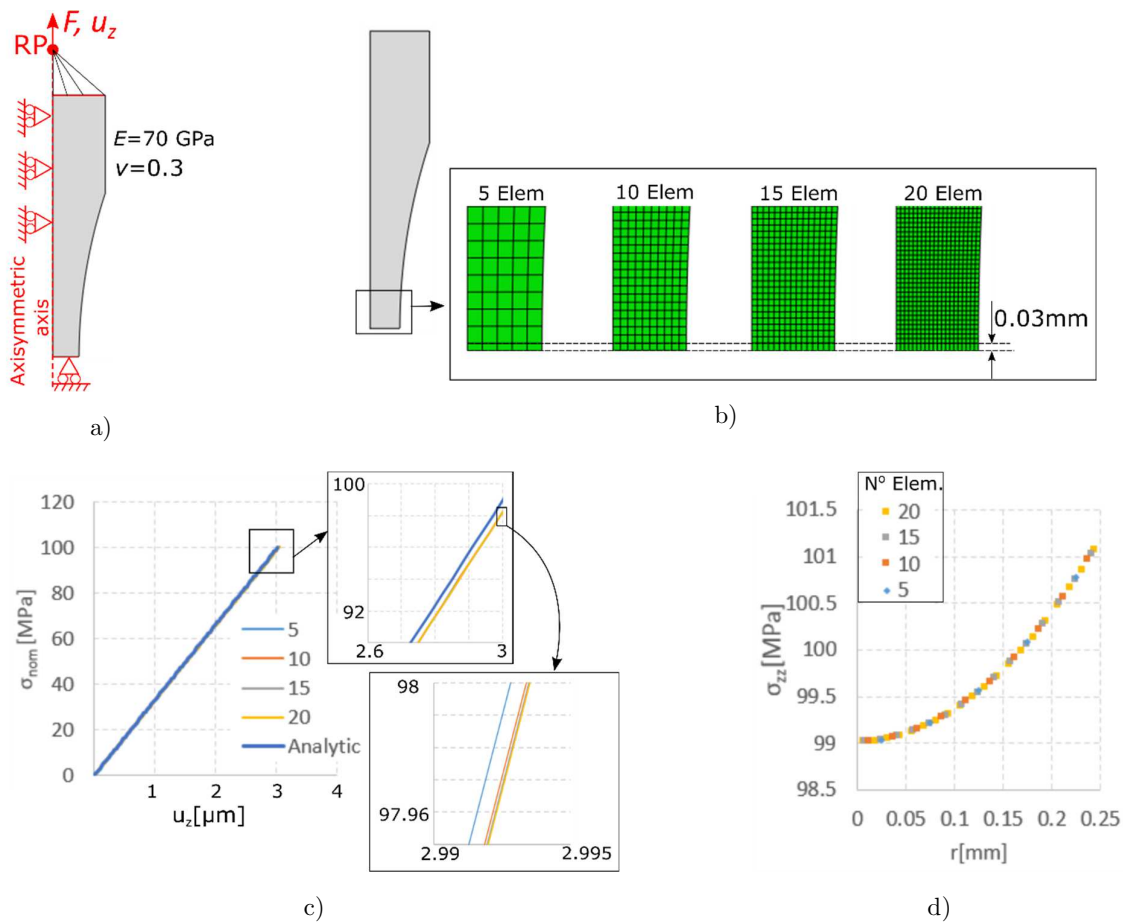


Figure 3-4 Mesh convergence study for elastic simulations of tensile loaded hourglass-shaped samples. a)

Boundary conditions used for the simulation. b) Meshes used for comparison. c) Nominal stress vs displacement results showing the very small differences between the analytical and the different meshed finite element solutions. d) Axial stress distribution at the mid cross-section evaluated using the meshes presented in (a).

Next, we contrast this analytical solution with finite element calculations, which also will allow us to analyze the distribution of the different components of the stress tensor in the groove zone of hourglass shaped samples.

### 3.1.1.2. Finite element solution

In order to analyze the evolution of the stress components of hourglass-shaped samples subjected to a monotonic tensile loading, we implemented an axisymmetric isotropic elastic model in ABAQUS-Standard, a commercial software suite for finite element analysis. In this way, we assessed the stress state of the material and the uniformity of the axial stress in the cross-section of the samples stated in the analytic solution.

The elastic material parameters, Young Modulus, and Poisson's ratio, used in the simulations were  $E=70\text{GPa}$  and  $\nu=0.33$ . The simulations were carried out using built-in ABAQUS elements type CAX4R. These elements are 4-node bilinear axisymmetric quadrilateral with one gauss point (reduced integration). They possess two degrees of freedom, the displacements in the axial direction  $\mathbf{u}_z$ , and the displacements along the radial direction  $\mathbf{u}_r$ . The boundary conditions for the simulations are illustrated in Figure 3-4a. Note that we simulated one quarter of the axisymmetric plane of the samples only. In order to simulate a monotonic loading, the axial displacement  $\mathbf{u}_z$  of a control node (referred as RP in Figure 3-4a) was constrained to the axial displacement of the nodes in the upper surface. Then, force or displacement constraints were imposed to RP. The simulations were carried out using the ABAQUS formulation for large displacements and rotations.

To begin with, we carried out a mesh convergence study. For this purpose, we performed simulations of a force controlled tensile loading on a sample of  $r_w = 0.5\text{mm}$ ,  $r_w = 10\text{mm}$  and  $r_n = 0.25\text{mm}$ , with four different mesh sizes. The samples were meshed in such a way that the cross-section contained 5, 10, 15, and 20 elements, keeping the height of the first element row equal to 0.03mm (Figure 3-4b). An incremental force  $F$  was applied to node control RP until the maximum nominal axial stress at the mid cross-section ( $F/(\pi r_n^2)$ ) was equal to 100MPa. After that, we evaluated the differences in the mechanical responses and the axial stress distribution at the mid cross-section of the sample.

Figure 3-4c-d show that the differences between the results obtained from coarse and fine meshes are negligible. Finer meshing, however, allows better spatial distribution of the material data points in the sample. The mechanical response in Figure 3-4c, shows a linear relationship between the applied nominal stress  $\sigma_{nom}$  and the resulting displacements  $\mathbf{u}_z$ , which barely differs from the analytical solution developed in the previous section. Hence, we may conclude that the cross-section reduction in hourglass shaped samples, for the simulation conditions studied, does not introduce geometric nonlinearities to the mechanical response. With respect to the axial stress distribution in the mid cross-section, as illustrated in Figure 3-4c, the resulted stress value in the sample axis was  $\sim 1\%$  lower than the nominal stress and  $\sim 1\%$  higher at the sample's surface, which is due to stress concentrations related to the shape of the groove.

In order to assess the impact of the geometry on the stress tensor components in hourglass-shaped samples, we carried out similar simulations (nominal stress up to 100MPa) on samples with  $r_w$  varying from 1-2mm,  $r_t = 10$ mm and radius reductions  $r_n/r_w$  between 0.5-0.9. The simulations were carried out using the 10-element mesh showed in Figure 3-4a. Moreover, in order to evaluate the stress state of the material we calculated in each integration point the triaxiality ratio  $M$  defined as

$$M = \frac{-p}{\sigma_{eq}} \quad (3.11)$$

where  $p$  and  $\sigma_{eq}$  are the hydrostatic pressure and the von Mises equivalent stress respectively. The stress tensor of this axisymmetric problem in cylindrical coordinates reads

$$\bar{\sigma} = \begin{bmatrix} \sigma_{rr} & \sigma_{rz} & 0 \\ \sigma_{zr} & \sigma_{zz} & 0 \\ 0 & 0 & \sigma_{\theta\theta} \end{bmatrix}, \quad (3.12)$$

therefore,

$$p = -\frac{1}{3}(\sigma_{rr} + \sigma_{zz} + \sigma_{\theta\theta}), \quad (3.13)$$

and

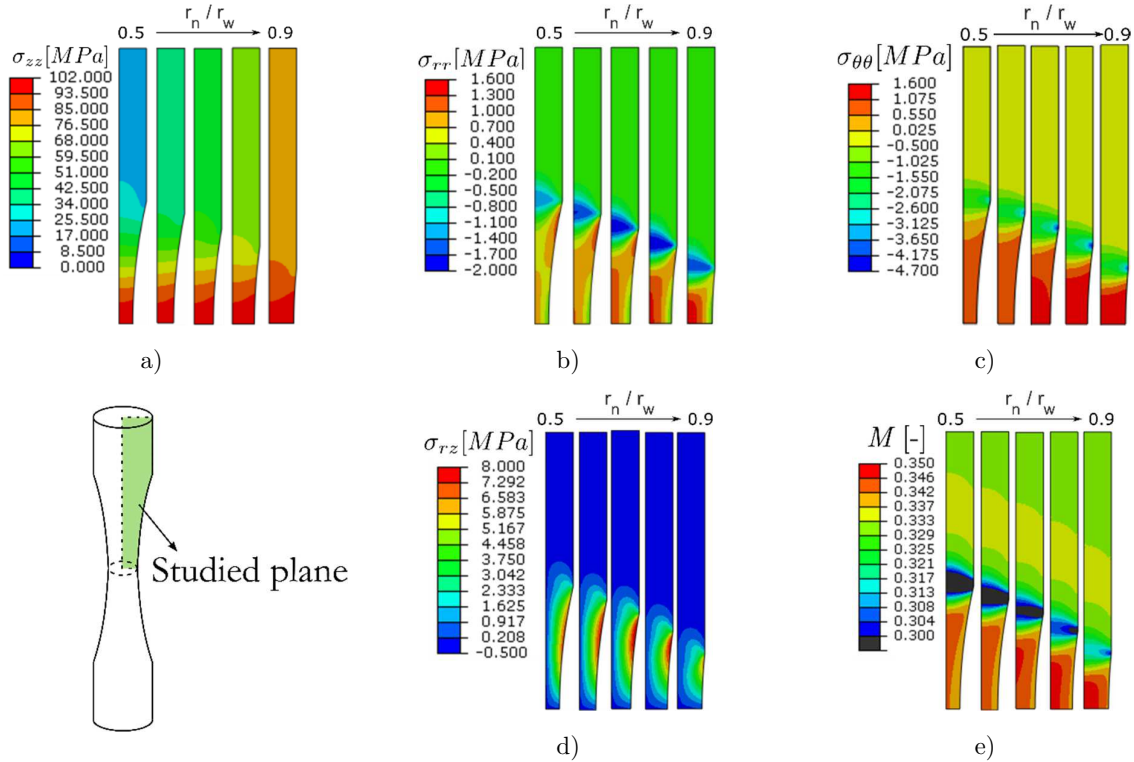


Figure 3-5 Axisymmetric simulation of an hourglass-shaped sample using an isotropic elastic constitutive law. We show contour plots of the stress tensor components in the studied plane of hourglass-shaped samples of  $r_w = 0.5$ mm and radius reductions between 0.5-0.9. Upon the simulations, the samples were subjected to a nominal axial stress of 100MPa. a) Axial stress. b) Radial stress. c) Transverse stress. d) Shear stress. e) Triaxiality ratio.

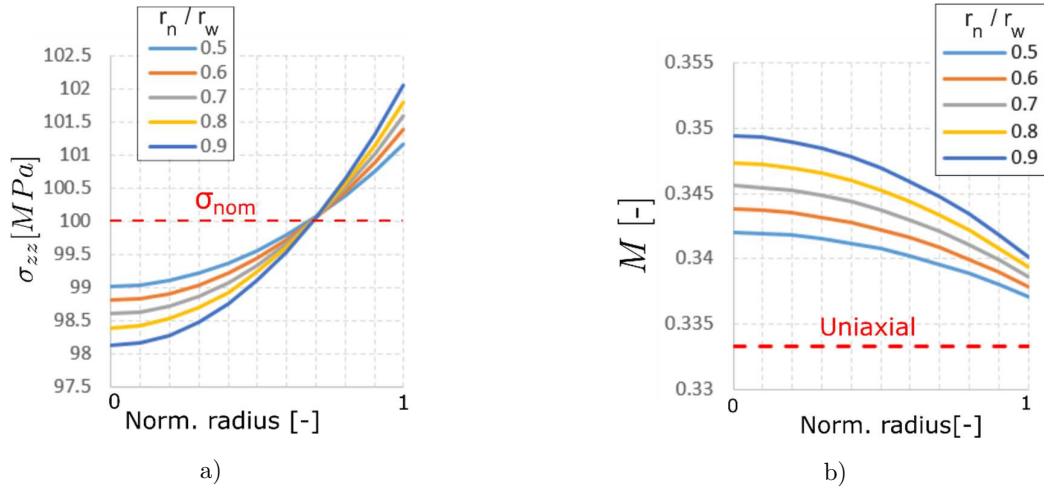


Figure 3-6 Axial stress (a) and triaxiality ratio (b) distributions at the mid cross-section of hourglass shaped samples ( $r_w = 0.5\text{mm}$ ,  $r_t = 10\text{mm}$ , and  $r_n/r_w = 0.5 - 0.9$ ) obtained from finite element simulations of a tensile loading up to  $\sigma_{nom} = 100\text{MPa}$ . The radius in the abscissa of both curves was normalized to  $r_n$ .

$$\sigma_{eq} = \sqrt{\sigma_{rr}^2 + \sigma_{zz}^2 + \sigma_{\theta\theta}^2 - \sigma_{zz}\sigma_{rr} - \sigma_{zz}\sigma_{\theta\theta} - \sigma_{\theta\theta}\sigma_{rr} + 3\sigma_{rz}^2}. \quad (3.14)$$

Note that a uniaxial stress state implies  $\sigma_{eq} = \sigma_{zz}$  and  $p = -\sigma_{zz}/3$ , therefore  $M = 1/3$ .

Figure 3-5 shows the distribution of the axial, radial, transverse, and shear stresses, and the distribution of the triaxiality ratio  $M$  in one quarter of the axisymmetric plane of hourglass-shaped samples. As observed, apart from the axial stress heterogeneity at the mid cross-section previously shown in Figure 3-4d, radial, transverse and shear stress are induced along the groove zone during tensile loading. On the one hand, positive radial and transverse stresses are induced in the groove zone (see Figure 3-5b&c). Higher magnitude radial stresses are observed towards the axis of the sample, while transverse stresses seem to be homogeneous throughout the groove zone. At the mid cross-section, where the nominal axial stress is the same for all the five cases, Figure 3-5b reveals that higher radial and transverse stresses are induced in samples with larger radius reduction ratios ( $r_n/r_w$ ).

With respect to the shear stress distribution, as observed in Figure 3-5c, higher magnitudes were calculated in the surface of the groove zone. The maximal magnitude of shear stress was found in the case where  $r_n/r_w=0.7$ , and the minimal when  $r_n/r_w=0.9$ . At the mid cross-section, the shear stresses become close to zero, hence in this zone the radial, axial and transverse stresses can be considered equivalent to the principal stresses  $\sigma_1$ ,  $\sigma_2$ , and  $\sigma_3$ .

The uniaxiality condition assumed by the analytical response was evaluated using the triaxiality ratio contour maps in Figure 3-5d. Triaxiality ratios closer to  $1/3$  in the groove were obtained for smaller radius reduction ratios  $r_n/r_w$ . This is explained by the fact that smaller radius reduction ratios resulted in lower values of radial and transverse stresses.

At the mid cross-section, we observe that the axial stress is maximal at the sample's surface, and that the triaxiality ratio is more distant from  $1/3$  at the sample's axis (Figure 3-6). Consequently, the material at the surface is closer to a pure uniaxial stress state than the material in the axis of the sample, but it is subjected to higher axial stresses. The increase

of the axial stress at the surface of the sample is commonly evaluated using the stress concentration factor  $K_{th}$ , defined as

$$K_{th} = \frac{\sigma_{max}}{\sigma_{nom}}. \quad (3.15)$$

In order to have a full view of the impact of the geometry on the stress concentration factor  $K_{th}$ , similar simulations as the ones presented in Figure 3-5 were performed on samples of radius  $r_w$  between 0.6-1.0mm. The resulting stress concentration factors were calculated for each case and gathered together in Figure 3-7a. The evolution of the stress concentration factor  $K_{th}$  was plotted with respect to  $r_t/(2r_n)$  with the aim of keeping the same format of stress concentration curves found in the literature [100]. As observed in Figure 3-7a, for the sample dimensions studied, the stress concentration factor is dependent only on the ratio  $r_t/(2r_n)$ ; as a result, for a fixed value of groove radius  $r_t = 10\text{mm}$ , the smaller the radius of the sample at the mid cross-section, the lower the stress concentration factor. The limit values of the increase of the axial stress at the surface with respect to the nominal stress were  $\sim 1.2\%$  and  $\sim 4.2\%$  respectively (Figure 3-7a).

On the other hand, the evolution of the maximum triaxiality ratio at the mid cross-section, (placed at the axis of the sample as shown in Figure 3-6) with respect to  $r_t/(2r_n)$  shows a similar evolution as the stress intensity factor curves. Here again, the stress state at the mid cross-section gets closer to  $1/3$  when the radius of the mid cross-section is smaller.

In conclusion, the progressive reduction of the cross section induces a tridimensional stress state in hourglass-shaped samples. However, for the samples geometries and elastic parameters utilized, at the mid cross-section, the nominal stress differs scarcely some percentage from the actual maximal axial stress. At the surface of the mid cross-section of the sample, even though the material is subjected to higher axial stresses, it gets closer to a pure uniaxial stress state.

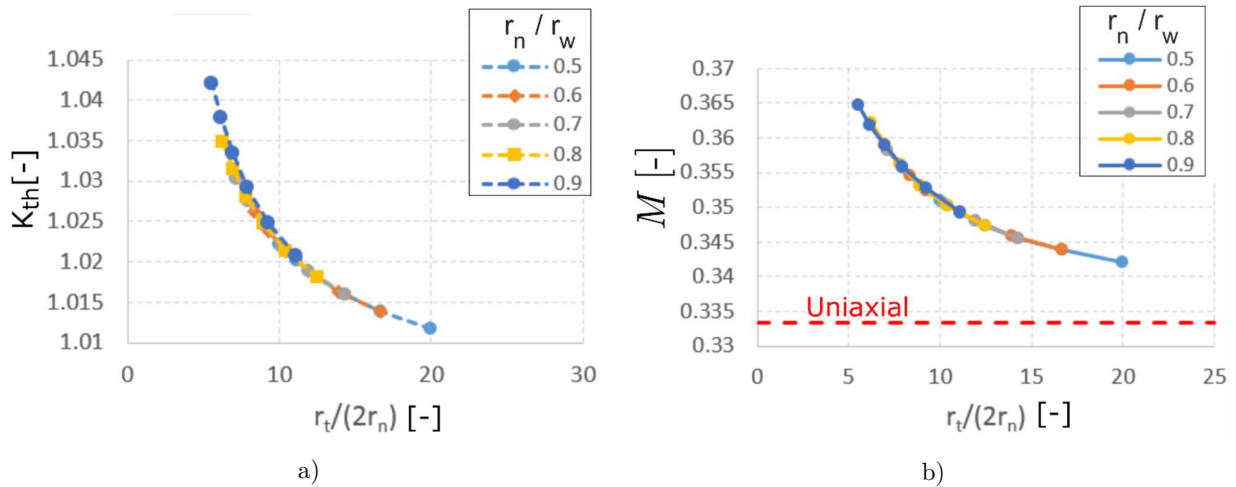


Figure 3-7 Stress concentration factor (a) and maximum triaxiality ratio (b) at the mid cross-section of hourglass shape samples with  $r_w$  between 0.5-1mm,  $r_t$  equal to 10mm and  $r_n/r_w$  between 0.5-0.9.

### 3.1.2. Non-linear material behavior

The previous results are valid only under isotropic elastic material conditions. Now, in order to evaluate the effects of a material non-linearity on the mechanical response and the stress components of tensile loaded hourglass-shaped samples, a simulation was performed using a classical metal plasticity model.

The material model used for the next simulation determined plastic yielding based on the von Mises criterion. After yielding no hardening was included (perfect plasticity case). The yield stress was 90MPa, and the elastic parameters were the same as the ones used in the previous section,  $E = 70\text{GPa}$  and  $\nu = 0.33$ . The constitutive response of the material is shown in Figure 3-8. The simulation was performed using displacement constraints to the control point RP (see Figure 3-4a). The sample dimensions chosen for this simulation were  $r_w = 0.5\text{mm}$ ,  $r_n = 0.3\text{mm}$ , and  $r_t = 10\text{mm}$ , and the mesh size was the 10-element mesh shown in Figure 3-4b.

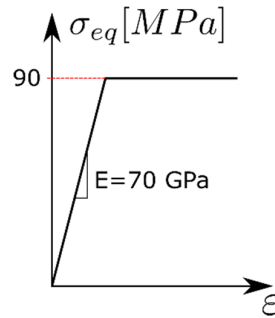


Figure 3-8 Perfect plasticity constitutive law.

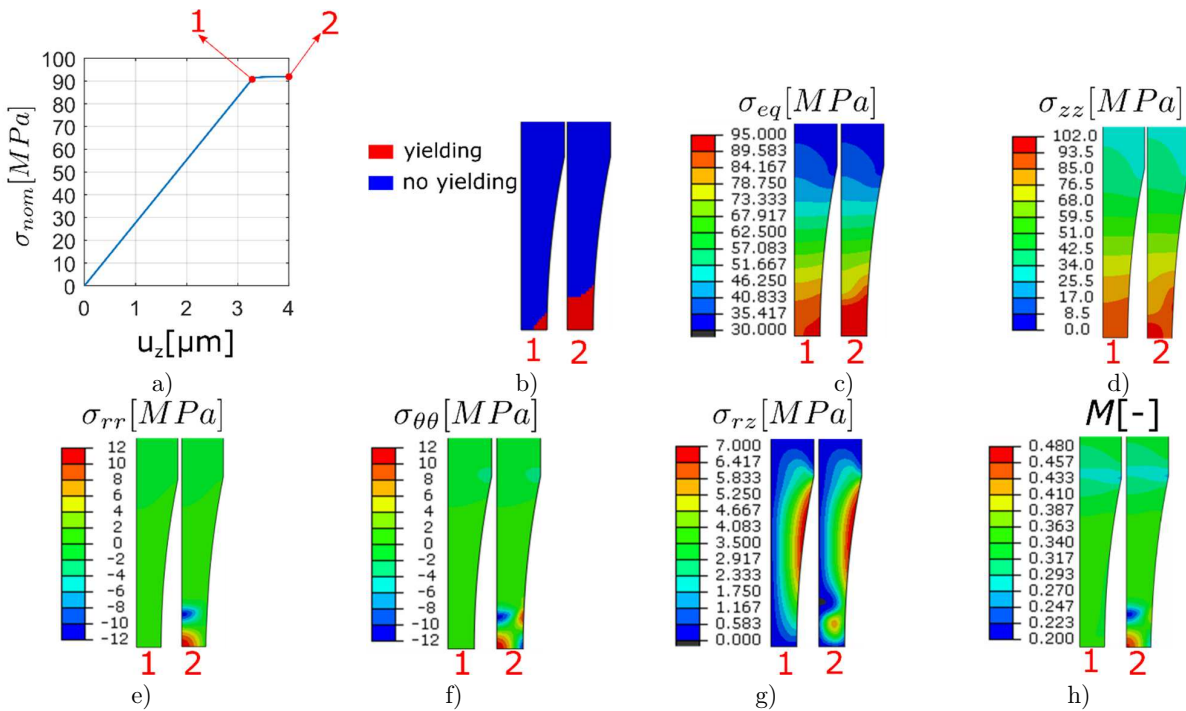


Figure 3-9 Simulation of the tensile response of a perfect-plastic hourglass shaped sample. a) Force-displacement macroscopic response. b) Evolution of the yielding zone. c-g) Stress tensor components distribution in the groove zone. h) Triaxiality ratio distribution.

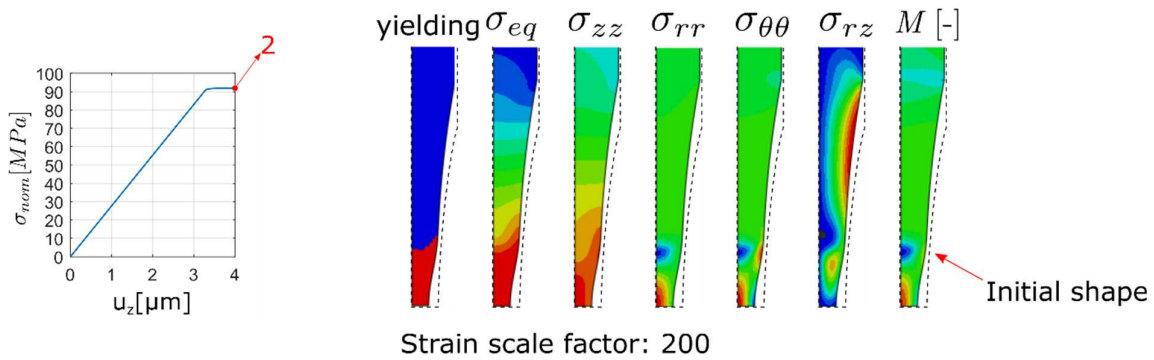


Figure 3-10 200x strain scaled contour plots of the stress tensor components upon plastic deformation (stage 2). The color maps are kept the same as previously in Figure 3-9.

The mechanical response of the sample shows a bilinear behavior as observed in Figure 3-9a. The response is linear up to the yielding stress indicated by the point 1. The yielding nominal stress indicated on the macroscopic response of the sample coincides with the plastic yielding at the surface of the mid cross-section (see Figure 3-9b). Upon further stretching, the plastic zone spreads, first towards the sample axis, then along the groove zone as indicated by the yielding region corresponding to point 2 in Figure 3-9b. During the plastic zone propagation, the equivalent von Mises stress keeps being maximal at the sample surface, reducing quadratic alloy towards the sample axis (Figure 3-9c).

The mid cross-section reduction induced by the large radial plastic deformation causes a shear stress  $\sigma_{rz}$  concentration zone just beneath the interface between yielded and non-yielded zones (Figure 3-9g). The magnitude of the shear stress reaches a much higher magnitude than in the elastic case, reaching up to 7% of the nominal stress at the mid cross-section. In addition, positive and negative radial and transverse stresses zones are generated at the sample axis (Figure 3-9e), both reaching up to 12% of the nominal stress magnitude at the mid cross-section. The positive radial and transverse stresses coincide with the maximal axial stress zone in the axis of the sample at the mid cross section. This reveals that the material near the sample axis in the mid cross section is subjected to high hydrostatic pressure, which increases the magnitude of the triaxiality ratio up to almost 0.5. In contrast, the material above the yielded zone, near the sample axis, is subjected rather to high deviatoric stresses (von Mises stress), reducing the triaxiality ratio down to 0.2 (Figure 3-9h). The impact of plastic deformation in the change of the shape of the sample can be visualized better in Figure 3-10, where we scaled the deformation at the stage 2. The complex stress state of the material in the middle of the sample is consequence of the pronounced cross-section reduction and the compatibility of strain.

Before contrasting the presented results with the mechanical behavior of NiTi hourglass-shaped samples, we describe in the next section the main characteristic of the NiTi alloy selected for fatigue testing. The characterization of the thermochemical behavior of the selected NiTi is presented later in section 3.3.

## 3.2. Material of the study

### 3.2.1. Cold-drawn NiTi wires

We selected a commercial cold-drawn 1.78mm diameter NiTi wire made by Fort Wayne Metals Ltd. (FWM) from a medical graded alloy denoted as NiTi#1 [101]. FWM certified a wire diameter tolerance of  $\pm 0.0254$ mm, final cold work of 41.1%, and  $\sim 50.9$  at.%Ni. The full chemical composition of the alloy is given in Table 3-1.

As described next, cold-drawn NiTi wires do not show superelastic, nor shape memory properties. It is only by applying adequate thermomechanical heat treatments that the characteristic shape memory behavior of NiTi is given to the wires. Next, we start by characterizing some of the mechanical properties of as-received cold-drawn NiTi wires. Then, we describe the manufacture of hourglass shaped samples and the influence of thermomechanical heat treatment on their thermomechanical tensile response.

#### 3.2.1.1. Tensile response

Cold-drawn NiTi wires were tested in tension at different temperatures using a servo-hydraulic tensile testing machine INSTRON 8855 equipped with a 25kN load cell. 60 mm straight wire samples were cut from the as-drawn wire, then clamped into the machine using mechanical action flat wedge grips. The gauge length was established at 40mm. The load cell and the lower grip body stayed stationary during the tensile tests while the upper grip moved vertically. In addition, we used a 10mm gauge length clip-on extensometer attached to the sample for better assessment of the strain during the tests. The tests were performed under controlled temperature conditions using a thermal chamber EURO THERM 3500. We tested individual samples at 40°C, 60°C, and 80°C.

Each tensile test consisted of four loading-unloading ramps carried out at a constant strain rate of  $5 \times 10^{-4} \text{s}^{-1}$  controlled by the clip-on extensometer. The maximum strains attained on

Ni	Ti	C	Cr	Cu	Co	Fe	H	O
55.98	Bal	0.026	0.0037	0.00039	0.0002	0.0097	0.003	0.0255

Table 3-1. Chemical composition of studied NiTi wires certified by FWM, the provider of the wires. The values are expressed in wt.%.

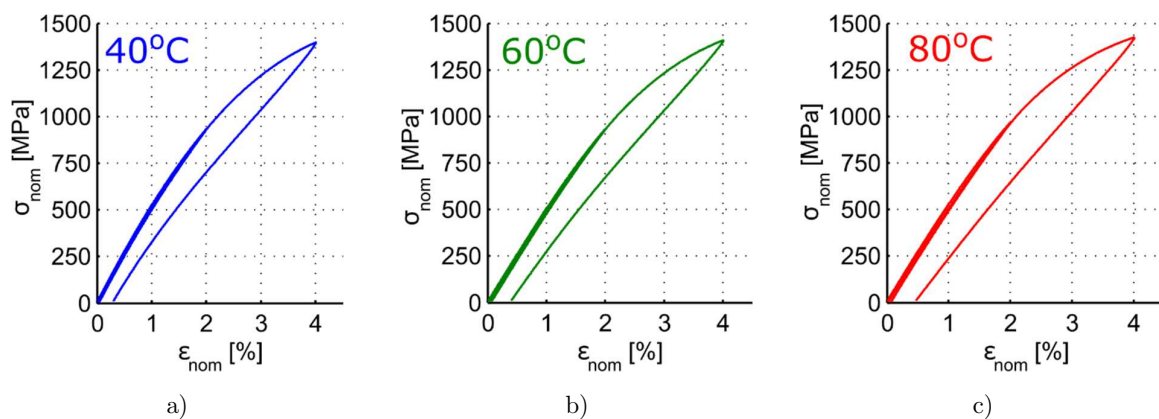


Figure 3-11. Tensile responses of cold-drawn NiTi#1 wires at 40°C(a), 60°C(b), and 80°C(c).

each loading ramp were 0.5%, 1%, 2%, and 4%. The stress vs strain curves resulted from these tests are shown in Figure 3-11.

The tensile responses of as-drawn NiTi wires, at first sight, exhibit an elastoplastic-like behavior. Upon the 0.5% and 1% max. strain loading-unloading cycles, the behavior is practically linear with no residual strains after unloading. Only after the 2% max. strain loading-unloading cycle, a very small amount of residual strain was obtained. The mechanical response finally yielded upon the 4% max. strain loading, and as a result, larger residual strains were obtained after unloading. The tensile responses shown in Figure 3-11 are barely affected by the temperature. This is observed clearer in Figure 3-12a where we compare the three temperature 4% max. strain responses.

The Young's modulus, calculated for each temperature using a linear regression of the stress-strain data in the first 0.5% max. strain loading remains almost the same for all three temperatures (blue curve in Figure 3-12b). The calculated values of Young's modulus upon tensile loading are higher than typical values reported for B19' martensite (~40GPa) and lower than those typically reported for B2 austenite (~80GPa). The Young's modulus was also calculated from the last unloading ramp applying a linear regression of the stress-strain data obtained upon unloading the sample 200MPa from the 4% max. strain. Unlike elastoplastic metals, where Young's modulus is the same upon either loading or unloading, when as-drawn NiTi wires were loaded above the yield stress, the Young's modulus upon

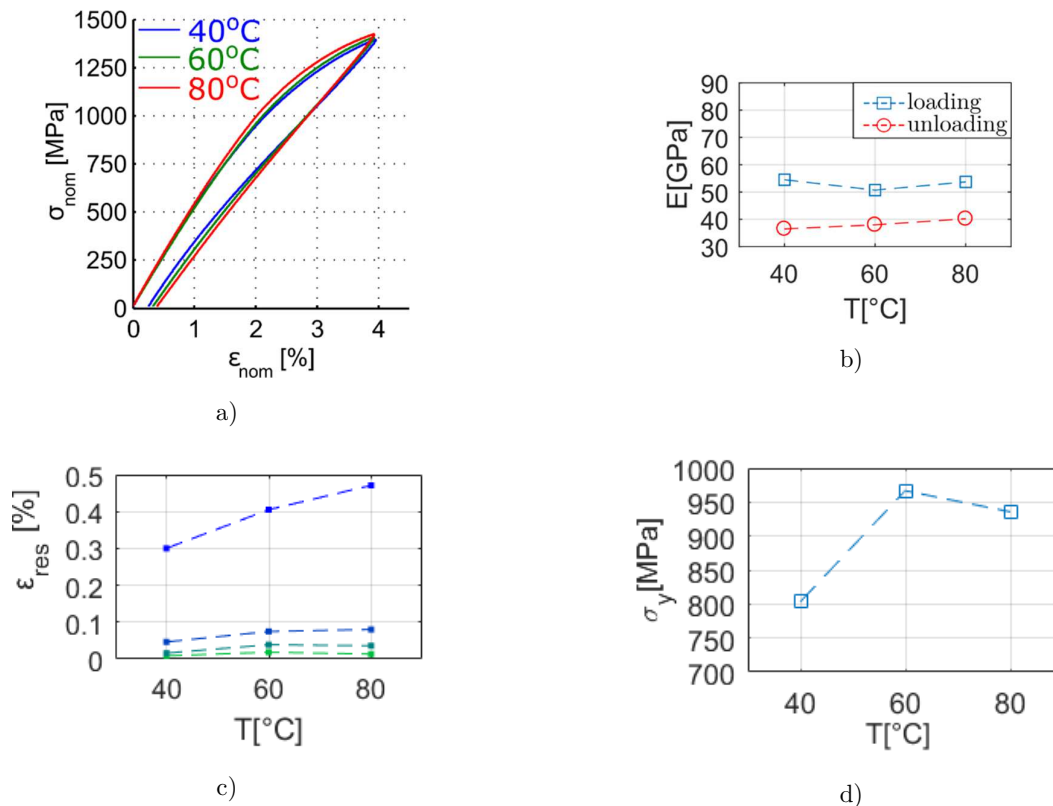


Figure 3-12 Evolution of the mechanical properties of cold-drawn NiTi wires with temperature: a) tensile responses, b) Young's Modulus, c) residual strain after different maximal strain loadings, and d) yield stress identified using the 0.2% offset yield criterion for elastoplastic materials.

unloading (red curve in Figure 3-12b) resulted lower than the Young's modulus upon loading (blue curve in Figure 3-12b). The values obtained upon unloading are closer to the martensite Young's Modulus, although it is interesting that slightly higher values were found at higher temperatures where the martensite phase is less stable.

On the other hand, the residual strain after the final 4% max. strain loading-unloading cycle clearly shows a monotonic increase with temperature (Figure 3-12c). This behavior may be associated with higher dislocation mobility aided by higher testing temperature, which results in plastic deformation.

The yield stress was established using the classic 0.2% strain offset criterion typically applied to metals. The evolution of the yield stress with temperature (Figure 3-12d) does not show the same trend as the residual strains. The yield stress at 40°C was 803MPa, at 60°C it was 966MPa (163MPa higher), and finally, at 80°C, it decreased down to 935MPa. Between 40 and 60°C the yield stress gained  $\sim 8\text{MPa}/^\circ\text{C}$ , which is around the values reported for the Clausius-Clapeyron slope that relates the stress needed for B2 austenite to B19' martensite phase transformation in NiTi alloys with temperature.

The structure of cold worked NiTi wires has been reported to have a high density of dislocations [102]. As a result, as-drawn NiTi wires are characterized for having high internal stresses. Their crystalline structure is often considered as amorphous; consequently, they show neither superelastic nor shape memory properties. However, according to the exposed behavior of Young modulus and yield stresses with temperature, we may suggest that there could exist a partial stress-induced phase transformation in the studied cold-drawn NiTi wires upon tensile loading. Stress-induced phase transformation would be combined with plastic deformation due to dislocation movement, which would explain the residual strain increase with temperature in Figure 3-12c.

### 3.2.2. Preparation of hourglass-shaped samples

MICRO-MEGA®, a French manufacturer of dental surgical instruments, produced the NiTi hourglass-shaped samples used in this study. The samples were machined from as-drawn 1.78mm diameter NiTi#1 wires by grinding, which is the same procedure used for manufacturing endodontic files. The samples' diameter was reduced from 1.78mm down to 1.14mm at the mid cross-section using a 10mm radius grinder wheel (Figure 3-13). After machining, the groove zone of each sample was subjected to 60s electro-polishing in order to reduce possible surface imperfections introduced during the grinding process.

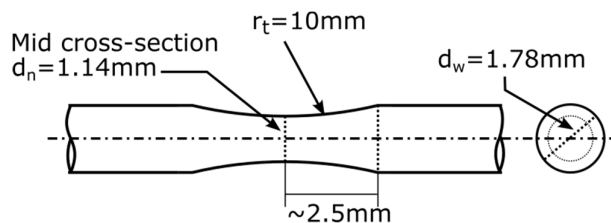


Figure 3-13 NiTi hourglass shaped samples used in this fatigue study.

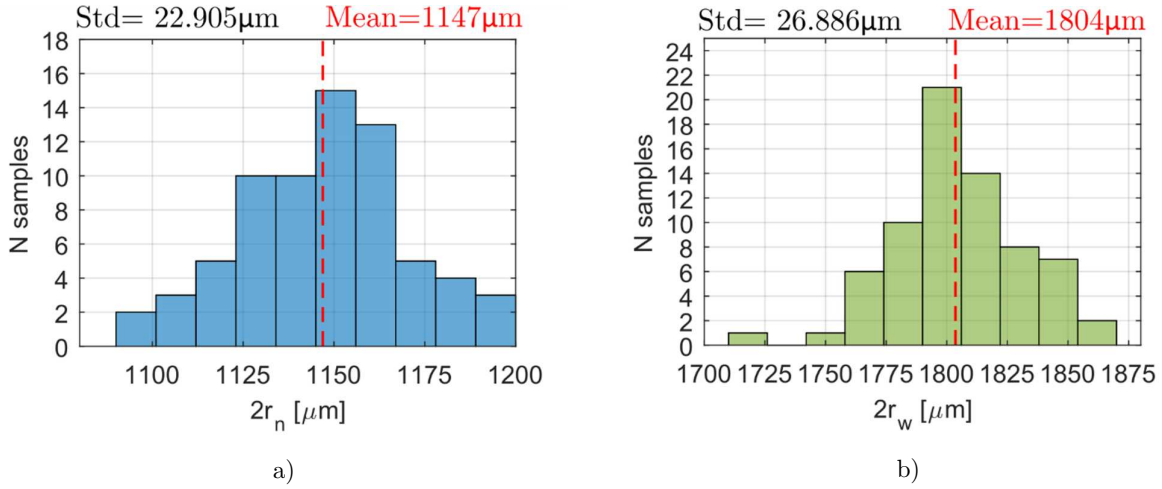


Figure 3-14 Dimensions of a group of 70 hourglass-shaped NiTi samples. a) Diameter at the mid cross-section. b) Wire diameter outside the reduced cross-section zone.

According to the geometry of our samples,  $r_n/r_w = 0.64$ , and  $r_t/2r_n = 8.77$ . As a result, the stress concentration factor  $K_{th} = 1.025$  (see Figure 3-7a), meaning that the stress at the surface in the mid cross-section is 2.5% higher than the nominal stress when the material behaves elastically. On the other hand, the triaxiality ratio at the mid cross section varies from  $M_s = 0.3418$  at the surface, up to  $M_{ax} = 0.3534$  at the axis (see Figure 3-7b).

After manufacturing and electropolishing, the samples' dimensions were measured using a multifocal plane optical microscope KEYENCE VHX-1000. For this purpose, we took  $2.165\mu\text{m}/\text{px}$  resolution images of the groove zone of each sample at 100X magnification. The diameter of a group of 70 samples at the mid cross-section ( $2r_n$ ), and out of the groove zone ( $2r_w$ ) were gathered in the histograms that we show in Figure 3-13.

The mean value of the diameters measured at the mid cross-section was 1.147mm, being  $7\mu\text{m}$  more than the nominal value (Figure 3-13a). The standard deviation (Std), on the other hand, was  $22.905\mu\text{m}$ , which give us an idea of the precision of the grinding technique. With respect to the diameter of the original wire ( $2r_w$ ), we found a mean diameter value equal to  $1804\mu\text{m}$ , which is inside the  $\pm 25\mu\text{m}$  tolerance range certified by FWM.

By using the multifocal plane optical microscope, we took depth-composed images at 1000X of the groove zone of grinded and electropolished hourglass-shaped samples with the aim of assessing their surface roughness. Depth-composed images allow recreating 3D aspects of the surface of an object. The images were taken at the mid cross section of the samples in a planar area equal to  $340 \times 254.5\mu\text{m}^2$  as illustrated in Figure 3-15a.  $340\mu\text{m}$  -length surface profiles were extracted from five randomly selected samples and plotted in Figure 3-15b. Then, the arithmetical mean deviation of each profile  $R_a$ , defined as

$$R_a = \frac{1}{n} \sum_{i=1}^n |y_i|, \quad (3.16)$$

was calculated. In (3.16),  $n$  is the number of points that define each profile, and  $y_i$ , the distance of the profile to the mean line, calculated as the arithmetical average of the entire

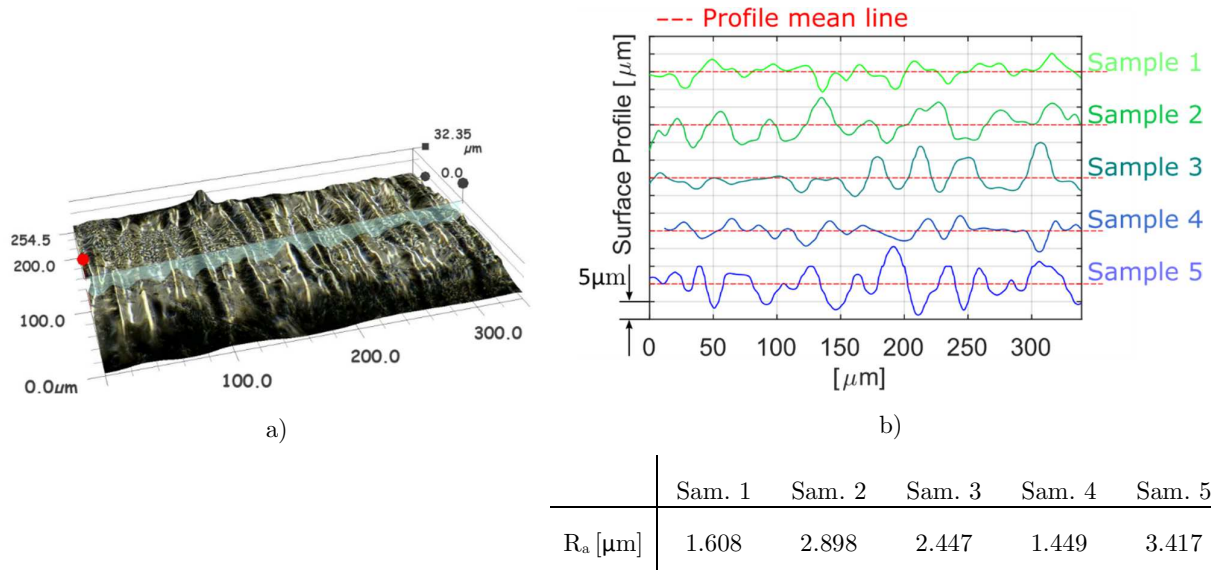


Figure 3-15 Surface roughness of grinded and electropolished hourglass NiTi samples. a) Example of a depth-composed 3D surface image taken at 1000x magnification in the middle of hourglass-shaped NiTi samples. b) Surface profiles of 5 hourglass-shaped NiTi samples.

profile. Averaging the  $R_a$  values of the selected samples, we obtain  $R_a=2.369\mu\text{m}$ , which is equivalent to an ISO N8 roughness grade number.

### 3.2.3. Effects of annealing temperatures

As shown in the previous section, although our selected cold-drawn NiTi wires may exhibit some amount of stress-induced phase transformations upon tensile loading, their great amount of cold work hinders the development of reversible phase transformations, and consequently superelasticity. In order to render as-drawn NiTi hourglass-shaped samples superelastic, we applied a thermomechanical heat treatment. Upon thermomechanical heat treatment, internal stress recovery and recrystallization processes take place, the reason why heat treatment is commonly referred as annealing. However, due to the narrow B2 phase region in the binary NiTi diagram, precipitation growth may also take place, hence the term aging is also used to define the process. After annealing, new defects-free austenite or martensite grains are created, allowing reversible transformations upon temperature or stress changes. In addition, the stress relieving that occurs upon heat treatment allows the possibility to set the shape of the samples. For this reason, the heat treatment of cold-worked NiTi wires is commonly combined with the shape setting of NiTi-based devices.

We applied 30min heat treatment to our NiTi hourglass-shaped samples at 400°C, 425°C, 450°C, 475°C, and 500°C. Each heat treatment was done in an air furnace using an especially intended device for straightening the samples illustrated in Figure 3-16. The device consisted of two stainless steel plates with six u-shaped grooves of the same radius of our NiTi wires machined on each plate. Straightening force was applied to the samples by compressing the upper plate to the lower one via six stainless steel screws.

The procedure used to heat treat hourglass-shaped NiTi samples consisted of the following steps: first, we preheated the straightening device for at least 1 hour inside the furnace at

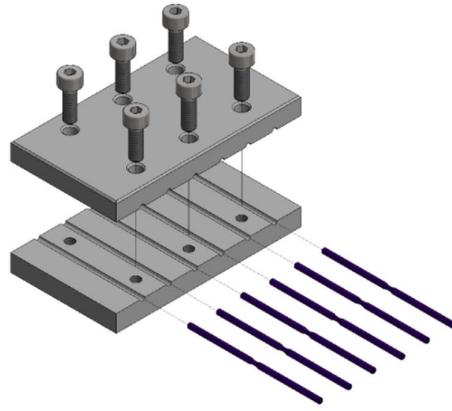


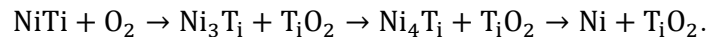
Figure 3-16 Straightening device for annealing of hourglass-shaped samples.

the intended heat treatment temperature. Then, we removed the straightening device from the furnace and installed a batch of six samples into it. After that, we put the device containing the samples inside the furnace, making sure that the time between removing and replacing the device inside the furnace was six minutes. With the samples inside the furnace, we waited until the temperature indicator of the furnace showed a stable value at the intended heat treatment temperature, and only then we started a clock count of 30 minutes. After 30 minutes, the device and the samples were quenched in ambient temperature water.

### 3.2.3.1. Oxide Layer

The first visible effect of heat treatment temperature on hourglass-shaped samples is the resulting samples' color. Figure 3-17 shows the evolution of the surface color according to the heat treatment temperature. The images presented in Figure 3-17 were taken under equal light conditions, and same contrast, brightness, and color saturation parameters using a KEYENCE VHX-1000 in High Dynamic Range mode (HDR), which is particularly useful for revealing the color of highly reflective NiTi wires.

The color of NiTi samples changes according to the thickness of a Titanium dioxide layer ( $\text{TiO}_2$ ) that forms on the sample's surface upon heat treatment [104], [105]. As a result, the surface of NiTi wires exhibits a gradient of chemical composition, from low Ni content at the surface up to the nominal at.%Ni content some nanometers beneath the surface [106]. According to Zhu et al. [106], the passivation of the titanium dioxide layer occurs as follows:



The characteristics of the  $\text{TiO}_2$  layer, such as thickness and chemical composition, depend mostly on temperature, time and previous surface preparation.

In order to characterize the surface state of our samples in terms of the temperature of the applied heat treatment, we utilized to the classification made by Velten et al. in [103],

TiO <sub>2</sub> Layer Thickness [nm]	10-25	25-40	40-50	50-80
Color	Golden	Purple	Deep blue	Light blue

Table 3-2. Relation between the thickness of  $\text{TiO}_2$  layer and its color according to Velten et al.[103]

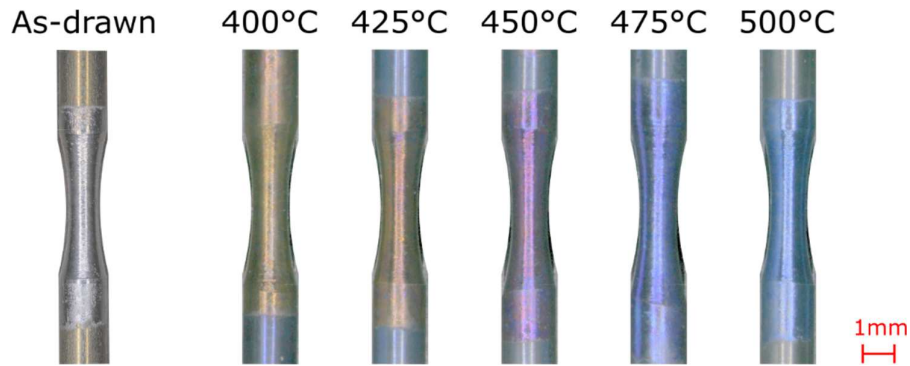


Figure 3-17 HDR optical microscope images from hourglass-shaped samples annealed during 30 minutes in an air furnace at temperatures between 400 and 500°C.

which relates the thermally produced  $\text{TiO}_2$  layer thickness to its color (Table 3-2). As observed in Figure 3-17, the color of the groove zone of hourglass shaped samples changes from silver (absence of  $\text{TiO}_2$  layer due to electro-polishing) to light blue for samples heat-treated at 500°C. This color evolution with heat treatment temperature reveals an increase of  $\text{TiO}_2$  layer thickness, which, according to Table 3-2, might be on a range between  $\sim 10\text{nm}$  and  $\sim 80\text{nm}$  for annealing treatments carried out between 400°C and 500°C.

### 3.2.3.2. Differential Calorimetry Scanning measurements

Differential Calorimetry Scanning (DSC) measurements were taken on 3mm-length cylindrical samples of our studied material heat-treated at 400°C and 500°C for 30 minutes (Figure 3-18). The samples were cut after heat treatment by electrical discharge machining (EDM). First, samples were heated up to 100°C, then cooled down to -150°C, and finally heated up again up to 100°C. The cooling and heating stages were carried out at 10°C/min.

The resulting heat-flow in terms of the temperature is shown in Figure 3-19. The 400°C annealed sample (Figure 3-19a) shows a single exothermic peak upon cooling and two endothermic peaks upon heating. The exothermic peak upon cooling reveals the transformation from B2 phase into R-phase. Although there is not a second peak that reveals the R-phase transformation into B19' martensite, it is clear from the two peaks appearing upon heating that this transformation took place during the cooling stage. These two endothermic peaks reveal the transformation from B19' martensite into R-phase and the following R-phase into B2 austenite. Since both peaks are overlapped, we can deduce that the transformation  $\text{B19}' \rightarrow \text{R}$  was not completed at the onset of the transformation into B2.

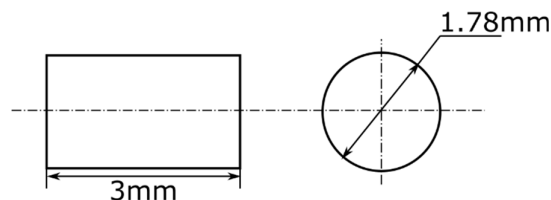


Figure 3-18 Geometry of samples used for DSC tests.

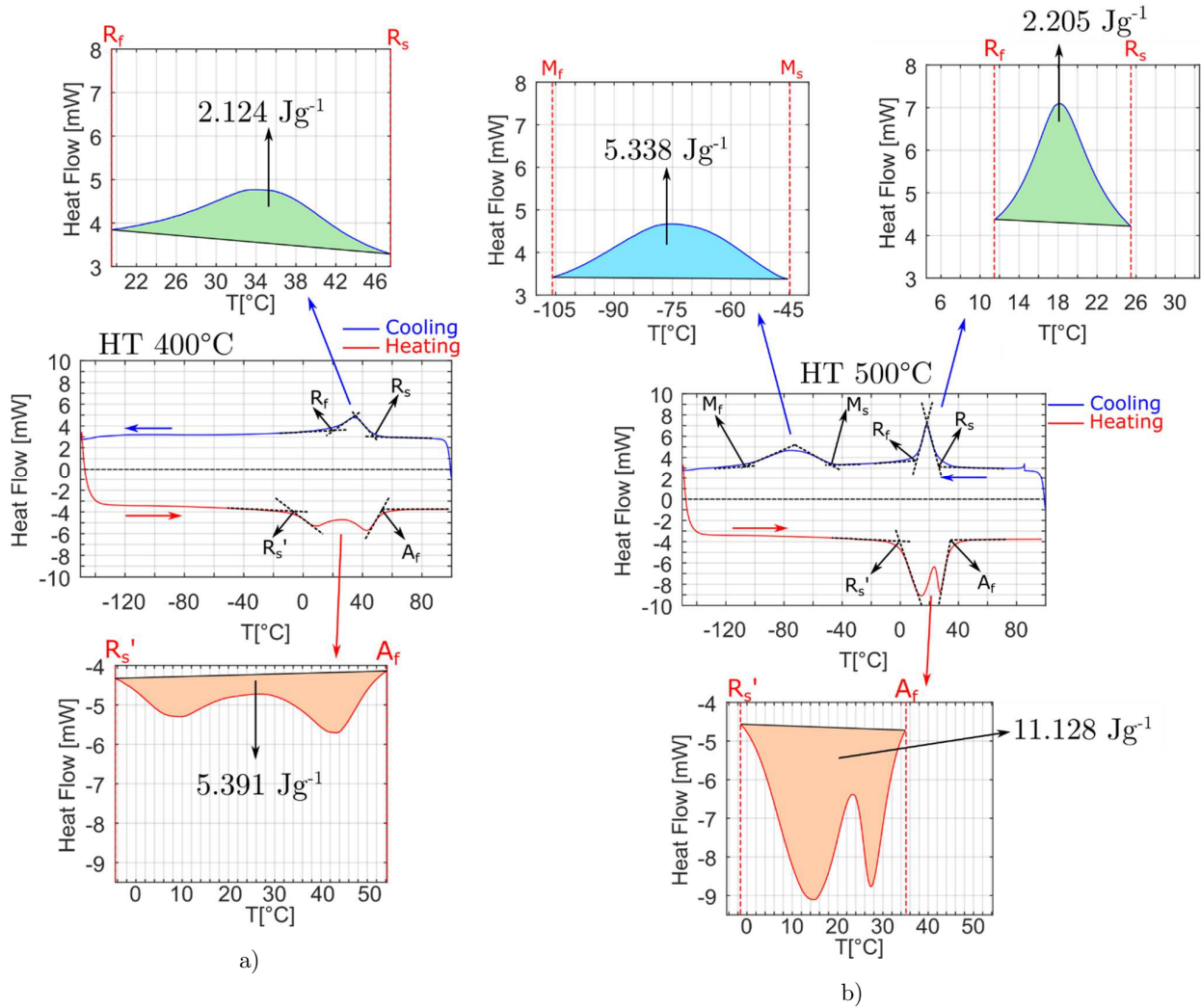


Figure 3-19 DSC curves for a NiTi annealed at 400°C (a) and 500°C (b) for 30 minutes.

T [°C]	Rs	Rf	Ms	Mf	Rs'	Af
400	47.5	19.5	-	-	-4.5	54.2
500	25.5	11.5	-45.2	-105.8	-1.3	34.8

Table 3-3 Transformation temperatures of 400°C and 500°C annealed NiTi.

On the other hand, the 500°C annealed sample shows two exothermic peaks upon cooling and two overlapped endothermic peaks upon heating, located at different temperatures.

The start and end of heat flux peaks allowed us to identify the start and finish of thermal induced phase transformations. The phase transformation temperatures, indicated in Table 3-3, were labeled from both calorimetry curves in Figure 3-19 according to the ASTM specification [107]. Comparing the transformation temperatures of the two studied materials, we observe that heat treatment temperatures have a significant impact on  $R_s$  and  $A_f$  temperatures, shifting them  $\sim 20^\circ\text{C}$  to lower values for 500°C heat-treated NiTi with respect to 400°C heat-treated NiTi. As a result, the thermal hysteresis of the  $B2 \leftrightarrow R$  phase transformation, calculated as  $\delta_{B2-R} = R_s - A_f$ , is larger for 500°C heat-treated NiTi ( $9.3^\circ\text{C}$ ) than for 400°C heat-treated NiTi ( $6.7^\circ\text{C}$ ). With regard to the impact of heat treatment

T [°C]	$\delta_{B2-R}$ ( $R_s - A_f$ ) [°C]	$\delta_{R-B19'}$ ( $M_s - R'_f$ ) [°C]	$\Delta Q_{B2-R}$ [Jg <sup>-1</sup> ]	$\Delta Q_{R-B19'}$ [Jg <sup>-1</sup> ]	$\Delta Q_{B19'-B2}$ [Jg <sup>-1</sup> ]	$C_p^{B2} \uparrow$ [J(g°C) <sup>-1</sup> ]	$C_p^{B2} \downarrow$ [J(g°C) <sup>-1</sup> ]	$C_p^R \downarrow$ [J(g°C) <sup>-1</sup> ]	$C_p^{B19'} \uparrow$ [J(g°C) <sup>-1</sup> ]
400	6.7	-	2.124	-	5.391	0.467	0.36	0.393	0.434
500	9.3	~68.45	2.205	5.338	11.128	0.469	0.371	0.422	0.425

Table 3-4. Phase transformation thermal hysteresis ( $\delta$ ), specific heat exchange upon transformation ( $\Delta Q$ ) and specific heat capacities ( $C_p$ ) of individual phases of NiTi annealed at 400 and 500°C. The heat capacities obtained upon heating and those obtained upon cooling are marked with  $\uparrow$  and  $\downarrow$  symbols respectively.

temperature on  $R \leftrightarrow B19'$  transformation temperatures, the analysis gets more complicated due to the lack of  $R \rightarrow B19'$  exothermic peak in the 400°C heat-treated NiTi DSC curve. We can only notice that the  $R_s$ ' temperature is shifted  $\sim 3^\circ\text{C}$  between 400°C and 500°C heat treatments.

Concerning the shape of the heat release/absorption peaks upon DSC testing, we observe that the  $B2 \leftrightarrow R$  exothermic and endothermic peaks of the sample treated at 500°C are narrower and more intense than the ones of the sample heat treated at 400°C. This implies that the  $B2 \leftrightarrow R$  transformation kinetics rates of the sample heat-treated at 500°C are higher than the ones of the samples heat-treated at 400°C. Moreover, the amounts of heat release ( $\Delta Q$ ), calculated as the area under the transformation peaks (see green areas in Figure 3-19), are similar upon  $B2 \rightarrow R$  transformation in both cases. Interestingly, the amount of heat absorbed upon heating was larger than the total heat released upon cooling.

In addition to the transformation temperatures and the amounts of heat exchanged during phase transformations, DSC measurements allow us calculating the specific-mass constant-pressure heat capacities of the studied materials. To this end, we averaged the heat flow values of the nearly flat, phase transformation-free parts of the curves. In this way, we obtained the heat capacity of B2 austenite upon heating and cooling, the heat capacity of R-phase upon cooling, and the heat capacity of B19' martensite upon heating. The calculated values oscillate around  $0.38 \text{ J}^\circ\text{C}^{-1}\text{g}^{-1}$  for all three phases (see Table 3-4).

### 3.2.3.3. Tensile responses

With the aim of evaluating the impact of annealing temperatures on the stress-induced phase transformation in NiTi, we performed a series of tensile tests on hourglass-shaped samples annealed at 400°C, 425°C, 450°C, 475°C, and 500°C. The hourglass shape results very useful for detecting the onset of stress-induced phase transformations as all deformation and transformation processes are confined to the mid cross-section of the samples.

The tests were performed on a tensile testing machine BOSE ElectroForce 3300 equipped with a 3kN capacity load cell. The elongation of the samples was tracked using a 10mm gauge length clip-on axial extensometer EPSILON 3442. The samples were clamped to the machine using V-grooved wedge clamps, leaving a gauge length of 20mm between the upper and lower grip. The tests were controlled by the displacement of the upper grip at a displacement rate of  $0.05\text{mm}^{-1}$ . The lower grip and the load cell remained fixed to the

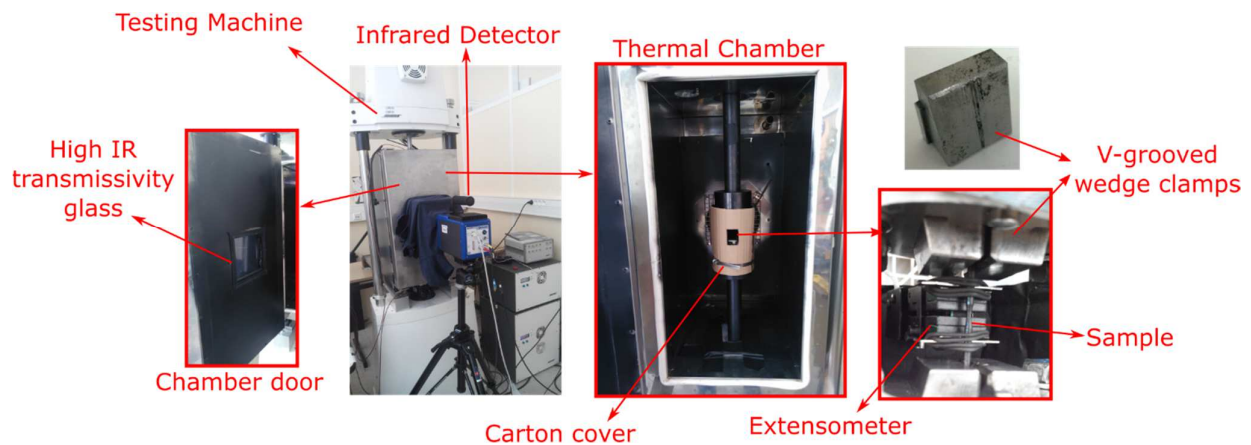


Figure 3-20 Experimental setup used for infrared thermal image acquisition upon tensile tests.

machine base during the tests. The tests were performed inside a thermal chamber at 32.5°C, 40°C, and 80°C.

In order to aid the detection of phase transformations upon tensile loading, the temperature of testing samples was tracked by means of an Infrared Cooled Detector FLIR SC7000. The experimental setup used for these measurements is illustrated in Figure 3-20. Infrared measurements required covering the samples' surface with a high emissivity matt black paint. In addition, the testing sample was protected from the air flux produced by the thermal chamber fan using a carton cover. This protection reduces the interference of random external infrared radiation that may reflect on the sample surface, and restricts the forced convection caused by circulating air inside the thermal chamber; thus, allowing more intense and less noisy temperature signals. The infrared detector allowed us to record thermal images with 20mK temperature resolution, and 15 $\mu$ m pixel resolution by using a magnification lens. To carry out the infrared measurements of tensile-loaded samples inside the thermal chamber, an electro-polished CaF<sub>2</sub> glass, transparent to infrared radiation, was adapted to the door of the heat chamber. The transmission coefficient of the glass was determined to be equal to 0.947, determined using a calibrated black body. As observed in Figure 3-20, we used a fabric cover around the glass and the detector lens in order to avoid infrared reflection from the surroundings on the glass.

Before each test, the testing sample was heated using a hot-air blower up to ~120°C to avoid possible discrepancies in the initial microstructure state of equal-annealed samples caused by their thermal history. After that, the testing sample was clamped into the testing machine and the thermal chamber preheated for about one hour up to the testing temperature. The start of the test was synchronized with the start of thermal images acquisition by means of a control signal generated by a functions generator connected to the infrared detector and the testing machine controller. The thermal images acquisition frequency used for these tests was 50Hz.

The temperature evolutions upon a single tensile loading ramp of hourglass-shaped samples annealed at 400°C, 425°C, 450°C, 475°C, and 500°C are presented in Figure 3-21. Separated samples were used for tests at 32.5°C, 40°C and 80°C. The temperature curves shown in

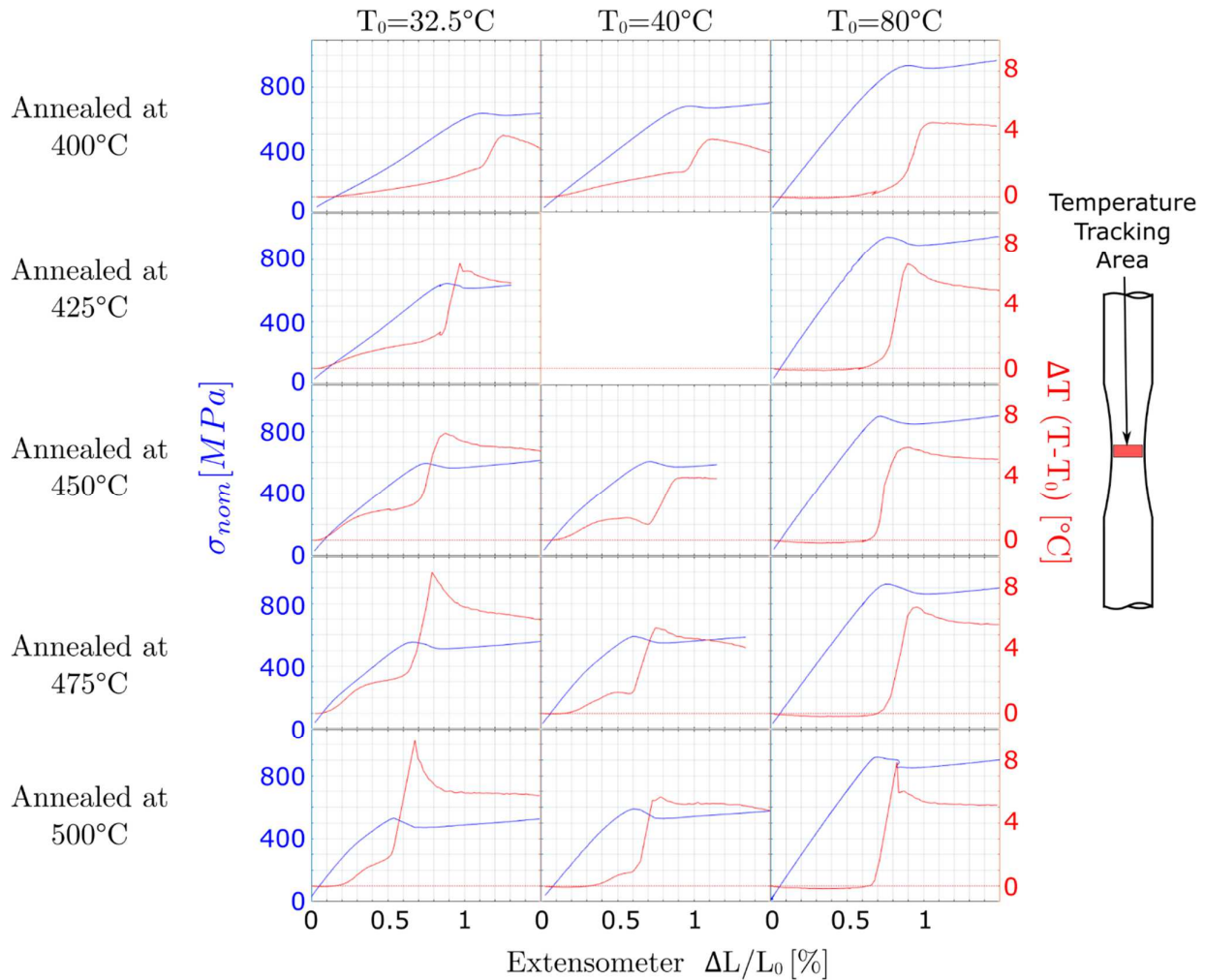


Figure 3-21 Tensile responses of NiTi hourglass-shaped samples issued from annealing treatments between 400 and 500°C.

Figure 3-21 corresponds to the mean temperature of a 15x50 pixels area at the mid cross-section. The temperature evolution curves were obtained with respect to a reference temperature  $T_0$ , calculated as the mean temperature at the mid cross-section of a reference thermal image. The reference thermal image was obtained by averaging ten thermal images recorded under static and stable temperature conditions before the start of the test.

The mechanical responses and the temperature recorded upon tensile loading are clearly dependent on the annealing and testing temperatures. At 32.5°C and 40°C the temperature of the 400°C and 425°C-annealed NiTi rises since the very beginning of the application of the tensile loading, contrarily to the temperature evolutions of 450°C, 475°C and 500°C-annealed NiTi's, which shows a temperature increase triggered only after reaching some loading level.

In the case of 400°C-annealed NiTi, the material is on a mix of B2 and R phases at 32.5°C and 40°C, as we can deduce from the  $R_s$  and  $R_f$  temperatures identified in DSC experiments (see Table 3-3). As a result, the temperature rise shown by 400°C and 425°C-annealed NiTi's

may be explained by a continuous stress-induced B2→R phase transformation and R-phase microstructure distortion.

The 500°C-annealed NiTi, on the other hand, showed an  $R_s$  temperature equal to 25.5°C according to DSC experiments; therefore, its initial state at 32.5°C and 40°C is B2 austenite. When the 500°C-annealed sample is first loaded, it behaves elastically and the temperature does not show a significant evolution until the stress-induced B2→R phase transformation occurs. Following the same logic, we can infer that at 32.5°C, the 425°C-annealed NiTi is in a mix of B2 and R-phase, whereas the 450°C and 475°C-annealed NiTi's are in the B2 austenitic state.

The characteristic yield point of the stress-extensometer elongation curves in Figure 3-21, allowed us to identify the onset of stress-induced R/B2→B19' transformations. When stress reaches the yield point, an accelerated temperature increase was recorded in all tests. The evolution of the onset of stress-induced R/B2→B19' transformations ( $\sigma_{MT}$ ) with respect to the testing temperature and annealing heat treatment is shown in Figure 3-22a. As observed, the annealing temperature exhibits a greater impact on  $\sigma_{MT}$  at low testing temperatures

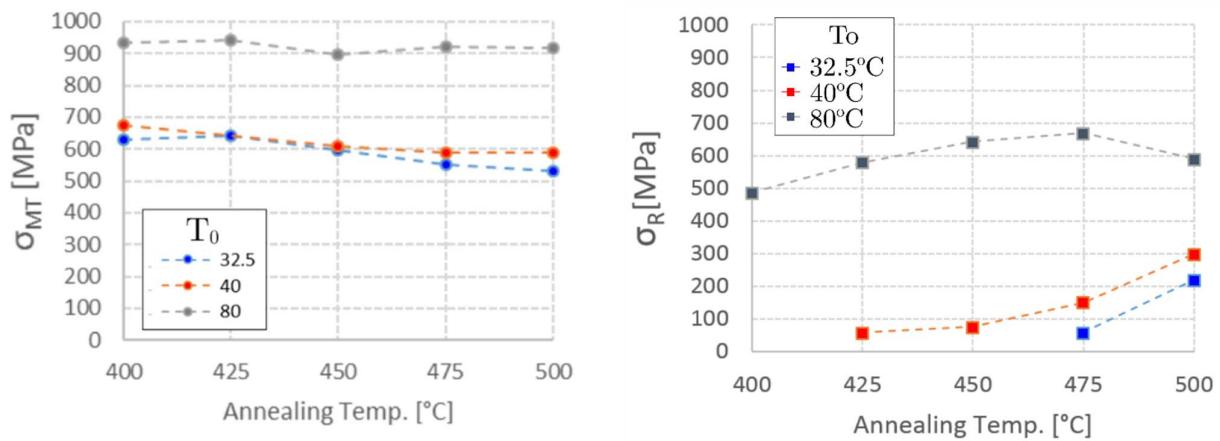


Figure 3-22 Onsets of phase transformations of NiTi#1 with respect to the annealing temperature:

a) R/B2→B19'. b) B2→R.

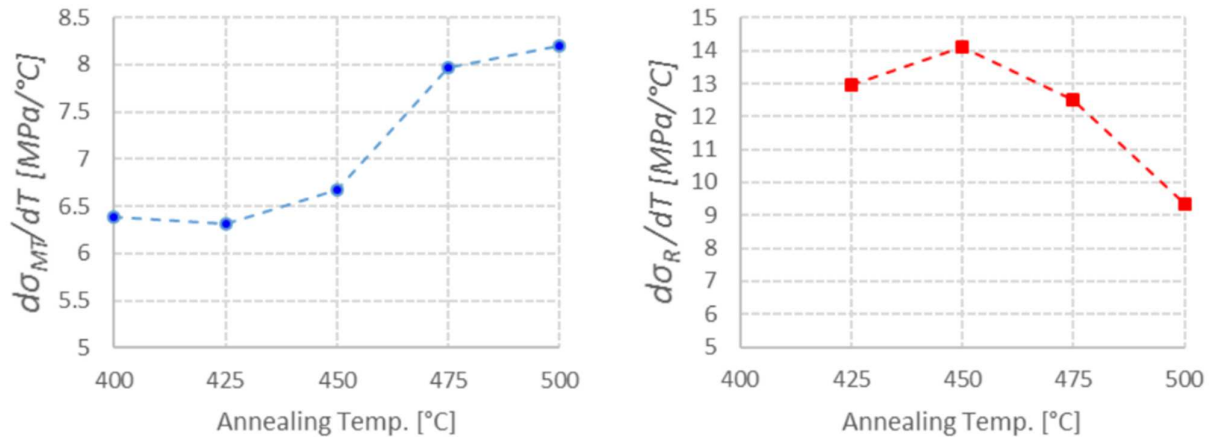


Figure 3-23 Stress-temperature slopes of phase transformations in NiTi#1 evaluated with respect to the annealing temperatures: a) R/B2→B19'. b) B2→R.

(32.5 and 40°C), becoming higher by increasing the annealing temperature. On the other hand, the  $\sigma_{MT}$  values obtained upon tensile tests at 80°C remains almost the same, regardless of the annealing temperatures.

The onset of the stress-induced B2→R phase transformation ( $\sigma_R$ ) was identified as the applied stress at the inflection point of the temperature evolution when the material starts to heat up before reaching the yield point of the R/B2→B19' transformation. As illustrated in Figure 3-22b, the annealing temperature has a greater impact on  $\sigma_R$  than on  $\sigma_{MT}$ . Higher annealing temperature shifts the stress need for B2→R phase transformation to higher values.

The evolution of the onsets of stress-induced phase transformations with temperature shown in Figure 3-23 was determined by carrying out a linear regression of the group of values identified for each annealing temperature. The stress-temperature slope of the R/B2→B19' transformation ( $d\sigma_{MT}/dT$ ) changes from ~6.4MPa/°C for the 400°C-annealed NiTi, up to ~8.2MPa/°C for the 500°C-annealed NiTi. The inverse behavior is observed in the B2→R phase transformation slope ( $d\sigma_R/dT$ ), where the 500°C-annealed NiTi exhibits the lowest values.

#### 3.2.3.4. Heat treatment choice for fatigue testing

So far, we presented the effects of annealing temperatures on the surface state, transformation temperatures and thermomechanical coupling of cold-drawn NiTi wires. Moreover, it is well known that annealing temperatures of cold-drawn NiTi wires also affects the grain size and dislocation density of the material, which together with the surface state are determinant in the fatigue performance of traditional alloys. As a result, NiTi fatigue studies based on testing different heat treatments or alloy compositions, necessarily mix grain sizes, surface states, and cold-worked structures, casting doubts on the real impact of the crystallographic phase transformations on NiTi's fatigue performance.

In order to simplify the assessment of the impact of stress-induced phase transformations on the high cycle fatigue performance of NiTi, we decided to use a single annealing treatment for our cold-drawn NiTi#1 samples, then to test them at different temperatures. We chose an annealing temperature at 500°C, as it allows us to tackle the fatigue in the B2→R and

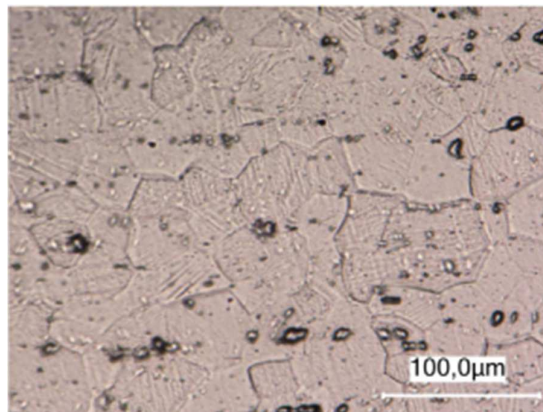


Figure 3-24. Optical microscope image revealing the grained microstructure of 500°C-annealed NiTi.

B2/R→B19' regimes at temperatures near the room temperature, and the B2 elastic regime just by increasing the temperature. In this way, other factors, such as grain size, dislocation density, and surface state remain the same for all samples.

The grained microstructure of NiTi#1 heat-treated for 30 minutes at 500°C is presented in Figure 3-24. The image was obtained from optical microscopic observation on a flat sample carefully polished using SiC abrasive paper of different denominations. After obtaining a mirror-like surface, the sample was etched using an acid solution consisting of:

- 10ml of m(HF),
- 40ml of m(HNO<sub>3</sub>),
- and 50ml of m(H<sub>2</sub>O),

based on the work of Undiszet al.[108].

The annealing treatment at 500°C resulted in an average grain size of ~30µm. Moreover, the optical image reveals the existence of inclusions, the size of which goes from less than 1µm up to ~10µm. According to the literature, these inclusions are most probably TiC carbides introduced upon the melting process of most of commercial NiTi alloys [109], [110]. Inside some of the grains, we observe a needle-like structure, which, according to X-ray diffraction experiments presented later in Chapter 4 may be related to twinned R-phase, although further analysis is needed to verify it.

In the following sections, we detail the mechanical response, microstructure evolution and thermal behavior of 500°C-annealed NiTi. After that, we present the fatigue performance of the material at different temperatures, which allow us to extract conclusions about the impact of phase transformations on the lifetimes of cyclically loaded NiTi.

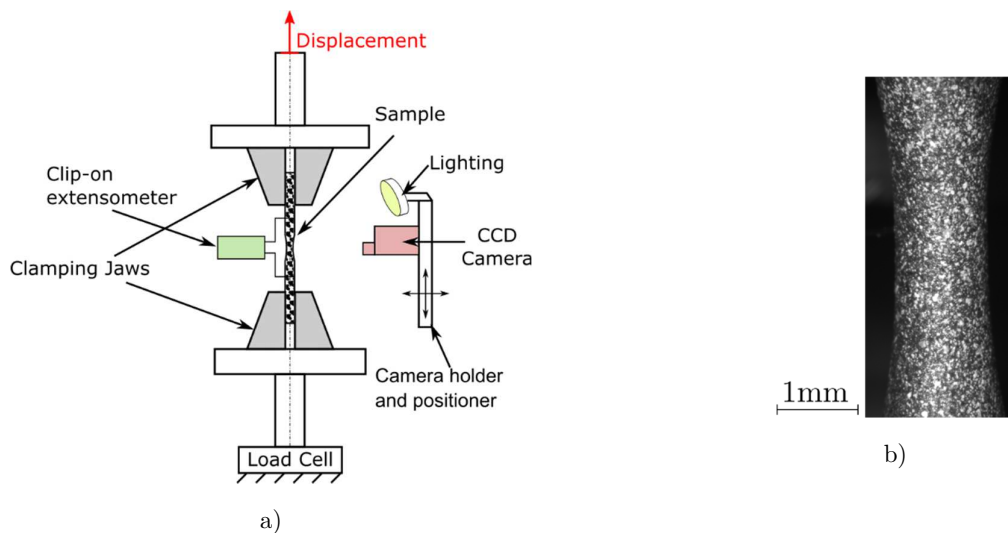


Figure 3-25 2D-DIC technique for strain field measurements upon tensile testing of hourglass-shaped samples: a) experimental setup, b) surface speckle pattern applied to the surface of an hourglass-shaped sample.

### 3.3. Thermomechanical behavior of 500°C-annealed NiTi

The thermomechanical response and microstructure evolution of 500°C-annealed NiTi hourglass shaped samples are characterized in more details in this section. To begin with, we present a detailed evaluation of the axial strain distribution in the groove zone of hourglass shaped samples upon axial loading-unloading tensile cycles using the 2D Digital Image Correlation technique (DIC). The deformation processes tracked by DIC were correlated with a phase distribution analysis carried out using X-ray diffraction. After that, we introduce a thermomechanical constitute model suitable for Shape Memory Alloys implemented in a Finite Element Analysis software suite. The model was used for evaluating the stress-strain state of the material at the mid cross-section of tensile loaded hourglass-shaped samples; therefore, it allowed us to correlate the macroscopic response of hourglass-shaped samples to the local behavior of the material.

#### 3.3.1. Stress-strain response

We carried out two tensile tests for characterizing the mechanical behavior of hourglass shaped samples, one upon the B2↔R phase transformation regime, and the other upon the B2/R↔B19' phase transformation regime. The tests were performed at room temperature (32.5°C) on a testing machine INSTRON 8872 equipped with a 25kN load cell. The elongation of the samples was measured via a 10mm-gauge length 2620-series INSTRON

<b>Image Acquisition</b>	
Camera	Stingray F504B ASG
Image Size and Digitalization	2452x2056, 8-bit
Cell size	3.45 $\mu$ m x 3.45 $\mu$ m
Camera noise (% of range)	1.5%
Lens and imaging distance	50.2mm C-mount, 112.526mm
Total number of Images	B2↔R phase transformation regime: 124 B2/R↔ B19' phase transformation regime: 442
Pixels to mm conversion	1pixel = 1.67 $\mu$ m
Region of Interest (pixels)	B2↔R phase transformation regime: 352x1626 B2/R↔ B19' phase transformation regime: 303x1615
<b>Displacements</b>	
Technique used	2D Digital Image Correlation
Subset radius, step (pixels)	20, 15
Interpolation	Biquintic B-spline
Shape Functions	Affine
Correlation Criterion	Normalized Sum of Square Differences (NSSD)
Pre-smoothing	None
Displacement resolution	0.05pixels – 0.0835 $\mu$ m
<b>Strain</b>	
Smoothing technique	Local polynomial
Strain window	7x7 data points
Virtual Strain Gauge (VSG)	110x110 pixels
Resolution	5x10 <sup>-4</sup>

Table 3-5 2D-DIC parameters

clip-on extensometer. We programmed the testing machine to apply tensile loading at a constant extensometer elongation rate up to a certain nominal axial stress limit depending on the studied transformation regime. The loading rate was set up to provide isothermal conditions during the tests, which was verified by the temperature measurement of J-type thermocouple welded to the surface of the sample at the mid cross-section.

The 2D Digital Image Correlation technique (2D-DIC) was employed to track the strain field of the surface of the groove zone of the testing hourglass-shaped sample. In order to use the 2D-DIC, we applied a white and black paint speckle pattern on the sample's surface by means of an airbrush Iwata CMC-C Plus. The resulting pattern obtained after airbrushing had an average speckle size of  $\sim 40\mu\text{m}$  (Figure 3-25b). Additionally, a 11x16 white LED array was used to provide a stable light source during image acquisition. The schematic representation of the experimental setup used for 2D-DIC strain measurements is shown in Figure 3-25a. A detailed description of the CCD camera and the characteristics of the acquired images are presented in the first part of Table 3-5.

The images acquired during tensile testing were post-processed into strain fields using NCORR[111], an open-source MATLAB-based software suitable for 2D-DIC. Only the central zones of the sample images were correlated, in order to reduce the error related to out of plane displacements. The parameters for the calculation of displacement and subsequent strain fields using the 2D-DIC algorithm are presented in Table 3-5. We highlight that DIC correlation allowed us a strain and displacement resolutions of  $5 \times 10^{-4}$  and  $0.083\mu\text{m}$  respectively. Moreover, the virtual strain gauge size for these experiments was  $110 \times 110$  pixels, equivalent to  $65.4 \times 65.4\mu\text{m}^2$ ; thus, allowing a sound spatial strain fields resolution.

### 3.3.1.1. B2 $\leftrightarrow$ R phase transformation regime

The tensile loading-unloading macroscopic response of an hourglass-shaped sample in the B2 $\leftrightarrow$ R phase transformation regime is presented in Figure 3-26a. In this experiment, the sample was loaded at an extensometer elongation rate of  $3 \times 10^{-3} \text{mms}^{-1}$  up to 0.035mm, then unloaded it down to zero load at the same extensometer elongation rate. The nominal stress in the y-axis of Figure 3-26a corresponds to the tensile force measured by the load cell divided by mid cross-section of the sample.

The macroscopic loading-unloading response of the tested hourglass-shaped sample under the mentioned limits exhibits a non-linear behavior. We associate this behavior with the stress-induced B2 $\rightarrow$ R phase transformation occurring mainly in the groove of the tested sample. Since any material non-linearity at the mid cross-section has a direct impact on the macroscopic response of hourglass-shaped samples (recall section 3.1), we can identify the onset of stress-induced B2 $\rightarrow$ R phase transformation at the inflection point of the macroscopic response in Figure 3-26a. In such a way, we observe that the onset of the B2 $\rightarrow$ R transformation ( $\sigma_R$ ) is  $\sim 220\text{MPa}$ , similar to the value obtained upon thermal measurements in the previous section. Moreover, the macroscopic response exhibits a small hysteresis and no residual strain after unloading.

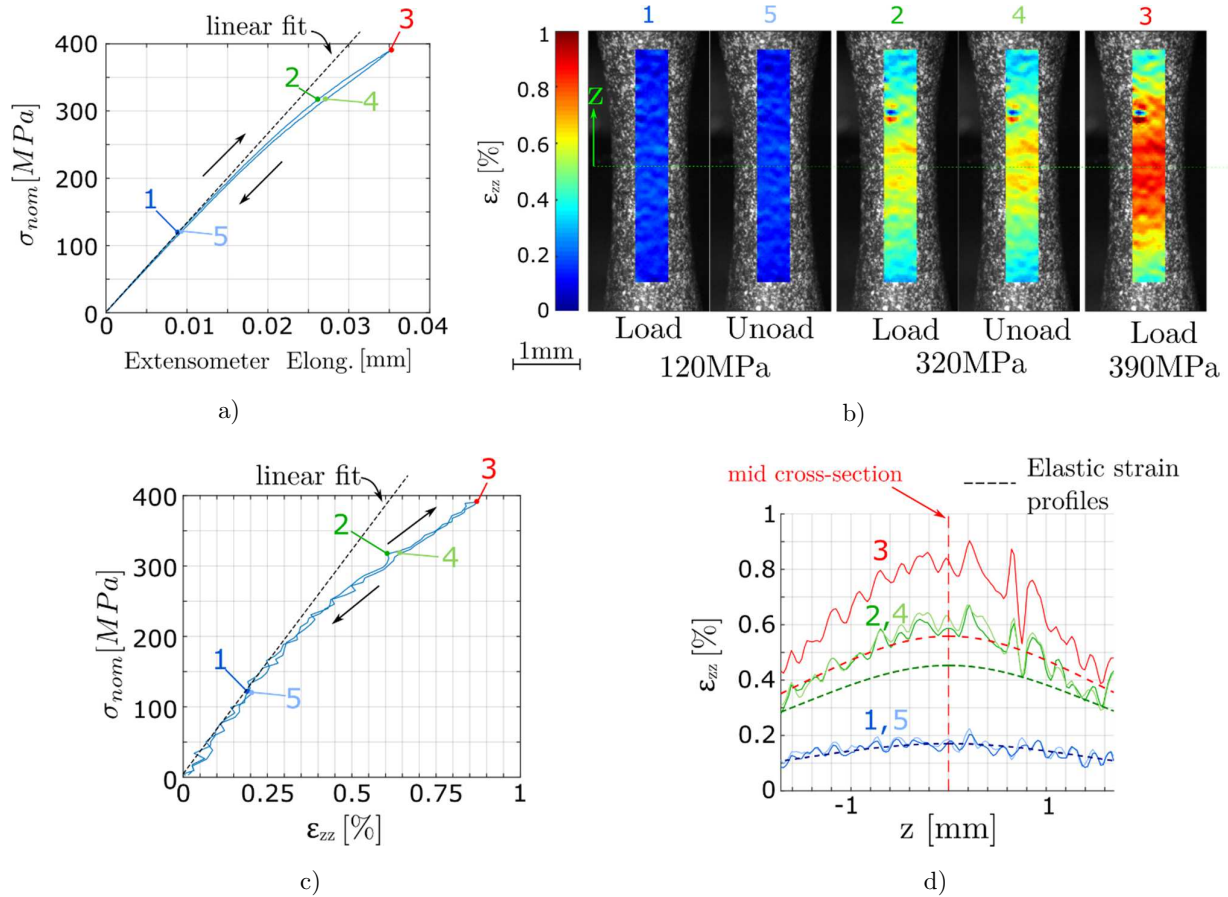


Figure 3-26 Tensile response of hourglass-shaped samples in the B2↔R phase transformation regime: a) Macroscopic response. b) Axial Lagrangian strain fields obtained using 2D-DIC at points highlighted in part (a). c) The local response of the material at the mid cross-section of the sample. d) 3.4mm-length axial strain profiles along the axis of the sample centered at the mid cross-section. The elastic strain profiles, plotted in dotted lines along with the experimental strain ones, were calculated via the Hooke's law using the material Young's modulus (70GPa), the sample's geometry and the nominal stresses at points 1 (dark-blue), 2 (green) and 3 (red).

The axial strain fields with respect to the undeformed initial state (Lagrangian configuration) of the five highlighted points in Figure 3-26a are shown in Figure 3-26b. There, we compare the axial strain distribution in the groove zone of the tested hourglass-shaped sample at three stress levels upon loading and unloading. As observed, the strain fields upon loading and unloading do not show significant differences, which follows the small hysteresis observed in the macroscopic response. By extracting a single data point of the strain field placed at the mid cross-section, we deduced the local response of the material (Figure 3-26c). The local response in Figure 3-26c can be defined as bilinear, without hysteresis nor residual plastic strain. The unexpected absence of hysteresis in the local response may be caused by lack of strain resolution of the 2D-DIC method. We associated the first linear-elastic part of the local response to the elasticity of B2 austenite and the second part to a progressive transformation from B2 austenite into R-phase. Assuming that the surface at the mid cross-section of the tested sample remains in a uniaxial stress state,

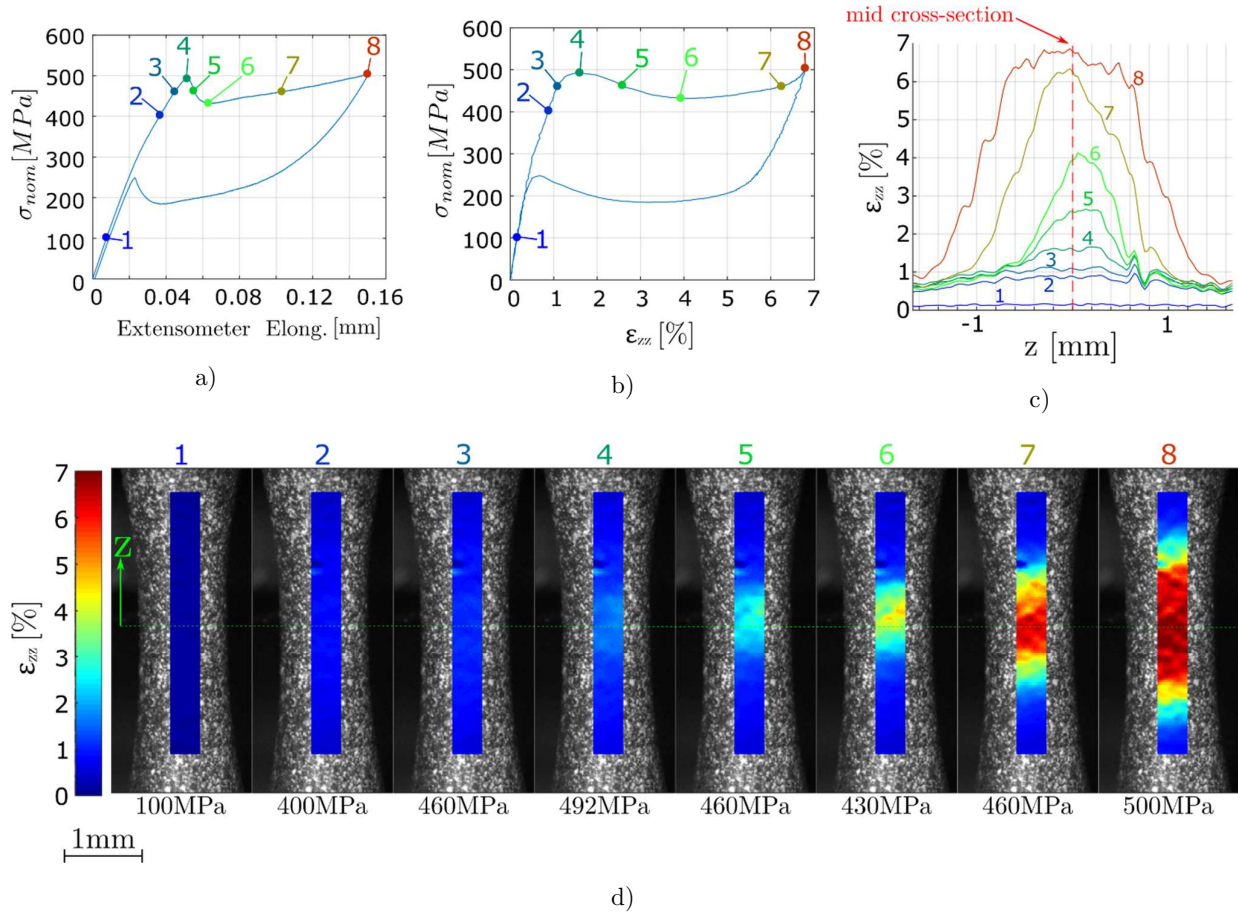


Figure 3-27. Tensile response of hourglass-shaped samples in the B2/R→B19' phase transformation regime upon loading. The macroscopic response is shown in (a). The lagrangian axial strain fields at the points highlighted in part (a) are shown in (d). The local response at the mid cross-section is plotted in (b) and the 3.4mm-length axial strain profiles along the axis of the sample in (c).

we can define the constitutive response of the 500°C-annelaed NiTi at 32.5°C by the local response in Figure 3-26c. As a result, the Young's modulus of B2 austenite was calculated equal to 77GPa, and the hardening rate of the second linear part of the local response equal to 30GPa. The uniaxiality stress state hypothesis will be verified in an oncoming section when simulating the mechanical response of hourglass-shaped samples using 3D model suited for finite element analysis.

An estimate of R phase transformed and B2 untransformed zones in the groove of the tested sample can be evaluated by comparing the measured axial strain profiles along the sample's axis with the linear elastic strain profiles calculated by the Hooke's law (Figure 3-26d). At points 1 and 5, at which the material is in the elastic B2 regime, the elastic strain profile fits well with the experimental strain profiles; thus we can deduce that no R-phase is induced in the sample. By increasing the applied stress, the B2→R transformation starts at the mid cross-section of the sample, then it spreads symmetrically along the groove zone. As a result, the experimental strain profiles deviates from the elastic one, especially at the mid cross-section. At points 2 and 4, two transformation fronts can be identified at ~1.6mm from

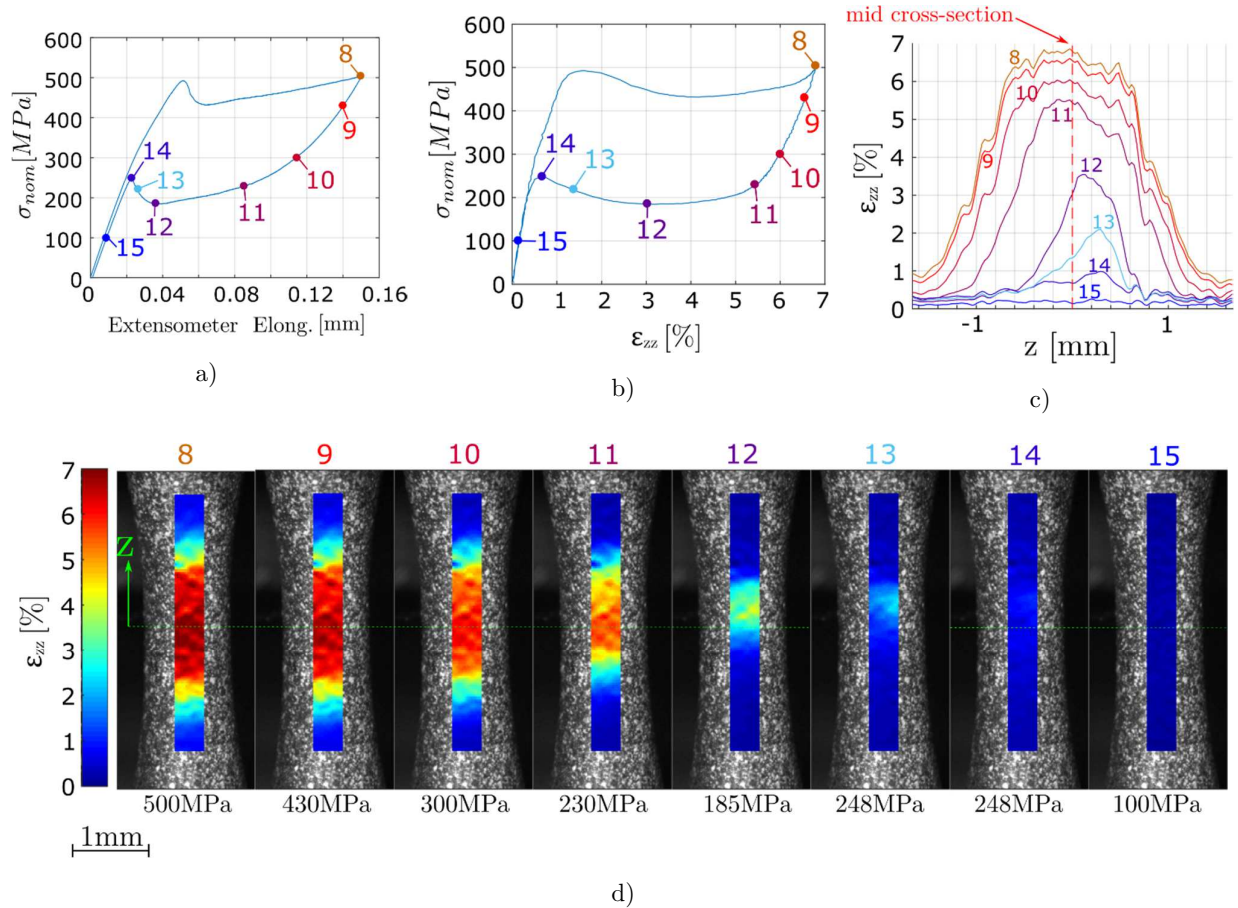


Figure 3-28 Tensile response of hourglass-shaped samples in the B2/R→B19' phase transformation regime upon unloading. The macroscopic (a) and local (b) responses are the same shown in Figure 3-27. The lagrangian axial strain fields at the points highlighted in part (a) are shown in (d), and the 3.4mm-length axial strain profiles along the axis of the sample are shown in (c).

the mid cross section, where the elastic strain profiles and the ones extracted from 2D-DIC strain fields start matching again. At the maximal stress (point 3), the mid cross-section sees an axial strain of more than 0.8% whereas the elastic strain reaches 0.56%.

### 3.3.1.2. R/B2→B19' phase transformation regime

Now, in order to assess the mechanical response of hourglass-shaped samples in the R/B2↔B19' transformation regime, we subjected the sample to a constant extensometer elongation rate of  $1 \times 10^{-3} \text{mm s}^{-1}$  up to 0.15mm, then unloaded it down to zero load at the same extensometer elongation rate. We divided the analysis of these experimental results into two parts. First, we describe the axial strain distribution upon loading (Figure 3-27), then upon unloading (Figure 3-28).

The nominal stress vs the extensometer elongation curve is presented in Figure 3-27a. The first part of the loading curve, up to the stress peak at 490MPa (point 4), corresponds to the B2→R phase transformation described before. This is supported by the strain profiles shape at the points 1, 2, and 3 (Figure 3-27c), which are similar to the ones presented back in Figure 3-26d. At the stress peak in point 4, the transformation from the mix B2/R into

B19' proceeds, as we can deduce from the local response at the mid cross section (Figure 3-27b), which resembles to the typical superelastic response of NiTi. After the stress peak, the macroscopic response shows sudden stress decrease down to 430MPa (point 6) followed by a constant stiffness response up to 500MPa (point 8).

The local response of the material differs from the typical NiTi tensile superelastic response by the continuous material softening observed after the onset of the stress-induced R/B2→B19' phase transformation between point 4 and point 6. Moreover, the axial strain profiles 4, 5, and 6 (Figure 3-27c) show how, when the transformation begins, the axial strain of a ~1mm length zone, centered at the mid cross section, increases while the material outside this zone keeps the same strain level as before the transformation (point3). As a result, an upper and a lower transformation fronts are created, which start spreading away from the mid cross-section after point 6. Between points 6 and 7, the axial strain at the mid cross-section increases rapidly together with a spread of the transformed volume. From point 7 to point 8, most of the elongation of the extensometer is caused by a spread of the two transformation fronts along the sample, while the strain at the mid cross-section slightly increases. The final B19' transformed zone at point 8 spreads ~1.4mm away symmetrically from both sides of the mid cross-section.

Upon unloading (Figure 3-28), the material behaves elastically from point 8 until point 10, as we can observe in the local response in Figure 3-28b. The Young's modulus of B19' martensite, obtained by a linear regression between points 8 and 10, was calculated equal to 27GPa. The macroscopic response, on the other hand, exhibits a nonlinear behavior right after the unloading begins. This is caused by the gradient of microstructure, from B19' martensite in the ~1.4mm-length zone from the mid cross-section to R-phase and B2 austenite in the rest of the sample; hence, the reverse R→ B2 transformation initiates when the stress starts decreasing in some zones of the sample away from the mid cross-section. Due to elastic unloading, the axial strain profile (Figure 3-28c) in the vicinity of the mid cross-section keep its shape from point 8 to 10. After point 10, the B19' zone begins to shrink, keeping the strain maxima at the mid cross-section. Then, between points 12 and 14, a fast decreasing of the axial strain from 3% down to 0.6% completes the reverse

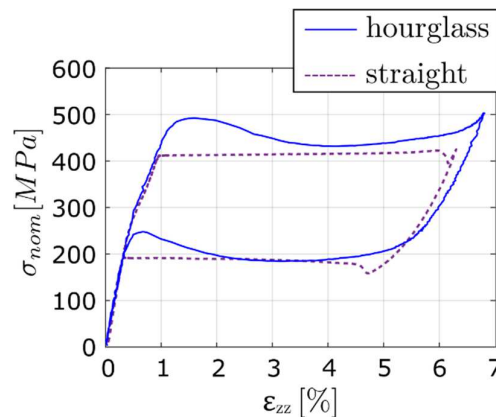


Figure 3-29 Comparison of the tensile responses of 500°C-annealed NiTi#1 at 32.5°C using a hourglass shaped sample and a straight sample.

transformation at the mid cross-section. Note that between points 12 and 14, the strain at the zones at least  $\sim 0.5$ mm further from the mid cross-section remains the same. Moreover, this fast strain recover at the mid cross-section correlates with the merge of the two B19' martensite fronts and a sudden increase of the axial nominal stress. After that, a short transition zone is observed before the material enters the linear unloading path of the B2 austenite phase. This short transition would suggest that the material transforms from B19' martensite into R-phase before returning to the initial austenite phase.

Finally, we carried out a complementary tensile test on a 1.78mm-diameter NiTi#1 straight wire prepared in the same conditions as the described hourglass shaped sample (annealing at 500°C for 30min). This time, the deformation of the sample was tracked using a 20mm-gauge length virtual extensometer. The virtual extensometer applies the 2D-DIC method in two small zones on the sample in order to track the relative distance between them. Two small white marks were painted on the surface of the sample in order to define the tracking zones. The test was performed in the same testing machine as the hourglass-shaped sample in similar temperature conditions (room temperature  $\sim 32.5^\circ\text{C}$ ). The tensile loading was applied at a constant upper grip displacement rate of  $3 \times 10^{-3} \text{mms}^{-1}$ , equivalent to a nominal strain rate of  $1.2 \times 10^{-4}$ , as the initial sample length, between the upper and the lower grip, was 25mm.

Figure 3-29 shows the tensile response of the straight sample together with the previous local response obtained in the hourglass-shaped sample. The tensile response of the straight sample looks like the commonly reported superelastic response of NiTi: constant stress forward and reverse transformation plateaus and hysteresis. Note that the B2 $\rightarrow$ R regime of the hourglass and straight samples are practically the same. The more remarkable differences come after the onset of the transformation into B19': while the hourglass-shaped sample response exhibits a softening right after the B19' transformation start, the straight sample shows a constant stress B19' transformation plateau with a small softening at the end of it. Contrarily, upon the reverse transformation, the straight sample experiences a sudden increase of stress right at the beginning of the transformation, whereas the hourglass response shows a similar stress increase but at the end of it. Moreover, the straight sample response suggests that the reverse transformation brings the material directly into B2 phase instead of R-phase, as we deduced from the local hourglass-shaped sample response.

### **3.3.2. Microstructure evolution resolved via X-ray diffraction**

In order to track the evolution of the microstructure in the volume confined at the mid cross-section of hourglass-shaped samples upon tensile loading, we performed in-situ synchrotron source x-ray diffraction experiments. These experiments were carried in the beamline ID11 at the European Synchrotron Radiation Facility (ESRF) at Grenoble. The results that we present next correspond to the experiment no. MA-2880 in the ESRF experimental report database.

### 3.3.2.1. Experimental setup

The hourglass-shaped sample used for this study was subjected to different tensile stress levels at room temperature ( $\sim 24^\circ\text{C}$ ). The sample was tested deformed using a tensile rig, the tensile axis of which was aligned with the rotation axis of the platform of the diffractometer at the beamline ID11 at the ESRF (see Figure 3-30). The tensile stress was monitored via a 1kN load cell mounted on the deformation rig.

All the studied samples in the experiment no. MA-2880 were evaluated using a square monochromatic microbeam of size  $\sim 6 \mu\text{m}$  and wavelength of  $0.18964 \text{ \AA}$ . The microbeam allowed us to carry out spatially resolved microdiffraction analysis along the axis of the hourglass samples. The diffracted beam was recorded using ESRF Frelon 2D detector of size  $100 \times 100 \text{ mm}$  and resolution of  $2048 \times 2048 \text{ px}$ , with a pixel size of  $50 \mu\text{m}$ . The distance between the sample and the 2D detector was  $\sim 250 \text{ mm}$  allowing a maximal scattering angle of  $16^\circ$  (see angle  $2\theta$  in Figure 3-30). The detector position and tilt with respect to the beam were found using the software pyFAI [112], which provides a tool called pyFAI-calib, designed for the calibrating the detector and the experimental setup. The calibration diffraction patterns were collected using CeO<sub>2</sub> referential powder sample. PyFAI library for Python programming language was used for azimuthal integration. After that, integrated diffraction patterns were evaluated by Rietveld refinement performed using GSAS II software [113], specially using its scripting tools for Python programming language, which enables to run the diffraction patterns analysis of large datasets in batch mode. The method of diffraction analysis in GSAS II is described in more details in the following paragraph.

In the diffraction analysis of collected data, the presence of three crystallographic known phases was assumed, namely the presence of austenite (cubic B2 phase,  $a=3.015 \text{ \AA}$ ), R-phase (trigonal phase,  $a=b=7.314 \text{ \AA}$ ,  $c=5.2291$ ,  $\alpha=\beta=90^\circ$ ,  $\gamma=120^\circ$ ), and martensite (monoclinic B19' phase,  $a=2.898$ ,  $b=4.646$ ,  $c=4.108$ ,  $\alpha=\beta=90^\circ$ ,  $\gamma=97.78^\circ$ ). The scaling parameters, determining eventually the phase volume fractions, were set free to vary throughout the entire refinement procedure. Before the refinement, the instrument parameters were found using the referential powder diffraction patterns (CeO<sub>2</sub> powder sample) and the calibration procedure described in GSAS II tutorial. While the phase scaling parameters were free to vary throughout the entire Levenburg-Marquardt based optimization, the rest of the parameters intervening in the optimization were freed sequentially in individual steps of the

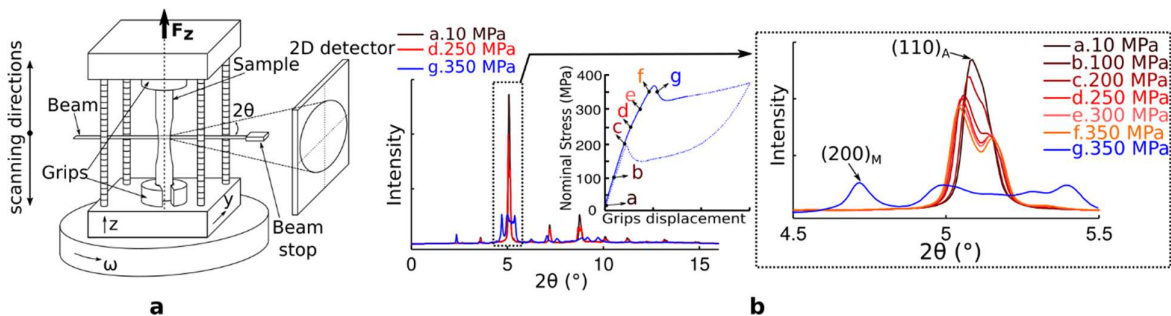


Figure 3-30 Experimental setup for in situ synchrotron source x-ray diffraction experiments in tensile loaded hourglass NiTi samples.

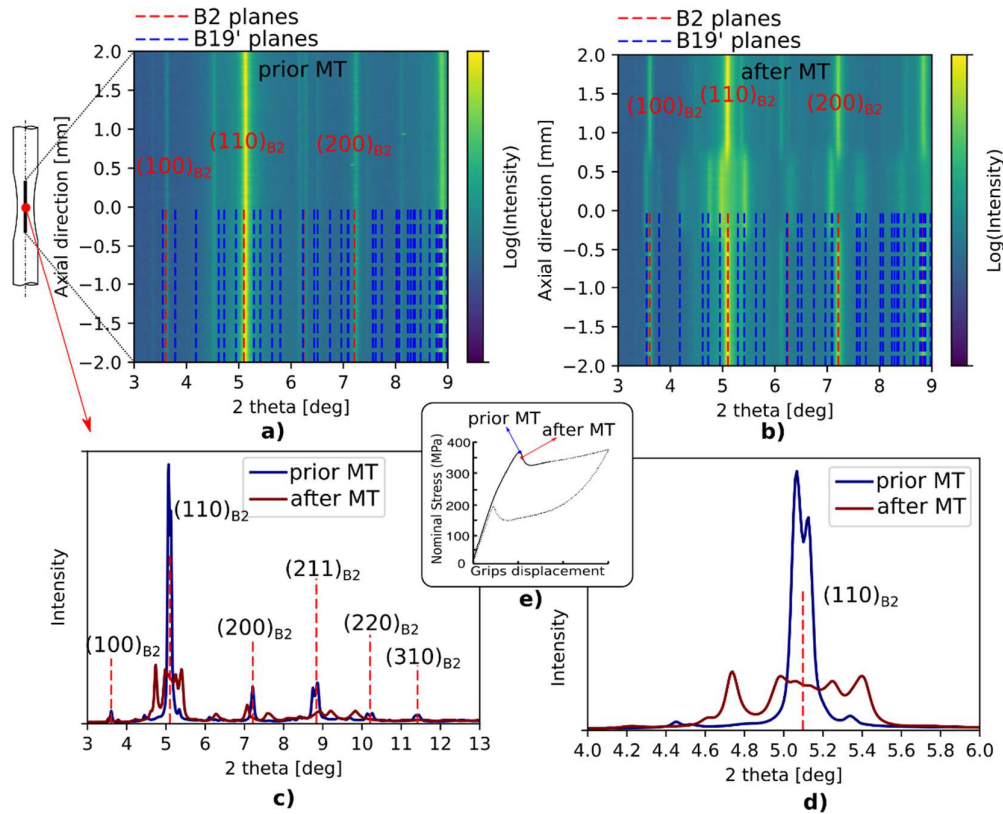


Figure 3-31 Comparisons of diffraction patterns recorded on a single sample prior (a) and after the stress-induced martensitic transformation (b). Colormaps in (a) and (b) represent diffraction patterns acquired during scans along the axial direction. Diffraction patterns shown in (c) and (d) were recorded approximately in the center of the concave zone of the sample.

refinement. The refinement was carried out employing a pseudo-Voigt profile function through the following five steps:

1. Refinement of the background using second-order Chebyshev polynomial function. The low order of the function is justified by the fact that we systematically subtracted the referential background and dark images from acquired 2D diffractograms.
2. Refinement of the cell parameters of the R-phase in order to take into account its rhombohedral distortion [114].
3. Refinement of the peak shifts considering the hydrostatic and elastic strain due to the applied loadings and/or internal stresses.
4. Refinement of the peak broadening assuming variable microstrains and crystallite size
5. Refinement of the texture of R-phase and martensite. The texture refinement was used to take into account the variant selection of stress-induced R-phase and/or martensite. The texture model implemented in GSAS II was described by [115].

The refinement was performed within the diffraction angle range of 2°- 12° where all significant reflections of all phases appeared. The quantitative phase analysis was performed by refining diffraction patterns obtained from full azimuthal integration. In order to evaluate the spatial heterogeneity of the phase distributions, we present in the following figures sets

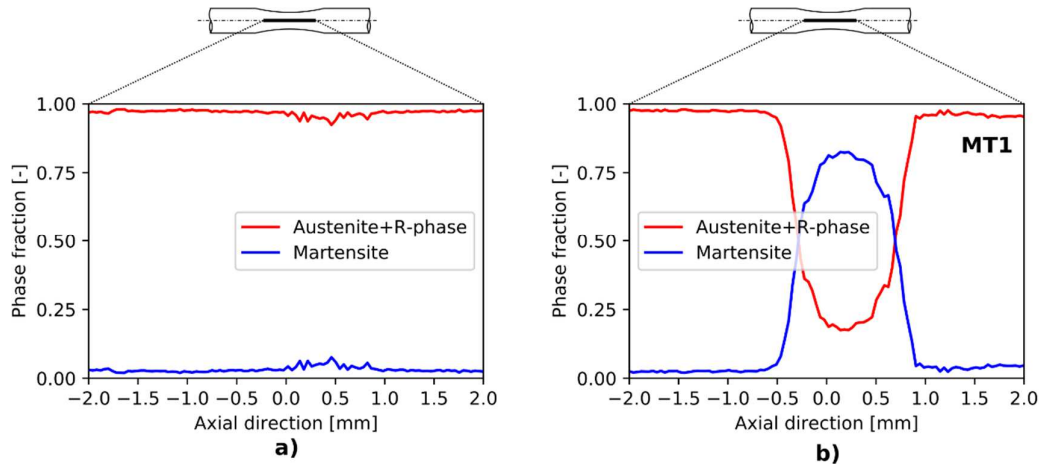


Figure 3-32 Results of spatially resolved quantitative phase analysis performed on a single sample prior (a) and after the martensitic transformation occurred (b).

of diffraction patterns along selected directions as colormaps. It is worth mentioning that the presented outcomes of the diffraction studies are not complete as the analysis of the large dataset is still ongoing.

### 3.3.2.2. Diffraction pattern evolution upon loading

Figure 3-30a presents the experimental setup where the sample was placed in the tensile rig while x-ray beam is scanning the sample along the axial direction. Scans were performed at different loading stages as shown in Figure 3-30b, where integrated patterns for selected loadings at room temperature (24°C) are illustrated. The integrated patterns show splitting of (110)A peak typical for austenite to R-phase transformation [114].

The hourglass shape of the sample is particularly suited for studies of the onset of the martensitic transformation as it occurs in a well-defined known place. In our experiment, we tested a virgin sample by applying small incremental loading steps until the martensitic transformation was triggered. On each loading step, we acquired diffraction scans to track microstructure changes. Surprisingly, the B19' martensitic transformation did not occur at any of the steps below the localization peak identified in DIC experiments. The B19' transformation occurred spontaneously during the incremental application of loading, resulting impossible to track the kinetics of the transformation. As a result, we got diffraction data right before and right after the martensitic transformation onset (see Figure 3-31).

Upon further loading, not only the transformed zone spread but also the artifacts of austenitic reflections disappears as seen in Figure 3-35, although quantitative phase analysis shown in Figure 3-34 reveals remaining austenite within the transformed zone.

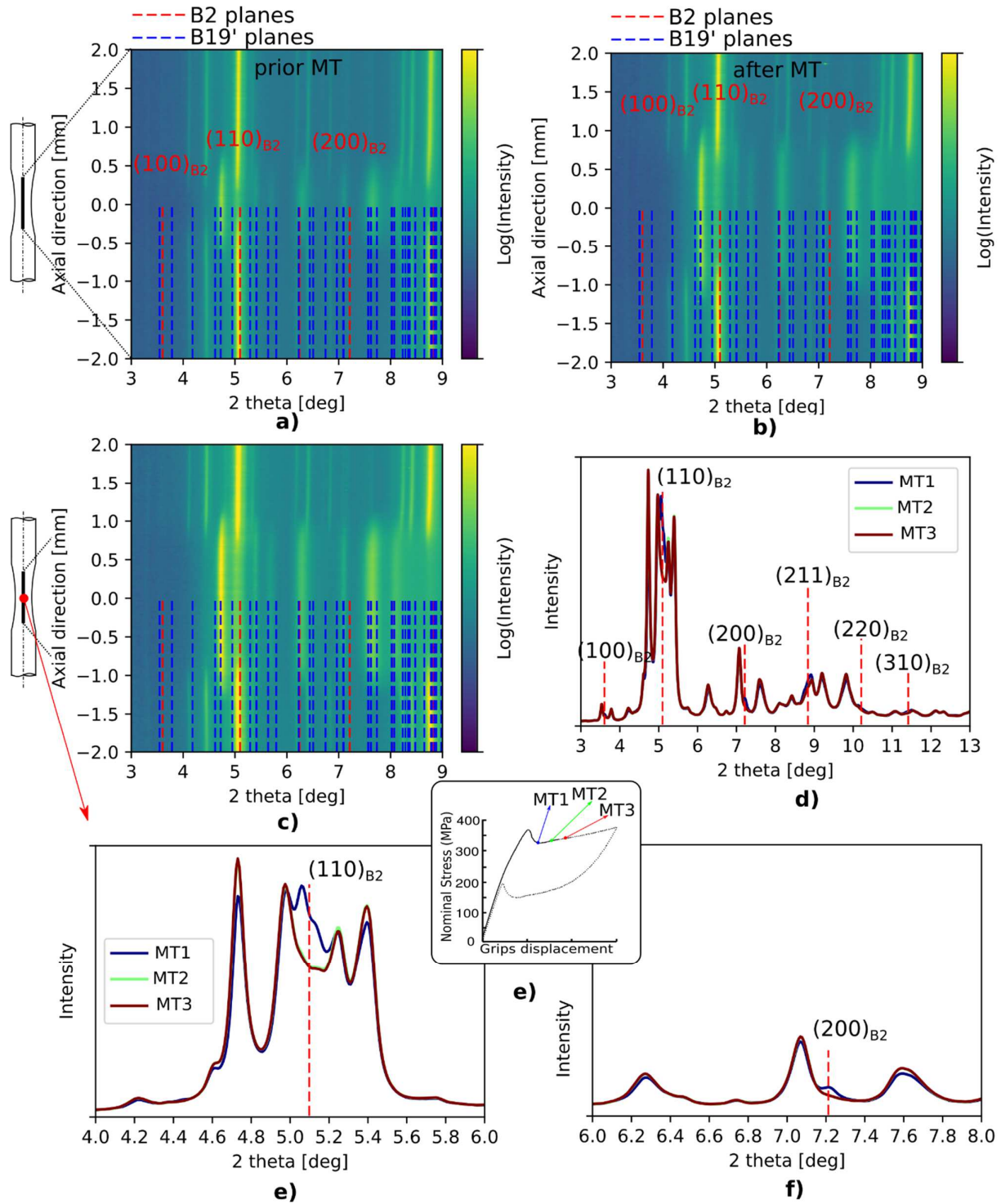


Figure 3-33 Comparisons of diffraction patterns recorded on a single sample during straining after the martensitic transformation occurred. Colormaps (a), (b), and (c) correspond to loading stages shown in (e), denoted as MT1, MT2, MT3. Diffraction patterns (d), (e), (f) were taken in the mid cross-section of the sample at loading stages MT1, MT2, MT3 respectively.

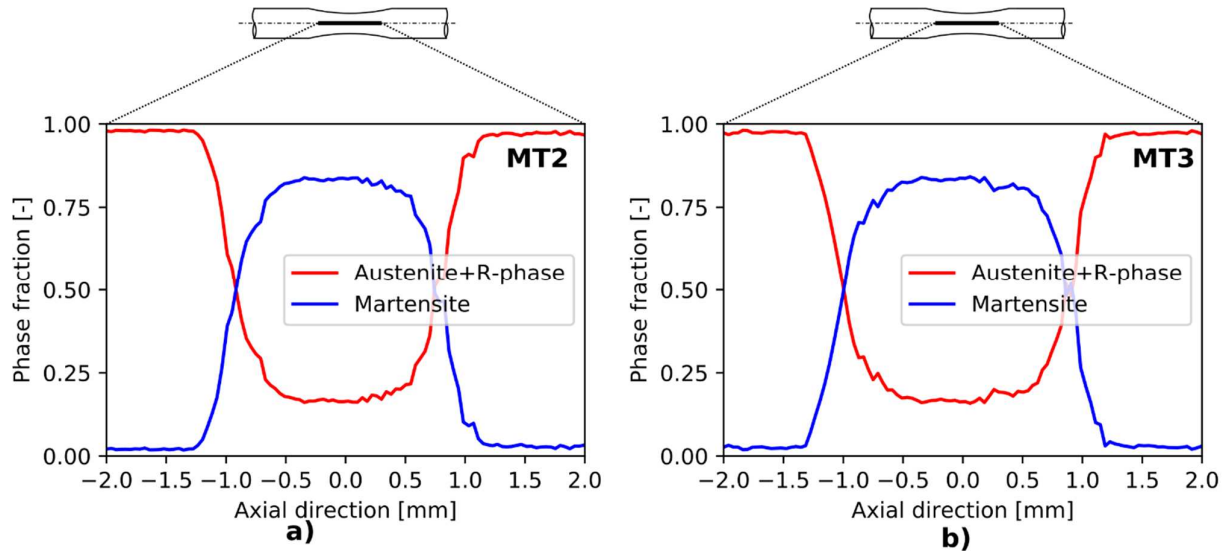


Figure 3-34 Results of spatially resolved quantitative phase analysis performed on a single sample after the martensitic transformation occurred. The results correspond to loading stages MT2 and MT3 shown in Figure 3-33e.

### 3.3.3. Simulation of the tensile response using 3D finite element analysis

In order to assist the analysis of the mechanical and crystallographic evolution of tensile tested NiTi hourglass shaped samples upon R and B19' phase transformations, we used the 3D constitutive model of Sedláč et al.[41]. In this section, we start by describing the equations of the model and its implementation in the finite element software suite ABAQUS. After that, we describe the process for identifying the model parameters, which allowed us reproducing the experimental results of our studied NiTi. Finally, we compare and analyze the simulation and the experimental tensile responses of hourglass-shaped samples carried out at different temperatures.

#### 3.3.3.1. Description of the model

The 3D thermomechanical model for polycrystalline NiTi-based shape memory alloys developed Sedláč et al.[41] was written within the framework of continuum thermodynamics of irreversible process. The model proposes an interaction of chemical and mechanical energy potentials as described by the phenomenological thermodynamic theory of thermoelastic martensitic transformations. It effectively couples the material mechanical behavior to the temperature, allowing a good description of thermal and stress-induced phase transformations between B2 austenite, R-phase, and B19' martensite.

The state variables of the model are the total strain of the material  $\boldsymbol{\varepsilon}$  and the temperature  $T$ . The total strain is described as the sum of elastic and inelastic contributions, which, adopting the small strain continuum mechanics formalism reads

$$\boldsymbol{\varepsilon} = \boldsymbol{\varepsilon}^{el} + \boldsymbol{\varepsilon}^{in}. \quad (3.17)$$

The inelastic strain contribution is related to the phase transformation into B19' martensite only. It is defined as

$$\boldsymbol{\varepsilon}^{in} = \xi \boldsymbol{\varepsilon}^{tr}, \quad (3.18)$$

where  $\xi$  is the volume fraction of B19' martensite, constrained by

$$0 \leq \xi \leq 1, \quad (3.19)$$

and  $\boldsymbol{\varepsilon}^{tr}$  is the transformation strain tensor. Since the transformation into B19' martensite is considered as volume constant,

$$tr(\boldsymbol{\varepsilon}^{tr}) = 0, \quad (3.20)$$

where  $tr(\boldsymbol{x})$  denotes the trace of the tensor  $\boldsymbol{x}$ . Furthermore, the transformation strain is constrained within a convex surface in the strain domain. The transformation strain surface is defined by the function  $\langle \cdot \rangle : \mathbb{R}^{3 \times 3} \rightarrow \mathbb{R}^+$ ,

$$0 \leq \langle \boldsymbol{\varepsilon}^{tr} \rangle = \frac{I_2(\boldsymbol{\varepsilon}^{tr})}{k} \leq 1, \quad (3.21)$$

where

$$I_2(\boldsymbol{x}) = \sqrt{\frac{2}{3} x_{ij} x_{ij}} \quad (3.22)$$

corresponds to the von Mises equivalent strain and  $k$  the magnitude of the maximal transformation strain (the plateau length in the case of a superelastic tensile curve). In their article, Sedláč et al., consider a more complex form of the transformation strain surface that includes the characteristic anisotropy and the well-known tension-compression asymmetry of the B19' transformation in NiTi. Since our problem can be reduced to a nearly uniaxial loading, we opted for the simplified form in (3.21).

Adopting the phenomenological framework of thermoelastic martensitic transformations, the model describes the evolution of the thermodynamic system by minimizing the sum of a volume specific free energy term

$$\boldsymbol{F} = f^{el} + f^{chem}, \quad (3.23)$$

consisting of an elastic (mechanic) and chemical component, plus an irreversible or dissipative term  $d$ .

The authors employed ruled of mixtures in order to determine the contribution of B2, R and B19' phases to each of the free energy terms. On the one hand, the elastic strain free energy potential is defined as

$$f^{el}(\boldsymbol{\varepsilon}, \boldsymbol{\varepsilon}^{tr}, \xi, \eta) = \frac{1}{2} K tr(\boldsymbol{\varepsilon})^2 + G(\xi, \eta) \left\| dev(\boldsymbol{\varepsilon}) - \xi \boldsymbol{\varepsilon}^{tr} \right\|^2, \quad (3.24)$$

where  $K$  is the bulk modulus and  $dev(\boldsymbol{\varepsilon})$  is the deviatoric part of the strain tensor. The bulk modulus  $K$  is considered the same for B2, R, and B19' phases ( $K = K^A = K^R = K^M$ ), based

on the very similar experimental values obtained by Wagner et al.[116]. The composed shear modulus  $G(\xi, \eta)$ , is determined from the Reuss rule of mixtures as follows:

$$\frac{1}{G(\xi, \eta)} = (1 - \xi - \eta) \frac{1}{G^A} + \eta \frac{1}{G^R} + \xi \frac{1}{G^M}. \quad (3.25)$$

The superscripts  $A$ ,  $R$ , and  $M$  correspond to the B2, R, and B19' phases respectively. The volume fraction of R-phase is denoted here as  $\eta$ , which is constrained by

$$0 \leq \eta \leq 1 - \xi; \quad (3.26)$$

as a result, the volume fraction of B2 austenite can be written as  $(1 - \eta - \xi)$ .

On the other hand, the chemical free energy potential is defined using the Voigt rule of mixtures in the following way:

$$f^{chem} = (1 - \eta - \xi)f^A + \eta f^R + \xi f^M, \quad (3.27)$$

where the contribution of each individual phase is defined by

$$f^i = u_0^i - s_0^i T + c^i \left[ (T - T_0) - T \ln \left( \frac{T}{T_0} \right) \right], \quad (3.28)$$

for  $i \in A, R, M$ . Here,  $c^i$  denotes the heat capacity, and  $u_0^i$  and  $s_0^i$  the specific internal energy and the specific entropy at the reference temperature  $T_0$  respectively. For practical reasons, the authors defined two reference temperatures: the first, simply denoted as  $T_0$ , at the chemical equilibrium between B2 and B19' ( $f^A(T_0) = f^M(T_0)$ ), and the other, denoted as  $T_0^R$ , at the chemical equilibrium between B2 and R-phase ( $f^A(T_0^R) = f^R(T_0^R)$ ); therefore,

$$T_0 = \frac{\Delta u^{AM}}{\Delta s^{AM}}, \quad (3.29)$$

and

$$T_0^R = \frac{\Delta u^{AR}}{\Delta s^{AR}}, \quad (3.30)$$

where  $\Delta x^{ij} = x^i - x^j$ .

Combining (3.27) and (3.28), the contributions of each phase to the chemical energy potential read

$$(1 - \eta - \xi)f^A = (1 - \xi) \left\{ u_0^A - s_0^A T + c^A \left[ (T - T_0) - T \ln \left( \frac{T}{T_0} \right) \right] \right\} - \eta \left\{ u_{R0}^A - s_{R0}^A T + c^A \left[ (T - T_0^R) - T \ln \left( \frac{T}{T_0^R} \right) \right] \right\}, \quad (3.31)$$

$$\eta f^R = \eta \left\{ u_{R0}^R - s_{R0}^R T + c^R \left[ (T - T_0^R) - T \ln \left( \frac{T}{T_0^R} \right) \right] \right\}, \quad (3.32)$$

and

$$\xi f^M = \xi \left\{ u_0^M - s_0^M T + c^M \left[ (T - T_0) - T \ln \left( \frac{T}{T_0} \right) \right] \right\}, \quad (3.33)$$

where the subscripts ‘0’ and ‘R0’ differentiates between quantities evaluated with respect to  $T_0$  and  $T_0^R$  respectively. Assuming that the heat capacities of the B2, R and B19’ are very close to each other (see Table 3-4), we can neglect the terms  $\Delta c^{ij} \left[ (T - T_0) - T \ln \left( T/T_0 \right) \right]$  resulting from adding up equations (3.31), (3.32), and (3.33); thus, the total chemical free energy potential finally reads,

$$f^{chem} = u_0^A - s_0^A T + c^A \left[ (T - T_0) - T \ln \left( \frac{T}{T_0} \right) \right] + \xi \Delta s^{AM} (T - T_0) + \eta \Delta s^{AR} (T - T_0^R). \quad (3.34)$$

In order to expand the temperature range in which the B2→R transformation takes place, the reference temperature  $T_0^R$  is defined as a function of the volume fraction of R-phase in the B2 austenite phase ( $\eta/1 - \xi$ ) as follows:

$$T_0^R(\eta, \xi) = R_s + \frac{\eta}{1 - \xi} \frac{R_f - R_s}{2}. \quad (3.35)$$

To describe the hystoelastic behavior of NiTi, Sedláč et al. [41] propose the following potential or dissipation term:

$$d = \begin{cases} \dot{\xi} \Delta s^{AM} \left[ (T_0 - M_s) + \xi (M_s - M_f) \right] + \sigma_{reo}(T) \left\| \dot{\boldsymbol{\varepsilon}}^{in} \right\| & \text{if } \dot{\xi} \geq 0 \\ \dot{\xi} \Delta s^{AM} \left[ (T_0 - A_f) + \xi (A_s - A_f) \right] + \sigma_{reo}(T) \left[ \left\| \frac{\dot{\xi}}{\xi} \boldsymbol{\varepsilon}^{in} \right\| + \left\| \dot{\boldsymbol{\varepsilon}}^{in} - \frac{\dot{\xi}}{\xi} \boldsymbol{\varepsilon}^{in} \right\| \right] & \text{if } \dot{\xi} < 0 \end{cases} \quad (3.36)$$

which suggests that only the transformation into B19’ dissipates energy, no matter if the parent phase is R-phase or B2. The neglect of the dissipation of the B2→R transformation is consistent with the very small mechanical and thermal hysteresis observed in our tensile and DSC experiments respectively (see Figure 3-26 and Table 3-4). Moreover, the dissipation form (3.36) allows differentiating between thermal and stress-induced phase transformations dissipations by including the effects of martensite reorientation  $\sigma_{reo}(T)$  and the strain produced by the B2/R→B19’ phase transformation  $\boldsymbol{\varepsilon}^{in}$ . The quantities  $A_s$ ,  $M_f$ ,  $M_s$ , and  $M_f$  correspond to the transformation temperatures of the alloy obtained at zero stress. Since

$$M_f < M_s < T_0 < A_s < A_f, \quad (3.37)$$

and

$$\sigma_{reo}(T) = \sigma_{reo}^0 + \Sigma^{reo} (T - T_0) \geq 0, \quad (3.38)$$

where  $\sigma_{reo}^0$  and  $\Sigma^{reo}$  are material parameters, the dissipation is always greater or equal to zero. This fulfills the Clausius-Duhem inequality, a necessary condition for describing thermodynamic irreversible process adopted in the framework of Generalized Standard Models in continuum mechanics. Within this framework, the thermodynamic forces  $\boldsymbol{\sigma}$ ,  $\boldsymbol{\pi}$ ,  $\mathbf{X}$

and  $\tau$  associated to the evolution of the state variable  $\boldsymbol{\varepsilon}$ , and the internal variables  $\boldsymbol{\varepsilon}^{tr}$ ,  $\xi$  and  $\eta$  are defined as

$$\boldsymbol{\sigma} = \frac{\partial \mathbf{F}}{\partial \boldsymbol{\varepsilon}} = K \text{tr}(\boldsymbol{\varepsilon}) \mathbf{I} + 2G(\xi, \eta) \left[ \text{dev}(\boldsymbol{\varepsilon}) - \xi \boldsymbol{\varepsilon}^{tr} \right], \quad (3.39)$$

$$\mathbf{X} = -\frac{\partial \mathbf{F}}{\partial \boldsymbol{\varepsilon}^{tr}} = 2G(\xi, \eta) \left[ \text{dev}(\boldsymbol{\varepsilon}) - \xi \boldsymbol{\varepsilon}^{tr} \right], \quad (3.40)$$

$$\begin{aligned} \boldsymbol{\pi} = -\frac{\partial \mathbf{F}}{\partial \xi} = & -\frac{\partial G(\xi, \eta)}{\partial \xi} \left\| \text{dev}(\boldsymbol{\varepsilon}) - \xi \boldsymbol{\varepsilon}^{tr} \right\|^2 + 2G(\xi, \eta) \left( \text{dev}(\boldsymbol{\varepsilon}) - \xi \boldsymbol{\varepsilon}^{tr} \right) : \boldsymbol{\varepsilon}^{tr} \\ & - \Delta s^{AM} (T - T_0) + \eta \Delta s^{AR} \frac{\partial T_0^R(\xi, \eta)}{\partial \xi} \end{aligned} \quad (3.41)$$

$$\tau = -\frac{\partial \mathbf{F}}{\partial \eta} = -\frac{\partial G(\xi, \eta)}{\partial \eta} \left\| \text{dev}(\boldsymbol{\varepsilon}) - \xi \boldsymbol{\varepsilon}^{tr} \right\|^2 - \Delta s^{AR} (T - T_0^R(\xi, \eta)) + \eta \Delta s^{AR} \frac{\partial T_0^R(\xi, \eta)}{\partial \eta}. \quad (3.42)$$

The governing equations that describe the problem of a NiTi element defined in the spatial domain  $\Omega$ , subjected to the external forces  $F_{surf}$  acting on the body surface  $\Gamma^N$ , together with external displacements  $U_{surf}$  acting on the surface  $\Gamma^D$ , are

$$\text{div}(\boldsymbol{\sigma}) = 0 \quad \text{in } \Omega, \quad (3.43)$$

$$\boldsymbol{\sigma} n = F_{surf} \quad \text{on } \Gamma^N, \quad (3.44)$$

$$u = U_{surf} \quad \text{on } \Gamma^D, \quad (3.45)$$

$$\mathbf{X} \in \partial_{\boldsymbol{\varepsilon}^{tr}} d \quad \text{in } \Omega, \quad (3.46)$$

$$\boldsymbol{\pi} \in \partial_{\xi} d \quad \text{in } \Omega, \quad (3.47)$$

$$\tau = 0 \quad \text{in } \Omega, \quad (3.48)$$

where  $n$  is the normal to the surface  $\Gamma^N$  and  $\partial_x d$  denotes the subdifferential of the dissipation function with respect to  $x$ . The evolution of the internal variables, in such a manner that the governing equations are fulfilled, is determined by carrying out the minimization of the sum of the free energy and the dissipation potentials:

$$\int_{\Omega} f(\boldsymbol{\varepsilon}, \boldsymbol{\varepsilon}^{tr}, \xi, \eta) + d(\boldsymbol{\varepsilon}^{tr}, \xi, \dot{\boldsymbol{\varepsilon}}^{tr}, \dot{\xi}) d\Omega \quad (3.49)$$

subjected to  $\langle \boldsymbol{\varepsilon}^{in} \rangle \leq 1$ ,  $0 \leq \xi \leq 1$ ,  $0 \leq \eta \leq 1 - \xi$ , and the boundary conditions on  $\boldsymbol{\varepsilon}$ , which derives from equation (3.45) according to the infinitesimal strain theory by

$$\boldsymbol{\varepsilon} = \frac{1}{2} \left( \nabla u + (\nabla u)^T \right), \quad (3.50)$$

where the superscript ‘ $T$ ’ refers to the transpose of the displacement vector. The solution of the problem considers the temperature as a prescribed parameter and the evolution of the internal variables as rate-independent.

The minimization problem of (3.43), with the boundary conditions (3.44) and (3.45), was spatially-discretized using finite element analysis. For this purpose, the model was

implemented in the finite element software suite ABAQUS Standard, via a subroutine referred as UMAT written in C++. The subroutine is called by ABAQUS on each material point for every computational increment  $k$ . Based on the boundary conditions of the problem, ABAQUS provides the strain increment at  $k$  and the previous values of the internal variables to the subroutine (at  $k-1$ ). The stress tensor components and the new values of the internal variables for each material point are calculated by the subroutine, which carries out the minimization of

$$f(\boldsymbol{\varepsilon}_k, \boldsymbol{\varepsilon}^{tr}, \xi, \eta) + d(\boldsymbol{\varepsilon}_{k-1}^{tr}, \xi_{k-1}, \boldsymbol{\varepsilon}^{tr} - \boldsymbol{\varepsilon}_{k-1}^{tr}, \xi_k - \xi_{k-1}) + r(\boldsymbol{\varepsilon}^{tr}, \xi, \eta), \quad (3.51)$$

with respect to  $\boldsymbol{\varepsilon}^{tr}$ ,  $\xi$  and  $\eta$ . The added regularization term  $r(\boldsymbol{\varepsilon}^{tr}, \xi, \eta)$  is equal to the maximum number attainable in computer precision (corresponding to  $+\infty$ ) whenever any of the restrictions (3.19), (3.21), or (3.26), is violated. Otherwise, it is defined as

$$r(\boldsymbol{\varepsilon}^{tr}, \xi, \eta) = c^r \left[ \operatorname{arctanh}^2(2\xi - 1) + \operatorname{arctanh}^2\left(\frac{\eta}{1 - \xi} - 1\right)(1 - \xi) \right] + kE^{int}\xi \frac{\langle \boldsymbol{\varepsilon}^{tr} \rangle^2}{1 - \langle \boldsymbol{\varepsilon}^{tr} \rangle^4}, \quad (3.52)$$

where  $c^r$  and  $E^{int}$  are positive regularization material parameters. The minimization problem is solved using the derivative-free Nelder-Mead optimization algorithm [117]. The implementation of the UMAT in ABAQUS, notably the minimization algorithm and the calculation of the tangent operator

$$L = \frac{d\boldsymbol{\sigma}}{d\boldsymbol{\varepsilon}}, \quad (3.53)$$

necessary for accelerated convergence of the main finite element routine, are detailed in [41] [118].

### 3.3.3.2. Model parameters identification

Most of the parameters of the model can be identified using tensile tests and DSC experiments. The parameter fitting procedure was divided into three stages. First, we fitted the parameters related to the stress-induced B2→R transformation, then those related to the stress-induced B2/R→B19' transformation, and finally those that determine the energy dissipation rate and the mechanical hysteresis.

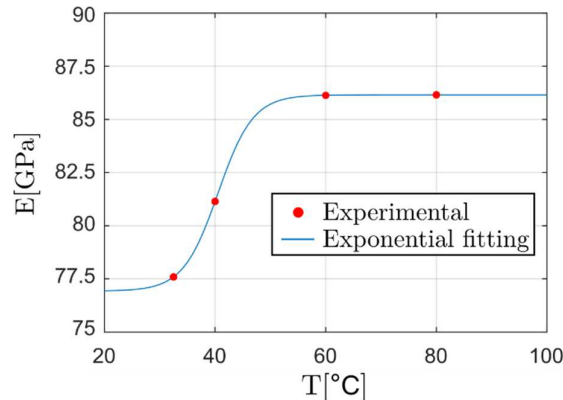


Figure 3-35 B2 phase Young's Modulus evolution with temperature.

To begin with, we identified the Young's Modulus of the B2 phase at four different temperatures: 32.5, 40, 60, and 80°C. The Young's Modulus was determined as the slope of the best-fit straight line passing through the stress-strain data recorded upon the first 100MPa loading of straight wire samples. The calculated values evolved from 77.46GPa at 32.5°C, up to 86.15GPa at 80°C as we illustrate in Figure 3-35. In order to simulate the tensile response of hourglass-shaped samples using Sedláč et al. model, we defined the Young's modulus of the B2 phase as

$$E^A(T) = \frac{9.23}{1 + \exp\{-0.32[T - (R_s - 5)]\}} + 76.92, \quad (3.54)$$

where the  $R_s$  transformation temperature is the same one identified in DSC curves (25.5°C). On the other hand, the Young's Modulus of B19' martensite was determined as the best-fit straight line passing through the first 100MPa unload upon the local superelastic response at 32.5°C (see Figure 3-29).

The Young's moduli of the B2 and B19' phases allowed us to calculate their correspondent shear moduli  $G^A$  and  $G^M$  by using the following relationship for homogeneous elastic isotropic materials:

$$G^i = \frac{3KE^i}{9K - E^i}, \quad (3.55)$$

for  $i \in A, M$  (B2 and B19' phases respectively). The phase-independent bulk modulus  $K$  was established equal to 150GPa, based on the experimental evidence reported by Wagner et al.[116].

The elastic properties of the R-phase resulted more complicated to determine since when R-phase is stress-induced at ambient temperature and above, it is always mixed with B2 austenite. In order to determine suitable elastic constants that reproduce well the tensile response of our material, we carried out a least-squares error minimization (LSEM) between the local experimental response shown in Figure 3-26a and the model, with  $G^R$  and  $\Delta s^{AR}$  as the minimization variables. For this fitting process, the  $R_s$  and  $R_f$  temperatures, which may

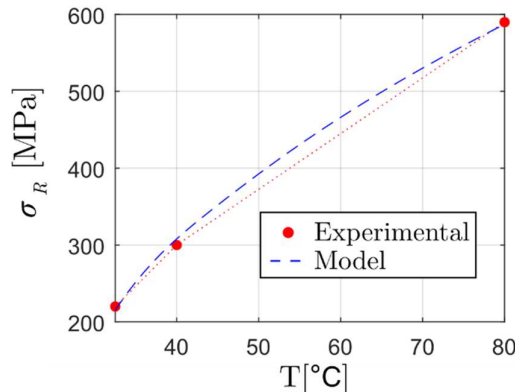


Figure 3-36 Evolution of the B2→R transformation stress onset with temperature.

also affect the mechanical response upon the B2→R transformation, were set equal to the temperatures identified in DSC experiments.

After determining the shear modulus of R-phase, we proceeded to better fit the specific entropy difference  $\Delta s^{AR}$ , which rules the evolution of the onset of the stress-induced B2→R transformation with temperature. We defined an expression for the B2→R onset stress by evaluating the governing equation (3.48) at the point  $(\xi, \eta, \boldsymbol{\varepsilon}^{in}) = [0, 0, \mathbf{0}]$ . The above turns out in the following relationship:

$$\frac{G^A - G^R}{2G^A G^R} s_{II} - \Delta s^{AR}(T - R_s) = 0 \quad (3.56)$$

where  $s_{II}$  is the second invariant of the deviatoric stress, defined as

$$s_{II} = \frac{1}{2} dev(\boldsymbol{\sigma})_{ij} dev(\boldsymbol{\sigma})_{ij}, \quad (3.57)$$

with

$$dev(\boldsymbol{\sigma}) = 2G^A dev(\boldsymbol{\varepsilon}) \quad (3.58)$$

as deduced from the equation (3.39). We may consider equation (3.56) as a von Mises-like yield surface

$$f^y = \sigma_{eq} - \sigma_R(T) = 0 \quad (3.59)$$

where

$$\sigma_{eq} = \sqrt{3s_{II}} \quad (3.60)$$

is the von Mises equivalent stress, and

$$\sigma_R(T) = \sqrt{\frac{6G^A G^R \Delta s^{AR}(T - R_s)}{G^A - G^R}} \quad (3.61)$$

the temperature-dependent transformation stress. Note that, apart from  $\Delta s^{AR}$ , the model establishes that the evolution of the B2→R transformation stress with temperature is also affected by the elastic constants of the B2 and R (already identified) and  $R_s$  (determined by DSC).

Considering a pure uniaxial stress state ( $\sigma_{eq} \equiv \sigma_z$ ), we determined the specific entropy difference  $\Delta s^{AR}$  using a least-square error minimization between equation (3.59) and the B2→R transformation stress onsets at 32.5, 40 and 80°C previously presented in Figure 3-21. The resulting evolution of the onset of the stress-induced B2→R transformation with temperature is illustrated in Figure 3-36.

Now, concerning the evolution of the B2→R transformation upon loading, the model establishes a transformation kinetics independent of the temperature; therefore, the stress-induced B2→R transformation is delayed at higher temperatures but proceeds at the same hardening rate. However, the tensile response upon the B2→R transformation on straight samples (see Figure 3-37) clearly shows that the hardening rate actually decreases with lowering temperature. In order to render the stress-induced R-phase transformation kinetics temperature-dependent, we defined an upgraded definition of the equilibrium temperature between B2 and R:

$$T_0^R(\eta, \xi, T) = \begin{cases} R_s + \frac{\eta}{1-\xi} \frac{(R_f - R_h(T - R_s)^2) - R_s}{2} & \text{if } T \geq R_s \\ R_s + \frac{\eta}{1-\xi} \frac{R_f - R_s}{2} & \text{if } T < R_s \end{cases} \quad (3.62)$$

where  $R_h$  is a material parameter. In this way, we enlarge the  $R_s$ - $R_f$  difference at higher temperatures, which turns out to spread the phase transformation over a wider stress range upon mechanical loading; thus, reducing the hardening rate. The  $R_h$  value was determined using the LSEM fitting method, whereas the transformation temperature  $R_f$  was identified from DSC experiments.

The onset of the B2/R→B19' transformation was determined by evaluating the subderivative established in the governing equation (3.47) when  $\dot{\xi} \rightarrow 0^+$ :

$$\pi \in \partial_{\dot{\xi}} d = \lim_{\dot{\xi} \rightarrow 0^+} \frac{d(\boldsymbol{\epsilon}^{tr}, \xi, \dot{\boldsymbol{\epsilon}}^{tr}, \dot{\xi}) - d(\boldsymbol{\epsilon}^{tr}, \xi, \dot{\boldsymbol{\epsilon}}^{tr}, 0)}{\dot{\xi}}. \quad (3.63)$$

For a uniaxial loading at a stress just below  $\sigma_{MT}$ ,  $\|\boldsymbol{\epsilon}^{tr}\| = k$ ,  $\dot{\boldsymbol{\epsilon}}^{tr} = 0$ , and  $\xi = 0$ . Then, replacing (3.41) in (3.63) results in the following expression:

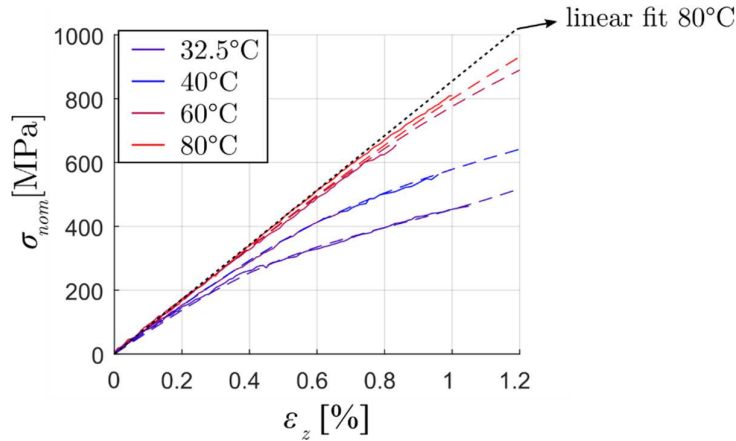


Figure 3-37 Tensile responses of NiTi upon stress-induced B2 → R phase transformation at 32.5, 40, 60, and 80°C. The experimental curves are plotted in solid lines while the modeled ones are plotted in dashed lines.

The experimental curve at 32.5°C was extracted from the local response of an hourglass-shaped sample, whereas the experimental responses at 40, 60, and 80°C were obtained from tensile tests of straight wires.

$$-\frac{\partial G(0, \eta)}{\partial \xi} \frac{\sigma_{MT}^2}{6G(0, \eta)^2} + \sigma_{MT} k - \Delta s^{AM} (T - M_s) + \eta \Delta s^{AR} \frac{\partial T_0^R(0, \eta)}{\partial \xi} - \sigma^{reo} \frac{\partial \|\dot{\xi} \mathbf{e}^{tr} + \xi \dot{\mathbf{e}}^{tr}\|}{\partial \xi} = 0, \quad (3.64)$$

where  $dev(\sigma): \mathbf{e}^{tr}$  have been replaced by  $\sigma_{MT} \mathbf{k}$ , as we consider an uniaxial loading case. In order to ease the parameter identification, we neglected the dissipation term related to the martensite reorientation (i.e.  $\sigma^{reo}(T) = 0$ ). In this way, the evolution of the onset of the B2/R→B19' transformation with temperature is affected by the shear moduli of the material, the transformation strain  $k$ , and by the material parameters  $M_s$  and  $\Delta s^{AM}$ . The transformation strain  $k$ , was made equal to the length of the stress plateau of the straight sample tensile response shown in Figure 3-29. On the other hand, the values of  $M_s$  and  $\Delta s^{AM}$  were fitted using the LSEM method with respect to experimental B2/R→B19' transformation onset stresses identified using hourglass-shaped samples at 32.5, 40 and 80°C (see Figure 3-39b-d).

The  $M_s$ - $M_f$  difference and the  $E^{int}$  affect the hardening rate upon the B2/R→B19' transformation. Since the model is not suited to reproduce the fast nucleation of martensite that gives rise to the softening-like response obtained experimentally via DIC and x-ray diffraction experiments, the closest fit that we are capable to obtain is a stress-plateau response, in which the material transforms progressively into B19'. To reproduce a stress-plateau response, we established the  $M_f$  value close to  $M_s$  and gave  $E^{int}$  a value in the order of some MPa's.

The final step to complete the model parameters fitting consisted in establishing the transformation temperature  $A_s$ , which defines the onset of the reverse transformation stress plateau. We determined the  $A_s$  value so the lower plateau of the constitutive response of the material fitted with the lower stress valley shown by hourglass-shaped samples experiments at different temperatures, which are presented in Figure 3-39. Upon reverse transformation, the plateau stress response is again reproduced by making  $A_f$  close to  $A_s$ .

The list of the parameters that allow describing the thermomechanical behavior of our studied material is presented in Table 3-6. The constitutive mechanical responses at 32.5, 40, and 80°C are presented in Figure 3-38.

In the following section, we proceed to contrast simulation of the tensile responses of NiTi hourglass-shaped samples at different temperatures with experimental results. In addition, we analyze the impact of phase transformations, as predicted by the model, on the stress field of upon tensile loading.

Parameter	Value	Unit	Comment
Elastic constants			
$K$	150	GPa	Bulk Modulus: obtained from Wagner et al. [116].
$G^A$	27.4 @32.5°C 28.7 @40°C 30.6 @80°C	GPa	Shear Moduli: the values were obtained from equation (3.55), using the Young's Modulus measurements on tensile responses of straight wires.
$G^R$	15.05	GPa	
$G^M$	9.18	GPa	
Transformation strain			
$k$	0.053	mm/mm	Transformation strain: equal to the superelastic stress plateau of the straight wire tensile response 32.5°C (Figure 3-29).
Chemical potential			
$T_0$	-	°C	Equilibrium temperature between B2 and B19'. It was not used in our simulations since $\sigma^{reo}$ was neglected.
$M_s$	-11.6	°C	B19' transformation temperatures. The values here were obtained using the LSEM fitting method. They affect mainly the stress onsets for forward and reverse transformations.
$M_f$	-12	°C	
$A_s$	15	°C	
$A_f$	16	°C	
$R_s$	25.5	°C	R-phase transformation temperatures. The values here were extracted from DSC experiments (Table 3-3).
$R_f$	11.5	°C	
$R_h$	0.358	°C <sup>-1</sup>	$R_f$ temperature correction parameter. The value was obtained from LSEM fitting method.
$\Delta s^{AR}$	0.036	MPa/°C	Entropy differences between B2 and R and B2/R and B19' phases. Their values were obtained through LSEM fitting method. They control the evolution of the stress onsets of transformations with temperature.
$\Delta s^{AM}$	0.588	MPa/°C	
Mechanical dissipation function			
$\sigma_{reo}^0$	0	MPa	Neglected. $\sigma_{reo}(T)$ describes the low temperature material yielding ( $\xi = 1$ ) and affects the evolution of the hysteresis with temperature in the case of superelastic simulations.
$\Sigma_{reo}$	0	MPa/°C	
Regularization term			
$c^r$	30	MPa	These parameters affect mainly the start and the end of the kinetics of phase transformations.
$E^{int}$	7	MPa	

Table 3-6 Model parameters used for simulating the tensile response of the studied material in a range of temperatures between 30-80°C.

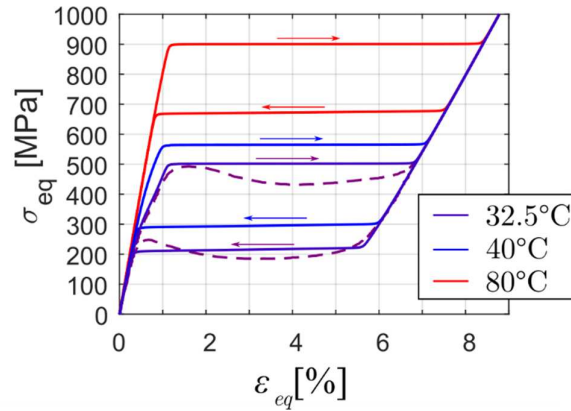


Figure 3-38 Constitutive responses of NiTi at 32.5, 40, and 80°C using the Sedláč model and the parameters identified in Table 3-6.

### 3.3.3.3. Simulations vs Experiments

In order to simulate the tensile response of NiTi hourglass shaped samples by finite element analysis in ABAQUS, we used an axisymmetric version of the model of Sedláč et al. The material calculations were performed by ABAQUS through a so-called UMAT subroutine coded in C++ containing the model equations. The boundary conditions used for the simulations were the same as the ones that we presented before for elastic analysis of tensile loaded hourglass-shaped samples (Figure 3-4a). We used bilinear axisymmetric quadrilateral elements referred as CAX4R in ABAQUS, allowing for two displacement degrees of freedom and one integration point. In order to have reasonable calculation lengths, guarantee the convergence, and have a good spatial distribution of material points, we used the 10-element mesh size previously introduced in Figure 3-4b and recalled in Figure 3-39a.

The simulations were carried out by imposing an axial displacement to the control point RP, connected to the upper surface of the sample (see Figure 3-39a). The reaction force vs the applied displacement responses was contrasted with the load cell vs extensometer elongation responses upon quasi-static experiments performed on hourglass-shaped samples at 32.5°C (DIC experiment described in section 3.3.1), 40°C, and 80°C. The simulated and experimental curves are shown in Figure 3-39.

As observed in Figure 3-39, the model reproduces well the mechanical behavior of hourglass-shaped samples at nominal stresses below the B19' yielding point, defined at the stress peak of the experimental curves. The soft nonlinearity that supposes the stress-induced B2→R phase transformation is well captured by the von Mises-like yielding surface proposed by the model. In addition, the redefinition of the equilibrium temperature  $T_0^R$  by equation (3.62) allows describing correctly the subtle loss of stiffness exhibited by the macroscopic response at 80°C. We also validated the axial strain distribution at the surface of the sample resulted from simulations with respect to the strain profiles obtained via DIC (see Figure 3-40b). The simulation axial strain values shown in Figure 3-40b were extracted from the integration points of the elements placed at the surface of the sample. As observed there,

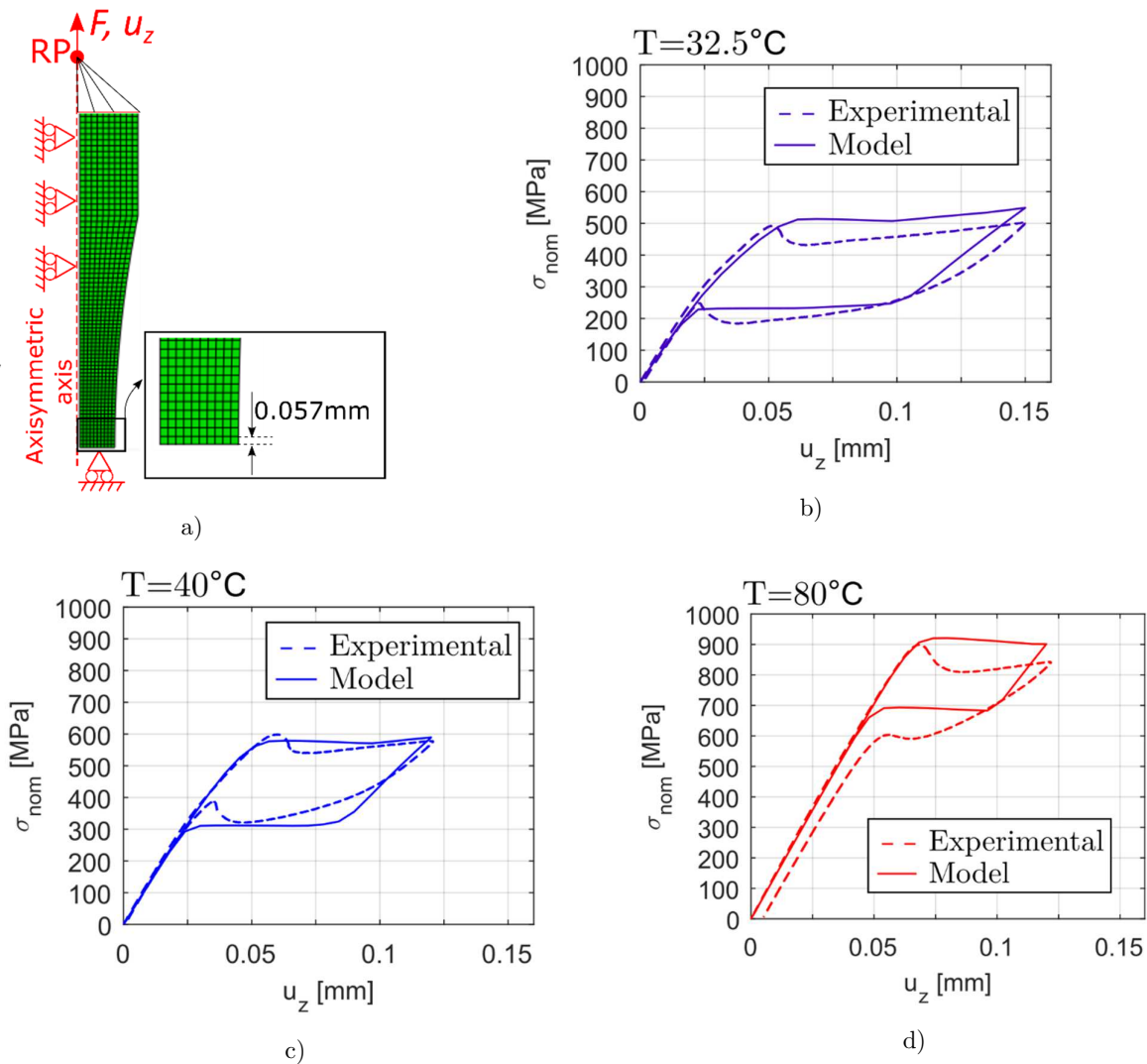


Figure 3-39 Superelastic tensile response of hourglass-shaped samples of NiTi#1 heat-treated at  $500^\circ\text{C}$  for 30 minutes obtained experimentally and by simulations: a)  $32.5^\circ\text{C}$ , b)  $40^\circ\text{C}$ , and c)  $80^\circ\text{C}$ . The curves are presented in terms of the elongation of a clip-on ( $u_z$ ) attached outside the groove zone of the samples, and the nominal stress ( $\sigma_{\text{nom}}$ ), calculated as the force measured by the load cell divided by the initial mid cross-section of the sample.

the simulated profiles reproduce well the axial strain distribution around the mid cross-section upon the  $B2 \rightarrow R$  transformation. These results reassure the following analysis of the stress distribution upon stress induced  $B2 \rightarrow R$  transformation at  $32.5^\circ\text{C}$  presented in Figure 3-40c.

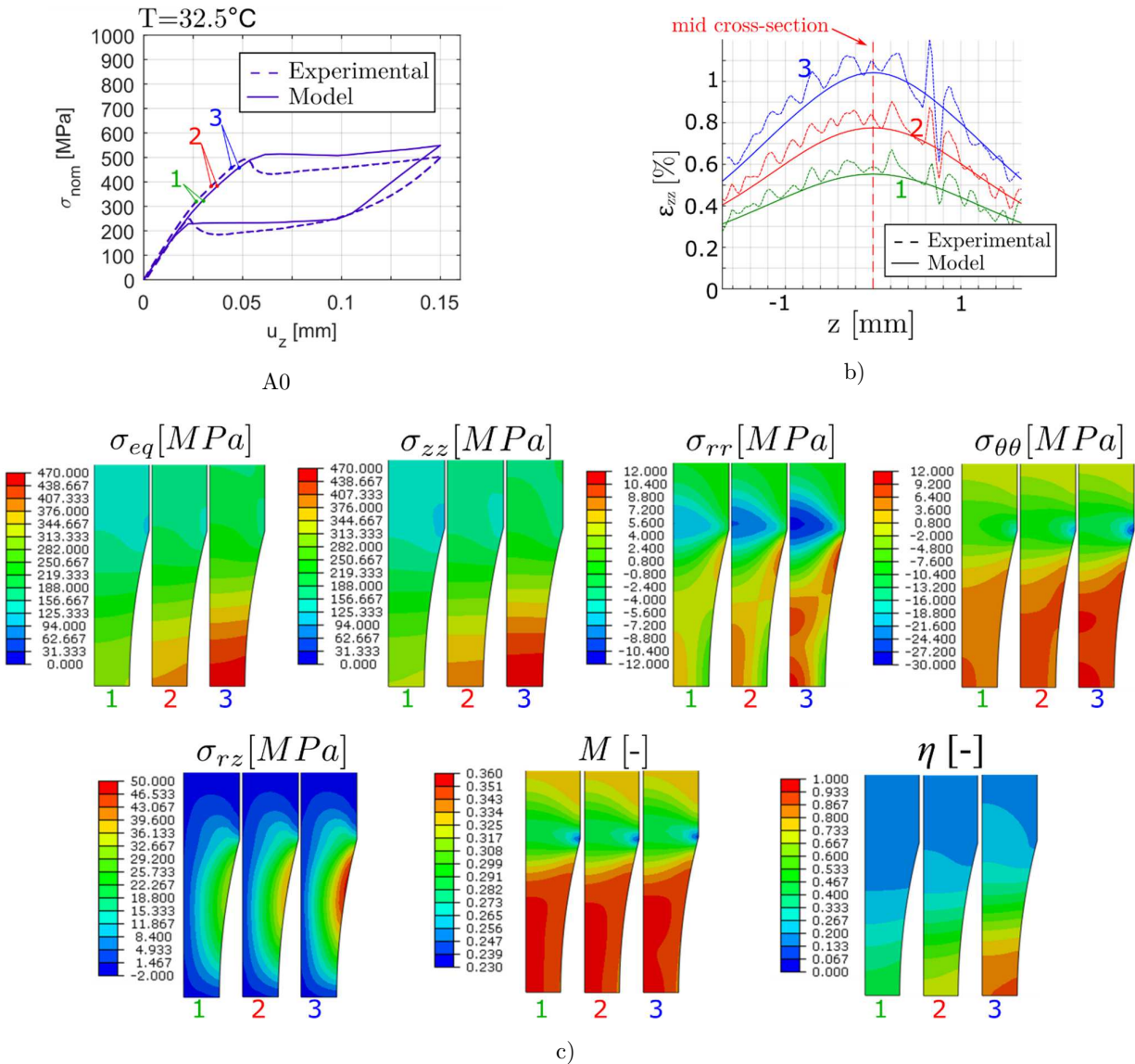


Figure 3-40 Tensile response of an hourglass-shaped sample at  $32.5^\circ\text{C}$  in the **B2→R** regime. a) Comparison between experimental and simulated macroscopic responses. b) Comparison between experimental and simulated axial strain profiles centered at the mid cross-section. c) Evolution of the stress tensor components, triaxiality ratio  $M$  and volume fraction of R-phase.

Upon elastic loading of B2 austenite, the maximal axial stress and von Mises equivalent stresses are located at the surface of the mid cross-section. As a result, the stress-induced B2→R transformation is initiated at this location, and then it propagates towards the axis of the sample and along the groove. The larger inelastic axial deformation at the mid cross-section caused by the transformation entails a more intense cross-section reduction in the middle of the sample (see 100x scaled deformed sample in Figure 3-42a). Such a heterogeneous cross-section reduction is compensated by a positive shear stress in the surface of the groove and positive radial and transverse stresses in the sample's axis. However, since the magnitudes of the shear, transverse and radial stresses are small compared to the axial stress ( $\sim 2\%$ ), the material remains close to a pure uniaxial stress state, which is reflected by the closeness of the triaxiality ratio contour map to  $1/3$  (see  $M$  in Figure 3-40c).

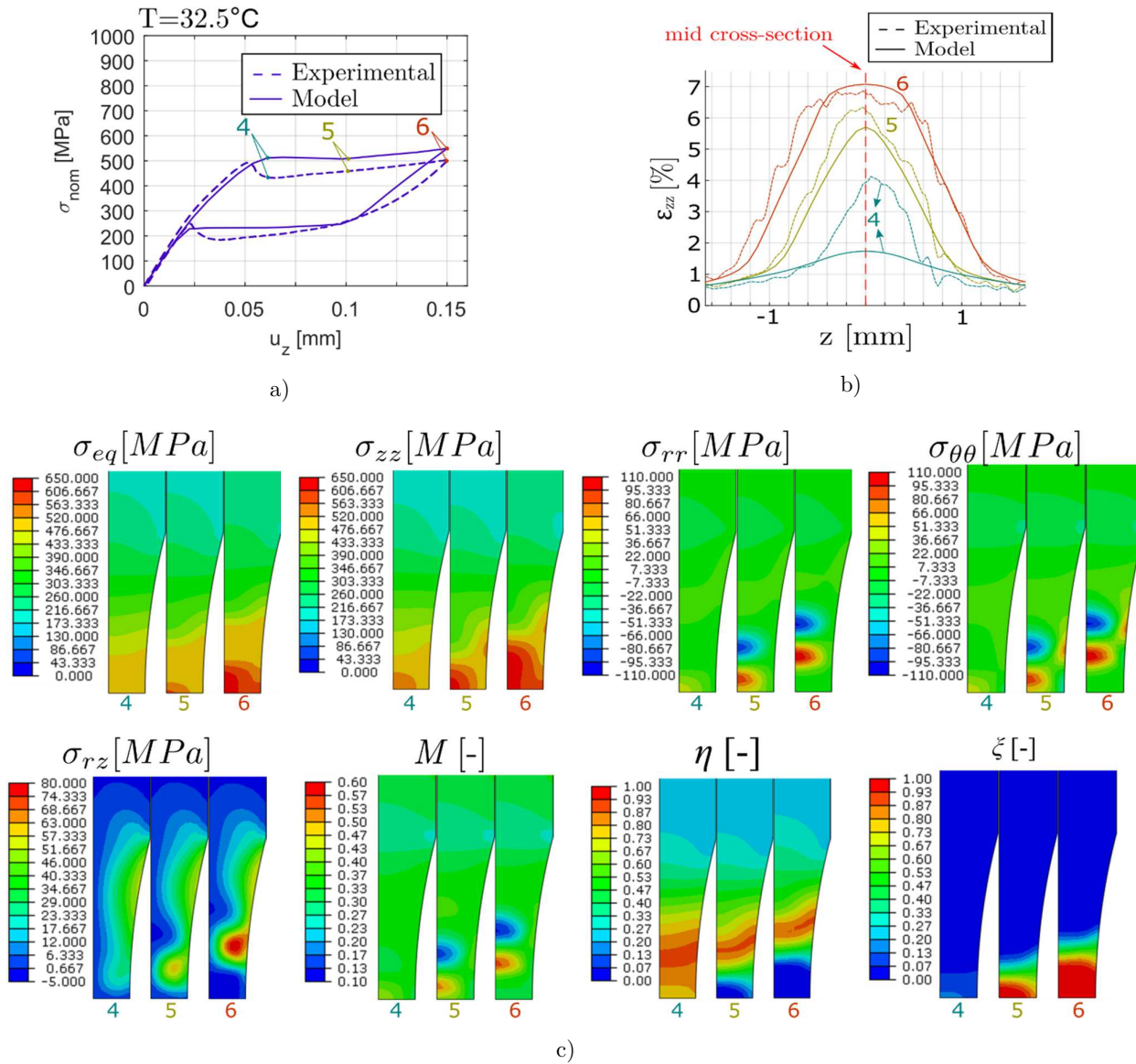


Figure 3-41 Tensile response of an hourglass-shaped sample at  $32.5^{\circ}\text{C}$  in the **B2/R $\rightarrow$ B19'** regime upon loading. a) Experimental and simulated macroscopic responses. b) Experimental and simulated axial strain profiles centered at the mid cross-section. c) Stress tensor components, triaxiality ratio  $M$  and volume fraction of R-phase and B19'.

Once the stress reaches the onset of the B2/R $\rightarrow$ B19' transformation, the model supposes a continuous evolution of the volume fraction of B19' along the stress plateau of the constitutive response. As a result, the sudden decrease of the axial force and the rapid increase of the axial deformation at the mid cross-section, caused by a very fast transformation of a confined volume in the middle of the sample, are not well reproduced by the model. However, the simulated macroscopic responses shown in Figure 3-38 exhibits actually a small decrease of the axial force (nominal stress) upon the first stage of the loading after the B2/R $\rightarrow$ B19' transformation starts. This is due to a severe cross-section reduction in the mid cross-section as we observe in the shape changes suffered by the sample along the B19' transformation shown in Figure 3-42b. In fact, the simulated axial stress at the mid

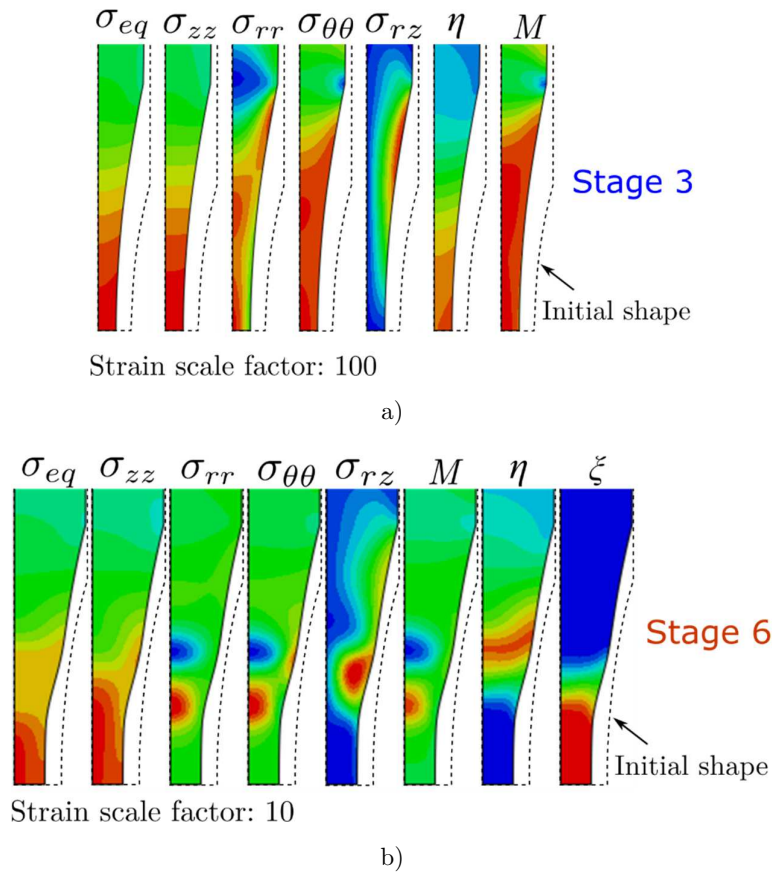


Figure 3-42 Scaled deformed stress contour maps upon stress-induced B2→R (a) and B2/R→B19' (b) phase transformations. The color scale for each contour plot was kept the same as in Figure 3-40 and Figure 3-41.

cross-section (see contour plots in Figure 3-41c) continues to increase in spite of the drop of macroscopic force.

The difference between the stress-induced B19' nucleation in experiments and simulations is observed clearer in the strain profiles at stage 4 in Figure 3-41b. After the transformation starts the DIC strain profile 4 shows a rapid axial strain increase of ~3% at the mid cross-section during the axial force drop. In contrast, the simulated profile shows an axial strain increase of only ~1%. Interestingly, in numerical simulations, between stages 4 and 5, the transformed zone remains locked in a ~2mm length zone centered at the mid cross-section. Between these stages, only the axial strain inside the locked zone keeps increasing while it remains almost the same outside of it. A similar behavior was captured by DIC analysis but in much short extensometer elongation range during the nominal stress drop that follows the transformation onset (see Figure 3-27). After stage 5 in Figure 3-41a, the simulated nominal stress starts increasing and the B19' phase propagates along the groove. Consequently, at stage 6, the resulting strain profile is broader and flat at the mid cross-section. Surprisingly, even though the simulated nominal stresses between stages 5 and 6 resulted higher than the experimental ones, the simulated axial strain profiles correlate with the experimental axial strain profiles.

The characteristic cross-section gradient of hourglass-shaped samples becomes nearly homogeneous once the transformation into B19' is completed (see Figure 3-43b). As a result, at the transformation front, there is an abrupt change of the cross-section that leads to a complex stress state around of it. Above the front, in the B2/R zone, positive shear stresses are generated in response to the high shear strain produced by the abrupt cross-section change. Because of the shear stresses, a positive and a negative radial and transverse stresses zones are induced below and above the front respectively. In addition, the shear stress zone, generated at the surface beneath of the transformation front, restricts the axial stress at the surface of the sample, which becomes maximal at the samples axis upon the transformation propagation.

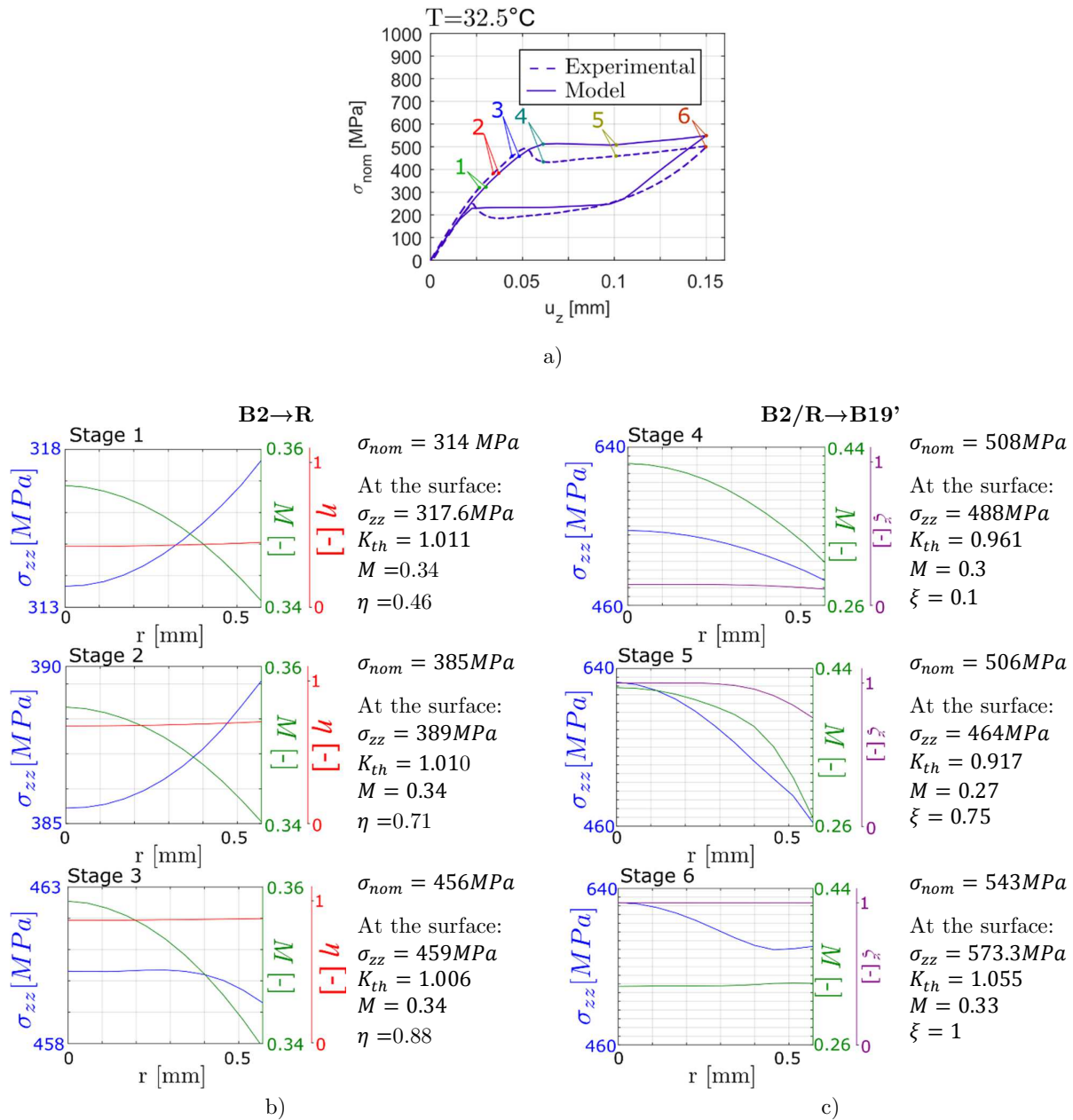


Figure 3-43 Distribution of the axial stress, triaxiality ratio and crystallographic phases upon stress-induced B2→R transformation (b), and B2/R→B19' transformation (c) at highlighted stages shown in (a).

According to these observations, when the material transforms from B2/R mixed-phase into B19', it does it first at the surface of the sample. However, since the deformation related to the transformation entails cross section disparities at the transformation front, and shear stresses at the surface of the groove, the maximal von Mises stress starts shifting towards the sample axis; therefore, the B19' transformation, although starting at the surface, is completed first at the sample axis. The resulting transition zone, between fully transformed B19' phase and untransformed B2/R mixed phase, is defined by two concave boundaries opposed to each other. The magnitudes of the maximal radial and transverse stresses in the transformation front remain ~17% of the maximal axial stress at the mid cross-section during the propagation. The maximal magnitude of the shear stress, on the other hand, increases as the front moves up in the z-direction. As a result, the triaxiality ratio at the transformation front distance from 1/3 (pure uniaxial loading state) especially at the sample's axis. Otherwise, once the transformation into B19' is completed and the microstructure becomes homogeneous, the stress state returns near to pure uniaxiality.

Figure 3-43 details the evolution of the axial stress, triaxiality ratio and crystallographic phases along the radius at the mid-cross section upon the B2→R (Figure 3-43b) and B2/R→B19' transformations (Figure 3-43c). The inelastic deformation induced by the B2→R transformation acts as a stress reliever similar to plasticity in traditional alloys. As a result, the stress concentration factor  $K_{th}$  decreases as the transformation proceeds, dropping from 1.025 in elasticity down to 1.006 at stage 3 upon transformation. On the other hand, the distributions of the axial stress at stages 1 and 2 remain the same as in elasticity, being higher at the surface and decreasing quadratically towards the sample axis. At stage 3, some small amount of B19' starts to develop, which relieve stress at the surface and boost the axial stress at the sample axis. Moreover, during the B2→R transformation, the triaxiality ratio  $M$  across the mid cross-section keeps a similar distribution as in elasticity, being closer to 1/3 at the surface and higher at the axis. The red curves in (Figure 3-43b) denote a nearly homogeneous distribution of the R-phases upon nominal stress increase; therefore a nearly homogeneous distribution of the von Mises equivalent stress across the mid cross-section.

Upon the B2/R→B19' transformation, the axial stress distribution changes drastically compared to elastic loading and stress-induced B2→R transformation. At stage 4, the small amount of B19' phase already induced in the mid cross-section (~10%), shifts the maximum axial stress to the sample axis; thus, releasing the stress at the surface, where the triaxiality ratio  $M$  remains close to 1/3. As a result, the stress concentration factor  $K_{th}$  becomes lower than one at the surface and keeps decreasing until the mid cross-section transforms almost entirely at stage 5. Between stages 5 and 6, the mid cross-section, being in a near 100% B19' phase, is loaded elastically, which makes the axial stress at the surface to increase slowly while the one at the axis is kept constant. The resulting homogenization of the cross-section radius after B2/R→B19' transformation completion makes the triaxiality ratio to become practically 1/3 in the mid cross-section.

### 3.3.3.4. Approximation of the local material response of NiTi using the macroscopic response of hourglass-shaped samples

Based on the DIC experiments presented in section 3.3.1 and the previous finite element simulations analysis, we propose an alternative method for calculating the strain of a confined material volume located at the surface of the mid cross-section of hourglass-shaped samples. The following method uses the force vs extensometer elongation macroscopic responses. The aim of this procedure is to evaluate the maximal strain at the mid cross-section when the use of DIC is limited e.g. high-frequency fatigue testing or temperature controlled tensile tests carried out inside a thermal chamber.

The method consists in separating the confined strain at the mid cross-section into a linear-elastic and an inelastic part:

$$\boldsymbol{\varepsilon}_z = \boldsymbol{\varepsilon}_z^{el} + \boldsymbol{\varepsilon}_z^{in}. \quad (3.65)$$

The elastic part  $\boldsymbol{\varepsilon}_z^{el}$  is calculated by inserting the experimental force  $F$  and the initial cross section  $S_0$  into the Hooke's law:

$$\boldsymbol{\varepsilon}_z^{el} = \frac{F}{S_0 E}. \quad (3.66)$$

Here, the Young's modulus  $E$  is calculated using the equation (3.10):

$$E = \frac{2F}{\pi u_{gt}} \left[ C + \frac{1}{r_w^2} \left( \frac{L_G}{2} - L_n \right) \right],$$

which was previously introduced in section 3.1.1. In this case,  $F$  and  $u_{gt}$  correspond to the load cell and extensometer data respectively lying on the linear regime of the macroscopic response at low stresses. The final value of  $E$  is calculated by averaging the array of values obtained from the equation (3.10).

The inelastic strains  $\boldsymbol{\varepsilon}_z^{in}$ , are calculated from the inelastic macroscopic displacements  $u_z^{in}$  using the relationship plot in Figure 3-44. Similar to the strain partition, the inelastic displacements are calculated from extracting the elastic displacements from the total displacements measured by the extensometer:

$$u_z^{in} = u_z - u_z^{el}. \quad (3.67)$$

The linear-elastic strains  $u_z^{el}$  are calculated using the equation (3.8):

$$u_{gt}^{el} = \frac{2F}{\pi E} \left[ C + \frac{1}{r_w^2} \left( \frac{L_G}{2} - L_n \right) \right],$$

for the complete force data set  $F$  of interest.

The curves in Figure 3-44, showing the relationship between inelastic displacements and the confined inelastic strain at the mid cross-section, were obtained from finite element simulations at 32.5, 40, and 80°C. With the aim of validation, we plotted the relationship obtained from DIC measurements as well.

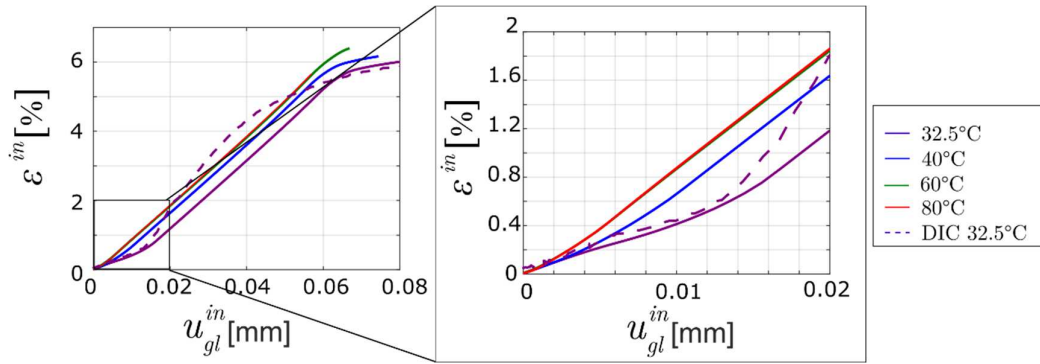


Figure 3-44 Inelastic local strain evolution in terms of inelastic macroscopic displacement.

As observed in Figure 3-44, the predicted inelastic strains are underestimated when the material enters the B19' transformation regime, as the rapid strain increase at the mid cross-section at the transformation onset is not captured by the model. Otherwise, the nonlinearity entailed by the B2→R transformation is well reproduced by the model at 32.5°C.

As a result, this strain calculation procedure is valid only upon monotonic loading in the B2→R transformation regime, considering the material is loaded from a pure B2 austenite state. In the following chapter, we employ this relationship in order to analyze the high-cycle fatigue phenomena occurring in NiTi using hourglass-shaped samples.

### 3.4. Summary

Hourglass-shaped samples are the most appropriate geometry for carrying out High Cycle Fatigue studies. They provide an effective way for confining the deformation and damage process occurring in the material upon repetitive tensile loadings. However, they introduce stress concentrations due to their progressively reduced cross-section, which may play a detrimental role in the fatigue performance of tested materials. Consequently, the characterization of the stress in the mid cross-section of hourglass shaped samples is required before carrying out fatigue studies. In this chapter, we showed finite element simulation results of tensile loads applied to hourglass-shaped with diameters between 1-2mm and cross-section reductions between 50-90%. The simulations were carried out in the first place using an isotropic elastic constitutive law. From these numerical simulations, we may extract the following conclusions:

- The hourglass-shape does not introduce nonlinearities in the macroscopic tensile response of the samples.
- Upon elastic loading, the material in the surface in the mid cross-section of the sample bears the highest axial stress. However, the triaxiality ratio shows that the material at the surface also experiences a more uniaxial stress state compared to the material in the axis of the sample.
- For the range of sample dimensions simulated by FEA, keeping in mind that we fixed the groove radius to 10mm, the more pronounced the cross-section reduction, the lower the axial stress concentration in the surface. This is a direct effect of the length of the

reduced cross-section zone on the stress distribution in the mid cross-section of the samples.

- The analytical formulation of the tensile response of hourglass shaped samples results valid for the range of samples dimension simulated. In the worst-case scenario, the tensile stress at the surface differed from the nominal stress value in only 2%.

In addition, we simulated the tensile response of hourglass-shaped samples with a perfect-plasticity constitutive law. Upon these simulations, we evidenced prominent changes in the stress state of the material in the reduced cross-section zone, notably, a high shear stresses concentration in the interface between the yielded and the elastic material, together with an increase of the hydrostatic pressure in the axis of the sample. These stress concentrations directly related to the pronounced cross section reduction entailed upon plastic yielding.

After the characterization of the stress in the reduced cross-section zone of hourglass-shaped samples, we introduced the material of this study: nearly equiatomic NiTi, prepared via cold-drawn. We evidenced how the heat treatment applied to the material affects its thermomechanical behavior. Annealing heat treatments between 400°C and 500°C affect notably the response of the material in the B2-elastic and B2→R phase transformation loading regimes. We concluded that low heat treatment temperatures tend to stabilize more R-phase at room temperature. As a result, their mechanical responses resulted more compliant. Interestingly, when comparing the tensile responses of samples that received different heat treatments at 80°C, we observed smaller differences in their mechanical responses. This suggests that in the absence of R-phase, B2→B19' transformation is unaffected by the temperature of the applied heat treatment. Based on these results, we decided to focus on the study of NiTi annealed at 500°C for 30 minutes, as it facilitates the assessment of the fatigue behavior in the B2-elastic, B2→R, and B2/R→B19' loading regimes in a temperature range close to the ambient temperature. By testing a single heat treatment, we discard the sample preparation from the list of factors that affect the fatigue of NiTi.

We concluded this chapter by carrying out a detailed study of the mechanical response of NiTi hourglass-shaped samples heat-treated at 500°C for 30 minutes using Digital Image Correlation (DIC), high-resolution X-ray diffraction, and finite element analysis. From this study, we can draw the following conclusions and observations:

- B2→R transformation shows a hardening-like response with an almost imperceptible hysteresis. The transformation occurs gradually by increasing the stress, as evidenced by the progressive x-ray diffraction patterns changes and the smooth strain increase observed via DIC.
- When the B2/R→B19' transformation is stress-induced, a volume ~1mm height transforms almost instantaneously in the mid cross-section of the sample. This phenomenon was observed in both DIC and x-ray diffraction experiments. The phase transformation generates large axial strains and at the same time, pronounced cross-section reductions.

- We fitted a thermomechanical model suitable for SMA, which allowed us to reproduce the B2→R transformation responses of hourglass-shaped samples at different temperatures.
- From finite element simulations, we determined that the cross section reduction entailed by the B19' transformation contributes to the softening phenomena observed in the macroscopic response of the samples.
- The B2→R transformation acts as a stress reliever on the surface of the sample causing a decrease of the stress concentration factor with respect to elastically loaded B2 austenite.
- On the contrary, when B19' transformation is achieved, the material experiences a complex multiaxial stress state which was to be reproduced by the applied thermomechanical model.

# Chapter 4. Fatigue of NiTi hourglass-shaped samples

The previous chapter focused on the behavior of hourglass-shaped NiTi samples upon external tensile loading. We explained the mechanical behavior of the stress-induced phase transformations in hourglass-shaped samples, which lay the foundation for the following fatigue analysis. In this section, we address the cyclic stress and strain conditions that affect the lifetime of hourglass-shaped NiTi samples especially in the stress regime underneath the B19' transformation stress, commonly denoted as the high cycle fatigue regime (HCF). Next, we begin with a description of the experimental protocol adopted for the fatigue tests. Then, we present the S-N curves obtained from fatigue tests carried out at different temperatures. The S-N data permitted us to evaluate several commonly used fatigue criteria and a prediction model. After that, we complemented the S-N analysis with macroscopic strain-N curves, which aid to clarify the role of phase transformations and temperature on the lifetime of superelastic NiTi wires. The fracture surfaces of the samples that failed upon fatigue testing are analyzed afterward allowing to picture the crack initiation and propagation processes upon repetitive pull-pull loadings. This analysis is complemented by observations of the evolution of the mechanical response of the samples, supported by DIC and fast infrared thermography.

## Contents

<b>4.1. Experimental protocol .....</b>	<b>107</b>
<b>4.2. S-N curves.....</b>	<b>109</b>
4.2.1. Effects of the mean stress .....	112
4.2.2. Hints for superelastic NiTi fatigue modeling.....	118
<b>4.3. Stress-Strain-N representation .....</b>	<b>119</b>
<b>4.4. Fatigue crack characterization.....</b>	<b>122</b>
4.4.1. Fracture surfaces.....	122
4.4.1.1. Crack initiation zone (Sin) .....	122
4.4.1.2. First crack propagation zone (Scl).....	125
4.4.1.3. Fatigue striations zone (Sst).....	125
4.4.1.4. Transition zone and overload fracture zone (Sdf and Sov) .....	127
4.4.2. Characterization of the crack's size.....	127

4.4.3. Tensile response evolution.....	130
4.4.3.1. Monotonic rupture of an arrested fatigue test .....	131
4.4.3.2. Detection of crack initiation via fast thermography .....	133
<b>4.5. Microstructure evolution evaluated via high resolution x-ray diffraction .....</b>	<b>136</b>
<b>4.6. Summary.....</b>	<b>137</b>

## 4.1. Experimental protocol

NiTi#1 hourglass-shaped samples, heat-treated for 30 minutes at 500°C, were subjected to pull-pull fatigue cycles in the force-controlled regime at temperatures of 40°C, 60°C and 80°C. The tests were carried out on a servo-hydraulic testing machine INSTRON 8872 equipped with a 25kN load cell. The tests were performed inside a thermal chamber EUROTERM 28400 for guaranteeing isothermal conditions. In addition, a thermocouple type E was placed near the sample to verify the test environment temperature. The macroscopic deformation was tracked by a 10 mm gauge length dynamic clip-on extensometer attached to the sample. A picture of the experimental setup is presented in (see Figure 4-1a). The tensile machine applied sinusoidal-shaped force cycles with a ratio between the maximum and minimum nominal stresses ( $R = \sigma_{min}/\sigma_{max}$ ) equal to 0.1. The load frequency for all tests was 25Hz and the runout of the fatigue testing was set to 1.5 million cycles.

Upon cyclic testing, the characteristic localized B19' transformation of tensile loaded NiTi wires makes them prone to fatigue fracture inside the grips, even when using reduced cross-

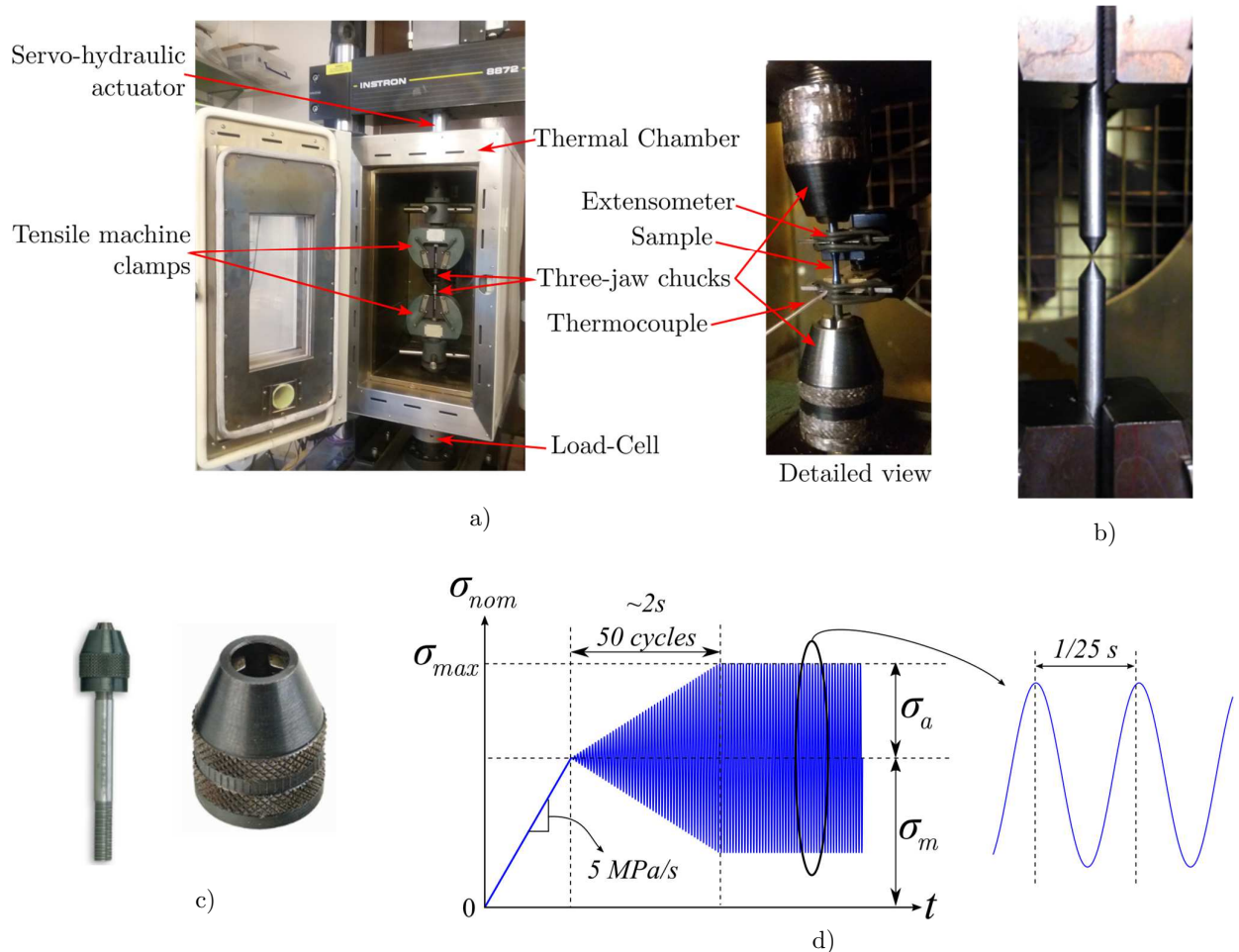


Figure 4-1 Fatigue tests experimental protocol. a) Experimental setup. b) Clamps alignment verification. c) Three-jaw chucks used for clamping the samples. d) Schematic representation of the load applied to a sample during a fatigue testing.

section samples (e.g. hourglass-shaped samples). In order to prevent fracture outside the groove zone, we clamped both sides of the samples using three-jaw keyless chucks Proxxon 28941 MICROMOT (see Figure 4-1c). These jaws are a self-tightening and allow a good distribution of the clamping force around sample surface. In order to reduce bending stresses that inadvertently occur due to misalignment between the applied force and the sample axis during the application of tensile forces, we verified the relative position between the upper and lower machine clamps using cone-shaped alignment bars as illustrated in Figure 4-1b. The position of the lower clamp could be eventually modified by tightening or loosening a set of six balance screws mounted on its base.

Before testing a sample, we heated it up to  $\sim 120^\circ\text{C}$  using a hot air blower intending to equalize the initial microstructure of all fatigue tests. Then, the sample was clamped in the machine and the heat chamber set at the desired testing temperature. Upon heating, the tensile machine was transferred into force control mode in order to prevent increasing of external stresses due to the thermal expansion of the sample and clamps. The test was run once the temperature near the sample stabilized at the desired temperature (verified by means of the type E thermocouple). Each test started by loading the sample up to the nominal mean stress of the fatigue cycle ( $\sigma_m$ ) at 5MPa/s. After that, the amplitude of the sinusoidal-shaped nominal stress increased linearly during 2s up to the target amplitude  $\sigma_a$  was achieved (see Figure 4-1d).

The applied nominal stress amplitudes involved deformations through elasticity, R-phase transformation, and B19' martensitic transformation. Note that the effect of the test temperature is twofold. First, it affects the R-phase transformation being almost suppressed at  $80^\circ\text{C}$  while well pronounced at  $40^\circ\text{C}$ ; therefore, testing at  $40^\circ\text{C}$  emphasized the deformation through the  $\text{B2} \leftrightarrow \text{R}$ -phase transformation involved in most applied amplitudes, while testing at  $80^\circ\text{C}$  emphasized the elastic deformation of austenite at amplitudes below the onset of the B19' martensitic transformation. Second, the temperature changes the critical stress for the onset of the B19' martensitic transformation. At  $80^\circ\text{C}$ , the onset appears

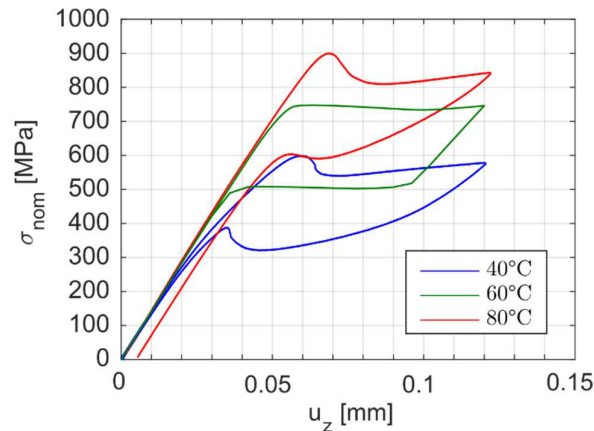


Figure 4-2 Nominal stress vs extensometer elongation responses of hourglass-shaped samples tensile tested at 40, 60, and  $80^\circ\text{C}$ . The response at  $60^\circ\text{C}$  was obtained from finite element simulations.

at 900 MPa, at 60°C it does at 775MPa, and at 40°C, it appears at 600 MPa (see Figure 4-2).

## 4.2. S-N curves

The S-N curves obtained from fatigue tests at 40, 60 and 80°C are presented in Figure 4-3. The curves are presented in terms of the maximal cyclic nominal stress applied to the samples ( $\sigma_{max}$ ) and the number of complete sinusoidal cycles before failure ( $N_f$ ). Note that on each curve we highlighted the onset stresses for B2/R→B19' and B2→R phase transformations. In the case of samples tested at 40°C and 80°C, the onsets were established using thermography and by evaluating inflection points in their mechanical responses as explained in the previous chapter. In the case of samples tested at 60°C, the phase transformation onsets were obtained by finite element simulations.

The endurance limits referred as  $\sigma_e$  in Figure 4-3, were obtained using the Dixon and Mood method [119]. The method assumes that the fatigue endurance limit follows a normal distribution. It provides formulas for the mean endurance limit and the standard deviation. The method consists in evaluating an odd number  $N$  of fatigued samples near the infinite life regime, and determine whether failure or runout had the lowest occurrence. Then, the samples corresponding to the lowest occurrence event are indexed from  $i=0$  to  $i=N_E$ , where  $N_E$  is the total number of occurrences of the selected event. Indexes  $i$  are given according to the applied stress; thus, the index  $i=0$  is given to the lowest maximal applied stress and  $i=N_E$  is given to the highest maximal applied stress. After that, we determine the number of events per index  $P_i$ , from which we calculate,

$$P = \sum_i^{N_E} P_i, \quad (4.1)$$

and

$$Q = \sum_i^{N_E} iP_i. \quad (4.2)$$

Finally, the average endurance limit is calculated using the following equation:

$$\sigma_e = \sigma_{e=0} + p \left( \frac{Q}{P} \pm \frac{1}{2} \right) \quad (4.3)$$

where  $\sigma_{e=0}$  is the lowest stress value in the group of  $N_E$  samples and  $p$  is the stress step, denoted as the lowest stress difference magnitude between the group of  $N$  fatigue points. If the lowest occurrence event is the failure, the equation (4.3) is calculated using  $+1/2$ . On the contrary, if the lowest occurrence event is the runout, it is done using  $-1/2$ . The standard deviation, on the other hand, is calculated by:

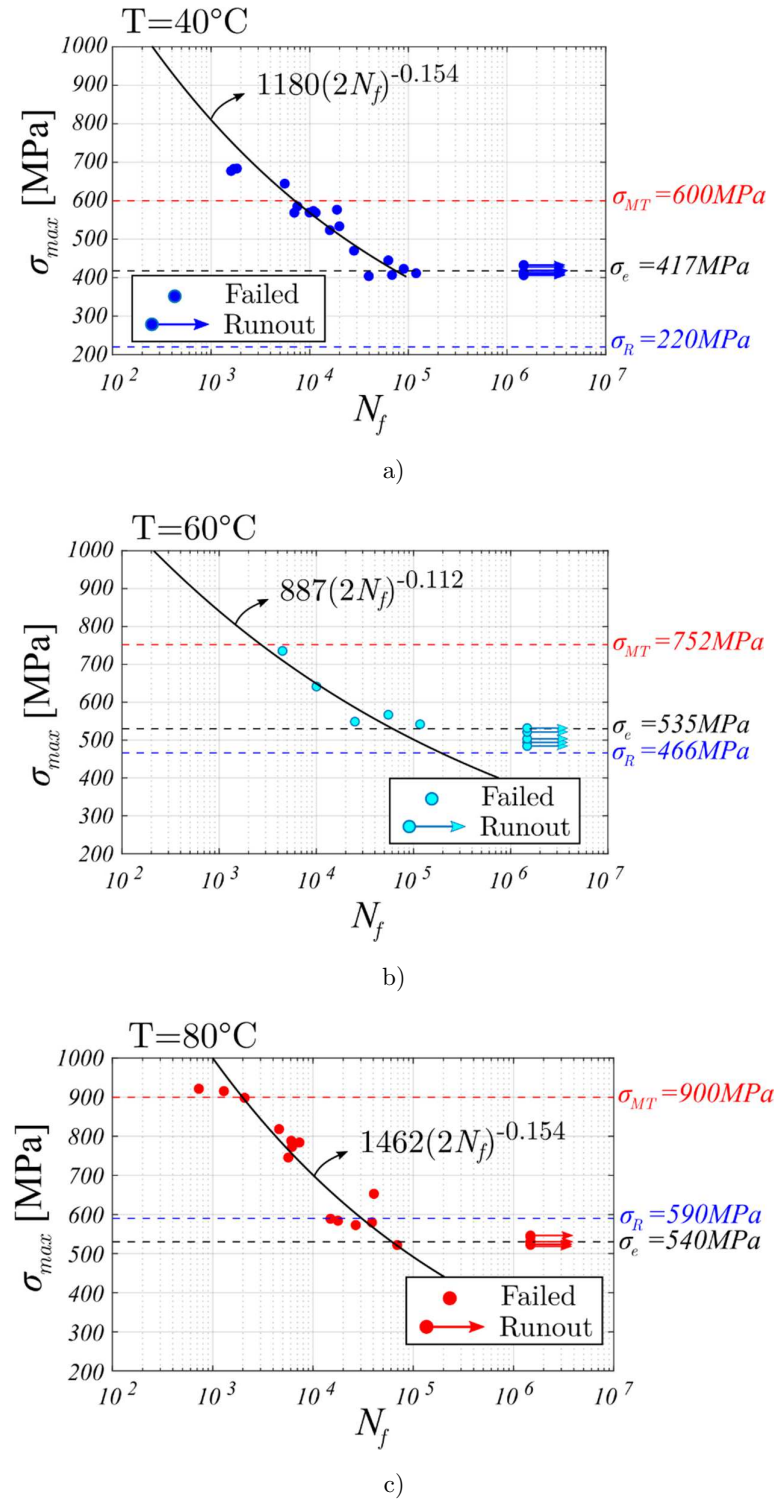


Figure 4-3 S-N curves at 40°C (a), 60°C (b), and 80°C (c).

$$s = 1.62\sigma_e \left( \frac{PR - Q^2}{P^2} + 0.029 \right), \quad (4.4)$$

where  $R = \sum_i^{N_E} i^2 P_i$ .

The list of samples used for calculating the average endurance limits at 40, 60, and 80°C is presented in Table 4-3, Table 4-2, and Table 4-3 respectively. The calculated values for  $P$ ,  $Q$ ,  $\sigma_e$  and  $s$ , for the temperature are presented in Table 4-4 to Table 4-6.

The endurance limit at 80°C was established equal to 540 MPa, being 123 MPa higher than the endurance limit at 40°C (417 MPa), but practically equal to the endurance limit at 60°C (535MPa). For stresses above the endurance limit, the number of cycles decreases exponentially with the maximum applied stress, as commonly observed in S-N of structural alloys. The best-fit lines, plotted together with the fatigue data for each temperature in Figure 4-3, were obtained by linear regression of the data points above the endurance limit and below the B19' transformation onset stress in  $\log(\sigma_{max})$  vs  $\log(2N_f)$  scale. As we observe, the exponents of the resulting exponential equations are the same at 40°C and 80°C (-0.154), showing that the trend of the lifetime with the maximum stress remains the same regardless of the temperature. As we will present later, when plotted together, the evolution of the fatigue strengths at 60 and 80°C are very close to each other; therefore, we attribute the difference in the exponent value at 60°C to the lack of data points used for the log-log straight-line equation estimate.

These tests promote elastically deformed NiTi as a more resistant material to fatigue damage in the HCF regime compared to NiTi exhibiting intermediate R-phase

$\sigma_{nom}$ [MPa]	Fatigue at 40°C - Number of samples												
	1	2	3	4	5	6	7	8	9	10	11	12	13
400	O		O		O								
410		X		X		O				O			
420							O		X		O		
430								X				O	
440													X

Table 4-1 Selection of fatigue tests used for the calculation of the endurance limit at 40°C. The tests marked as X represent failure and those marked as O represent runout.

$\sigma_{nom}$ [MPa]	Fatigue at 60°C - Number of samples				
	1	2	3	4	5
530	O		O		O
540		X		X	

Table 4-2 Selection of fatigue tests used for the calculation of the endurance limit at 60°C. The tests marked as X represent failure and those marked as O represent runout.

$\sigma_{nom}$ [MPa]	Fatigue at 80°C - Number of samples						
	1	2	3	4	5	6	7
510				O			
530	O		X		O		
550		X				O	
570							X

Table 4-3 Selection of fatigue tests used for the calculation of the endurance limit at 80°C. The tests marked as X represent failure and those marked as O represent runout.

$\sigma_{nom}$ [MPa]	$i$	$P_i$	$iP_i$	$i^2P_i$
410	0	2	0	0
420	1	1	1	1
430	2	1	2	4
440	3	1	3	9
Sum		$P=5$	$Q=6$	$R=14$
$\sigma_e$	<b>417 MPa</b>			
$s$	<b>22.5 MPa</b>			

Table 4-4 Calculation of the mean endurance limit at 40°C.

$\sigma_{nom}$ [MPa]	$i$	$P_i$	$iP_i$	$i^2P_i$
540	0	2	0	0
Sum		$P=2$	$Q=0$	$R=0$
$\sigma_e$	<b>535 MPa</b>			
$s$	<b>-</b>			

Table 4-5 Calculation of the mean endurance limit at 60°C

$\sigma_{nom}$ [MPa]	$i$	$P_i$	$iP_i$	$i^2P_i$
530	0	1	0	0
550	1	1	1	1
570	2	1	2	4
Sum		$P=3$	$Q=3$	$R=5$
$\sigma_e$	<b>540 MPa</b>			
$s$	<b>22.5MPa</b>			

Table 4-6 Calculation of the mean endurance limit at 80°C

transformation. The worsening effects of the temperature in the fatigue of typical structural alloys seem to play a minimal role with respect to the R-phase transformation in this case.

#### 4.2.1. Effects of the mean stress

In the attempt to provide a better understanding of the fatigue performance of superelastic NiTi in the HCF regime, we hereby analyze the obtained results using a commonly applied fatigue prediction model. The model is based on the Basquin's law:

$$\sigma_{a0} = \sigma_f' (2N_f)^b, \quad \text{for } \sigma_{a0} > \sigma_{e0}, \quad (4.5)$$

which establishes an exponential relationship between the stress amplitude ( $\sigma_{a0}$ ) of a fully-reversed, constant amplitude fatigue test (i.e. mean stress  $\sigma_m = 0$ , hence  $R = -1$ ) and the number of load reversals to failure  $2N_f$ . In (4.5),  $\sigma_f'$  is known as the fatigue strength coefficient, which is approximated to the true fracture strength  $\sigma_f$ , corrected for necking, in a monotonic tensile test. The Basquin's exponent  $b$ , on the other hand, determines the rate of the lifetime decrement with increasing the loading amplitude.  $b$  is in the range of -0.05 to -0.12 for most metals [120].  $\sigma_{e0}$  is the fatigue endurance limit under fully reversed conditions.

Since the characterization of the fatigue behavior of the studied NiTi wires was performed at a fixed stress ratio ( $R = \frac{\sigma_{min}}{\sigma_{max}} = 0.1$ ), the fatigue data points previously presented in Figure 4-3, involve different combinations of stress amplitudes ( $\sigma_a$ ) and mean stresses ( $\sigma_m$ ). In order

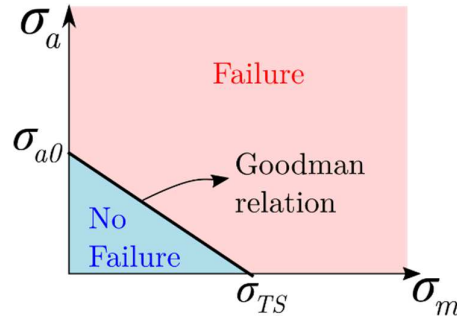


Figure 4-4 Schematic representation of a constant life diagram

to account for the role of the mean stress on the fatigue predictions using the Basquin's law (4.5), it is necessary to project the mean stress and stress amplitude values in Figure 4-3 into equivalent fully-reversed stress amplitude values. For this, we propose the following expressions:

$$\text{Goodman:} \quad \sigma_a = \sigma_{a0} \left( 1 - \frac{\sigma_m}{\sigma_{TS}} \right), \quad (4.6)$$

$$\text{Soderberg:} \quad \sigma_a = \sigma_{a0} \left( 1 - \frac{\sigma_m}{\sigma_{MT}} \right), \quad (4.7)$$

$$\text{Soderberg modified:} \quad \sigma_a = \sigma_{a0} \left[ 1 - \left( \frac{\sigma_m}{\sigma_{MT}} \right)^2 \right]. \quad (4.8)$$

The expressions (4.6)-(4.8) allow the construction of constant-life diagrams, which determine the loading conditions under which the material is expected to fail after a definite number of loading cycles. A schematic representation of a constant-life diagram for  $N$  number of cycles, represented by the Goodman relation (4.6), is illustrated in Figure 4-4. The combination of mean stress and amplitudes lying beneath the linear Goodman curve represent safe loading conditions, i.e. no failure is expected before  $N$  cycles. In contrast, the mean stress and stress amplitude combinations above the Goodman curve define the loading conditions that would lead the material to fail before completing  $N$  cycles.

In order to assess the validity of expressions (4.6)-(4.8), we performed additional fatigue tests under fully-reversed loading conditions ( $R = -1$ ). These tests intended to determine the endurance limit  $\sigma_{e0}$  at 40°C, 60°C, and 80°C, rather than the full fatigue curves. The tests were carried out in force control mode, starting from the unloaded state, and then applying a constant-amplitude sinusoidal tension-compression force at 25Hz. In order to avoid buckling upon the application of compressive stresses, the samples were clamped at the end of the groove zone, using a three-jaw chuck on each side. Consequently, the 10mm gauge length clip-on extensometer, previously used in  $R = 0.1$  fatigue tests, was not employed this time. The tests were performed in the same testing machine and heat chamber illustrated previously in Figure 4-1a.

	40°C. X: failed O: runout(1e6 cycles)				
$\sigma_a$ [MPa]	187	197	207	217	227
Sample 1	O	O	O	O	X (62350 cycles)
Sample 2					X (70720 cycles)
Sample 3					X (60207 cycles)

Table 4-7 Estimate of the endurance limit in fully-reversed conditions at 40°C. The failure of the tested samples occurred in the mid cross-section.

	60°C. X: failed O: runout (1e6 cycles)													
$\sigma_a$ [MPa]	240	250	...	290	300	310	320	330	...	380	370	...	450	460
Sample 1	O	O	O	O	O	O	X*							
Sample 2							O	O	O	X*				
Sample 3										O	O	O	O	X*

Table 4-8 Estimate of the endurance limit in fully-reversed conditions at 60°C. The failure of the tested samples occurred inside the clamps. The sample 1 failed after 15718 cycles under a stress amplitude of 320MPa, sample 2 did it after 34504 cycles under a stress amplitude of 380MPa, and sample 3 failed after 198310 cycles under a stress amplitude of 460MPa.

	80°C. X:failed O:runout (1e6 cycles)															
$\sigma_a$ [MPa]	243	253	263	273	293	303	313	323	333	343	353	363	373	383	393	403
Sample 1	O	O	O	O	O	O	O	O	O	O	O	O	O	O	O	X*
Sample 2																X*

Table 4-9 Estimate of the endurance limit in fully-reversed conditions at 80°C. The failure of the tested samples occurred inside the clamps. The samples 1 and 2 failed under a stress amplitude of 403MPa. The sample 1 failed after 126204, while sample 2 did it after 234800 cycles.

The R=-1 cyclic tests were performed by blocks of one million constant-stress amplitude cycles. The stress amplitude of the first block of cycles was set equal to the stress amplitude corresponding to the mean endurance limit found in  $R = 0.1$  fatigue tests. If no failure occurred upon the first one million cycles, a second block of one million cycles was applied to the sample with a stress amplitude increased by 10MPa. The process was repeated until failure occurred. In order to corroborate a failure event, a new sample was tested at the same stress amplitude that led the previous sample to failure.

At 40°C, three samples were tested. The first sample bore four blocks of one million cycles under a stress amplitude going from 187MPa up to 217MPa. Upon testing at a stress amplitude of 227MPa, the sample failed after 62350 cycles. After that, two more tests were carried out at a stress amplitude of 227MPa, both resulting in failure after 70720 and 60207 cycles respectively. At 60°C, the first sample failed upon the 320MPa stress amplitude cycles' block. However, the rupture occurred on the part of the sample placed inside the clamps. After that, two more samples were tested, both presenting failure inside the clamps. The first did it at 380MPa stress amplitude and the second at 460MPa. Finally, at 80°C, failure inside the clamps occurred upon the 403MPa stress amplitude cycles' block for the first sample. A second sample, tested under the same conditions, failed inside the clamps after 234800cycles. The list of the fatigue tests carried out at 40°C, 60°C, and 80°C is presented in Table 4-7 to Table 4-9.

From these experimental results, we estimate that the endurance limit under fully reversed loading conditions at 40°C is 217MPa, which coincidentally is about the same stress as the onset for the B2→R transformation detected previously upon monotonic tensile stress. At 60°C and 80°C, since the fatigue failure occurred inside the clamps, we can infer that the endurance limit under fully reversed conditions is higher than 450MPa and 393MPa respectively.

The values estimated for the endurance limits  $\sigma_{e0}$  were plotted together with the infinite-life diagrams described by equations (4.6)-(4.8) in Figure 4-6. The infinite-life curves were plotted using the amplitude and mean stresses corresponding to the endurance limits found in R=0.1 tests, the B19' onset stresses at 40, 60, and 80°C, and the ultimate  $\sigma_{TS}$  obtained upon tensile tests carried out until rupture at 40°C and 80°C, which we describe in the following paragraph.

The tensile curves of two samples led to rupture at 40°C and 80°C are shown in Figure 4-5. The tests were carried out using the experimental setup presented in Figure 4-1a, in extensometer control conditions at  $2.4 \times 10^{-3} \text{ mm s}^{-1}$ . The ultimate stresses ( $\sigma_{TS}$ ) were 1490MPa and 1460MPa at 40°C and 80°C respectively. The sample tested at 80°C, failed when the nominal stress reached 1350MPa. At 40°C, the test was stopped when the extensometer elongation reached 1mm. The nominal stress at this stage was equal to 1355MPa. Comparing the trend of these two tensile curves, we deduce that the test stopped at 40°C was near to the final rupture. The sample tested at 40°C was observed in an optical microscope after the test in order to measure the change of its mid cross-section. As observed in Figure 4-5, the sample shows necking caused by a large localized plastic deformation at the mid cross-section of the sample. The resulting mid cross-section reduction, calculated using the diameter measured by means of the optical microscope, was ~22%. As a result, the fracture strength ( $\sigma_f$ ) was corrected to 1600MPa (calculated as the force at the interruption point divided by the necking-reduced cross-section). Since we did not have enough experimental data to provide statistical support of the measured values, and because they

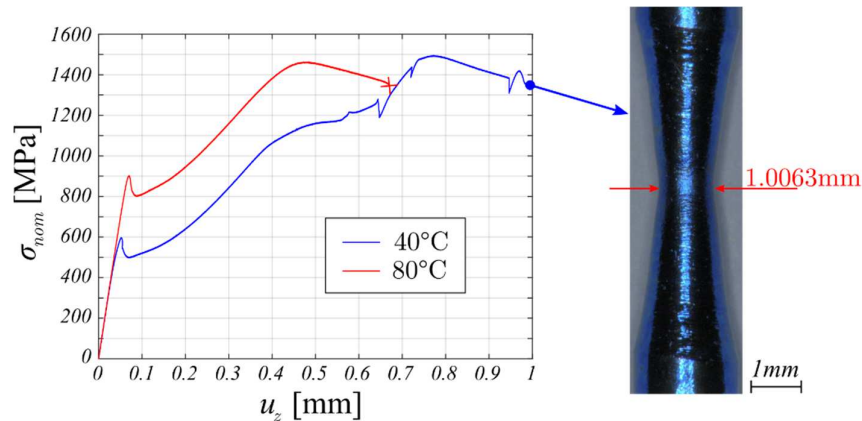


Figure 4-5 Tensile tests carried out until rupture. The test at 40°C was stopped when the extensometer elongation reached 1mm, then the sample was observed under an optical microscope to measure the diameter of the reduced cross-section (picture on the right).

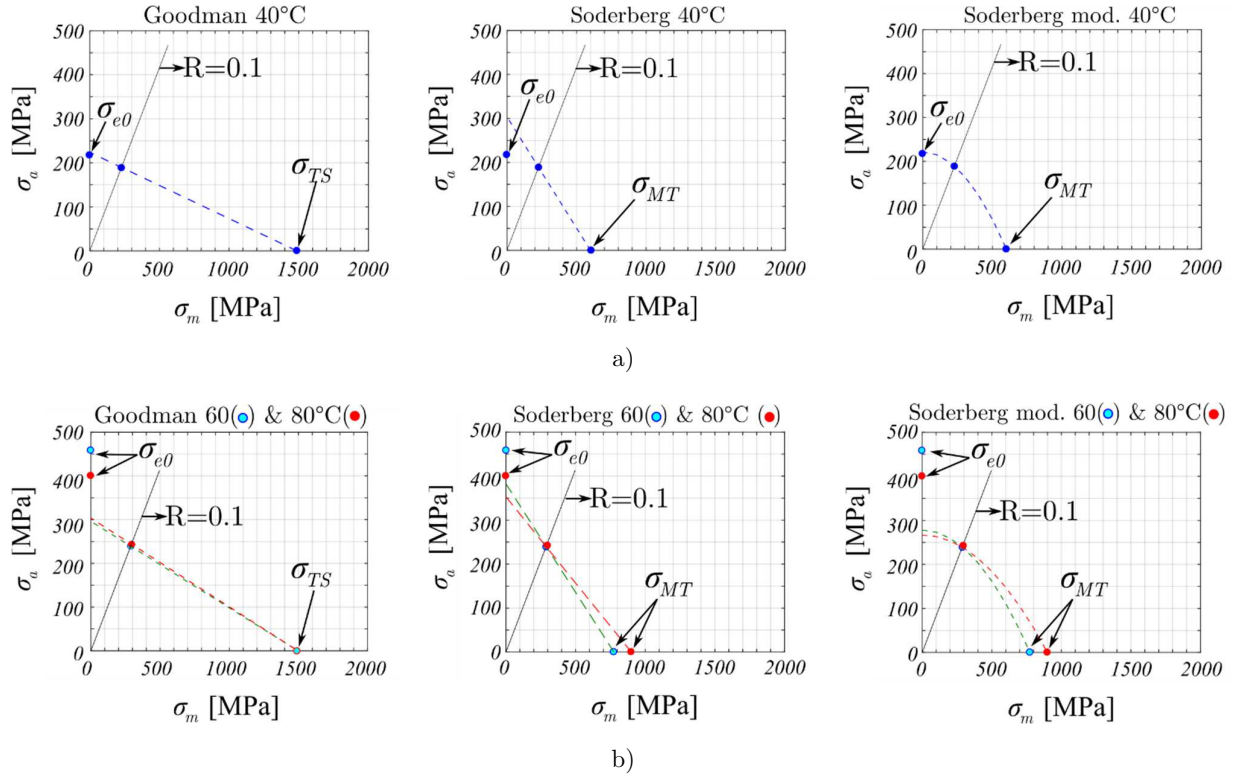
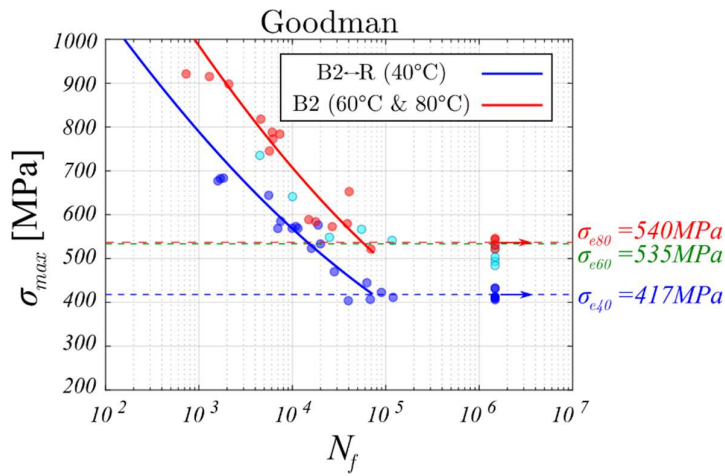


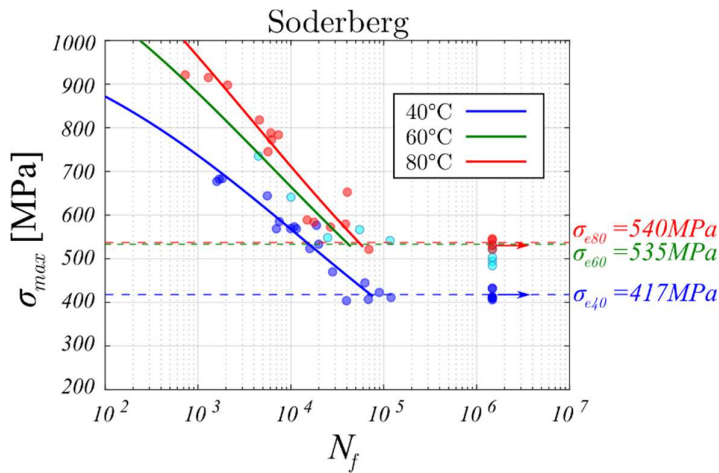
Figure 4-6 Infinite-life diagrams. The boundaries between failure and runout are plotted using the constant-life relations (4.6) to (4.8). a) B2→R loading regime (40°C). b) B2 elastic loading regime (60°C and 80°C).

were similar at 40°C and 80°C, we assume that  $\sigma_f$  (1600MPa) and  $\sigma_{TS}$  (1475MPa) are temperature independent material parameters.

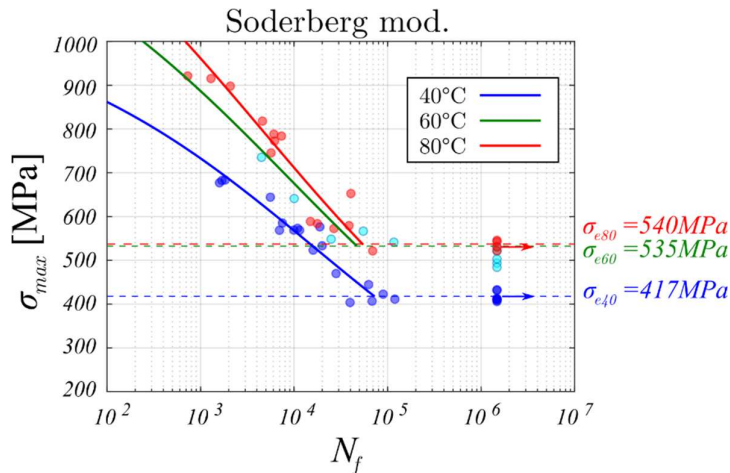
The infinite-life diagrams in Figure 4-6 are divided into two parts. In part (a), we show the endurance limit evolution, predicted in terms of the mean stress and stress amplitudes in the B2→R transformation regime (i.e. tests at 40°C) using the constant-life relations (4.6)-(4.8). In part (b), we show equivalent predictions in the B2 elastic regime (i.e. 60°C and 80°C). As observed, the Goodman relation (4.6), predicts well the fully reversed endurance limit  $\sigma_{e0}$  at 40°C, however, it largely underestimates the fully reversed endurance limit in the B2 elastic regime (60 and 80°C). In contrast, the Soderberg relation (4.7), shows a less conservative prediction of the fully reversed endurance limit in the B2 elastic regime, but it overestimates the endurance limit in the B2→R transformation regime. The third constant-life relation, which we called here the Soderberg modified relation (4.8), shows a good agreement with the endurance limits obtained upon R=0.1 and R=-1 fatigue tests. Nevertheless, like the Goodman relation, it underestimates the endurance limit in fully reversed loading conditions of NiTi in the B2 elastic regime.



a)



b)



c)

<b>GOODMAN</b>		
<b>B2↔R (40°C)</b>		
$\sigma_f' = 2000 \text{ MPa}$		
$b = -0.186$		
$\sigma_{e0} (R = -1)$	Exp.	217 MPa
	Predict.	219 MPa
<b>B2 (60 &amp; 80°C)</b>		
$\sigma_f' = 3128 \text{ MPa}$		
$b = -0.203$		
60°C $\sigma_{e0} (R = -1)$	Exp.	>450 MPa
	Predict.	295 MPa
80°C $\sigma_{e0} (R = -1)$	Exp.	>393 MPa
	Predict.	298 MPa

<b>SODERBERG</b>		
<b>B2↔R (40°C)</b>		
$\sigma_f' = 8722 \text{ MPa}$		
$b = -0.282$		
$\sigma_{e0} (R = -1)$	Exp.	217 MPa
	Predict.	304 MPa
<b>B2 (60 &amp; 80°C)</b>		
$\sigma_f' = 8137 \text{ MPa}$		
$b = -0.269$		
60°C $\sigma_{e0} (R = -1)$	Exp.	>450 MPa
	Predict.	388 MPa
80°C $\sigma_{e0} (R = -1)$	Exp.	>393 MPa
	Predict.	362 MPa

<b>SODERBERG MOD.</b>		
<b>B2↔R (40°C)</b>		
$\sigma_f' = 3527 \text{ MPa}$		
$b = -0.235$		
$\sigma_{e0} (R = -1)$	Exp.	217 MPa
	Predict.	220 MPa
<b>B2 (60 &amp; 80°C)</b>		
$\sigma_f' = 3600 \text{ MPa}$		
$b = -0.223$		
60°C $\sigma_{e0} (R = -1)$	Exp.	>450 MPa
	Predict.	281 MPa
80°C $\sigma_{e0} (R = -1)$	Exp.	>393 MPa
	Predict.	273 MPa

Figure 4-7 Fatigue predictions. a) Goodman. b) Soderberg. c) Soderberg modified.

The fatigue strength coefficient  $\sigma_f'$  and the Basquin's exponent  $b$ , which constitute the Basquin's power law (4.5), were determined from the fatigue data points in Figure 4-3

transformed into the fully reversed fatigue space through equations (4.6)-(4.8). One set of Basquin's parameters were determined for the group of fatigue data points obtained at 40°C (B2→R transformation regime), and another using the group of fatigue data points obtained at 60°C and 80°C (B2 elastic regime).  $\sigma_f'$  and  $b$ , were determined by the best-fit straight line passing through the fully reversed fatigue data in terms of the number of reversals ( $2N_f$ ) in a log-log scale. The resulting prediction curves are plotted together with the R=0.1 fatigue data in Figure 4-7. The Basquin's parameters, obtained after the straight line fitting, are presented in the tables attached to each set of prediction curves and recapitulated in Figure 4-8.

The Goodman relation (Figure 4-7a) predicts that the fatigue behavior in the HCF regime is not affected by the onset stress for the B19' transformation  $\sigma_{MT}$ . Instead, it establishes that the fatigue behavior is affected by the appearance of R-phase, which results into different values of fatigue strength  $\sigma_f'$  (Figure 4-8a). A slightly higher value for the Basquin's exponent  $b$  was calculated in the case of elastic loaded B2 phase, which indicates a lower rate of lifetime degradation upon increasing the stress amplitude in comparison with the B2→R loading regime (Figure 4-8b). The Soderberg relation (Figure 4-7b) shows a similar, but not equal, fatigue predictions at 60 and 80°C, which results difficult to assess due to the lack of fatigue data points at 60°C. As the values calculated for the Goodman relation, the Basquin's exponents calculated using the Soderberg relation are almost equivalent. This time a slightly larger value was obtained in the B2→R regime in comparison with the B2 elastic regime. The modified Soderberg relation, results in similar fatigue prediction curves as the Soderberg relation. However, as mentioned previously, the parabolic formulation of the modified Soderberg relation might predict better the fatigue behavior in the B2→R transformation regime at mean stresses near to zero.

#### 4.2.2. Hints for superelastic NiTi fatigue modeling

The HCF of the studied superelastic NiTi wires shows a strong dependence on the B2→R phase transformation. On the one hand, the B2→R transformation has a detrimental impact on the fatigue behavior, evidenced by a lower the endurance limit than elastically loaded B2 austenite upon R=-1 and R=0.1 fatigue loadings. On the other hand, the mean stress might

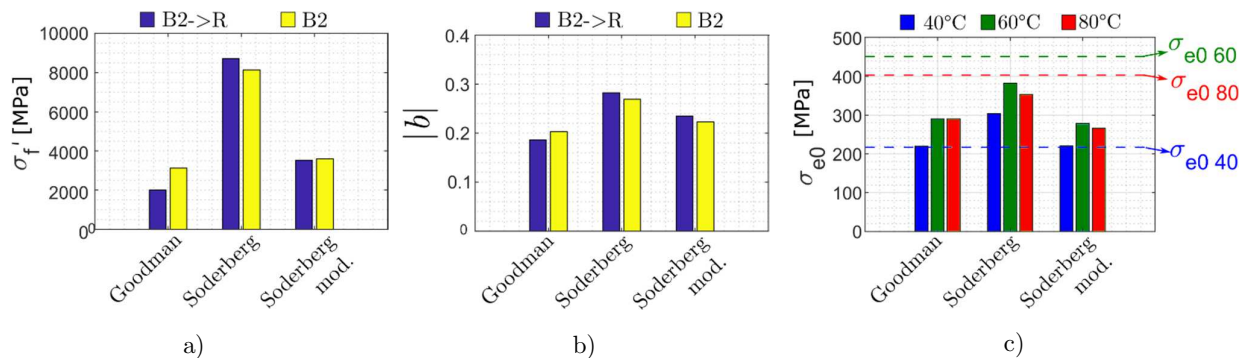


Figure 4-8 Parameters of the Basquin's law using three different constant-life formulations. a) Fatigue strength coefficient. b) Basquin's fatigue exponent. c) Fatigue endurance limit in fully reversed conditions.

have a lower impact on the fatigue behavior of NiTi loaded in the B2→R regime, as evidenced by the closeness of the endurance limits between R=-1 (220MPa) and R=0.1 (187.5MPa) fatigue loadings.

In contrast, the influence of the B2/R→B19' phase transformation in the fatigue crack initiation seems to be low when the maximum stress reached upon fatigue loading remains well below than the onset stress  $\sigma_{MT}$ . This explains the very similar fatigue strength trends obtained at 60°C and 80°C (see Figure 4-3b&c). When the maximum stress upon cyclic loading gets equal to  $\sigma_{MT}$ , it is expected a finite number of cycles till rupture, as reported multiple times in the literature (recall the state of the art chapter in section 2.5). Consequently, the Goodman relation, which is based on the ultimate tensile strength  $\sigma_{TS}$ , seems to be inappropriate for describing the HCF behavior of NiTi (see infinite life diagrams for the Goodman relation in Figure 4-6). The Soderberg relation, which is a more conservative option for most engineering alloys [121], arises as a more convenient constant-life formula to account for the B19' transformation onset stress  $\sigma_{MT}$  on the fatigue behavior of NiTi. However, Soderberg lifetime predictions might overestimate the lifetime of NiTi showing R-phase. To face this difficulty, we evaluated a modified Soderberg relation, which predicts well the mean stress effects on the lifetime of NiTi with R-phase, but results too conservative for predicting lifetimes for elastically loaded B2 austenite.

Since the effects of the mean stress in the fatigue behavior of NiTi change with R-phase transformation, a new Soderberg-like relation, written in the following form

$$\sigma_a = \sigma_{a0} \left[ 1 - \left( \frac{\sigma_m}{\sigma_{MT}} \right)^\gamma \right] \quad (4.9)$$

where the exponent  $\gamma$  is a temperature dependent function, might help describing the HCF behavior of NiTi. As observed in Figure 4-8a, the modification of the constant-life formulation implies changes of the fatigue strength  $\sigma_f'$  used in the Basquin's fatigue power law; therefore  $\sigma_f'$  may become temperature dependent as well. In what respect the Basquin's fatigue exponent, similar values were obtained regardless of the constant-life approximation or stress ratio; therefore, a temperature-independent value may be enough to describe the worsening of the fatigue performance with increasing mechanical loading.

The above-described particular fatigue behavior of NiTi, demonstrates the need for more reliable constant-life formulas for the HCF of superelastic NiTi, which may facilitate the prediction of fatigue lifetimes under different loading regimes.

### 4.3. Stress-Strain-N representation

Besides the stresses, large transformation strains that do not scale with stresses play an important role in fatigue of SMA. In order to account for the strain experienced by the material upon fatigue tests, we constructed a Stress-Strain-N graph showing how the number of cycles to rupture evolved with both the maximum nominal stresses and the maximum local strains in the mid cross-section evaluated from stabilized cycles (see Figure 4-9). As

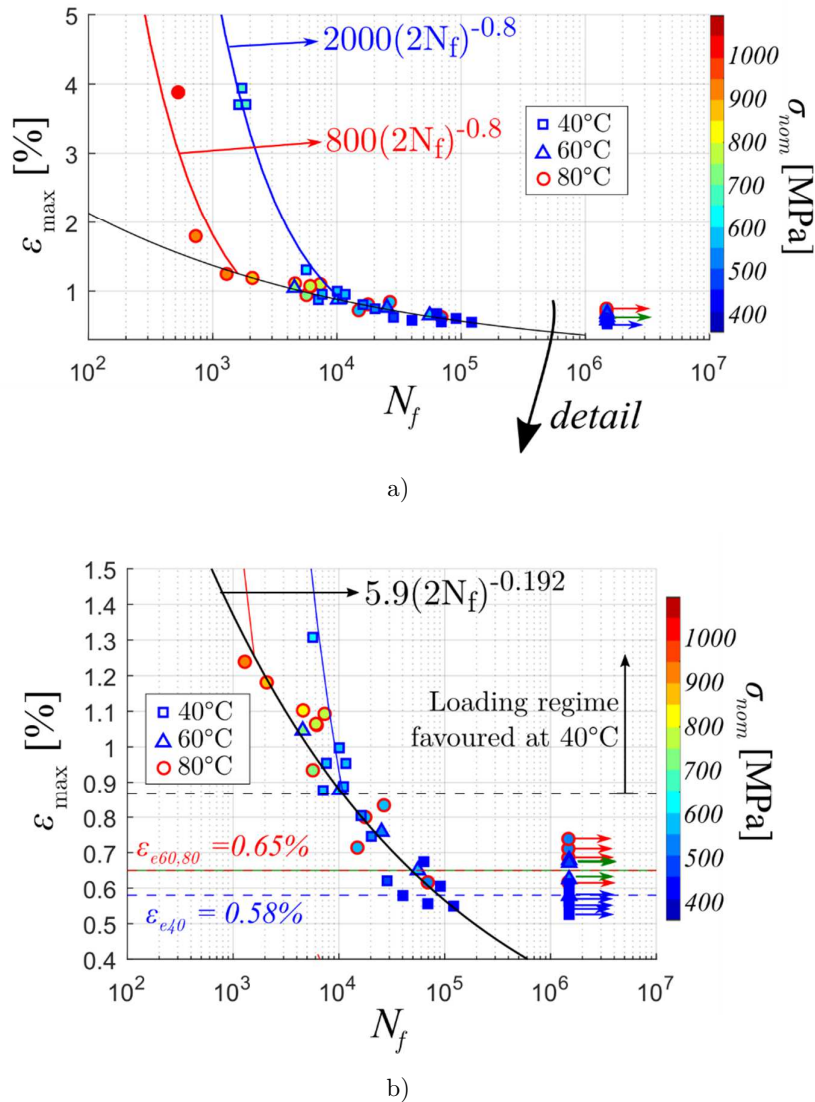
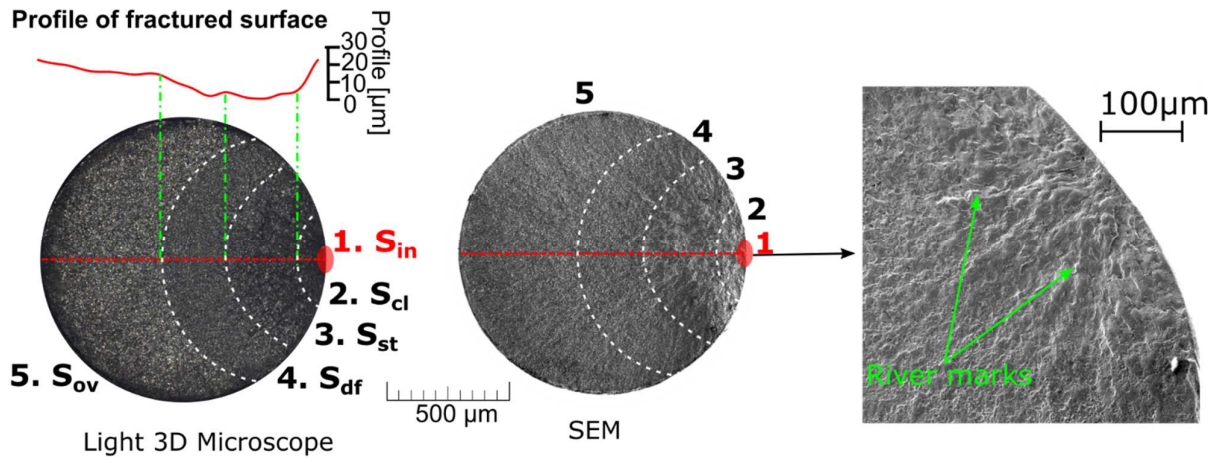


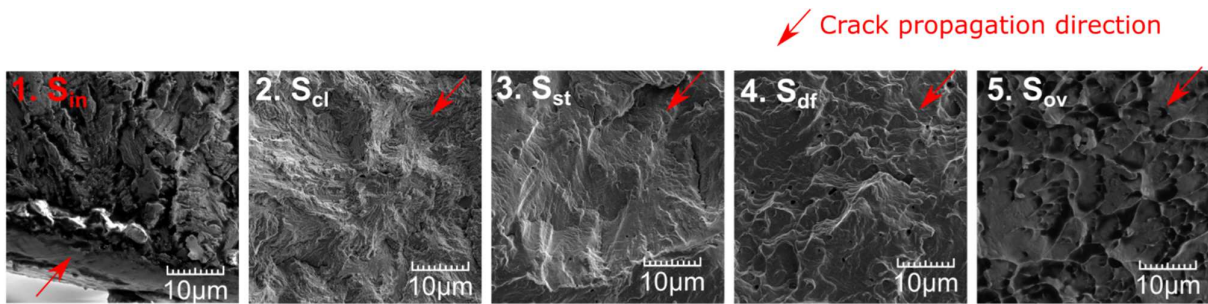
Figure 4-9 Strain-Stress-N representation of fatigue results.

explained previously in section 3.3.3.4, the maximum local strain was calculated as a sum of the local elastic strain of austenite, calculated through the Hooke's law, and the inelastic strain deduced from the inelastic elongations of the clip-on extensometer. As discussed later, the maximum elongation of the extensometer was stable over the complete fatigue test duration with exception of few tens of cycles before rupture. As a result, we can indeed consider this maximum as a representative value of the strain to which the samples were subjected in fatigue tests.

Unlike Stress-N curves in Figure 4-3, Stress-Strain-N graph in Figure 4-9 shows the fatigue curve in terms of strains while stresses are represented by markers' colors. The Stress-N curves clearly promote elastically deforming NiTi at 60°C and 80°C as best fatigue performers within the entire range of applied loadings. However, in the strain representation, NiTi cycled at 60°C and 80°C outperforms NiTi at 40°C within a limited range of applied loadings where strains stay below 0.65%. Beyond 0.65% the elastically, both the elastically loaded B2 NiTi and the NiTi in the B2→R phase transformation regime behave similarly.



a)



b)

Figure 4-10 a) Typical fatigue fracture surface as viewed from light 3D microscope and SEM. 3D optical microscopy allowed us to examine the topology of the fracture surfaces. **b)** Five zones with distinct morphology as identified on the fracture surface. River marks shown in (a) point towards the fracture initiation zone 1, followed by the zone 2 with quasi-cleavage morphology continued with fatigue striation zone 3, ductile fatigue crack zone 4, and ductile overload zone 5.

However elastically deformed NiTi develops much higher stresses compared to NiTi where the R-phase transformation acts as a stress reliever.

Approaching and finally reaching the critical stress for B19' phase transformation lead to continuous but not accelerated fatigue performance worsening (see that the number of cycles before failure does not exhibit a significant reduction in spite of local strain increase up to 4%). At maximum strain around 1%, B19' transformed NiTi at 40°C shows a better fatigue performance than elastically loaded NiTi at 80°C. However, once again, the stresses developed in the elastic case are much higher than the ones in the B19' transformed case.

Based on distinct conclusions drawn from both Stress-N and Strain-N representations, we believe that the dramatic drop in the fatigue performance of NiTi is not associated with large martensitic transformation strains typical of superelastic NiTi alloys (recoverable strains up to 10%). The dramatic drop in fatigue performance (from millions to some thousands of cycles) of superelastic NiTi appears in strains dominated by elastic deformation or inelastic deformation through the R-phase transformation. Moreover, we believe that Stress-Strain-N graph carrying information on both the strains and the stresses is the only

relevant fatigue life representation for SMA. Unfortunately, it can be used only in conjunction with specimens that do not display strain localization and continuous strain dependence on loading is guaranteed within the gauge volume.

## 4.4. Fatigue crack characterization

### 4.4.1. Fracture surfaces

In this section, we analyze the morphology and size of fatigue cracks to have a better understanding of the fatigue failure and fatigue crack propagation in superelastic NiTi wires. The fatigue surfaces that we analyze next were taken from the broken samples during  $R=0.1$  fatigue tests. We thoroughly examined the fatigue crack surfaces using a 3D optical microscope KEYENCE VHX-1000 and a scanning electron microscope (SEM) TESCAN FERA3. As a result, we drew a representative picture of the fatigue crack surface of superelastic NiTi wires loaded in the HCF regime and barely above the martensitic transformation regime (Figure 4-10).

We split the fatigue crack surface into five zones with distinct morphologies (unlike three zones described in [122]). The river marks, well visible in SEM and 3D optical microscope, point to the crack initiation zone (Figure 4-10 1.Sin). This zone merges into a second zone with quasi-cleavage morphology (Figure 4-10 2.Scl). The quasi-cleavage zone disappears into a third zone with fatigue striations (Figure 4-10 3.Sst) from which the fourth zone of mixed mode between striations and ductile fatigue crack with dimples emerges (Figure 4-10 Sdf). Finally, ductile overload surface is well noticeable beyond the fatigue beachmark in 3D light microscope images (Figure 4-10 Sov). This characteristic picture of the fatigue crack surface is preserved for nominal loadings below and above the stress-induced B19' transformations, however, the sizes of each zone change according to the applied loading. The difference in morphology between detected zones results in a change of light reflection; thus, images taken on the 3D optical microscope provide enough contrast to detect the boundaries between fracture modes. Moreover, 3D optical microscopy allowed us to characterize the surface profile across the fracture surfaces as shown in Figure 4-10a.

#### 4.4.1.1. Crack initiation zone (Sin)

All the fatigue tests performed during this study showed fractures that started at the samples' surface in the mid cross-section. Some SEM images of the initiation zone for different broken samples are shown in Figure 4-11. The temperature, maximum stress and the number of cycles before failure are indicated to the top of each image. As observed, river marks indicate several initiation crack spots along the surface of the Sin zone. Compared to the overloaded zone, the surface in the Sin does not present sheared lip (Figure 4-11b). Instead, high magnification images in Figure 4-11a reveal rubbing and pounding, which may be related to continue opening and closing of the cracks upon repetitive pull-pull axial loading. The fact that rubbing and pounding exist, even in the absence of compressive repetitive stresses, is explained by the crack direction upon the first stage of the propagation,

which for all observed samples was far from perpendicular to the sample axis (see surface profile in Figure 4-10a).

As observed in Figure 4-11a, multiple cracks initiate on the surface of the sample. The origin of the multiplicity of cracks in the surface of the sample might be the result of a combination of surface imperfections due to grinding manufacturing, surface inclusions (Figure 4-10c), radial stress-free condition and even corrosion [123].

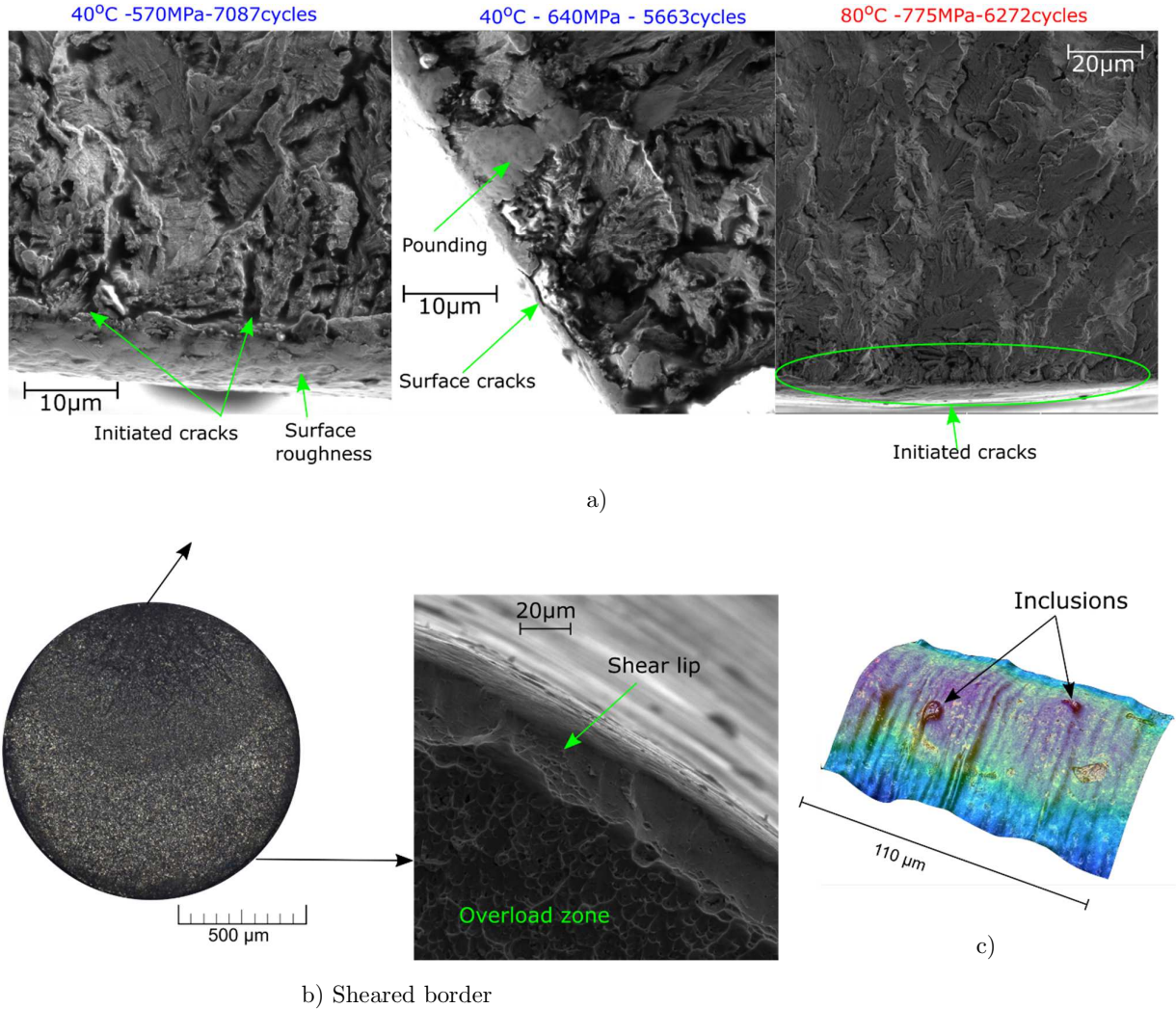
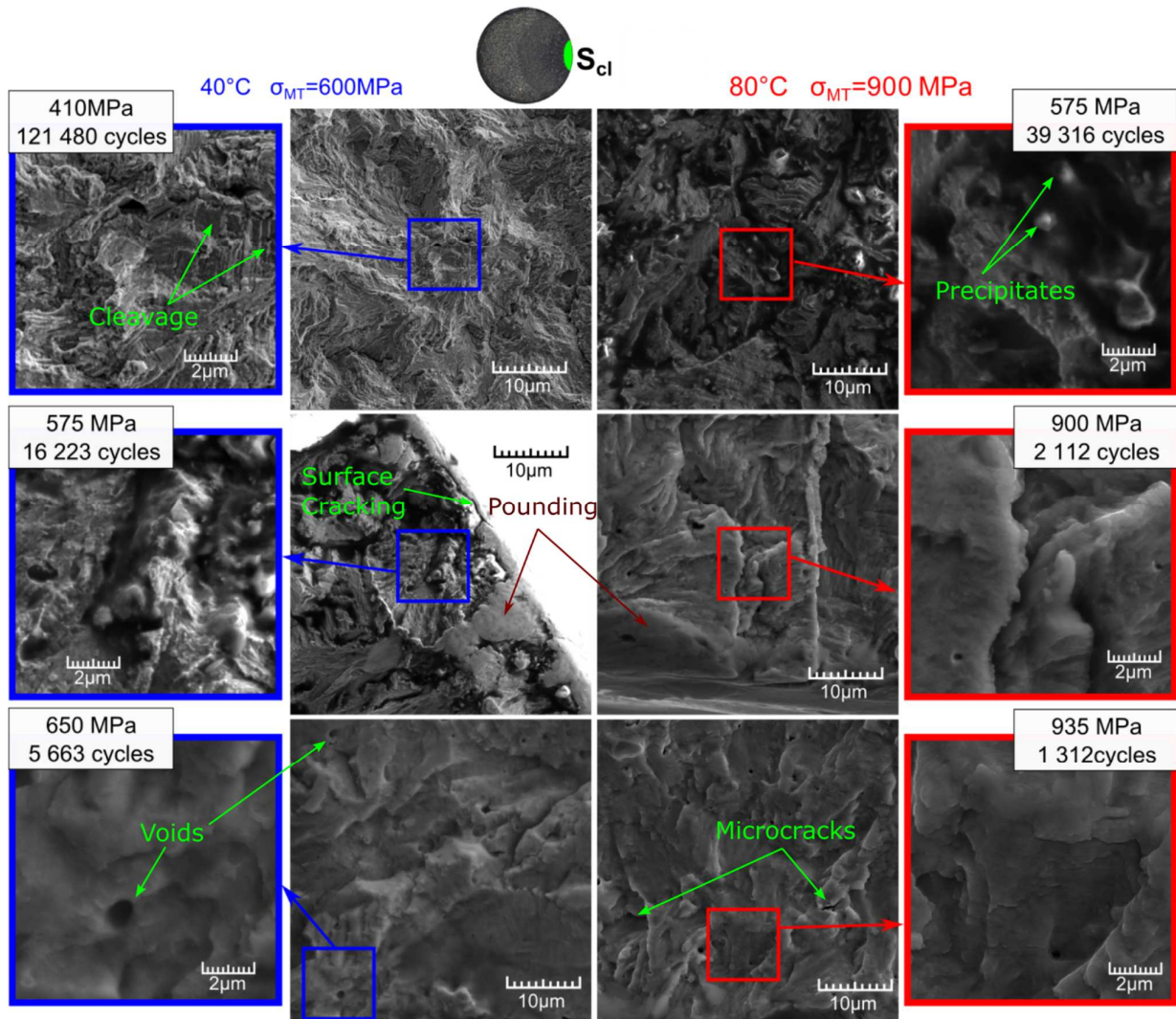
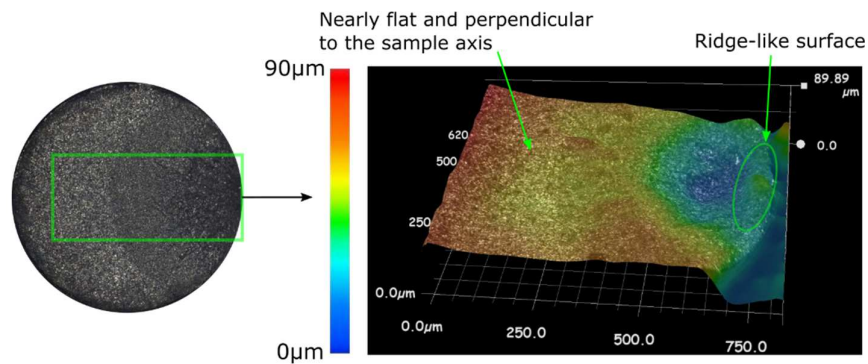


Figure 4-11 SEM images of the crack initiation zone are shown in (a). Compared to the overload part of the samples (b) no shear lip was detected near the crack initiation zones. 3D optical microscope allowed us to reconstruct a 3D image of the surface, where we clearly see inclusions and geometric imperfections created after machining.



a)



b)

Figure 4-12 First crack propagation zone with quasi cleavage morphology. a)SEM images. b)Fracture surface topology.

#### 4.4.1.2. First crack propagation zone (Scl)

After initiation, the surface cracks propagate in multiple directions. In this first propagation stage, the cracks propagate at the microscale, therefore, grain boundaries, precipitates and inclusions determine the most-attractive energy cracks paths. This results in the ridge-like appearance of the Scl zone as observed in the 3D image in Figure 4-12b. Detailed SEM images show a rough morphology in the Scl zone with microcracks, wrinkles and some voids (Figure 4-12a).

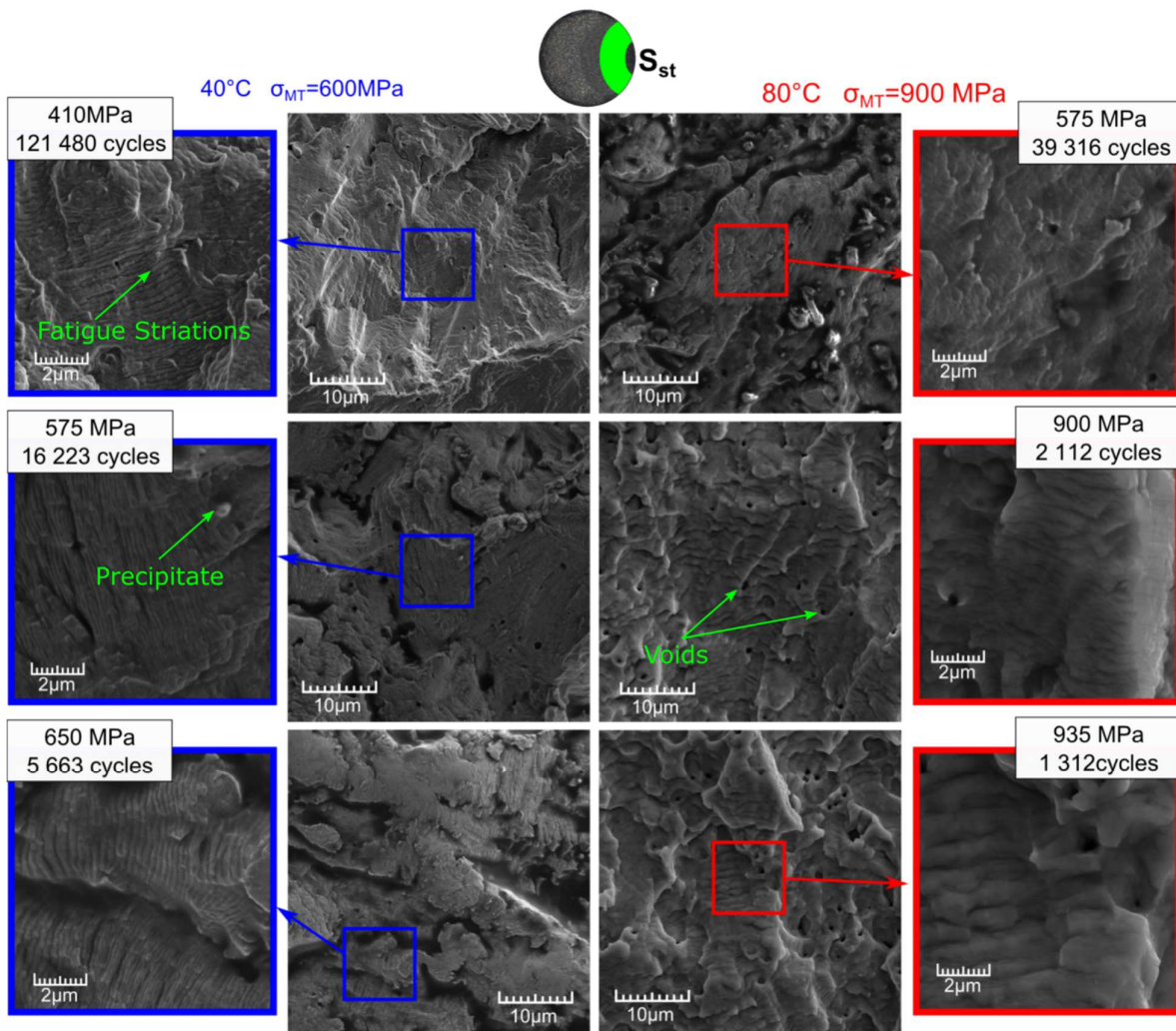
Higher magnification SEM images reveal sharp edges in the fracture surface of samples tested at lower stress. Particularly in the fracture surface of the sample tested under 410MPa at 40°C (note that this is below the mean average endurance limit), a special quasi-cleavage morphology is observed all across the Scl zone. This morphology shows similarities to cleavage fracture reported in NiTi single crystals by Yang et al. [124]. In this article, the authors attribute the cleavage planes to the highly symmetric B2 phase rather than to the habit planes of the low symmetry B19' martensite plates. At higher stress, the quasi-cleavage patterns are less evident and the local surface becomes more “wavy”, which implies an increased amount of local plastic flow during fracture.

These observations indicate that the first stage of the fatigue crack propagation in the HCF regime occurs through a dominant brittle rupture in the B2 phase when the applied stresses are low. With increasing the stress, local plastic deformation develops together with the quasi-cleavage rupture mode. Whether the plastic deformation is developed through locally transformed B19' martensite or through B2 austenite is a matter of further research.

#### 4.4.1.3. Fatigue striations zone (Sst)

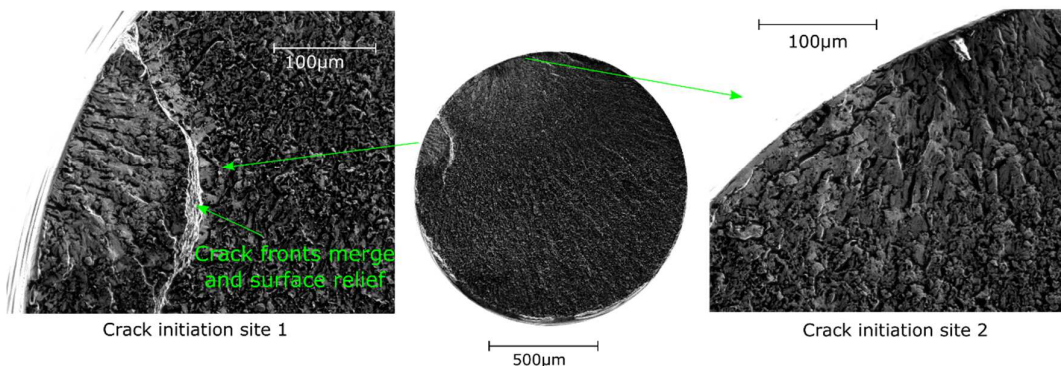
As the first cracks advance, some of them merge, creating greater crack fronts. The trace of the propagation of these fronts are the so-called fatigue striations. These are characteristic features of ductile materials. They denote the size of the plastic region around the crack tip. Moreover, it is a common practice to associate the distance between the striations to the crack propagation rate at middle values of stress intensity factor  $\Delta K$  (in the “Paris-law” regime of the crack rate vs stress intensity factor diagram). The average distance between striations in the acquired images is  $10^{-6}$ - $10^{-7}$ m, which correlates well with the crack propagation rates measured for NiTi in the Paris-law regime reported in different studies [125][126]. The distance between striations is greater at higher stresses, as it is observed in Figure 4-13a.

Unlike the sharp edges and wrinkles observed in the Scl zone, which were oriented randomly, the striations in the Sst zone tend to point radially out of the crack initiation zone Sin. In the Sst zone, the crack is dominated by the direction of the applied stresses rather than by the microstructure as it was in the Scl zone. For this reason, in most of the examined samples, the fracture surface morphology becomes relatively flatter (Figure 4-12b), more perpendicular to the sample's axis, and more homogeneous.



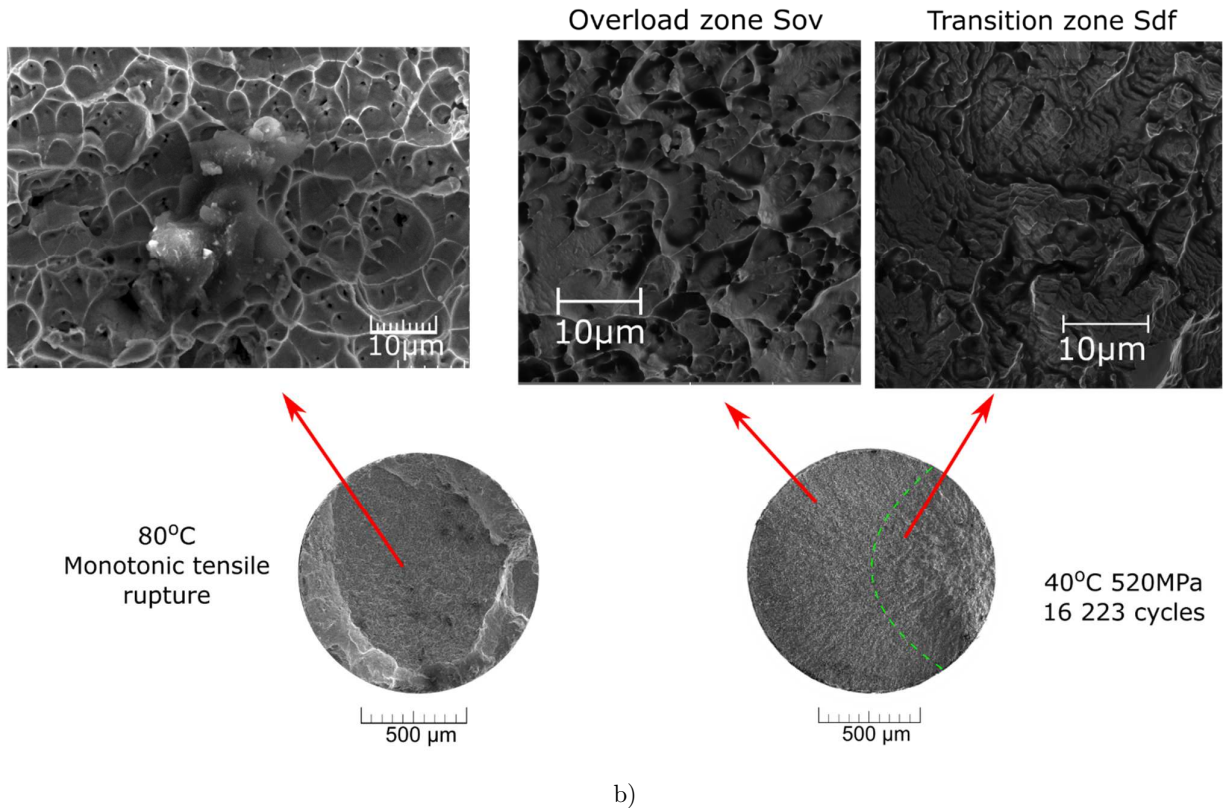
a)

40°C -680MPa-1618 cycles



b)

Figure 4-13 a)Morphology of the fatigue striations zone  $S_{st}$ . b)Case of accelerated crack propagation due to merge of two well-developed fatigue crack fronts.



b) Figure 4-14 Morphology of the transition and overload zones.

In some samples, we observed simultaneous crack fronts that initiated at different locations in the sample's surface. Upon the propagation, the crack fronts joined, creating a prominent surface relief, which ended by accelerating the final failure of the sample (Figure 4-13b).

#### 4.4.1.4. Transition zone and overload fracture zone (Sdf and Sov)

As the cracks advances, the stress towards the crack tip increases leading to large deformations (ductile failure mode) and microvoid coalescence processes. The resulting fracture mode surface shows an increase in the number of dimples, the size of which may be related to the size of carbide inclusions (5-10µm) and precipitates (1-5µm). In the transition zone Sdf, microvoid coalescence is observed together with striations. The dimples in the Sdf zone have similar morphology to the dimples obtained after monotonic tensile rupture (see Figure 4-14). In contrast, the dimples in the final overload zone Sov look more “sheared”, which might be caused by the bending stress applied in the mid cross-section product of the dissymmetric cross-section reduction during the crack advance.

#### 4.4.2. Characterization of the crack's size

The size of the final crack was measured using optical microscope images, based on the image contrast between the dark fatigue crack (zones Sin+Scl+Sst+Sdf) and the bright overload fracture surface (Sov). Additionally, the size of the Scl zone was measured based on the surface profile near the crack initiation site.

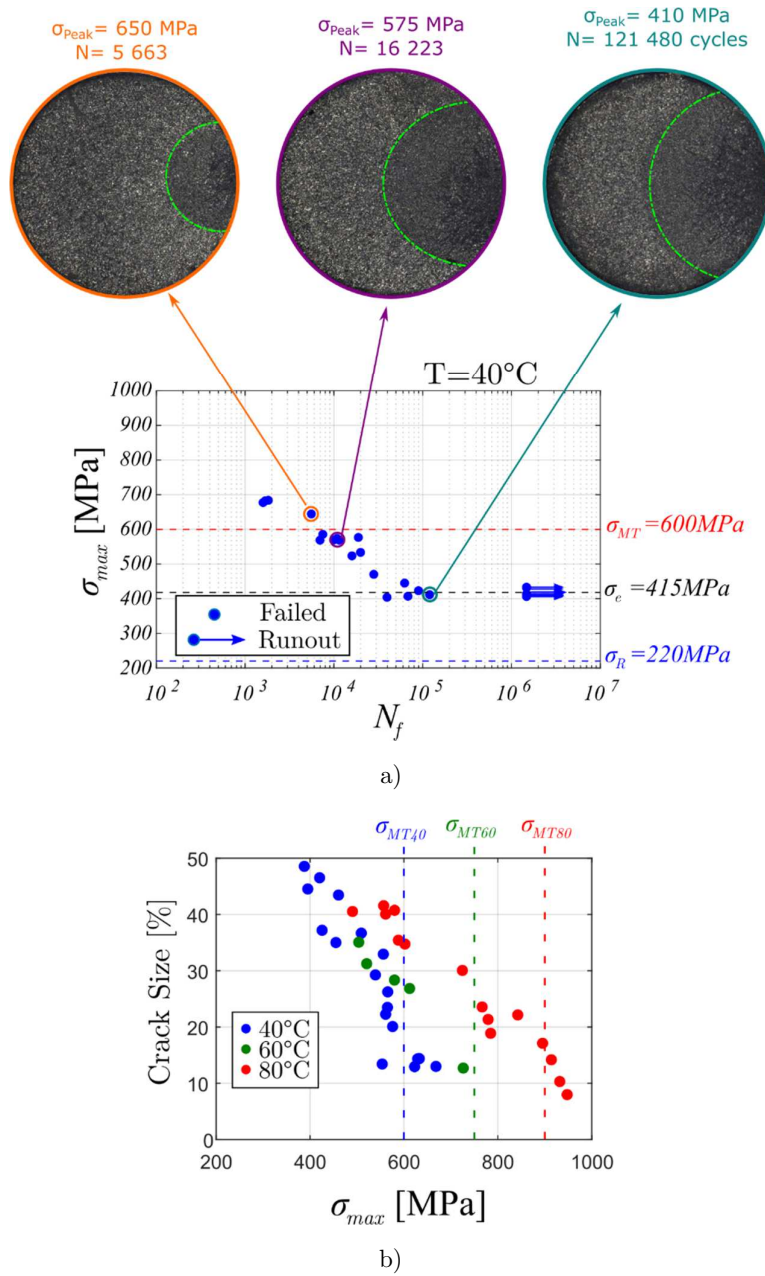


Figure 4-15 Size dependence of fatigue crack surfaces on the peak of nominal stress for two testing temperatures  $40^\circ\text{C}$  and  $80^\circ\text{C}$ . **a)** Fracture surface with denoted final overload surfaces for samples subjected to three different peaks of nominal stress. **b)** Dependence of the relative size of overload surfaces on the peak of nominal stress.

The size analysis of the fracture surfaces reveals that the total fatigue crack area scales inversely with the maximum nominal stress (Figure 4-15b). When the fatigue loading is near the endurance limit, the total crack area reaches almost 50% of the whole cross-section at  $40^\circ\text{C}$ , and 40% at  $80^\circ\text{C}$ . In contrast, for fatigue loadings near the martensitic transformation regime, the total crack size drops down to  $\sim 10\%$ . This evidences that the transformation of the entire cross-section into B19' results in a higher concentration of the stress at the crack tip, which accelerates the crack propagation. In addition, when nominal fatigue loadings

involve martensitic transformation, the crack initiation, quasi-cleavage, and fatigue striation zones occupy in total less than 5% of the initial cross-section (blue curve in Figure 4-16). Therefore, the quasi-cleavage zone of the crack may be often omitted in the analysis of fatigue cracks of NiTi wires cycled in the martensitic transformation regime [127].

In addition, we evaluated the axial nominal stresses at the final overload taking into account measured tensile force at the moment of rupture and the reduced cross-section measured on the optical microscope. As seen in Figure 4-17, the axial nominal stresses at rupture scatter around a constant average value for a given testing temperature and all applied loadings. The average axial nominal stress for the testing temperature of 80°C (~1000 MPa) was substantially higher compared to 60°C (~820MPa) and 40°C (~750 MPa). For most of the tests, the axial nominal stress acting at the final failure on the reduced cross-section exceeded the B19' transformation stress  $\sigma_{MT}$  (see Figure 4-17). Since we determined

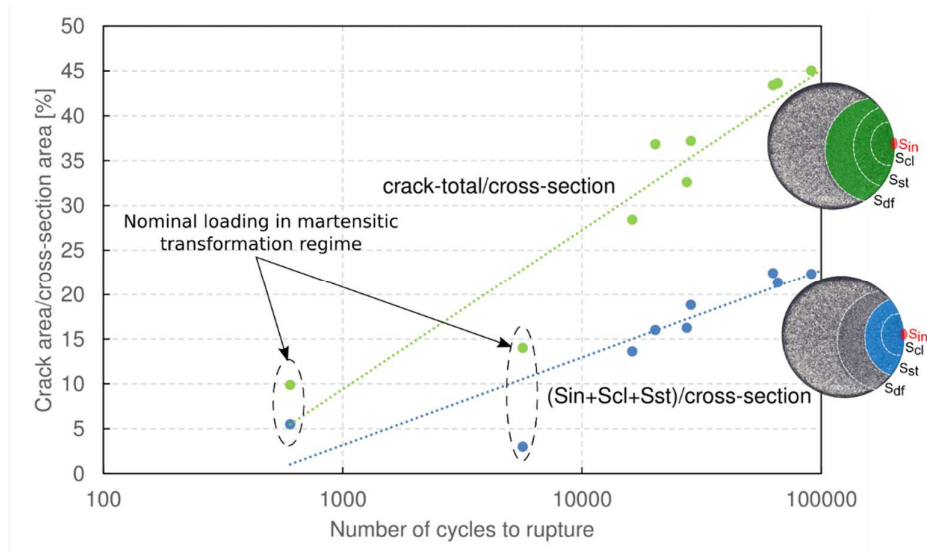


Figure 4-16 Evolutions of crack surface areas with the number of cycles to rupture identified for fatigue testing temperature of 40°C. The total crack area is plotted in green. A part of the crack area including crack initiation, quasi-cleavage, and fatigue striation zones is plotted in blue.

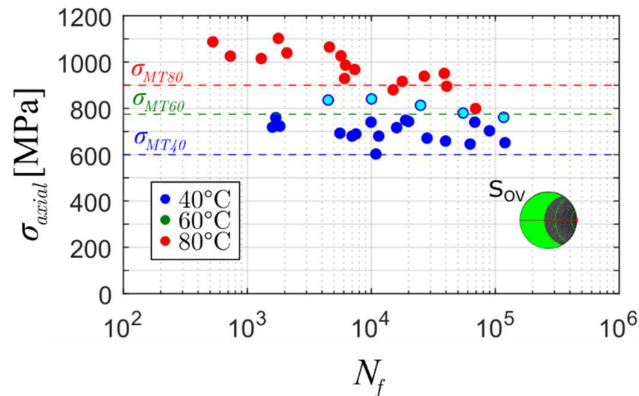


Figure 4-17 Nominal axial stresses at the final overload evaluated for testing temperatures of 40°C, 60°C, and 80°C. The stress in the y-axis was calculated as the ratio between the force at the instant of rupture and the overload surface identified by microscopy ( $S_{ov}$ ).

before that the ultimate strength of the material was  $\sim 1600\text{MPa}$  regardless of the temperature (Figure 4-5), the values shown in Figure 4-17 reveal an acceleration of the final rupture when the entire cross section transforms into B19' martensite.

#### 4.4.3. Tensile response evolution

The fatigue tests revealed that the lifetime of the studied NiTi wires is highly reduced from  $10^6$  to  $10^4$  cycles even before the nominal fatigue loadings reach the martensitic transformation regime and related high strains. However, analysis of fatigue crack surfaces showed that the normal stress acting in the reduced fatigue overloaded cross-section is well above the stress needed to induce the martensitic transformation. It suggests that the fatigue cycling in elastic or R-phase transformation regimes switches into the martensitic transformation regime once the crack reaches a critical size. Note that here we simplify and disregard the complex stress concentration at the crack tip where localized martensitic transformation may be triggered before the normal stress reaches the critical value. Nevertheless, to verify this scenario we performed dedicated experiments focused on the evolution of hysteresis, crack opening and temperature changes within the gauge volume. Note in advance that the fast thermography during complete fatigue tests indeed revealed that the fatigue damage triggers local transformation processes in  $2/3^{\text{rd}}$  of the lifetime and that the final failure is accompanied by inhomogeneous transformation processes. Moreover, the transformation deformation proved to assist the crack growth as it enlarges the crack opening.

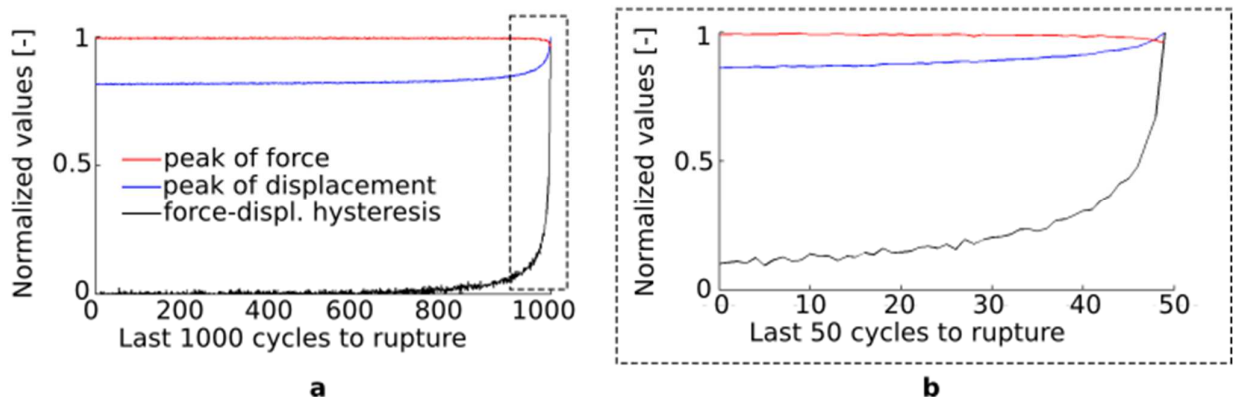


Figure 4-18 The evolution of fatigue loading in terms of peaks of force and extensometer displacement, and force-displacement hysteresis in last 1,000 cycles before failure (a) with a zoom to last 50 cycles (b) where the loading conditions evolve with the highest rate. The results correspond to fatigue cycling at  $40^{\circ}\text{C}$  with the maximum nominal stress of  $430\text{MPa}$ .

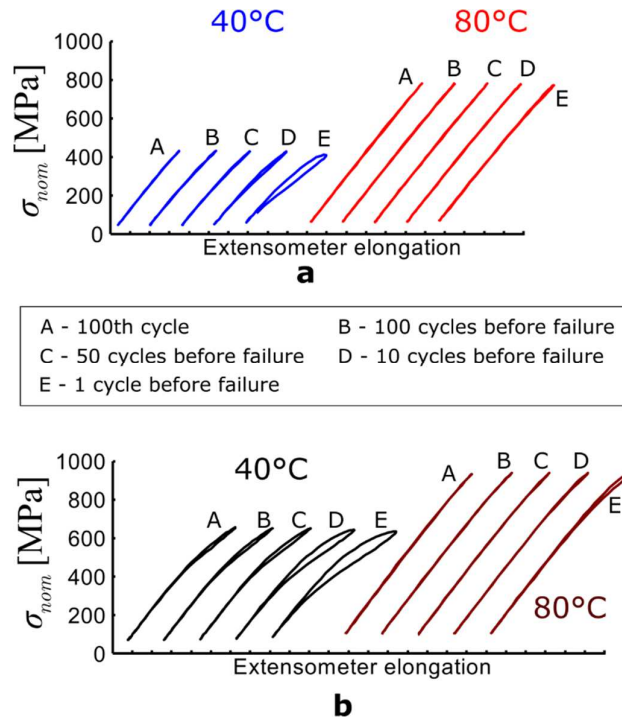


Figure 4-19 Evolution of tensile responses of hourglass shaped samples over 100 cycles before failure during fatigue cycling in a force controlled regime with peaks of nominal stresses below the martensitic transformation regime at 40°C a), 80°C b), and within the martensitic transformation regime at 40°C c). Related evolutions of force-displacement hysteresis are shown in d). Note that the cyclic responses and hysteresis do not change over cycling until few tens of cycles before fatigue failure.

The transition towards martensitic transformation regime is noticeable by tracking the evolution of force-displacement hysteresis during the tensile test. As seen in Figure 4-18 and Figure 4-19, the hysteresis starts to increase progressively a few tens of cycles before the rupture, which is due to an increase of the deformation as the fatigue tests were force controlled. In the very last stage of the fatigue tests, the deformation increased beyond the limits of elastic and R-phase transformation in an unstable manner so that the tensile machine was unable to control the force amplitude, which actually dropped while the displacement amplitude kept increasing as shown in Figure 4-18b. The increase in hysteresis is more pronounced for nominal fatigue loadings in R-phase or martensitic transformation regimes compared to the elastic regime at 80°C as illustrated in Figure 4-19.

#### 4.4.3.1. Monotonic rupture of an arrested fatigue test

The uncontrolled increase of the hysteresis indicates that an unstable crack growth occurs. To verify this, we arrested a fatigue test at the onset of the hysteresis increase (Figure 4-20). The arrested test was performed at 40°C, 25Hz, R=0.1 and maximum nominal stress of 580MPa being below the stress inducing the martensitic transformation. After the arrest, the sample was tensile loaded until rupture at room temperature (32°C) while measuring the crack opening and local strains near the crack using DIC (Figure 4-21). The fracture surface was then compared to the fracture surface of a sample cycled under the same conditions (Figure 4-20b). When comparing their respective fatigue surfaces, the fatigue crack

penetration depth from the arrested test was only  $81\mu\text{m}$  shorter and the crack surface 7% smaller, evidencing the advanced stage of fatigue crack propagation at which the test was arrested. At this stage, the maximum normal stress in the reduced cross-section was high enough to induce the martensitic transformation and related strains in the entire cross section.

Measurements of local strains near the crack upon post-fatigue tensile loading (Figure 4-21) revealed the critical effect of the transformation strain to the crack opening. In fact, the crack opening is enhanced by large strains ahead of the crack caused apparently by stress-induced martensitic transformation. For simplified interpretation, let us assume that the local tensile deformations increase more than to 1% when the B19' transformation is induced. Between stages A-D, local deformations larger than 1% appears gradually from the stress concentration at the crack tip (purple extensometer Figure 4-21a&b) towards the rest of the reduced cross-section (blue and green extensometers in Figure 4-21a&b). The red extensometer shown in Figure 4-21a measured the crack opening during the tensile loading, which is shown in Figure 4-21c together with the displacement and tensile force values measured during the test. From the material deformation values measured by the virtual extensometers, we deduced the evolution of the B19' martensite phase near the crack tip, illustrated by the red zone in Figure 4-21a. At the stage marked as B, the transformation reached already the blue extensometer, as presumed from the measured axial strain (3.5%). Some instants before the entire cross-section transformation (at stage C), the deformation at the crack tip is already 9% (purple extensometer). When the transformation proceeds,

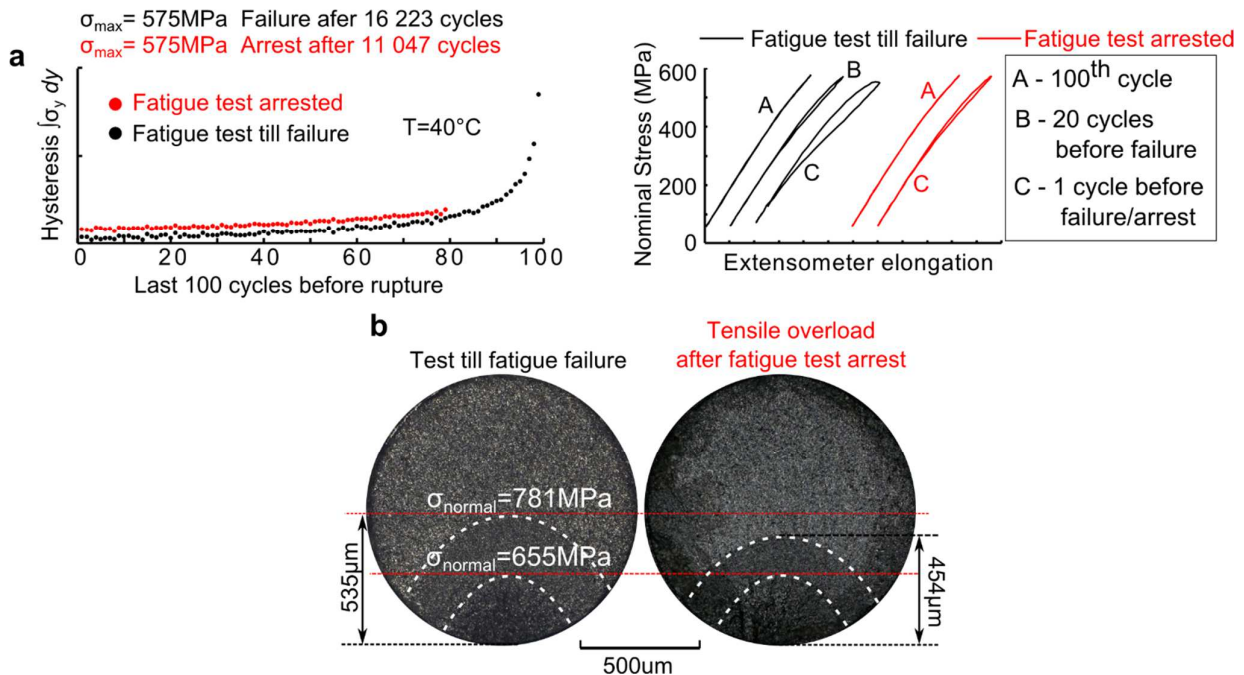


Figure 4-20 Observations of fatigue damage of an hourglass sample prior to fatigue failure at the onset of hysteresis increase upon which the fatigue test was arrested a). The arrested fatigue test was performed at  $40^\circ\text{C}$  with R ratio of 0.1, maximum nominal stress at 580 MPa being below the nominal stress for martensitic transformation. b) A large crack was located on the sample and its opening was measured upon quasistatic tensile overloading at room temperature ( $32^\circ\text{C}$ ).

the crack experiences a sudden opening of  $20\mu\text{m}$ , inducing a material deformation of 25% in the purple extensometer, 20% in the blue, and 6% in the green. The large deformations of the purple and blue extensometers are by far beyond the reversible strains accommodated at moderate plateau stresses by the B19' martensitic transformation. Hence, very high stresses must arise at the crack tip. Indeed, the rupture occurred immediately after stage D.

To sum up, the large macroscopic deformation associated to the stress-induced martensitic transformation in the entire cross-section leads to large local strains near the crack tip, which are far beyond the limits of transformed martensite, and presumably induce very high stresses; thus, assisting the crack opening and promoting the crack growth.

#### 4.4.3.2. Detection of crack initiation via fast thermography

In order to give a further insight of the course of the fatigue damage, we took advantage of the latent heat exchange due to the R-phase and B19' martensitic transformations for identifying the onset of cracks during cyclic loading. For this purpose, we performed fast thermography (800 frames per second) during complete fatigue tests at two different temperatures. Note that because of limited computer memory capacity, we could not perform the fatigue testing continuously but in several slots, each of them containing a limited number of cycles. The fatigue tests were performed with nominal loadings below the martensitic transformation regime expecting appearances of localized heat sources related to phase transforming zones triggered by stress concentrations at crack tips [128]. The test at  $40^\circ\text{C}$  was performed with a maximum nominal stress of 565 MPa. In this test, the failure occurred after 19518 cycles. The test at  $80^\circ\text{C}$  was performed with the maximal nominal stress of 900 Mpa, and failure reported after 1802 cycles. First, we evaluated time evolutions of temperature averaged over the gauge volume as shown in Figure 4-22a&b. The average temperature evolves within a cycle and over cycling as shown in Figure 4-22c&d.

For understanding the one-cycle temperature evolutions, one has to consider simultaneous actions of the thermoelastic effect and latent heat exchange due to both the R-phase and martensitic transformations. While the thermoelasticity cools down the sample upon loading and heats up the sample upon unloading, the transformation heats up the sample upon loading due to latent heat release and cools down the sample by latent heat absorption upon unloading. Furthermore, large transformation enthalpies that characterize NiTi make the heat effects of transformations higher by orders of magnitude compared to thermoelasticity [129].

With the previous paragraph in mind, one can see in Figure 4-22c&d that the extent of R-phase transformation, i.e. heating/cooling upon loading/unloading, is higher at  $40^\circ\text{C}$  than at  $80^\circ\text{C}$ . Moreover, as seen in Figure 4-22a&b, the temperature maxima starts rising in the final stage of the fatigue life with a noticeably earlier onset of the increase for the test at  $40^\circ\text{C}$ . Recall that a similar effect was pointed out upon the onset of the hysteresis increase (Figure 4-18). However, unlike the hysteresis rising few tens of cycles before rupture, the temperature maxima start rising earlier – few hundreds of cycles before the failure.

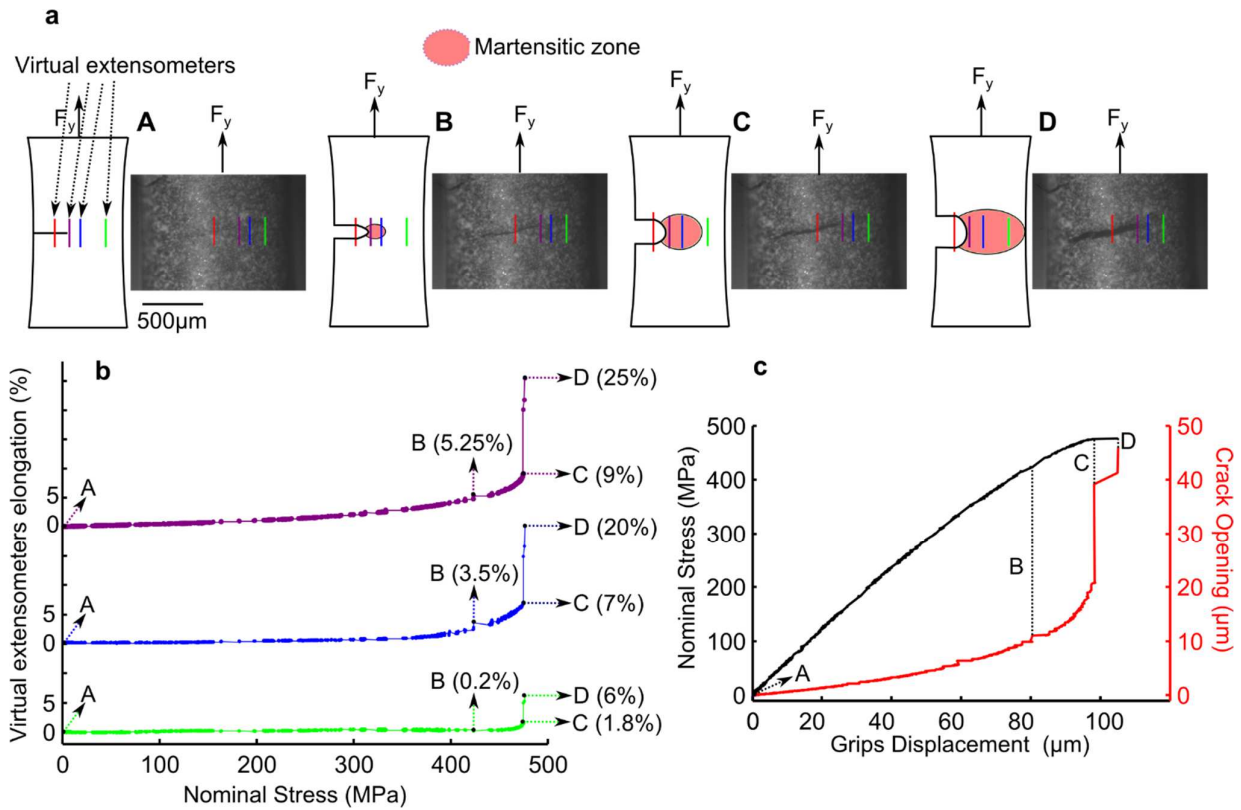


Figure 4-21 The crack opening and local strains near the crack as measured on the sample after a fatigue test arrest prior to failure as described in Fig. 12. The measurement was performed during a force controlled tensile test till failure. Spread of martensitically transforming zone illustrated in **a**) is based on three virtual extensometers' elongation measurements near the crack tip **b**) and on the crack opening measurement **c**) all realized using DIC method.

Besides spatial temperature averaging, thermographs reveal local heat effects that, in the case of phase transforming NiTi, may be related to localized damage acting as a stress riser; thus, triggering transformations locally [128]. However, transformations triggered by nominal loadings give rise to noticeable periodic temperature changes as seen in Figure 4-22c&d, which hide weaker local heat phenomena. Therefore, we created what we called “differential thermographs”, which show the temperature changes upon fatigue loading with respect to the temperature changes observed upon one reference cycle in the non-damaged state. To be more specific, a cycle of differential thermographs was computed by subtracting the thermographs of the first cycle from the thermographs of a later fatigue cycle recorded at equal cyclic force phase. In addition, a moving average was applied over few tens of cycles to filter out random noise. Differential thermographs allow revealing weak local heat effects giving rise to temperature changes smaller than 0.1°C. Using this technique, we were able to capture first periodic appearances of localized heat sources at approximately 2/3<sup>rd</sup> of the fatigue life, i.e. 6,000 cycles before rupture for the test at 40°C (Figure 4-23a) and 600 cycles before rupture for the test at 80°C (Figure 4-23b). In the case of the test at 40°C, a second localized heat spot appeared 3,000 cycles before rupture as seen in Figure 4-23a. With further cycling, localized heat sources develop and grow until finally becoming well visible large localized heat spots a few tens of cycles before rupture (Figure 4-23c&d). The temperature

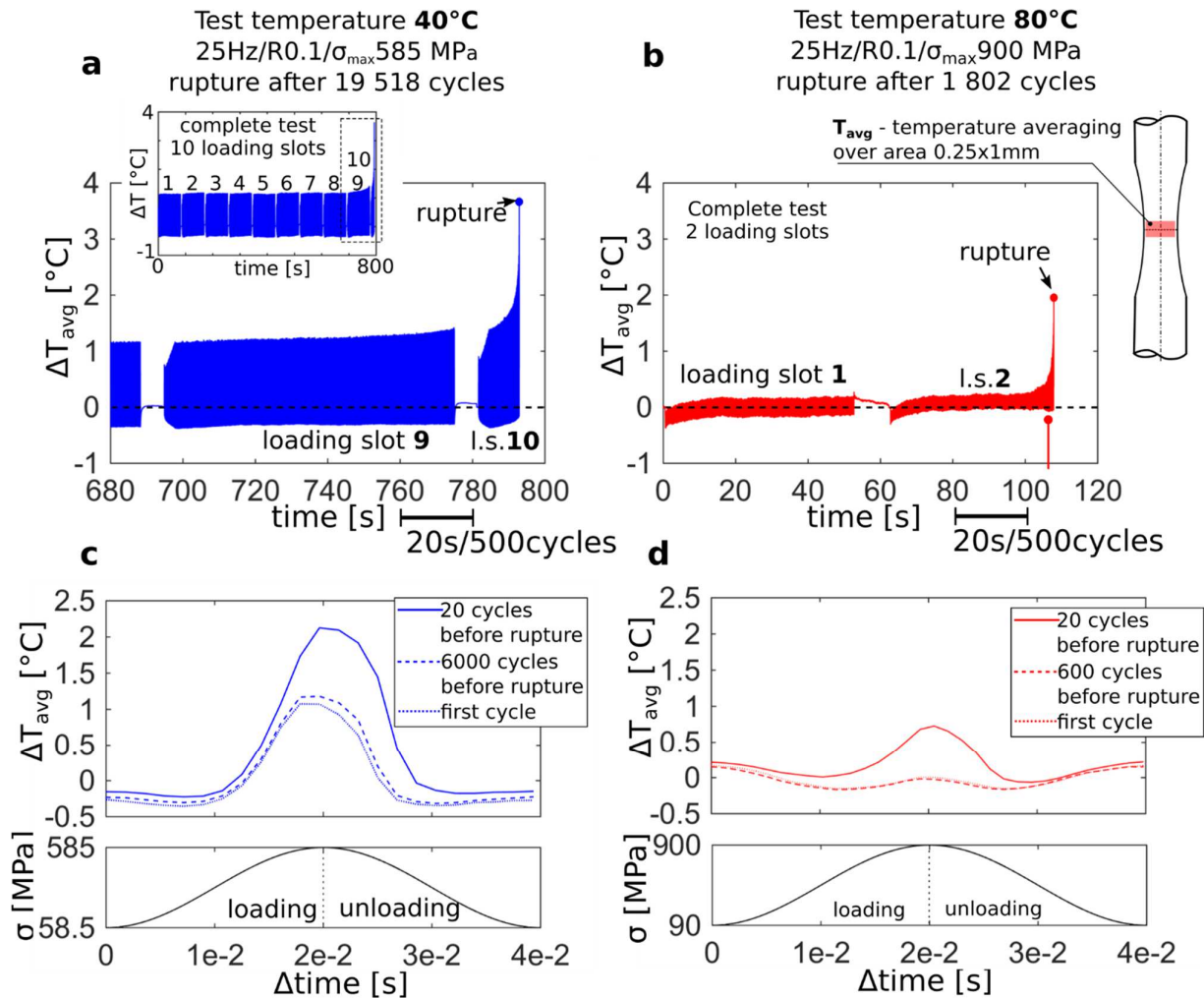


Figure 4-22 Evolutions of temperature averaged over the gauge volume as recorded by IR camera during two fatigue tests performed for limited RAM in several interrupted slots; the first test lasting  $\sim 20\text{e}3$  cycles was performed at  $40^\circ\text{C}$ ,  $R=0.1$ , 25 Hz, a maximal nominal stress 585 MPa; the second test lasting  $\sim 2\text{e}3$  cycles was performed at  $80^\circ\text{C}$ ,  $R=0.1$ , 25 Hz, peak of nominal stress 900 MPa. Graphs a) b) show temperature evolutions during complete tests at  $40^\circ\text{C}$  and  $80^\circ\text{C}$ , respectively. Graphs c) d) show one cycle temperature and stress evolutions in selected cycles of tests at  $40^\circ\text{C}$  and  $80^\circ\text{C}$ , respectively.

in the latter case showed temperature changes up to a few degrees Celsius. Note that in the case of the test at  $40^\circ\text{C}$ , the secondly appeared heat effect grew faster than the one that appeared first, causing the final failure. The heat effects were more pronounced for the test at  $40^\circ\text{C}$ , likely due to higher number of cycles to rupture (20,000 vs. 1,800) and, hence, larger crack size (Figure 4-23c); thus, allowing for larger crack openings. We attribute the appearance of localized periodic heat effects with progressive intensity to the B19' martensitic transformation triggered by the stress concentration at the tip of a well-developed steadily growing crack, i.e. zone 3 of the fatigue crack marked with fatigue striations (Figure 4-13).

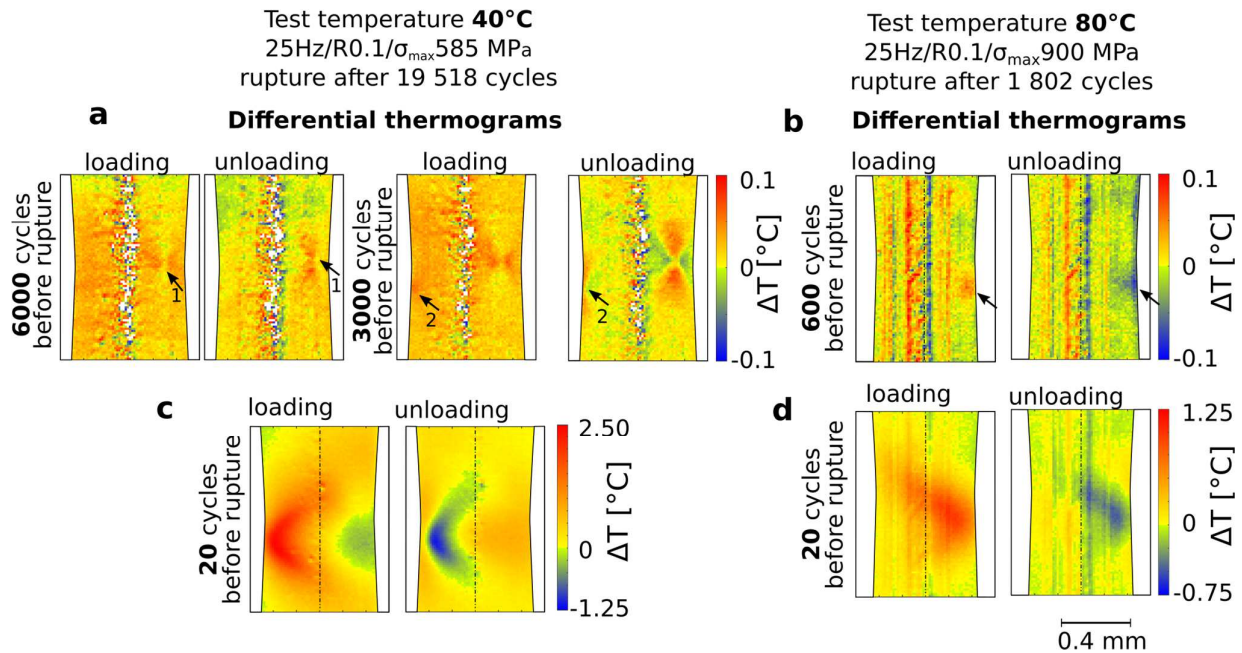


Figure 4-23 Differential thermographs that evaluate spatially temperature changes with respect to the virgin state recorded in the first fatigue cycle. Thermographs show temperature changes within the gauge volumes of hourglass samples at different cycles of two fatigue tests. The first test, lasting  $\sim 20 \times 10^3$  cycles, was performed at 40°C,  $R=0.1$ , 25 Hz and a maximal nominal stress of 585 MPa. The second test, lasting  $\sim 2 \times 10^3$  cycles, was performed at 80°C,  $R=0.1$ , 25 Hz and a maximal nominal stress of 900 MPa. Thermographs in (a) show two localized heat sources as first spotted 6,000 and 3,000 cycles before rupture during the test at 40°C. Thermographs in (b) show localized heat source as first spotted 600 cycles before rupture during the test at 80°C. Thermographs in (c) & (d) show localized heat sources 20 cycles before rupture of both the tests.

## 4.5. Microstructure evolution evaluated via high resolution x-ray diffraction

In order to better understand microstructure changes and the course of martensitic transformation in superelastic NiTi subjected to cyclic loadings, two diffraction studies were performed using high synchrotron X-ray at ESRF facility, Grenoble, which provided proposal based beamtime. The first study of the experiment no. MA-2880 focused on the microstructure assessment of hourglass superelastic NiTi samples subjected ex-situ and in-situ cyclic loadings in the elastic and transformation regimes. The second study focused on the role of stress risers on the course of the martensitic transformation and related irreversible microstructure changes. However, the large dataset recorded during the second experiment is still ongoing and, therefore, its results will not be presented.

The main aim of probing the hourglass samples by high energy synchrotron x-ray was to evaluate the effect of fatigue cycling in elastic regime on microstructure changes that might be a sign of early fatigue failure. However, the very first on-site comparison of diffraction patterns of virgin and fatigued samples revealed very little changes.

In order to assess the microstructural changes due to fatigue cycling in the elastic regime of superelastic NiTi, we compared axial diffraction scans at stress free conditions of a virgin

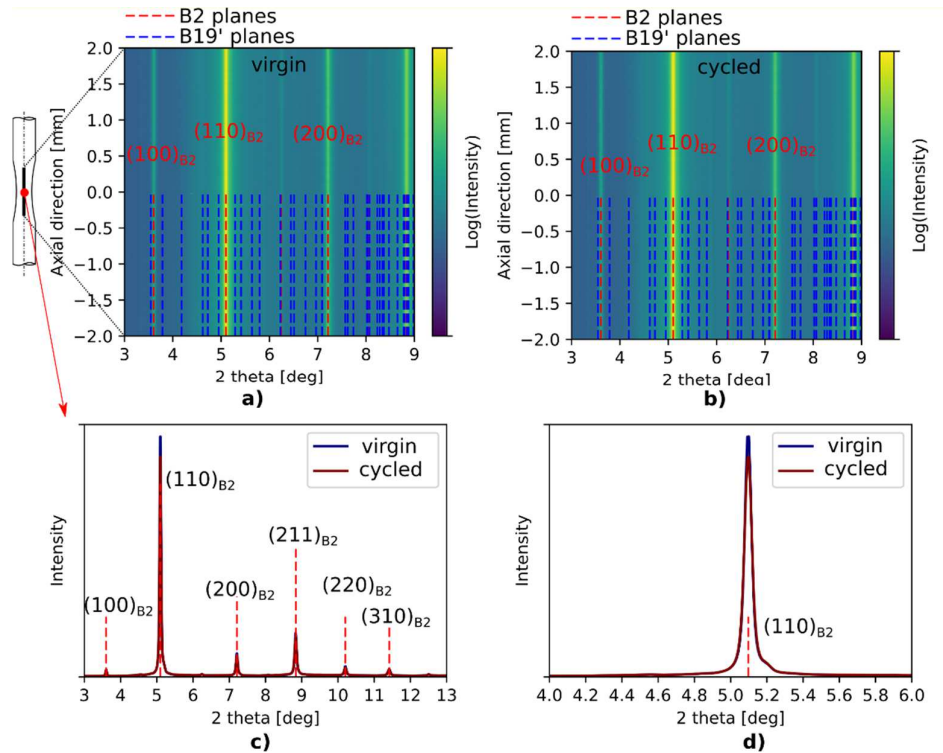


Figure 4-24 Comparisons of diffraction patterns recorded on a virgin sample a) and sample that was subjected to 1000 cycles at 80 °C, R=0.1 and maximum stress of 880 MPa b). Colormaps in a), b) represents diffraction patterns acquired during scanning along the axial direction. Diffraction patterns shown in c), d) were recorded approximately in the center of the concave zone of the sample.

sample and a sample that was subjected to 1000 fatigue cycles at 80 °C, R = 0.1, and maximum stress of 880 MPa. Note that the cycling was performed in the elastic regime; however, the plateau stress was only few MPa above the maximum applied stress. Surprisingly, as seen in Figure 4-24, either the changes in the microstructure due to this fatigue cycling had negligible effect on the diffraction patterns or the effect was below the angular resolution provided by the experimental setup.

## 4.6. Summary

In the present experimental work, we studied the fatigue performance of superelastic NiTi wires processed into hourglass shaped samples in order to analyze the effect of deformation processes and related strains involved in individual stress controlled pull-pull fatigue tests. Elastic deformations and deformations due to stress-induced transformations to R-phase and martensite were considered and carefully assigned to individual test amplitudes and temperatures using thermography and DIC. The main experimental data obtained in the present study is summarized in Stress-Strain-N fatigue curves for NiTi tested at 40°C, 60°C and 80°C (Figure 4-9). At 40°C, the R-phase transformation is more pronounced than at 60°C and 80°C. The B19' martensitic transformation was triggered at 600 MPa at 40°C, while at 60°C and 80°C, the B19' martensitic transformation was triggered at 775MPa and 900 MPa respectively. Furthermore, fracture surfaces were analyzed allowing us to identify

five zones of distinct fracture morphologies related to the degree of the fatigue fracture advancement (Figure 4-10). To give a further insight of the course of the fatigue damage, we investigated force-load hysteresis (Figure 4-19) and temperature evolutions over cycling (Figure 4-22) and crack opening of a fatigue cracked sample (Figure 4-21). To track down the fatigue damage we used fast thermography during complete fatigue tests to spot localized heat effects expected to arise from phase transformation events localized at the advancing crack tip (Figure 4-23).

To sum up, our experiments showed that the fatigue performance of superelastic NiTi wires at 40°C, 60°C and 80°C drops down from millions to thousands of cycles at stress of 417 MPa 535MPa and 540 MPa respectively, being well below the stresses inducing the B19' martensitic transformation that were 600 MPa, 775MPa and 900 MPa respectively. Moreover, the strain endurance limits were reached at low strains of 0.58 % (40°C) and 0.65 % (80°C). It suggests that high strains related to martensitic transformation are not necessarily responsible for fast crack nucleation and early crack growth reported in superelastic NiTi. On the one hand, the R-phase transformation proved to prolong the low cycle fatigue as it acts as a stress reliever reducing largely the stresses at higher strains above 0.9%. On the other hand, the martensitic transformation proved to assist the crack growth when its critical size is reached. In fact, when the critical crack size is reached, the strains due to martensitic transformation provide additional driving force for the crack opening. Unfortunately, the critical crack size is reached sooner when nominal loadings are closer to the plateau stress i.e. the critical stress for the onset of martensitic transformation. Nevertheless, our results preserve the hope for high cycle superelasticity that might be possible if the plateau stresses for martensitic transformation are lowered down below the structural fatigue limits inducing early crack nucleation and growth.

Conclusions drawn from different aspects of our experimental work are further detailed and summarized hereinafter.

The following conclusions were drawn from the Stress-Strain-N fatigue curves (Figure 4-9) measured on commercial cold drawn superelastic NiTi of diameter 1.78 mm. The fatigue testing was performed in pull-pull force controlled regime with nominal stress ratio 0.1, frequency 25 Hz, and runout limit set to 1.5e6 cycles.

1. The endurance limits in terms of the maximum nominal stress were reached at 417MPa, 535MPa and 540 MPa for NiTi exhibiting R-phase transformation at 40°C, and NiTi with retarded R-phase transformation at 60°C and 80°C respectively.
2. The endurance limits in terms of the maximum nominal stress were reached at 183MPa 240MPa and 360MPa below the critical stress for the onset of B19' martensitic transformation at 40°C, 60°C and 80°C.
3. The mean stress proved to have a higher detrimental impact on the fatigue behavior of elastically loaded NiTi. In contrast, when NiTi develops R-phase, the mean stresses are relieved through the transformation strains, thus lowering their impact on the lifetime of the material.

4. The equivalent endurance limits in terms of the maximum stabilized strain were reached at 0.65 % and 0.70 % for NiTi exhibiting R-phase transformation and NiTi with retarded R-phase transformation, respectively.
5. The fatigue life drops down to  $10^4$  cycles before the maximum nominal stress reaches the critical value for the onset of martensitic transformation.
6. The fatigue life drops down to  $10^4$  cycles before the peak of stabilized strains reaches 1%.
7. The fatigue life drops from  $10^4$  to  $10^3$  cycles when the maximum nominal stress enters the regime of martensitic transformation.
8. NiTi with retarded R-phase performs better than NiTi with pronounced R-phase for maximum strains lower than 0.65%. Beyond 0.65% the R-phase transformation acts as a stress reliever, hence, improving the fatigue behavior, which equals that of the elastically loaded NiTi.

Thorough analysis of fracture surfaces using 3D light microscope and SEM resulted in the following conclusions:

1. In terms of the percentage of the initial cross-section, the fatigue fracture size drops from 50% in the case of runout tests ( $1.5 \times 10^6$  cycles) down to 10% in the case of tests lasting few thousands of cycles.
2. The fracture surface contains in general five distinct zones (Fig. 6) successively forming during fatigue crack growth as follows – 1. Fracture initiation at the surface; 2. Quasi-cleavage zone; 3. Fatigue striation zone; 4. Ductile fatigue crack zone; 5. Ductile final overload zone.
3. Multiple cracks initiate at the surface of the wire. The brittle fracture features in the quasi-cleavage zone near the crack initiation points denote failure of NiTi in the B2 austenite state. Upon propagation, plasticity evolves together with quasi-cleavage. Multiple initiated cracks forms a greater crack front that propagate at higher rates inducing local B19' phase transformations at the crack tip.
4. Independently of the applied fatigue loading, the normal stress acting on the overload surface is higher than the stress needed for martensitic transformation to proceed (Fig. 9).

Dedicated supporting experiments based on the measurement of force-displacement hysteresis and fast thermography (Figure 4-18 - Figure 4-23) enabled the following conclusions:

1. The last stage of the fatigue life lasting few tens of cycles is characterized by an unstable ductile fatigue fracture growth assisted by martensitic transformation proceeding massively and inhomogenously within the gauge volume.
2. In the last stage of the fatigue life, the martensitic transformation proceeding in the reduced cross-section dramatically decreases the resistance against the crack opening thus promoting high strains at the crack tip by far exceeding the reversible superelastic strains.

3. Periodic localized phase transformation events probably arising from stress concentrating crack tips were spotted in 2/3rd of the fatigue life.
4. The periodic localized transformation events are believed to be linked to the steady crack growth marked with fatigue striations formation. At this stage, the crack growth is thus assisted by the martensitic transformation enhancing the crack opening that leads to large strains beyond superelastic limits.

The present experimental study used some particular techniques enabling better analysis of fatigue processes in phase transforming NiTi such as:

1. The hourglass type shape of samples enables to effectively confine all transformation and fatigue processes into a well-defined gauge volume.
2. The hourglass type shape of specimens enables to avoid transformation deformation localization, and, hence, to study a true strain dependence of fatigue life in phase transforming NiTi.
3. The thermography is a unique tool that enables to precisely associate transformation processes to individual applied fatigue loadings.
4. The last stage of the fatigue life can be effectively captured by measuring the evolution of the force-displacement hysteresis that increases noticeably few tens of cycles before rupture.
5. The fast thermography using sensitive photon detectors enables to spot, well before rupture, the stress concentrating fatigue damage giving rise to localized heat effects through phase transformation latent heat exchange.

# Chapter 5. Fatigue Assessment of NiTi Wires through the Self-Heating Method

The self-heating method has been developed as an alternative to the classic stress-life approach (based on obtaining S-N curves), with the purpose of evaluating the HCF properties of engineering materials in a much faster way. The main idea of the method consists in characterizing the dissipated heat of samples tested under constant amplitude loading conditions. Hence, the method presumes that the origin of fatigue damage is the same as the one that generates the heat dissipation. The success of the method in predicting the lifetimes of several engineering materials has popularized it among engineers. In principle, the self-heating method permits to assess the fatigue behavior with only one sample and a couple of hours of testing, instead of weeks or even months of tests using a considerable amount of samples in order to complete an S-N curve.

In this chapter, we start by introducing the fundamentals of the self-heating method and its relationship with fatigue processes, especially in structural alloys. After that, we present the experimental protocol designed for applying the self-heating method to our NiTi hourglass-shaped samples. Then, we present the experimental results obtained upon tests at different temperatures and loading frequencies. The analysis of the observed phenomena is then carried out using modeling techniques, Fourier spectrum analysis, and supplementary monotonic tensile tests.

## Contents

<b>5.1. Description of the self-heating method.....</b>	<b>143</b>
5.1.1. Background.....	143
5.1.1.1. Basic experimental setup.....	144
5.1.1.2. Study Cases.....	146
5.1.1.3. Concurrent sources of heat dissipation and fatigue damage.....	148
5.1.2. Thermodynamic framework.....	149
5.1.2.1. <i>Zero-dimensional</i> diffusion problem.....	150
5.1.2.2. <i>One-dimensional</i> diffusion problem.....	151
<b>5.2. Experimental protocol.....</b>	<b>153</b>
5.2.1. Experimental setup.....	153
5.2.2. Post-processing of temperature data.....	155

5.2.2.1. Identification of the stabilized temperature elevation.....	156
<b>5.3. Experimental results.....</b>	<b>158</b>
5.3.1. Self-heating curves .....	158
5.3.2. Effects of the loading frequency .....	160
5.3.3. Evolution of the temperature harmonics.....	162
5.3.4. Influence of the shape of the sample .....	165
5.3.5. Temperature evolution during monotonic tensile tests.....	167
<b>5.4. Modeling of the thermomechanical behavior of NiTi.....</b>	<b>172</b>
5.4.1. 1D diffusion problem in hourglass-shaped samples.....	172
5.4.1.1. Thermoelastic coupling .....	175
5.4.1.2. Phase transformation thermomechanical coupling.....	178
5.4.2. Identification of the heat exchange coefficients .....	178
5.4.3. Cyclic thermoelastic effect .....	181
5.4.4. Cyclic phase transformation latent heat .....	182
5.4.5. Interaction between the thermoelastic effect and the transformation latent heats .....	184

## 5.1. Description of the self-heating method

### 5.1.1. Background

The first measurements of the temperature elevation of a piece of material subjected to cyclic loading and its relation to fatigue phenomena date back to experiments carried out by Stromeyer in 1914 [131]. Stromeyer developed a dedicated system for performing reversed torsion cyclic tests with *in situ* calorimetry measurements. He was able to correlate the fatigue endurance limit of three mild steels, two cast steels and one aluminum alloy to the heat evolved during tests performed at different alternating stress amplitudes. Although he left the door open to further analysis of the relationship between heat sources and fatigue processes, very few studies tackled this issue before the 1980's [132], [133].

The technological advances in the field of temperature measurement and signal acquisition from the 1980's, notably the development integrated circuits allowing analog to digital

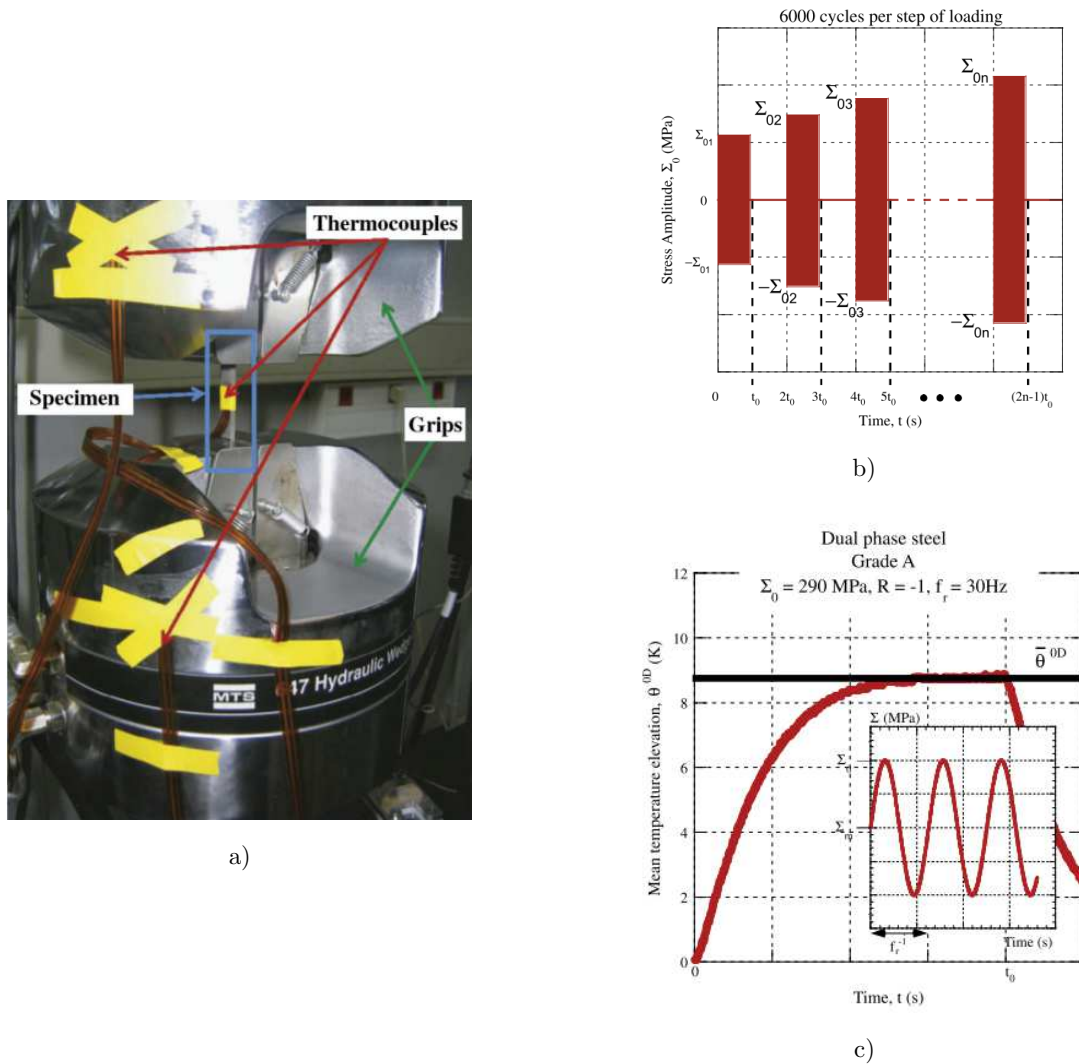


Figure 5-1 Basic experimental protocol for assessing the fatigue properties of materials using the self-heating method. The experimental setup image is shown in (a). The applied loading is presented in (b), and the equivalent temperature elevation in one block of constant amplitude cycles is illustrated in (c). The images were taken from [130].

conversion of thermocouple signals and more exciting focal plane array infrared detectors, facilitated the assessment of the temperature evolution during the application of mechanical loading [134]–[136]. As a result, the identification of stress amplitudes causing temperature elevation of samples subjected to repetitive alternating loading became a common matter of discussion among researchers dealing with the fatigue of materials.

Since the 1980’s, different methodologies for fast characterizing the fatigue properties of materials have been developed based on the coupling between cyclic loadings, temperature elevations and fatigue damage. The measurement principles of all of these techniques knock into shape the so-called “self-heating method”. In some works, such as in [134], the evaluation of fatigue properties through thermal measurements is also called “thermographic fatigue method”, which emphasize the use of full-field infrared thermography.

Next, we describe the basic experimental setup for carrying out self-heating measurements, thus, allowing in the first instance to determine the endurance limit of a material using only one sample and a couple of hours of testing. After that, we will present some case studies in which the self-heating method has been proved as an efficient fast fatigue characterization technique.

#### 5.1.1.1. Basic experimental setup

The basic experimental setup for measuring the self-heating of a material sample in laboratory conditions is described in Figure 5-1 after Munier et al[130]. In this example, a constant cross-section dual phase steel flat sample was subjected to blocks of 6000 cycles of constant stress amplitude (denoted as  $\Sigma_0$  in Figure 5-1) at a stress ratio  $R = -1$  (tension-compression repetitive stresses). The temperature of the sample upon cyclic loading was measured by means of a thermocouple type K attached to its surface. In order to determine the mean elevation temperature, two additional thermocouples were attached to the grips of

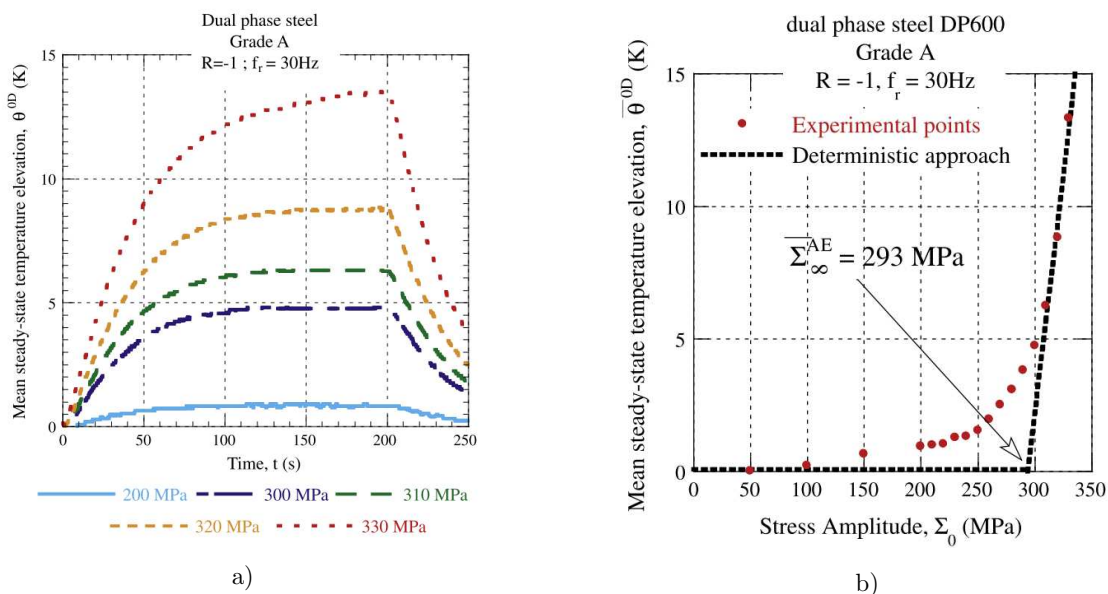


Figure 5-2 Deterministic approach for determining the endurance limit. Image replotted from [130].

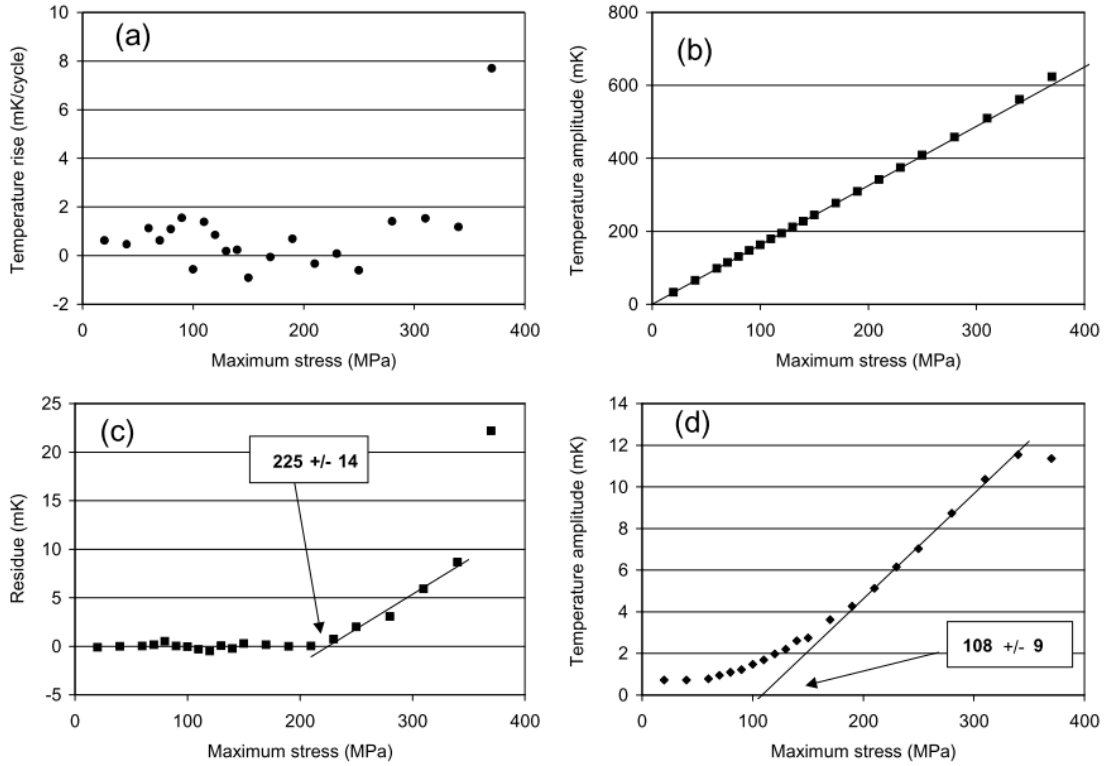


Figure 5-3 Lock-in technique used in the fast estimation of the endurance limit of a 7010 aluminum alloy.  
a) Mean temperature elevation. b) Amplitude of the first Fourier component. c) Difference between the amplitude of the first Fourier component and the linear fit of the first part of the curve shown in (b).  
d) Amplitude of the second Fourier component.

the testing machine (see Figure 5-1a); thus, the mean elevation temperature was calculated as

$$\theta = T_{sample} - \frac{T_{up} + T_{do}}{2} \quad (5.1)$$

where  $T_{sample}$  is the temperature in the middle of the sample, and  $T_{up}$  and  $T_{do}$  are the temperatures of the upper and lower grips respectively. The mean temperature elevation  $\theta$  resulted after one block of constant-amplitude cycles is illustrated in Figure 5-1c. Successive blocks of cycles following an increase of the stress amplitude are applied to the same sample in a range of stresses beneath the yield limit of the material (see Figure 5-1b). The steady-state temperature elevation, here denoted as  $\bar{\theta}$ , associated to each block of cycles is then plotted against the applied stress amplitude to construct the so-called “self-heating curve” (see Figure 5-2). The inflection point of the self-heating curve, at which the steady-state temperature elevation rise significantly, is correlated then with the endurance limit of the material (referred as  $\Sigma_{\infty}^{AE}$  in Figure 5-2a). This approach is denoted as deterministic since the shape of the curve is solely dependent on the applied loading, the thermal boundary conditions, and the material properties.

Another interesting possibility to capture the cyclic thermal behavior of a sample subjected to repetitive alternating loading consists in the use of the so-called “Lock-in technique”

applied together with infrared thermography. Krapez et al. [135] were one of the firsts to employ this technique to track the temperature elevation of samples subjected to alternating cyclic tensile-compressive stresses. By means of a focal plane array infrared detector, they evaluated the mean temperature elevation together with the first and second order harmonic amplitudes of the temperature signal, obtained after demodulation through Fourier spectral analysis. Hence, they wrote the temperature evolution of a sample ( $T$ ) subjected to cyclic loading as:

$$T = T_0 + \Delta Tft + T_1 \sin(\omega t + \varphi_1) + T_2 \sin(2\omega t + \varphi_2), \quad (5.2)$$

where  $t$  denotes the time,  $T_0$  is the temperature before the loading start,  $\Delta T$  is the mean temperature elevation,  $f = \omega/2\pi$  is the frequency of the cyclic loading and  $T_1$ ,  $\varphi_1$ ,  $T_2$ , and  $\varphi_2$  are the amplitude and phase components of the first and second Fourier components respectively. Figure 4-2 shows experimental results on a 7010 aluminum alloy sample. Figure 4-2a shows the evolution of  $\Delta T$  in terms of the maximum applied stresses per block of cycles, Figure 4-2b shows the equivalent for  $T_1$ , and Figure 4-2d the equivalent for  $T_2$ . In addition, Figure 4-2c illustrates the evolution of the difference between  $T_1$  and the linear fit of its linear part (shown in Figure 4-2b). In this example, the noise of the mean temperature evolution  $\Delta T$  (Figure 4-2a) hindered the deterministic identification of the endurance limit as presented above. However, the trend of the residuals in (Figure 4-2c) and in a lower degree the trend of the second Fourier amplitude component (Figure 4-2d), allowed the fast identification of the endurance limit of the material, estimated at  $210 \pm 20$ MPa.

#### 5.1.1.2. Study Cases

The self-heating method has been applied with success for determining the fatigue endurance limit of different alloys such as steels [135][130], aluminum alloys [135][137][138] and chrome-cobalt alloys [139]. It has been also effective for providing a fast characterization technique of the endurance limit of composite materials [140] and elastomers [141]. Figure 5-4 illustrates some representative examples reported in the literature. In all these cases, the method was applied to pieces of material processed into standard testing sample geometries. However, recent experimental results reported in the literature show that the self-heating method is also applicable to structural components such as connecting rods and welded assemblies [141], [142].

Apart from the fast prediction of the endurance limit, significant efforts have been made lately to provide a full characterization of the S-N-P curves (with P denoting the probability of rupture) based on the self-heating behavior of the material. Energy based fatigue models, combined with the characterization of the energy dissipation of the material from self-heating curves, provide a solid framework to explain the relationship between fatigue and thermal processes. The fundamentals of these models are based on the assumption that potential fatigue damage is localized in small and randomly distributed sites all over the material, which, upon the application of cyclic loading, dissipate energy/heat (see Figure 5-5a). For

## Self-heating curves

## S-N-P curves

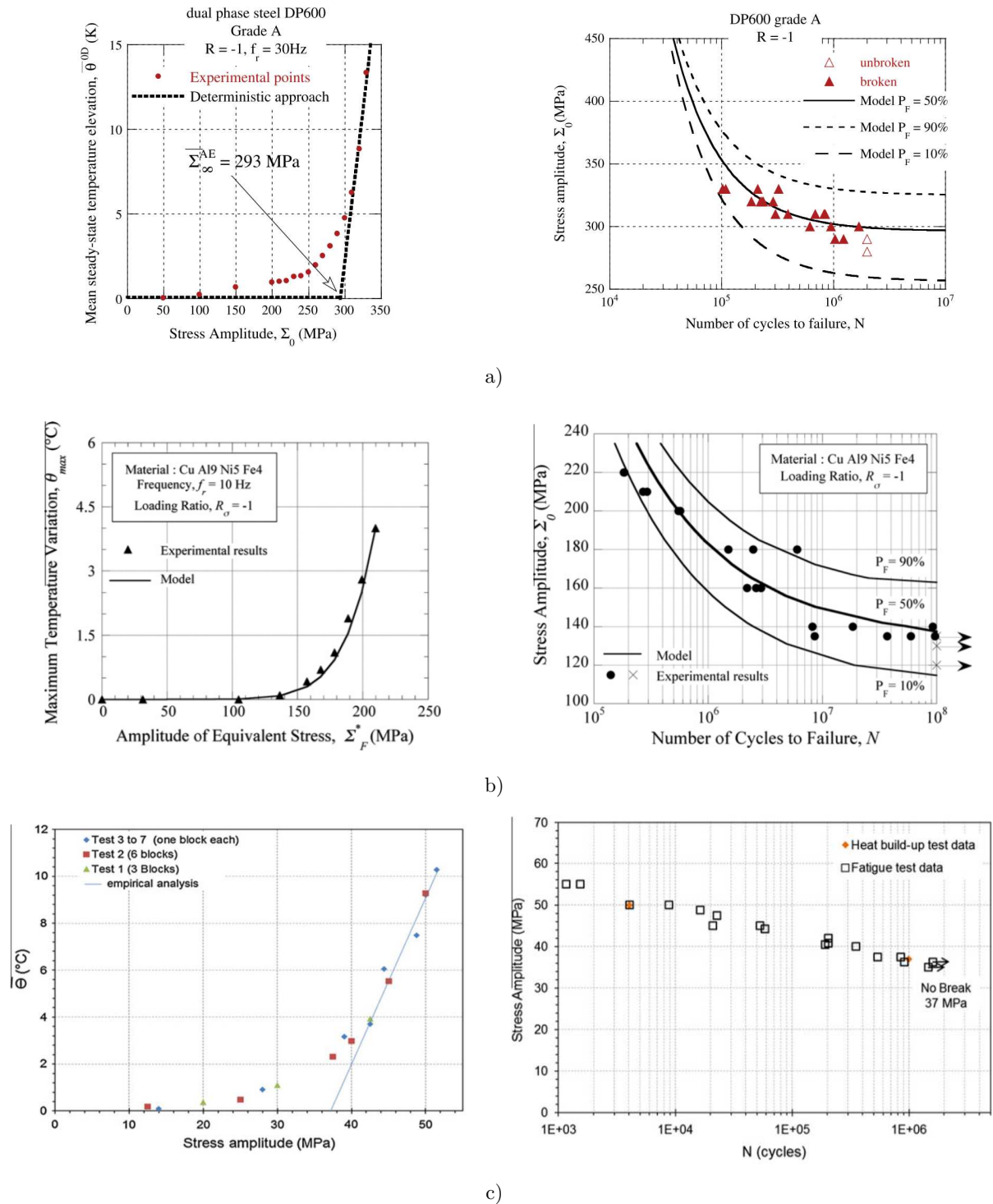


Figure 5-4 Validation of the self-heating fatigue prediction method for different materials. a) Dual phase steel [130]. b) Aluminum bronze [138]. c) Short fiber reinforced plastic [140].

modeling this phenomenon, multiscale approaches have been used. In [143], the problem is tackled by an Eshelby-type solution, in which the representative elementary volume of the material (REV) was described as an elastoplastic inclusion embedded in an infinite elastic

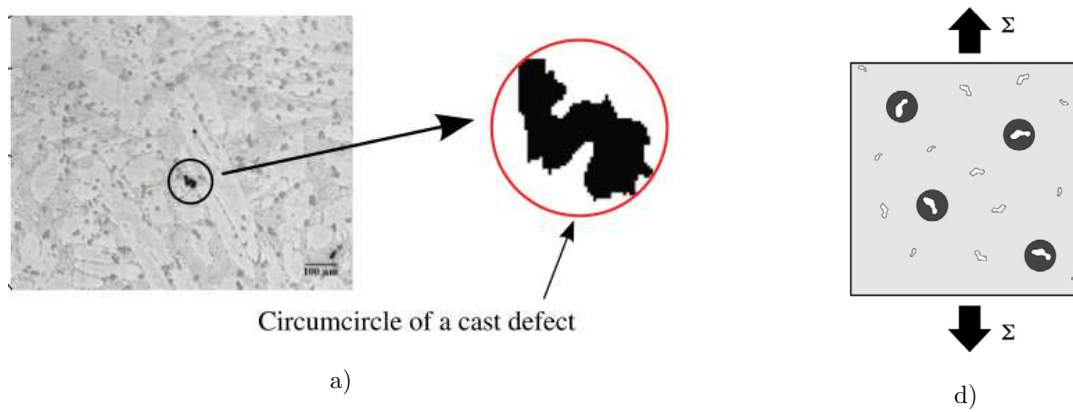


Figure 5-5 Material heterogeneities at the grain scale. a) Cast defects and phase segregation in a copper aluminum alloy [138]. b) Schematic of the representative elementary volume (REV) used for multiscale modeling of the self-heating curves.

matrix (see Figure 5-5b). In this model, the macroscopic stress that leads the inclusion to plastic yielding, and hence causing energy dissipation, is correlated to the endurance limit of the material. Modifications of this approach made in [144], propose that the plastic activation of an inclusion follows a Poisson distribution; thus, it included the probabilistic nature of fatigue phenomena. In order to improve the mathematical description of self-heating exhibiting temperature elevations even at low-stress amplitudes (e.g self-heating curve in Figure 5-4a), alternatives solutions such as the modeling of inclusions with dual-dissipative phenomena [145] and the modeling of elastoplastic inclusions embedded in an elastoplastic matrix [130] have been formulated. For instance, the probabilistic curves plotted with fatigue data in Figure 5-4a&b, have been modeled following the latest approach.

### 5.1.1.3. Concurrent sources of heat dissipation and fatigue damage

According to the material, different mechanisms of heat dissipation and fatigue damage are evidenced. For instance, in structural alloys, one of the most encountered fatigue mechanisms are the persistent slip bands (PSB). They are sites of highly localized plastic deformation that forms extrusion-intrusion patterns in the surface of a piece of alloy subjected to cyclic loading (Figure 5-6a). Such surface heterogeneities serve as initiation sites for microcracks, which, even at low rates of propagation engender localized plastic deformation and crystal debonding, both resulting in heat release. Other material heterogeneities such as precipitates, inclusion, grains segregation, etc., have an impact on both the thermal response of the material and its fatigue behavior.

However, one must bear in mind that there exist heat phenomena that are “inoffensive” from a fatigue point of view. Such is the case of small elastic movements of pinned dislocations a low stress levels, which even being mechanically reversible engage heat dissipation [145](Figure 5-6b). Other mechanisms such as the thermoelasticity are fully reversible from a mechanical and a thermal point of view; thus, they do not contribute to the self-heating of the material. In SMA, the interaction between phase transformations and typical fatigue and self-heating mechanisms of structural alloys represents new interesting challenges for assessing the self-heating fatigue characterization technique.

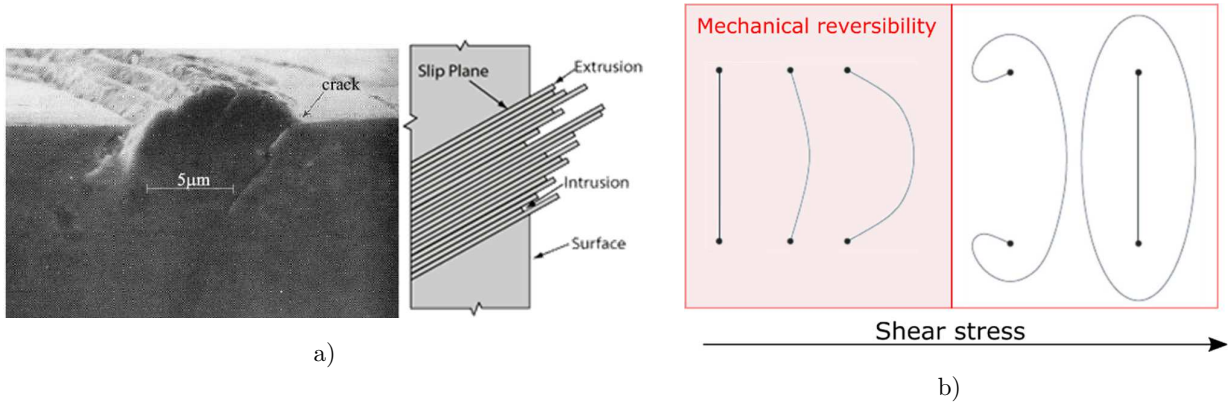


Figure 5-6 Examples of common mechanisms of heat dissipation and fatigue damage in structural alloys. a) Persistent slip bands (PSB). b) Dislocation movements: mechanically reversible under low shear stress but yielding plastic deformation when Frank-Read mechanisms are generated.

The localized phenomena that occur in the HCF of structural alloys are imperceptible from macroscopic mechanical measurements, where the response of the material is apparently linear. Therefore, the fatigue approaches based on mechanical energy dissipation cannot be applied using exclusively mechanical data. Alternatively, the self-heating technique brings the possibility to extract the energy dissipated in the form of heat and relate it to the intrinsic dissipation of the material. For this, it is necessary to couple a heat diffusion formulation with constitutive material models.

### 5.1.2. Thermodynamic framework

The characterization of the energy dissipated upon cyclic mechanical loading is based on the solution of the heat equation, which is derived from the principle of energy conservation. The local form of the heat equation can be written as:

$$\rho C_p \dot{T} + \text{div}(\vec{q}) = \Delta + r_e + \rho T \frac{\partial^2 \psi}{\partial V_k \partial T} : \dot{V}_k + \rho T \frac{\partial^2 \psi}{\partial \epsilon \partial T} : \dot{\epsilon} = s_t. \quad (5.3)$$

The left-hand side of the equation (5.3) defines the absorption heat capacity ( $\rho C_p T$ ) and the heat losses by conduction ( $\text{div}(\vec{q})$ ). It is defined in terms of the mass-specific Helmholtz free energy  $\Psi = u - sT$ , with  $u$  referring to the internal energy and  $sT$  the entropy-temperature energy; the constant pressure heat capacity  $C_p = -T \partial^2 \Psi / \partial T^2$ ; the mass density  $\rho$ , and the heat flux vector  $\vec{q}$ . On the other hand, the right hand side of the equation (5.3) describes the local heat sources  $s_t$  generated upon chemical and mechanical processes for example. In solid mechanics, the heat source term is usually divided into three parts:

- the intrinsic dissipation  $\Delta = \boldsymbol{\sigma} : \boldsymbol{\epsilon}^p - \mathbf{A}_k : \dot{\mathbf{V}}_k$ , where  $\boldsymbol{\sigma}$  is the stress tensor,  $\boldsymbol{\epsilon}^p$  is the tensor of strains other than elastic ( $\boldsymbol{\epsilon}^p = \boldsymbol{\epsilon} - \boldsymbol{\epsilon}^e$ ), and  $\mathbf{A}_k$  denotes the group of thermodynamic forces associated to the group of the internal variables  $\mathbf{V}_k$  of the considered system;
- the external heat supply  $r_e$ ;
- the thermodynamic coupling source  $\rho T \frac{\partial^2 \psi}{\partial \epsilon \partial T} : \dot{\epsilon} + \rho T \frac{\partial^2 \psi}{\partial V_k \partial T} : \dot{V}_k$ .



Zero dimensional diffusion problem

One dimensional diffusion problem

Figure 5-7 Simplification of the thermal diffusion problem.

Since the temperature variations upon self-heating tests are considered small, it is assumed that [146]:

- $C_p$  is independent of the internal state of the material,
- the external heat supply  $r_e$  is time-independent,
- the convective terms of the material time derivative are negligible (i.e.  $\frac{dT}{dt} = \frac{\partial T}{\partial t}$ ).

In spite of the abovementioned hypothesis, solving the equation (5.3) requires the knowledge of the temperature evolution in each material point, which results impossible. In laboratory conditions, the testing samples have usually a simplified geometry; thus, allowing a reduction of the solution of the heat equation to either *two-dimensional*, *one-dimensional* or even *zero-dimensional* heat diffusion problems. Next, we consider the zero-dimensional and one-dimensional heat equation solutions for a cylindrical bar of height  $L$  and radius  $r_b$  (Figure 5-7).

#### 5.1.2.1. Zero-dimensional diffusion problem

In a zero-dimensional diffusion problem, the heat source  $s_t$  is considered as homogeneous throughout the volume  $V = \pi r^2 L$ , and only heat losses with the surroundings are considered. For the cylindrical bar problem (Figure 5-7a), the heat equation follows:

$$\frac{1}{V} \int_V \rho C_p \dot{T}(r, \phi, z, t) dV + \frac{1}{V} \int_V \text{div}(\vec{q}(r, \phi, z, t)) dV = \frac{1}{V} \int_V \rho C_p s_t(r, \phi, z, t) dV. \quad (5.4)$$

Note that the equation (5.4) was written in cylindrical coordinates (see ).

By applying the divergence theorem, we can rewrite the term of the heat conduction losses as follows:

$$\frac{1}{V} \int_V \text{div}(\vec{q}(r, \phi, z, t)) dV = \frac{1}{V} \int_{\partial V} \vec{q} \cdot \vec{n} dS, \quad (5.5)$$

where  $\partial V$  denotes the boundary enclosing  $V$  oriented by outward-pointing unit normals  $\vec{n}$ . For the cylindrical bar problem, the equation (5.5) reduces to

$$\begin{cases} \vec{q} \cdot \vec{n} = h_e \theta^{0D}, & \text{for } \vec{n} = \vec{r} \\ \vec{q} \cdot \vec{n} = \pm h_c \theta^{0D}, & \text{for } \vec{n} = \pm \vec{z} \end{cases} \quad (5.6)$$

where  $\theta^{0D} = \frac{1}{V} \int_V (T(r, \phi, z, t) - T_{eq}) dV$ , is the elevation of the mean temperature in  $V$ , with respect to the equilibrium temperature  $T_{eq}$ . The heat exchange coefficient of the upper and lower faces of the cylindrical bar with its surroundings (e.g. testing machine clamps) is denoted here as  $h_c$ , and the heat exchange coefficient of the surroundings through the lateral area of the cylinder is referred as  $h_e$ . With these boundary conditions, the heat losses through conduction becomes

$$\begin{aligned} \frac{1}{V} \int_V \text{div}(\vec{q}) dV &= \frac{1}{V} \left[ 2\pi r^2 h_c \theta^{0D} + 2\pi r L h_e \theta^{0D} \right] \\ &= \left[ \frac{2h_c}{L} + \frac{2h_e}{r} \right] \theta^{0D}. \end{aligned} \quad (5.7)$$

Finally, by replacing (5.7) into the 0D heat equation (5.4) we obtain the following expression

$$\dot{\theta}^{0D}(t) + \frac{\theta^{0D}(t)}{\tau_{eq}} = s_t^{0D}(t), \quad (5.8)$$

where  $\tau_{eq} = \left[ \frac{1}{\rho C_p} \left( \frac{2h_c}{L} + \frac{2h_e}{r} \right) \right]^{-1}$  is the characteristic time of the 0D solution and  $s_t^{0D} = \frac{1}{V} \int_V s_t(r, \phi, z, t) dV$  is the mean value of the heat sources throughout the volume  $V$ .

### 5.1.2.2. One-dimensional diffusion problem

In a one-dimensional diffusion problem, the volume of the cylindrical bar is divided into successive slices of volume  $V = \pi r^2 dz$ . In this case the heat equation reads,

$$\frac{1}{\pi r^2 dz} \int_V \rho C_p \dot{T}(r, \phi, z, t) dV + \frac{1}{\pi r^2 dz} \int_V \text{div}(\vec{q}(r, \phi, z, t)) dV = \frac{1}{\pi r^2 dz} \int_V \rho C_p s_t(r, \phi, z, t) dV. \quad (5.9)$$

This time, the boundary conditions of  $V$  are defined by the heat conduction with adjacent material in the  $\vec{z}$  direction, and the heat losses through the lateral area of the cylinder (in the  $\vec{r}$  direction). The heat conduction through the material is defined by the Fourier's law

$$\vec{q}(r, \phi, z, t) = -\lambda \text{grad}(T)(r, \phi, z, t) \quad (5.10)$$

where  $\lambda$  denotes the isotropic thermal conductivity. As a result, the conduction heat losses term in the considered one-dimensional diffusion problem is written as follows:

$$\begin{aligned} \frac{1}{\pi r^2 dz} \int_V \text{div}(\vec{q}) dV &= \frac{1}{\pi r^2 dz} \int_{\partial V} \vec{q} \cdot \vec{n} dS \\ &= -\lambda \frac{\partial^2 T}{\partial z^2}(r, \phi, z, t) + \frac{2h_e \theta^{1D}}{r}. \end{aligned} \quad (5.11)$$

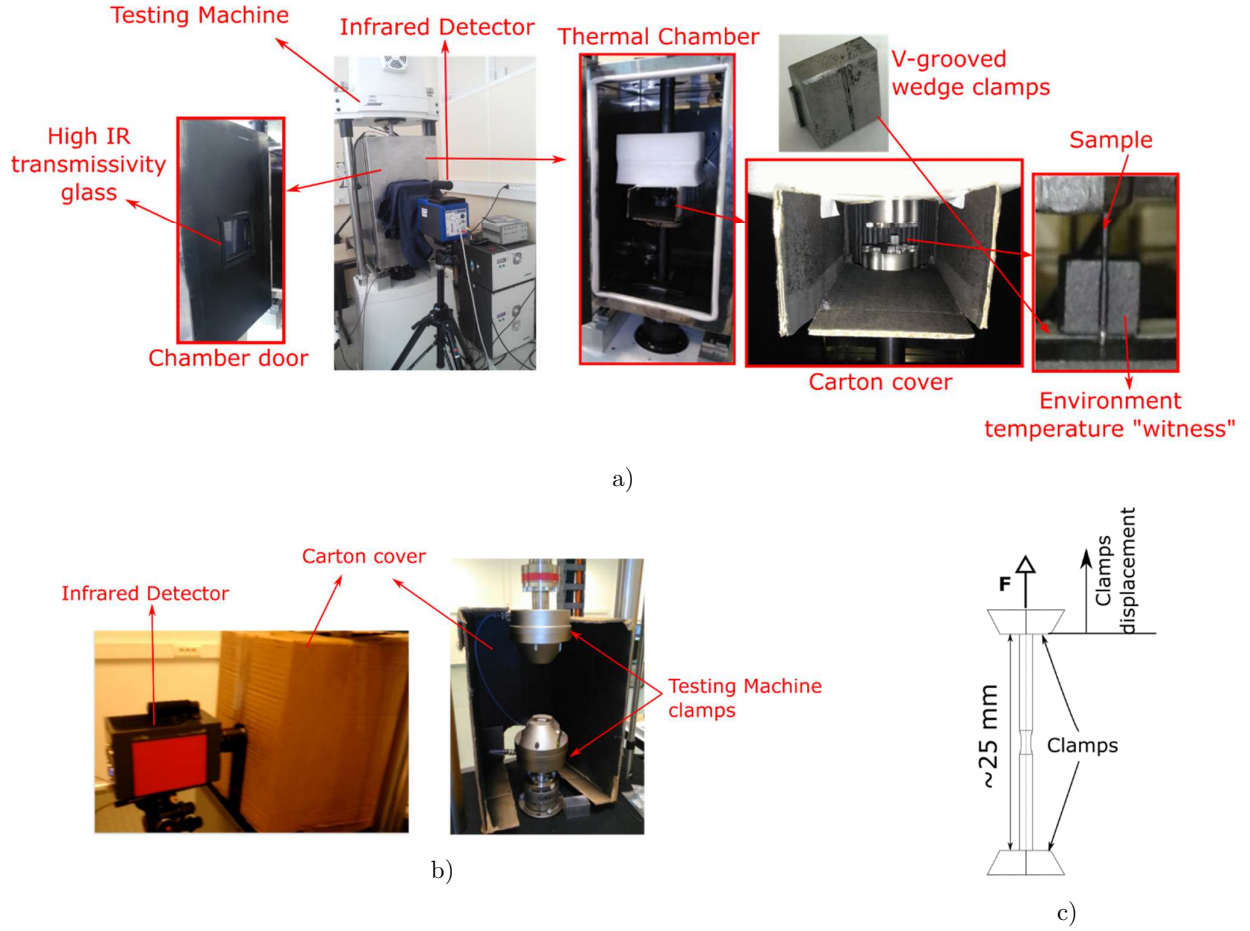


Figure 5-8 Experimental setup used for infrared thermographs acquisition upon self heating measurements. a) Tests performed inside the heat chamber (40° and 80°). b) Tests performed at ambient temperature (~25°C). c) Schematic representation of the position of the sample within the testing machine clamps.

Here,  $\theta^{1D}$  denotes the elevation of the mean temperature of the cross section  $S$  along the axis  $z$  of the cylindrical bar, i.e.:

$$\theta^{1D} = \theta^{1D}(z, t) = \frac{1}{S} \int_S (T(r, \phi, z, t) - T_{eq}) dS. \quad (5.12)$$

The characteristic time of the 1D diffusional problem is defined as

$$\tau_{eq} = \left( \rho C \frac{r}{2h_e} \right), \quad (5.13)$$

and the mean heat source in the cross-section as

$$s_t^{1D}(z, t) = \frac{1}{S} \int_{\partial S} s_t(r, \phi, z, t) dS, \quad (5.14)$$

which allows us to rewrite the 1D heat equation as follows:

$$\dot{\theta}^{1D}(z, t) - \frac{\lambda}{\rho C_p} \frac{\partial^2 \theta^{1D}}{\partial z^2} + \frac{\theta^{1D}(z, t)}{\tau_{eq}} = s_t^{0D}(t). \quad (5.15)$$

## 5.2. Experimental protocol

### 5.2.1. Experimental setup

Self-heating measurements were performed on the samples used for the fatigue study presented in the previous chapter: near equiatomic hourglass-shaped NiTi samples, annealed at 500°C for 30 minutes in an air furnace. The tests were performed at 25°C (ambient temperature), 40°C, and 80°C. The tests performed at 40°C and 80°C were carried out on an electromechanical

tensile testing machine BOSE ElectroForce 3330 equipped with a 3kN capacity load cell, and a dedicated heat chamber (see Figure 3-20a). On the other hand, the tests at 25°C were carried out on an electromechanical testing machine INSTRON Electropuls 1000, equipped with a load cell of 1kN (see Figure 3-20a). For all tests, the samples were clamped to the machine using V-grooved wedge clamps, leaving a gauge length of 25mm. The tests were performed in force control mode, applying sinusoidal pull-pull tensile force a nominal stress ratio of  $R = \frac{\sigma_{min}}{\sigma_{max}} = 0.1$  (same loading conditions as in fatigue tests).

The temperature elevations of the tested samples were recorded by means of a mid-wavelength range infrared (MWIR) detector FLIR SC7650 in the case of tests performed at 40°C and 80°C, and by an MWIR detector INFRA TEC IR8300 in the case of tests performed at ambient temperature. Both MWIR detectors were used together with 300mm focus length optical lenses allowing to record thermographs with a spatial resolution of 15µm. The infrared detectors had similar technical characteristics: 640x512 Focal Plane Arrays (FPA) detectors, temperature resolutions as low as 0.02K, and high acquisition frequencies. The main technical characteristics of both MWIR detectors are summarized in Table 5-1.

The samples were prepared using a matt black paint in order to avoid infrared reflection from the environment. Additionally, the surroundings of the sample were protected using carton covers. In the case of tests performed inside the heat chamber, the carton cover was fixed to the lower clamp, therefore providing protection against air flux coming from the fan of the heat chamber (see Figure 3-20a). Moreover, an electro-polished calcium fluoride CaF<sub>2</sub> glass, almost transparent to infrared radiation, was adapted to the door of the heat chamber, thus allowing infrared measurements. The transmission coefficient of the glass was calculated equal to 0.947 from infrared measurements on a calibrated black body. On the other hand,

Technical characteristics	FLIR SC7650	INFRA TEC 8300
Spectral range	1.5 – 5.1µm	2.0 – 5.5µm
FPA size	640x512	640x512
Cooling System	Stirling-cycle	Stirling-cyle
Dynamic range	14bit	14bit
Pitch	15µm	15µm
Detector	InSb	InSb
Temperature resolution	0.02K	0.02K
Full frame rate	100Hz	350Hz

Table 5-1 Main technical characteristics of MWIR detectors used for self-heating measurements.

for ambient temperature measurements the carton cover was placed around the sample and the camera lens (see Figure 3-20b). For ambient and temperature controlled tests, the temperature of the surroundings of the sample ( $T_s$ ) was tracked on a piece of steel painted with black matt paint placed behind the sample (see Figure 3-20a).

Before each test, the testing sample was heated up with a hot air blower up to  $\sim 120^\circ\text{C}$  in order to even its initial microstructure state. Besides, for tests performed inside the heat chamber, a preheating stage of about three hours preceded the test start in order to homogenize the temperature of the clamps.

Each self-heating test consisted of successive blocks of constant stress amplitudes cycles. In the case of tests performed at ambient temperature, the number of cycles per block was defined equal to 1000. In the case of tests performed at  $40^\circ\text{C}$  and  $80^\circ\text{C}$ , the number of cycles per block was 500. More cycles per block were applied in the case of ambient temperature measurements since the samples usually took longer times to stabilize their temperature. As illustrated in Figure 5-9, each block of cycles was started at the mean stress level. We programmed the testing machines to stop the cyclic loading at the mean stress level after each block of cycles; however, this was only achieved in the testing machine used for ambient temperature measurements. The samples were kept at constant stress after each block of cycles in order to record the stage of return to thermal equilibrium. Since the self-heating technique intends to characterize the mechanisms taking place in the HCF regime, we focus on stress levels lower than  $\sigma_{MT}$ . A schematic representation of the load sequence applied to one sample during a self-heating tests is presented in Figure 5-9.

We took advantage of the high acquisition frequencies allowed by the IR detectors in order to record thermographs at 500Hz in the case of ambient and  $40^\circ\text{C}$  measurements and at 800Hz in the case of tests performed at  $80^\circ\text{C}$ . Note that the maximum acquisition frequency is dependent on the integration time of the IR detector. Since shorter integration times are allowed at high temperatures, higher acquisition frequencies are possible. The use of high thermal frames acquisition frequency results attractive for a full description of the heating processes taking place all along one stress cycle, however, it requires large storage units.

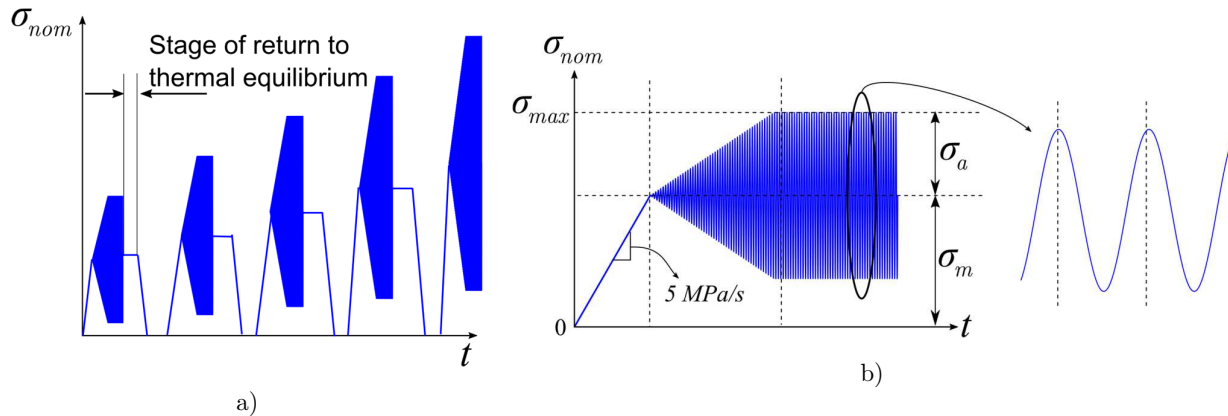


Figure 5-9 Schematic representation of the load sequence applied to one sample during a self-heating test. a) Successive blocks of constant stress amplitude cycles. b) Illustration of the cyclic loading applied in one block of cycles.

### 5.2.2. Post-processing of temperature data

The temperature evolution of the sample upon cyclic tensile tests was extracted from 2D thermographs of the sample surface. We assumed that the decrease of the infrared emissivity due to the curvature of the surface of the samples was negligible. This is valid as long as the measurement zones are kept within an angle of vision lower than  $45^\circ$  (see Figure 5-10).

In the first instance, the self-heating measurements in this study were carried out using a zero-dimensional approach. The temperature of interest ( $T$ ) was defined in the mid cross-section of the samples by a spatial average of the digitalized temperature values in a window of  $16 \times 39$  pixels ( $240 \times 585 \mu\text{m}^2$ ) (see Figure 5-11a). In order to get the temperature elevation at the mid cross-section ( $\theta$ ), the temperature of the surroundings ( $T_s$ ), spatially averaged in the steel plate behind the sample, was extracted from the temperature of interest, i.e.:

$$\theta_w(t) = \frac{1}{N} \sum_N T(x, y, t) - \frac{1}{N_s} \sum_{N_s} T_s(x, y, t), \quad (5.16)$$

with  $N$  denoting the group of pixels inside the  $16 \times 39$  window at the mid cross-section, and  $N_s$  denoting the group of pixels inside the measurement area of the temperature surroundings (defined in the steel plate). After that, the temperature elevation in the measurement window  $\theta_w$  was zero-corrected with respect to the temperature elevation at the beginning of the cyclic loading (see Figure 5-11b&c). For this purpose, we recorded images of the sample surface in a constant stress state during 5 seconds before starting the cyclic loading. Hence, the temperature elevation was finally defined as follows:

$$\theta(t) = \theta_w(t) - \frac{1}{F_s} \sum_{F_s} \theta_w(t) \quad (5.17)$$

where  $F_s$  is the number of thermographs recorded during the 5s constant-stress period before the cyclic loading.

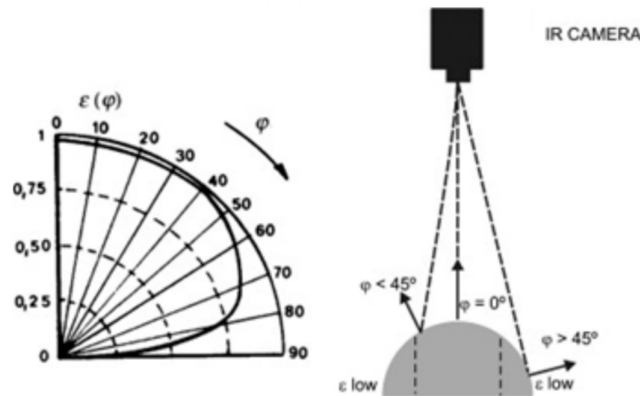


Figure 5-10 Infrared emissivity (here denoted as  $\epsilon$ ) evolution in terms of the angle of vision of the IR camera with respect to the normal of the sample surface ( $\varphi$ ). Schematic image taken from [147].

### 5.2.2.1. Identification of the stabilized temperature elevation

The temperature elevation signal of each loading stage was analyzed in the frequency domain. The frequency spectrum of the temperature elevation signal  $\theta(k)$  was obtained by computing the Fast Fourier Transformation algorithm [147]:

$$\theta(k) = \sum_{j=1}^n \theta(j) W_n^{(j-1)/(k-1)} \quad (5.18)$$

where  $n$  is the number of data points in the temperature elevation signal,  $k$  denotes one of the  $n$  spectral components calculated for  $\theta(t)$  and  $W_n$  is defined as

$$W_n = e^{(-2\pi i)/n}. \quad (5.19)$$

The resulting spectrum of the cyclic elevation temperature during a constant-amplitude cyclic stress block looks similar to the one illustrated in Figure 5-12b.

In order to obtain the stabilized temperature elevation after each constant stress amplitude block, we applied a Low-Pass Filter (LPF) to the spectrum  $\theta(k)$ . It was done by multiplying the spectrum  $\theta(k)$  by a rectangle window  $R(k)$  defined in the following form:

$$R(k) = \begin{cases} 0 & \text{for } k > f_c n / f_{ac} \\ 1 & \text{for } k \leq f_c n / f_{ac} \end{cases}, \quad (5.20)$$

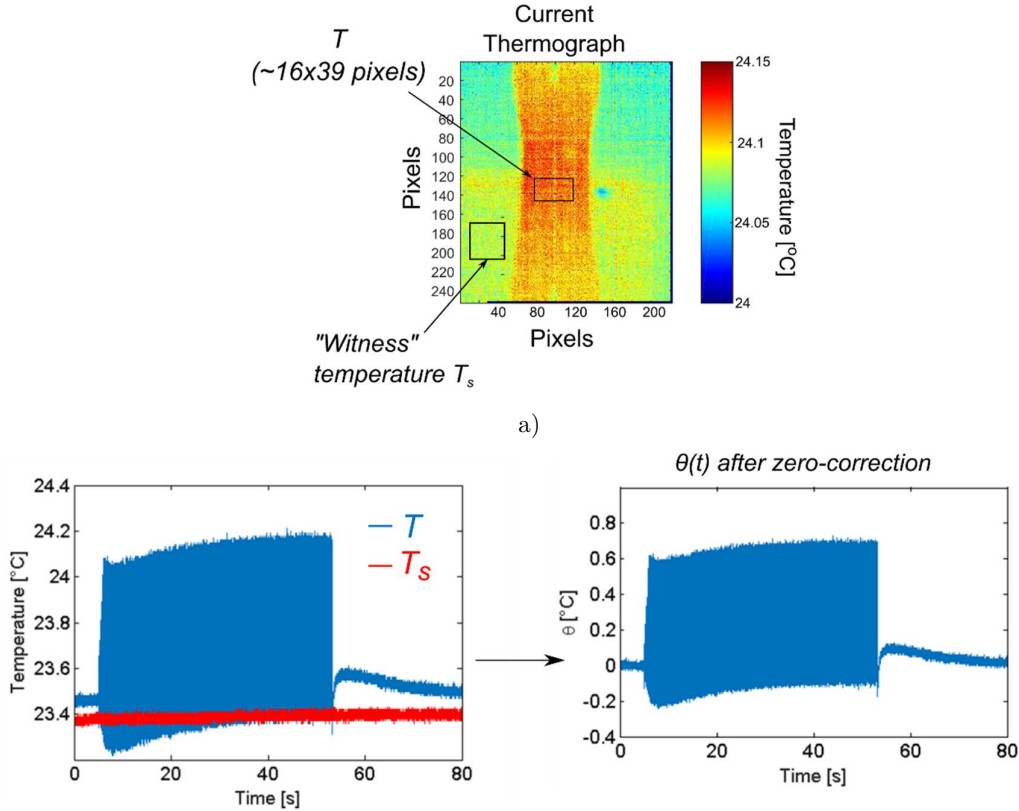


Figure 5-11 Post-processing of temperature data acquired during self-heating measurement. a) Evaluation zones for  $T$  and  $T_s$ . b) Example of the conversion of raw temperature data into temperature elevation data.

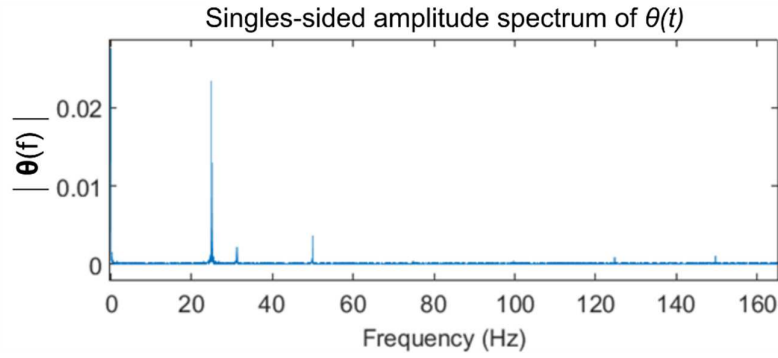


Figure 5-12 Example of the frequency spectrum obtained using a discrete Fourier transformation algorithm.

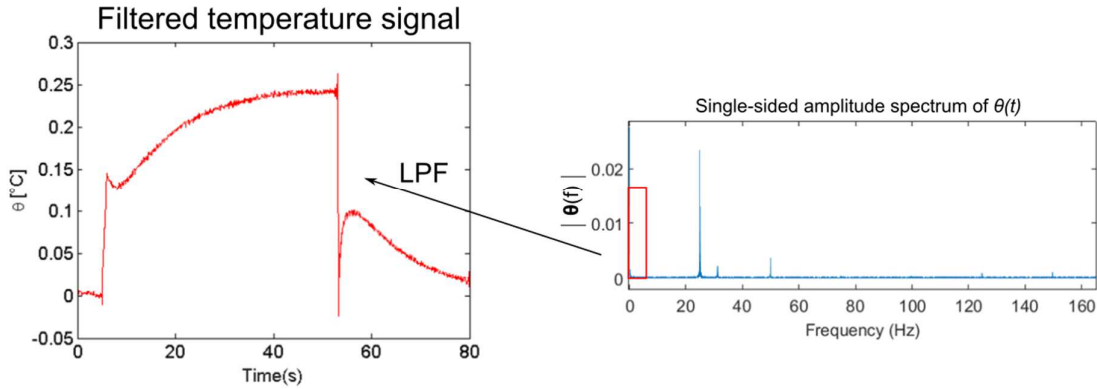


Figure 5-13 Low pass filtering of the temperature data recorded in the mid cross-section of the sample.

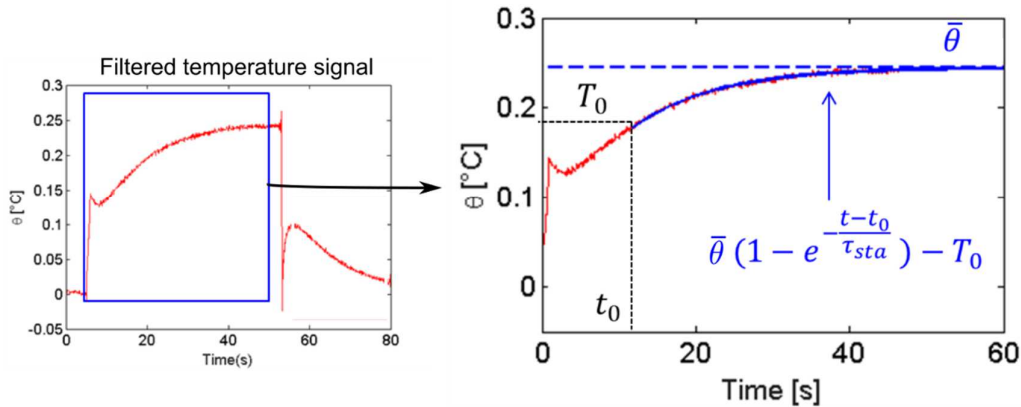


Figure 5-14 Identification of the steady-state temperature elevation  $\bar{\theta}$ .

where  $f_c$  is the filter cutoff frequency and  $f_{ac}$  is the acquisition frequency of the temperature signal. The cutoff frequency was chosen in the order of Hz, much lower than the applied load frequency. As a result, we obtained a smooth temperature elevation signal as illustrated in Figure 5-13a. After that, the following exponential function:

$$\theta(t) = \bar{\theta}(1 - e^{-t/\tau_{sta}}) \quad (5.21)$$

was fitted to the filtered elevation temperature of the cyclic loading as illustrated in Figure 5-14. The fitting process was carried out using the Least-Squares method, with  $\bar{\theta}$  and  $\tau_{sta}$  as the adjustable parameters.  $\bar{\theta}$  denotes the stabilized temperature of the corresponding constant stress amplitude block of cycles.

In addition, for each block of cycles, the amplitudes of the first, second, and third harmonics of the temperature elevation signal in the mid cross-section were evaluated. The harmonics evolution help to reveal the appearance of heat sources other than those synchronized with the applied loading cycles.

### 5.3. Experimental results

#### 5.3.1. Self-heating curves

The self-heating curves of the studied NiTi at 25°C, 40°C, and 80°C are presented in Figure 5-15. The stress in the x-axis denotes the maximal applied stress during each block of cycles, and the stabilized temperature elevation in the y-axis denotes the value obtained after the exponential function fitting (equation (5.21)). The curves were obtained after successive blocks of increasing stress amplitude cycles carried out at 25Hz. For each curve, the B19' martensite transformation stress onset  $\sigma_{MT}$  is mentioned in order to keep in mind the loading regime in each block of cycles. Only the  $\sigma_{MT}$  at 25°C (420MPa) was estimated from numerical calculations using the Sedláč model presented in a previous chapter. The  $\sigma_{MT}$  values at 40°C and 80°C were obtained from tensile tests (600MPa and 900MPa respectively).

At 25°C, the material is in a mixed state of B2 and R-phase under stress-free conditions, as presumed from the transformation temperatures ( $R_s=25.5$  &  $R_f=11.5$ ) identified in DSC curves (see Chapter 3). In consequence, the B2→R transformation is induced even at low stresses. On the other hand, from the characterization analysis made in chapter 3, we deduced that at 40°C, the samples are in B2 phase under stress-free conditions, but transform into R-phase when the axial stress increases beyond ~215MPa. Finally, at 80° the samples behave elastically up to ~590MPa, then a small amount of R-phase start developing before the axial stress attains the B19' transformation onset stress.

As observed in Figure 5-15, the stabilized temperature elevations  $\bar{\theta}$  obtained during self-heating tests are low under stress conditions below  $\sigma_{MT}$ : up to 1°C in tests performed at 25°C, up to 0.15°C in tests performed at 40°C, and less than 0.1°C in tests performed at 80°C. The self-heating curve at 25°C shows a continuous (nearly linear) heating with the increase of the stress. In contrast, at 40°C the sample shows practically no self-heating before attaining the B19' transformation onset stress. Similar behavior was evidenced upon tests at 80°C, although the self-heating at stresses near  $\sigma_{MT}$  was impossible to track since the sample (sample 1 in Figure 5-15c) broke during the  $\sigma_{max} = 860MPa$  block of cycles. In order to verify the unexpected self-heating behavior of samples tested at 40°C and 80°C, a second sample was tested under the same conditions. The results shown in Figure 5-15b&c exhibit similar self-heating trends as the first tests, i.e. noisy  $\bar{\theta}$  values below  $\sigma_{MT}$ , thus suggesting the annihilation of self-heating in this loading regime.

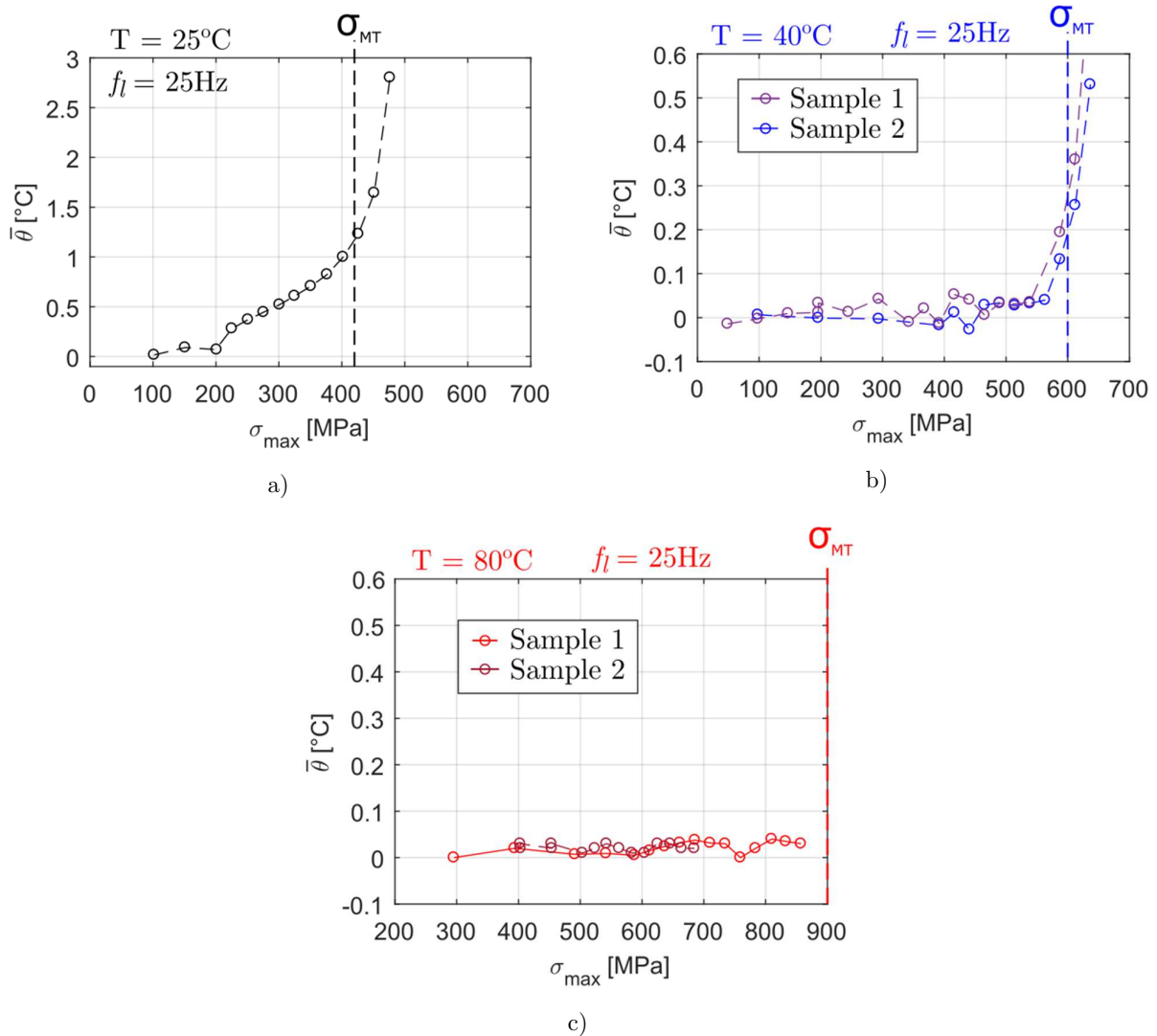


Figure 5-15 Self-heating curves

Taking a closer look at the temperature evolution in the mid cross-section (Figure 5-16), we observe that not only the self-heating responses of the samples tested at 25°C, 40°C and 80°C are different, but also the shape and amplitude of the temperature cycles. At 25°C (Figure 5-16a), the shape of the temperature signal follows the same sinusoidal shape of the applied loading. In contrast, 40°C and 80°C responses show a degraded sinusoidal response, with appearance of intermediate temperature peaks in the case of the test at 80°C (Figure 5-16c). Note that the temperature signal amplitude obtained at 80°C is considerable lower than the one obtained at 25°C in spite of the much higher applied stresses. As a result, we infer that the intermediate B2→R promoted at low temperatures have a dramatic impact in the self-heating behavior of NiTi as well as in the amplitude and shape of the temperature signal.

The results obtained at 25°C, shows that the B2→R transformation, although characterized by a small mechanical hysteresis, dissipates energy in the form of heat even at relatively low stress levels. The dissipation of heat in this loading regime can be attributed to internal friction, surface energy, phase boundary movements, and upon increasing the

stress, to micro plasticity. Although similar behavior was expected for tests performed at 40°C and 80°C the relatively small volume of the measured zone, plus the sample's shape and the thermal boundary conditions (notably the use of the heat chamber) hindered the detection of steady-state temperature elevations  $\bar{\theta}$ . In order to come up against these challenges, we performed additional tests with the aim of clarifying the role of the mentioned factors on the self-heating behavior of our samples.

### 5.3.2. Effects of the loading frequency

With the aim of boosting the self-heating response of the studied NiTi samples, we performed self-heating tests at load frequencies of 40Hz and 55Hz. The results are presented in Figure 5-17 together with the previous results obtained at 25Hz.

At 25°C ((Figure 5-17a), the load frequency of 55Hz resulted in a clear increase of the steady-state temperature elevations. In contrast, the self-heating curve obtained at 40Hz shows values barely above the 25Hz self-heating curve. Such a nonlinear loading frequency effect, instead of being attributed to viscous mechanisms, is rather the consequence of shifts of the B2→R transformation stress onsets caused by local temperature elevations in the material.

In the tests performed at 40°C and 80°C, the effects of the load frequency are less evident. In fact, at 40°C (Figure 5-17b), higher steady-state temperature elevations were obtained in the case of tests performed at 40Hz, whereas tests at 55Hz show a response that lies between the 25Hz and 40Hz curves. At 80°C (Figure 5-17c), the self-heating responses remained noisy

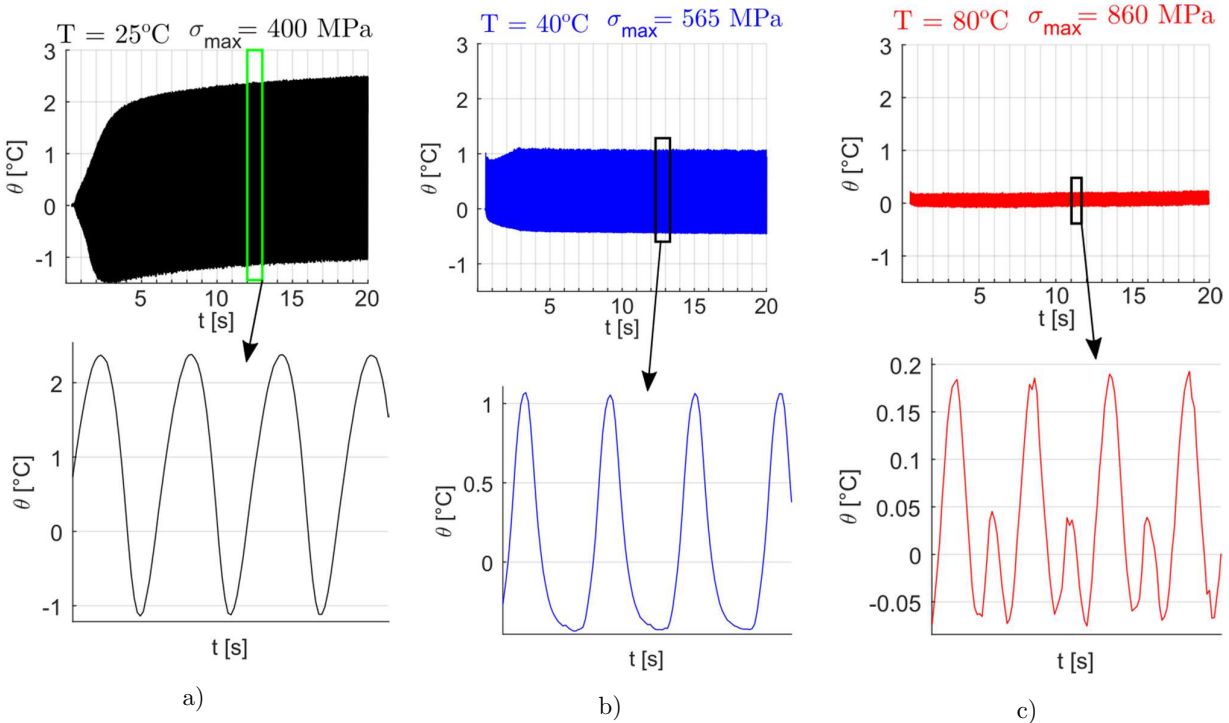


Figure 5-16 Comparison of the temperature elevations extracted from blocks of cycles at 25°C (a), 40°C(b), and 80°C (c).

in spite of the increase of the load frequency, confirming the apparent lack of heat dissipation upon cyclic loading.

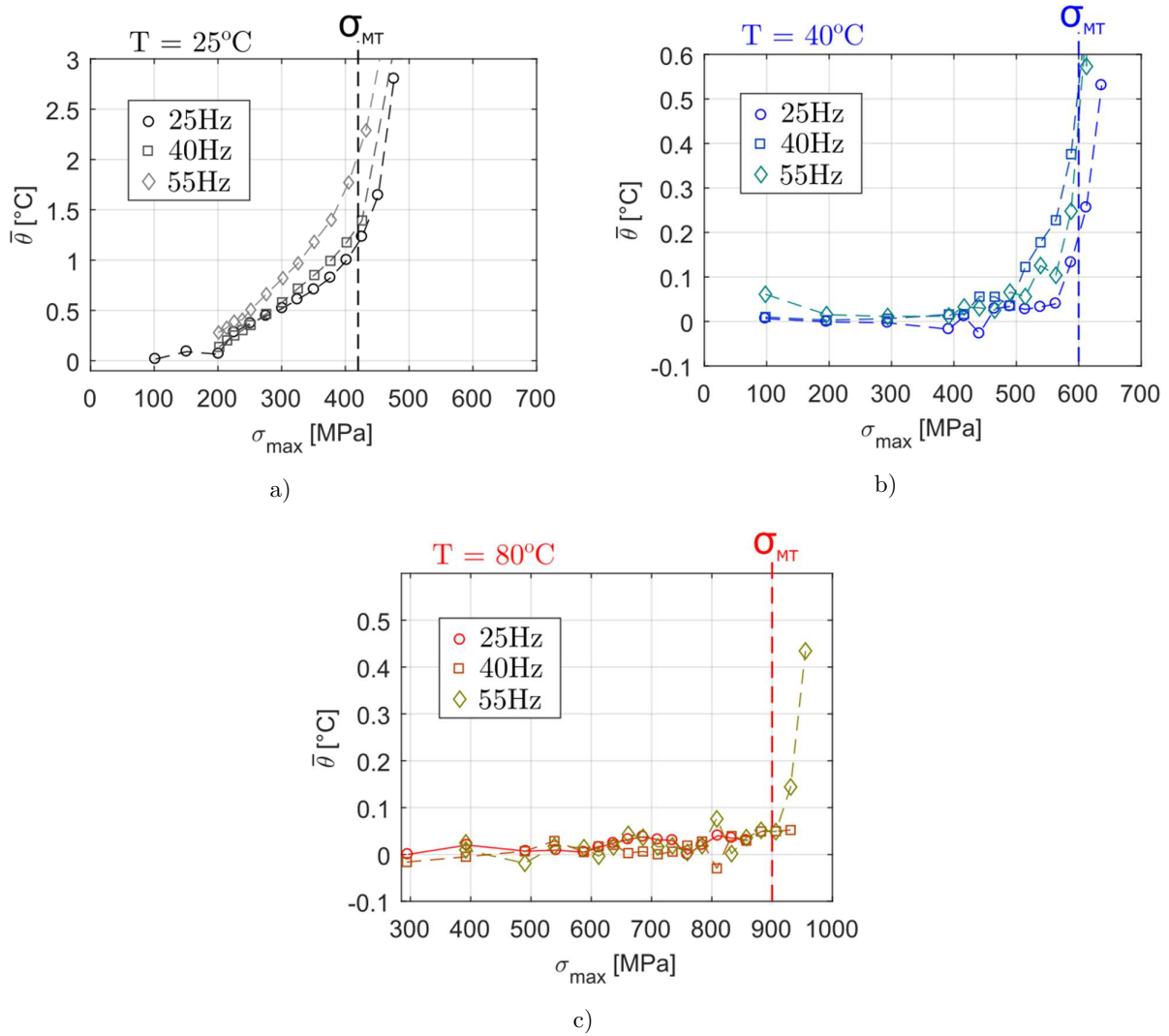


Figure 5-17 Effects of the loading frequency on self-heating behavior of NiTi samples.

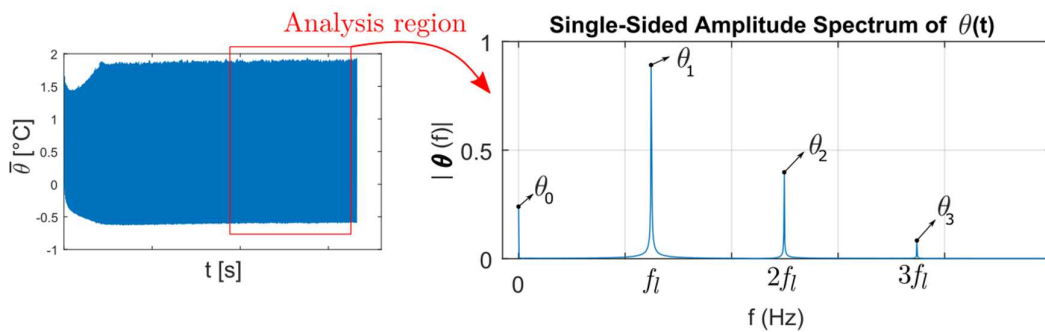


Figure 5-18 Harmonic decomposition of the temperature elevation signal

The uncommon self-heating behavior of NiTi suggests that the strong thermomechanical coupling related to phase transformations may play an important role in the interaction between dissipation sources. This subject will be tackled in later sections where the analysis of the cyclic thermomechanical response of hourglass-shaped NiTi samples will be assisted by means of modeling tools.

### 5.3.3. Evolution of the temperature harmonics

The low temperature elevations recorded during self-heating tests make the filtered temperature elevation responses more “wavy”, which hinders the identification of the steady-state temperature values  $\bar{\theta}$ . See for example in Figure 5-16c the order of magnitude of the temperature elevation of the material tested at 80°C under 860MPa of maximum stress. Even though the applied stress in this case was relatively high (well above the endurance limit of the material and close to the B19’ transformation onset stress), only a temperature elevation amplitude of about 0.05°C is obtained. Note that such a small temperature elevation value gets close to the sensitivity of the infrared detector. Moreover, under these conditions, the calculation of the steady-state temperature elevation becomes much more sensitive to small changes of the temperature of the surroundings. For the values of  $\bar{\theta}$  shown in the 80°C self-heating curves in Figure 5-17c, temperature surrounding changes as small as some tens of micro kelvins may result in significant noise in the self-heating response. In order to face these difficulties, we carried out the spectral analysis of the temperature elevations of each block of cycles. The procedure that we present next is similar to the so-called “Lock-in” technique used by Krapez et al. [135] (presented previously in Figure 4-2) for analyzing the self-heating response of a stainless steel and an aluminum alloy.

The technique consists in performing a harmonic decomposition of the temperature elevation signal, i.e.:

$$\theta = \theta_0 + \theta_1 \sin(2\pi f_t t + \varphi_1) + \theta_2 \sin(2\pi f_t t + \varphi_2) + \theta_3 \sin(2\pi f_t t + \varphi_3), \quad (5.22)$$

where  $\theta_1$ ,  $\theta_2$ , and  $\theta_3$  are the amplitudes of the fundamental frequency, the second harmonic and the third harmonic respectively. The magnitude of  $\theta_0$  corresponds to the so-called DC value, which in this case may be close to the steady-state temperature elevation  $\bar{\theta}$  as the

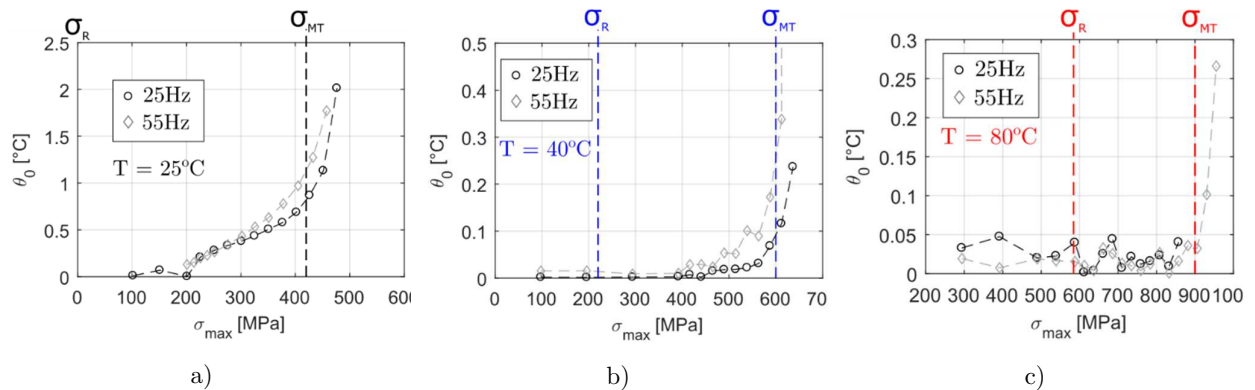


Figure 5-19 DC value of the temperature elevation signal. a) 25°C. b) 40°C. c) 80°C.

signal was zero-corrected. The fundamental frequency is the same as the applied loading frequency  $f_l$ .

The identification of the harmonic amplitudes was performed by extracting the values of the amplitude peaks at  $0$ ,  $f_l$ ,  $2f_l$ , and  $3f_l$  frequencies in the spectrum of the temperature elevation response. The spectrum was computed using a Fast Fourier Transformation algorithm over a segment of the temperature elevation signal in the stabilized region (see Figure 5-18). The evolutions of the harmonic amplitudes in terms of the maximum applied stress per block of cycles at  $25^\circ\text{C}$ ,  $40^\circ\text{C}$ , and  $80^\circ\text{C}$  are presented in Figure 5-19 to Figure 5-22. In each figure, we plot the responses obtained at 25Hz and 55Hz loading frequency.

The curves of  $\theta_0$  component in terms of the maximal stress (Figure 5-19) show similar trends as the self-heating curves presented in Figure 5-17. At  $25^\circ\text{C}$ , the  $\theta_0$  values increase almost linearly with the maximum applied stress up to the B19' stress onset. However, this time the response at 55Hz shows smaller differences with respect to the response obtained at 25Hz. At  $40^\circ\text{C}$ , we observe that the response at 55Hz starts raising after 400MPa, which was not noticeable in the self-heating curves in Figure 5-17b. At  $80^\circ\text{C}$ , as in the self-heating curves in Figure 5-17c, the evolution of the  $\theta_0$  component resulted noisy for all tested stresses below  $\sigma_{MT}$ .

The  $\theta_1$  curves in Figure 5-20 correspond to the components of the temperature signal that follows the cyclic amplitude imposed by the tensile machine. In traditional alloys, the component  $\theta_1$  corresponds to the thermoelastic effect (i.e. cooling upon loading, and heating upon unloading), which do not contribute to the self-heating of the material as the amount of heat released upon the unloading stage of a cycle is by definition the same as the amount of heat absorbed upon the loading stage. In Figure 5-20a, we observe that the material tested at  $25^\circ\text{C}$  exhibits a linear increase of  $\theta_1$  for the first low-stress blocks of cycles. The linear trend ceases at 250MPa in the case of tests carried out at 25Hz. After that, constant  $\theta_1$  values are obtained until the B19' transformation stress is attained. On the other hand, the  $\theta_1$  curve of tests performed at 55Hz shows a more subtle loss of heating rate after the threshold of linearity at 320MPa is exceeded. The first harmonic amplitudes in this case may correspond to the B2 $\leftrightarrow$ R transformation that takes place all along the loading cycle. At  $40^\circ\text{C}$  (Figure 5-20b), the evolution of  $\theta_1$  at 25Hz and 55Hz are practically the same. The

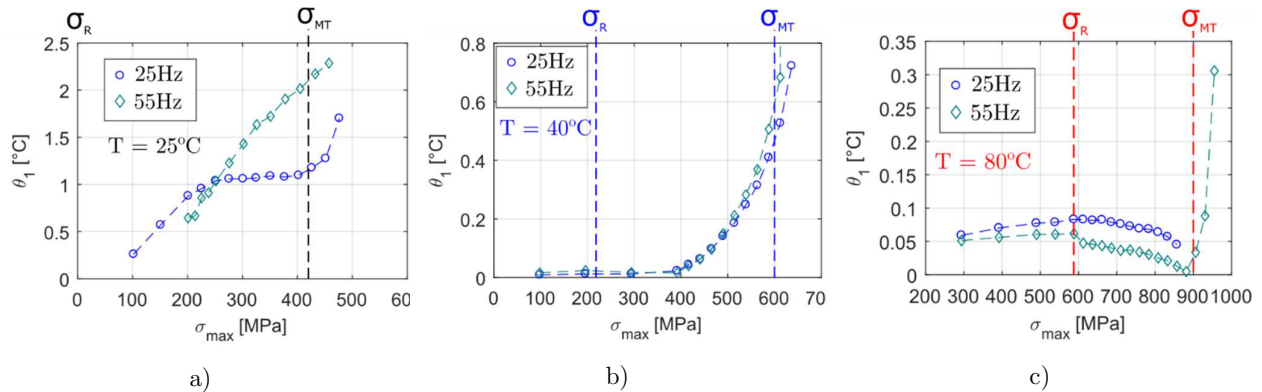


Figure 5-20 First harmonic amplitude of the temperature elevation signal. a)  $25^\circ\text{C}$ . b)  $40^\circ\text{C}$ . c)  $80^\circ\text{C}$ .

temperature amplitude starts raising after the 400MPa stress block, which is 180MPa higher than the onset of the B2→R transformation ( $\sigma_R$ ). At 80°C, unlike the trends observed in the self-heating and  $\theta_0$  curves, the  $\theta_1$  behavior exhibits a noise-free behavior (Figure 5-20c). The curves in Figure 5-20c show the interesting competition between the thermoelastic effect and the latent heat of the B2↔R transformation. For both tested frequencies, the  $\theta_1$  amplitudes increase slowly up to the 600MPa block, then they decrease until becoming almost null when the maximum stress reaches  $\sigma_{MT}$ . The inflection point of the curves at 600MPa coincide with the onset stress  $\sigma_R$  for the material at 80°C, which was previously identified at ~590MPa. At high stresses, the temperature elevation during one loading cycle is characterized by two temperature local maxima as shown in Figure 5-16c; therefore, the decrease of the first harmonic might be compensated by an increase of higher order harmonic components as we describe in the following paragraph.

Higher order harmonic components allow the identification of heating mechanisms other than those that follows the applied loading. Such is the case of intrinsic material dissipation yielded at intermediate stress levels in traditional alloys or stress-induced phase transformations in NiTi. The changes observed in the first harmonic amplitude curves (Figure 5-20) are somehow reflected in the second harmonic amplitude behavior (Figure 5-21). For instance, at 25°C, the slope changes of  $\theta_1$  detected at 250MPa and 320MPa in the tests at 25Hz and 55Hz (Figure 5-20a) correspond to local minima in the  $\theta_2$  curves (Figure 5-21a). At 40°C, the temperature raise threshold of 400MPa observed in the  $\theta_1$

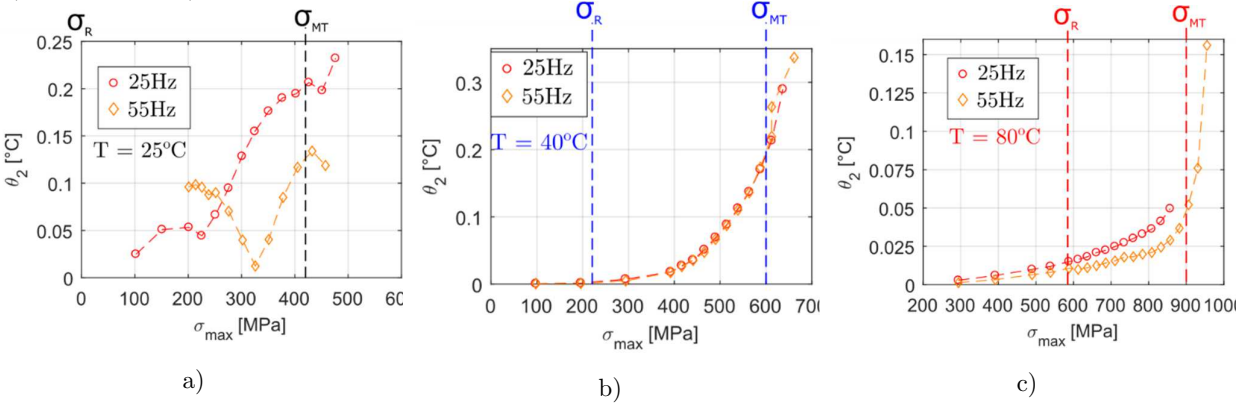


Figure 5-21 Second harmonic amplitude of the temperature elevation signal. a)25°C. b)40°C. c)80°C.

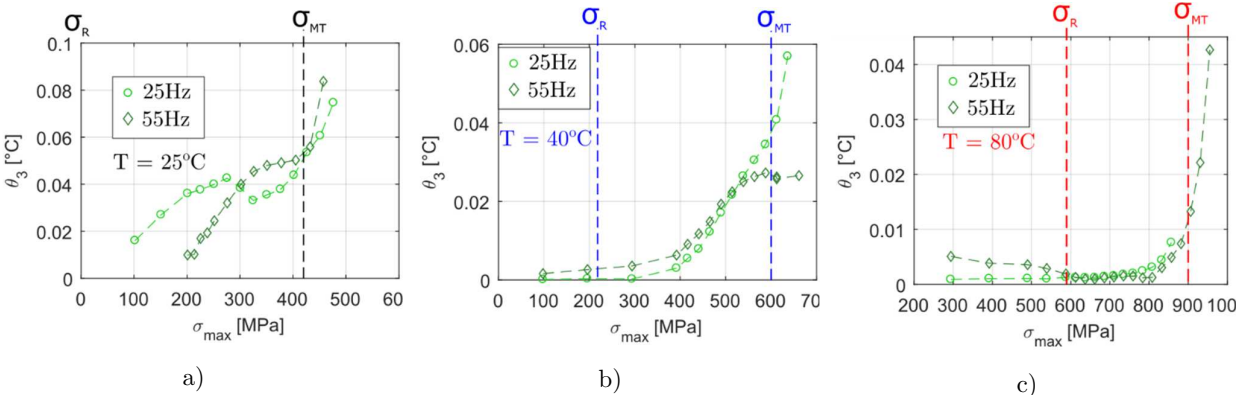


Figure 5-22 Third harmonic amplitude of the temperature elevation signal. a)25°C. b)40°C. c)80°C.

curves (Figure 5-20b) appears again in the  $\theta_2$  curves (Figure 5-21b), showing a resemblance to typical self-heating curves in traditional structural alloys. At 80°C (Figure 5-21c), the evolution of  $\theta_2$  shows a continuous increase from low stresses. This time, the  $\theta_1$  inflection point observed at 600MPa (Figure 5-20c) is vanished within the continuous increasing response of  $\theta_2$ .

The third order harmonic shows also interesting trends. However, we have to bear in mind that the low magnitude of the  $\theta_3$  peak in the spectrum makes it more sensitive to noise in the original temperature signal. At 25°C (Figure 5-22a), it is interesting that in both curves at 25Hz and 55Hz, a change of the  $\theta_3$  trend is observed at 320MPa. Above this threshold, higher applied stresses result in slight  $\theta_3$  amplitude increments until the  $\sigma_{MT}$  is reached. At 40°C (Figure 5-22b), the 400MPa temperature raise threshold is again observed in both tests at 25Hz and 55Hz. Finally at 80°C the  $\theta_3$  curve reveals no evolution below 800MPa, only 100MPa below  $\sigma_{MT}$ . At such high stress, the material may nucleate cracks already in the first hundreds of cycles as revealed by the fatigue study in Chapter 4; therefore, the  $\theta_3$  increase may be related to cyclic localized phase transformations at the crack tip accompanied by their correspondent latent heat release/absorptions.

### 5.3.4. Influence of the shape of the sample

So far, we have analyzed the temperature evolution of the sample by averaging the temperature in a small region in the mid cross-section. In order to calculate the energy related to the temperature changes upon cyclic loading, the heat equation (5.3) is used. The solution of the heat equation can be simplified by adopting different hypothesis according to the nature of the studied heat diffusion problem. In our case, since the IR detector records 2D temperature fields, only the temperature of the surface of the samples can be evaluated. Moreover, in hourglass-shaped samples, the cylindrical shape of the surface makes it

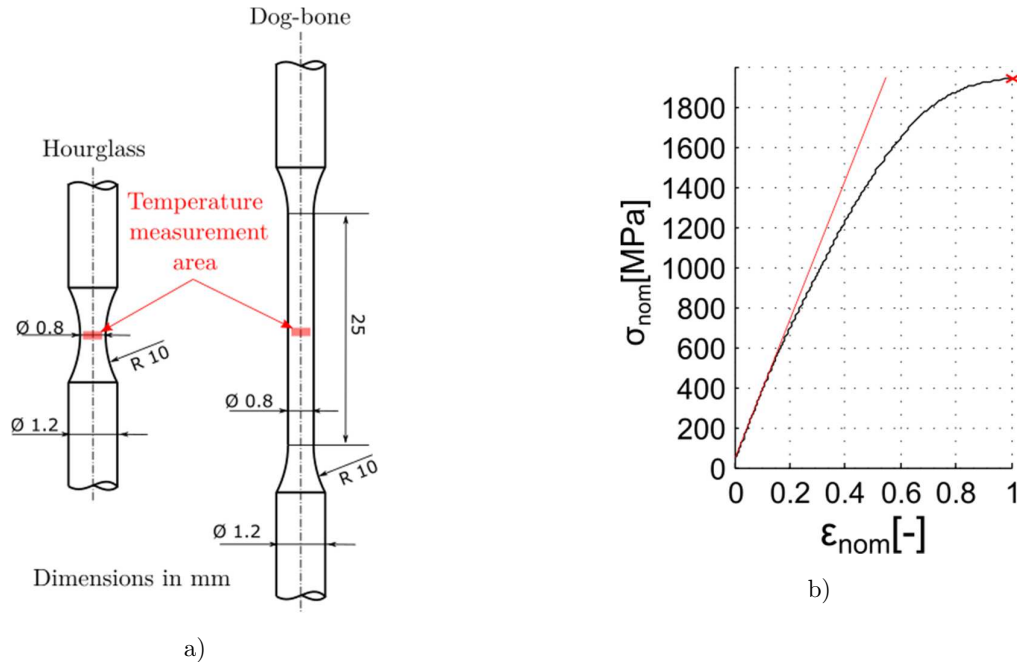


Figure 5-23 Steel samples. a) Geometry. b) Quasi-static tensile response.

impossible to carry out a two-dimensional heat diffusion analysis, reducing the possibilities to either a one-dimensional or a zero-dimensional diffusion problem. The zero-dimensional problem considers only the heat exchanges of the material with its surroundings; hence, it is assumed that the material heats and cools homogeneously. On the other hand, a one-dimensional problem takes into account the heat conduction in one direction, which makes it possible to analyze a longitudinal distribution of temperature and heat sources.

The evolution of the temperature in the mid cross-section of hourglass shaped samples upon tensile mechanical loading is mainly product of a constant activation of heat sources of the confined volume in the middle of the samples. However, the continuous cross-section reduction of the samples introduces a gradient of stress and consequently a heat sources distribution along its axis. In order to assess the impact of the shape of the samples on self-heating measurements, we carried out a series self-heating tests on stainless steel samples processed into dog-bone and hourglass shapes. Like NiTi hourglass-shaped samples, steel samples were prepared by grinding and electropolishing. Their geometric dimensions are presented in Figure 5-23a. Note that the 25mm gauge length of dog-bone samples allows a uniform distribution of tensile stresses since the cross-section is constant. In contrast, the nominal tensile stress in the mid cross-section of the hourglass shape sample results 2.25 times the stress outside the groove zone and introduces triaxial stress states in some zones

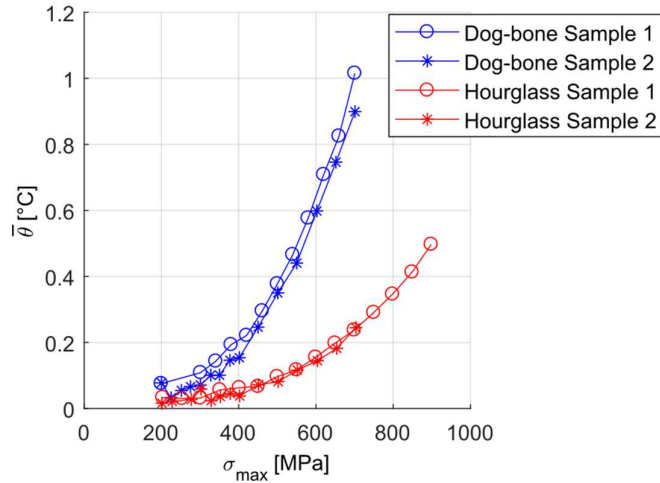


Figure 5-24 Self-heating of steel samples

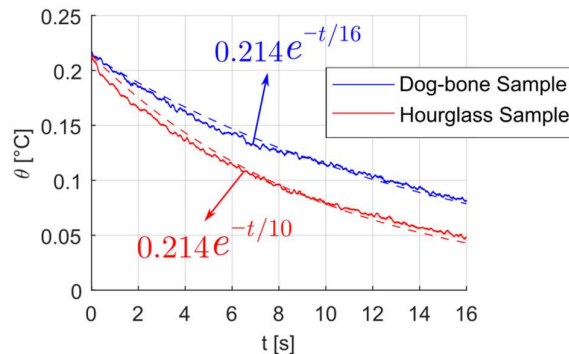


Figure 5-25 Cooling stage after cycling. a) Dog-bone sample. b) Hourglass sample.

of the groove as we discussed in Chapter 3. At the mid cross-section, where the stress remains practically in a uniaxial state, the stress at the surface of hourglass-shaped sample is 1.7% higher than the nominal stress ( $K_{th}=1.017$ ). The nominal tensile response of the material is presented in Figure 5-23.

The self-heating tests were carried out at 25Hz at room temperature and a stress ratio equal to 0.1. The experimental setup was the same described previously in Figure 3-20. Two samples were tested for each geometry in order to verify the repeatability of the results. Blocks of 1000 constant stress amplitude cycles were applied in the case of the hourglass shape, while 1500 blocks of cycles were applied to dog-bone samples. Longer block of cycles were performed on dog-bone samples because it took generally longer times to stabilize the temperature. The increase step of the maximum stress was 50MPa between successive blocks of cycles. For both sample shapes, the temperature measurement was obtained by averaging the temperature values on a 15x30pixels zone in the middle of the samples as illustrated in Figure 5-23a. The post-processing procedure to determine the steady-state temperature elevation per block of cycles was the same one presented in section 5.2.2.

The self-heating curves of stainless steel samples are shown in Figure 5-24. The dog-bone sample exhibits a more intense self-heating response compared to the hourglass one. As observed, the self-heating responses are well reproduced upon second tests in new samples. In addition, we compare in Figure 5-25 the cooling stages of two blocks of cycles resulted in nearly the same steady-state temperature elevation using dog-bone (blue curve) and hourglass (red curve) samples. We observe that the hourglass-shaped sample exhibits a more accelerated cooling compared to the dog-bone one. The characteristic time  $\tau_{eq}$  of the decreasing exponential function

$$\bar{\theta} e^{-t/\tau_{eq}} \quad (5.23)$$

fitted to the temperature recorded upon cooling in Figure 5-25, was 16s in the case of the dog-bone sample and 10s in the case of the hourglass sample.

In conclusion, the shape of the sample plays an important role on the self-heating behavior of good thermal conductors such as steel or NiTi alloys. Although the cross section reductions are not pronounced, it was evidenced that the heat produced in the mid cross-section of an hourglass sample dissipates faster than in a constant cross-section sample such as the dog-bone one. These heat losses are present even in the absence of complicated heat sources interaction such as in NiTi. Since the tests presented in Figure 5-24 were performed under the same experimental conditions, we attribute the difference in heating/cooling rates to differences in the heat conduction in the axial direction. These differences are induced by a more or less pronounced temperature gradient due to the geometry of the sample.

### 5.3.5. Temperature evolution during monotonic tensile tests

In order to have a better insight of the interaction of heat sources upon tensile loading in hourglass-shape samples, we performed high strain rate monotonic tensile tests at 40°C and 80°C. This time, we analyzed the axial profile distribution of the temperature near the mid cross-section. The tests were performed using the experimental setup presented in Figure

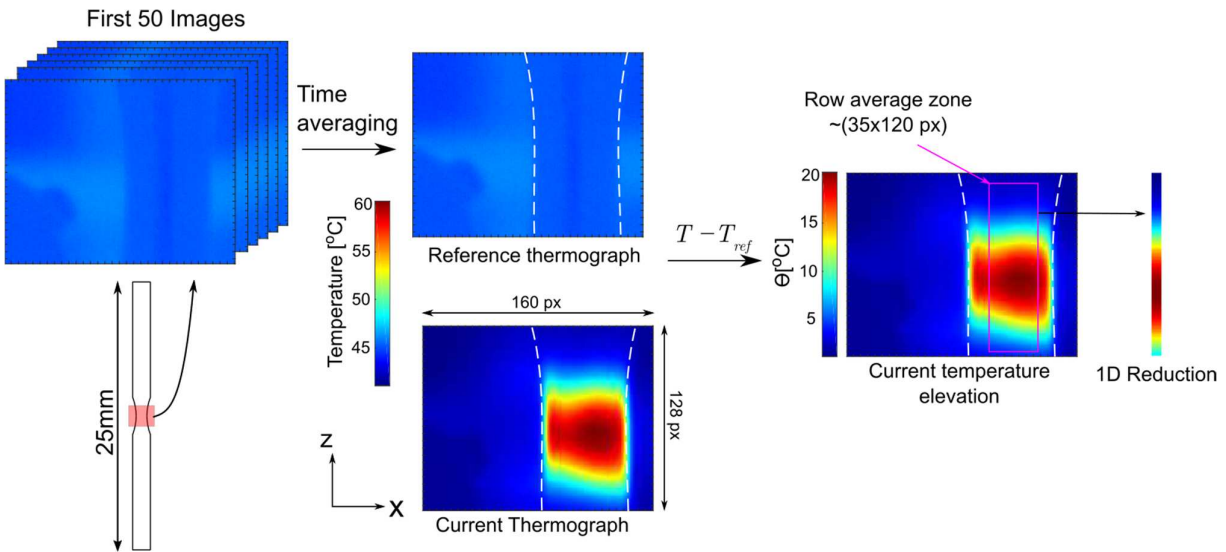


Figure 5-26 Schematic representation of the conversion of 2D thermographs into 1D array of temperature elevation values.

3-20a, except that this time we used a 10mm clip-on extensometer to track the mechanical response of the material. The IR detector acquired thermographs at 450Hz for tests at 40°C and at 800Hz for tests at 80°C, allowing excellent spatial and temporal resolutions. The monotonic load was applied in force control mode with a constant stress rate of 1000MPa/s. The thermomechanical responses up to two maximum stresses were evaluated, one below the B19' transformation onset and the second one above it. After reaching the maximum stress upon loading, the force was kept constant to allow the sample to reach the thermal equilibrium. Once the thermal equilibrium was reached, we proceeded to unload the sample at 1000MPa/s. After the unloading, we also recorded IR thermographs until the sample reached the thermal equilibrium. Two different samples were used at 40°C and 80°C for the group of load-unload tests in the B2↔R and B2/R↔ B19' loading regimes.

The acquired thermographs were converted into temperature elevation maps by subtracting a reference thermograph, which was calculated by performing a temporal averaging of 50 thermographs in the thermal equilibrium. The temperature elevation maps were converted into one-dimension arrays of temperature values by averaging the rows of pixels of a 35x120px rectangle in the middle of the sample. This post-processing procedure is illustrated schematically in Figure 5-26.

The 1D temperature evolution upon monotonic tensile loading are presented in the form of height-time-temperature maps in Figure 5-27-Figure 5-30, where the x-axis represents the time, the y-axis the z-position of a temperature point and the temperature is denoted by the color. In addition, the stress and temperature elevation at the mid cross-section are plotted together with each height-time-temperature map.

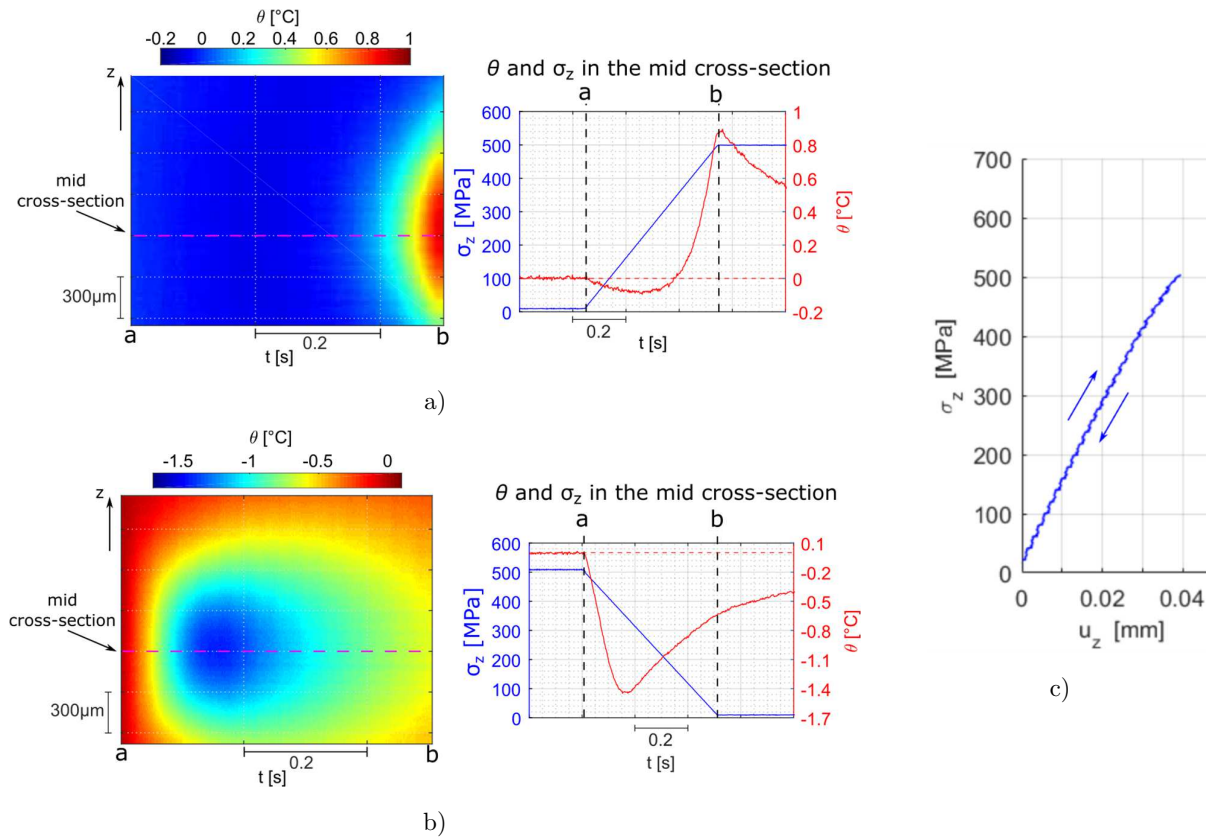


Figure 5-27 Temperature elevations upon high strain rate tests in the B2↔R loading regime at 40°C. a) Load up to 500MPa. b) Unloading down to 10 MPa. c) Nominal stress vs extensometer elongation response.

At 40°C, a first drop of temperature, characteristic of the thermoelastic effect in metals, is observed in the first stage of the loading (Figure 5-27a). When the stress reaches ~220MPa, the material starts heating up indicating the start of the B2→R transformation. The heating stage is continuous and spreads axially up to ~1mm from the mid cross-section. At the end of the load, when the stress reaches 500MPa, the temperature in the mid cross-section is almost 1°C. Upon the unloading (Figure 5-27b), the temperature drops since the very beginning of the stress relieve, indicating an early R→B2 reverse transformation. The temperature drop in this case is faster and more intense than the heating observed during the loading stage. Note that the temperature drop attains its minimum when the stress reaches 360MPa being 140MPa higher than the stress onset identified for the forward B2→R transformation. After that, natural return to the equilibrium temperature, together with thermoelastic heat release complete the unloading stage.

In contrast, the temperature elevations during the high strain rate tensile test at 80°C shows lower magnitudes and more homogeneous distribution than at 40°C even though the range of the applied stress was much higher (Figure 5-28). Upon the loading (Figure 5-28a), the weak thermoelastic heat source results in an apparent homogeneous temperature drop

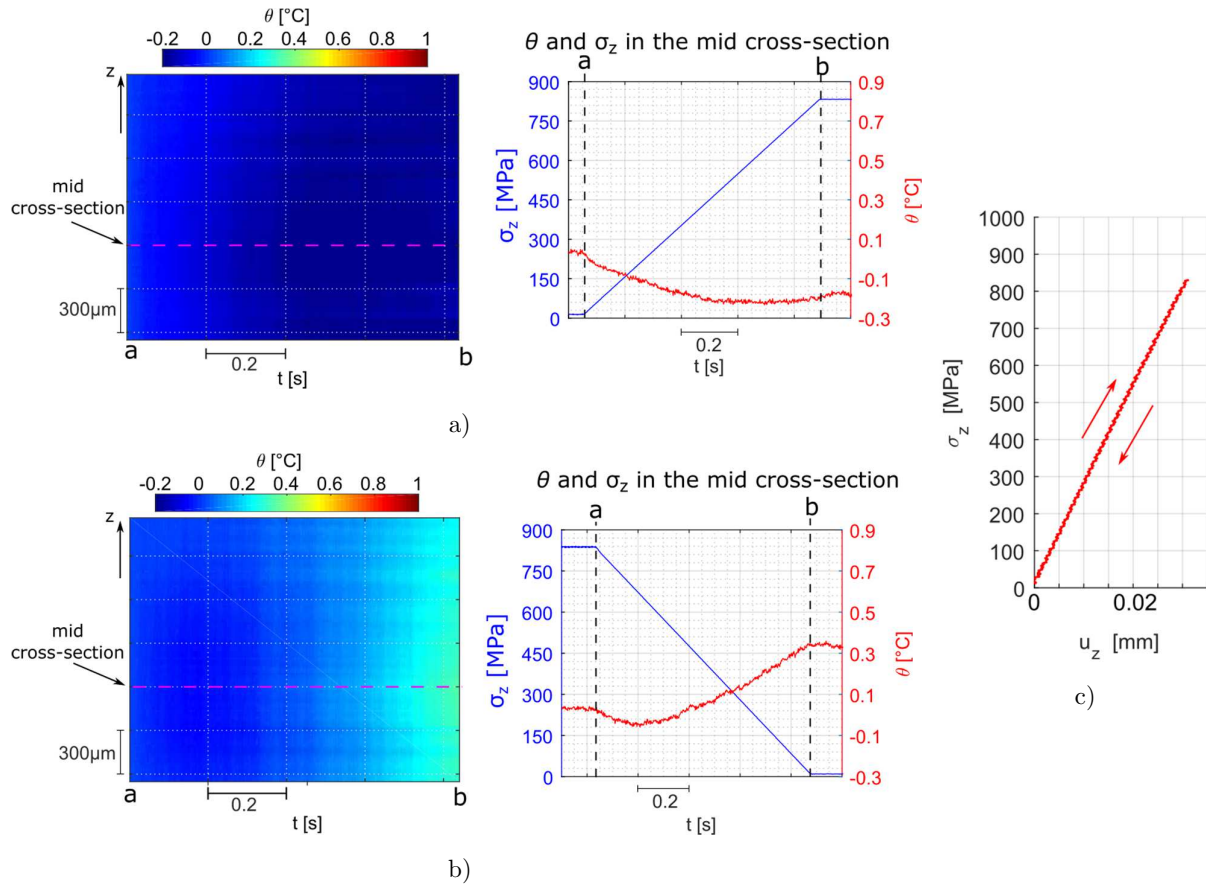


Figure 5-28 Temperature elevations upon high strain rate tests in the B2↔R loading regime at 80°C. a) Load up to 800MPa. b) Unloading to 10 MPa. c) Nominal stress vs extensometer elongation response.

distribution along the axis of the sample. At the mid cross-section, the temperature drops down to  $-0.2^{\circ}\text{C}$  when the stress reaches 580MPa. After that, a slight temperature increase is observed, which may indicate the onset of the B2→R phase transformation. This hypothesis is supported by the fact that the start of the unloading (Figure 5-28b) is accompanied by a drop of temperature instead of an increase as it would be expected if the material would behaves elastically. To sum up, at  $80^{\circ}\text{C}$ , the thermoelastic effect prevails over the latent heat of the B2→R transformation, contrarily to the behavior observed at  $40^{\circ}\text{C}$ . The latent heat of the B2→R transformation renders the temperature distribution in the sample heterogeneous.

The results of the tests performed up to stresses beyond the B19' transformation stress onset are presented in Figure 5-29 and Figure 5-30. Unlike the B2↔R loading regime, when the B19' transformation is stress-induced, a fast and intense temperature increase is observed. Similar maximum temperature elevation values in the mid cross-section are obtained at  $40^{\circ}\text{C}$  and  $80^{\circ}\text{C}$  ( $22^{\circ}\text{C}$  in Figure 5-29a and  $24^{\circ}\text{C}$  in Figure 5-30a respectively). The temperature increase occurs almost instantaneously in a volume of  $600\mu\text{m}$  height in the mid cross-section. Such a high temperature elevation prevents the transformation to spread outside the mid cross-section; consequently, once the heat is dissipated, and the material

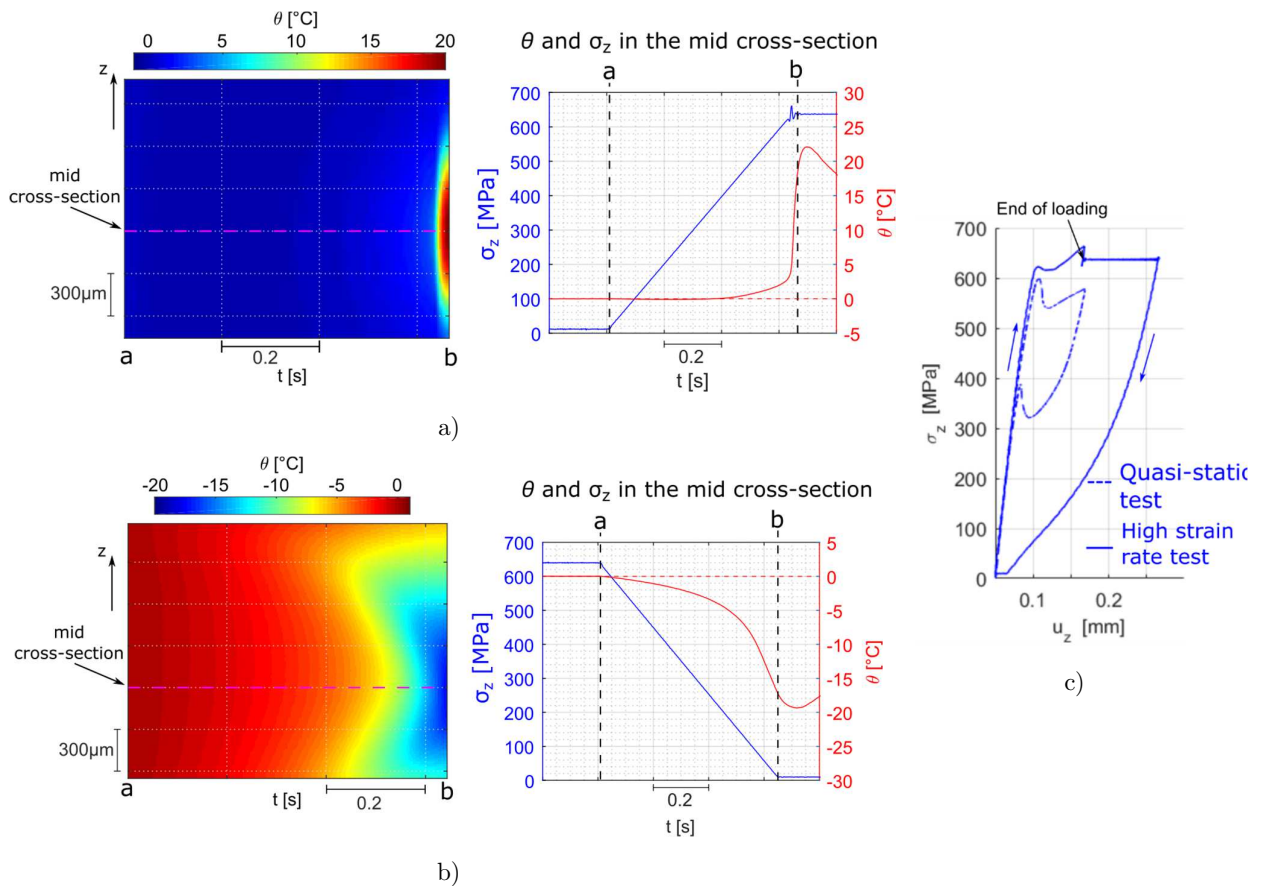


Figure 5-29 Temperature elevations upon high strain rate tests in the B2/R $\leftrightarrow$ B19' loading regime at 40°C. a) Load up to 630MPa. b) Unloading down to 10 MPa. c) Nominal stress vs extensometer elongation response.

cools down, the phase transformation spreads out of the mid cross-section due to the force constraint imposed after the loading end. This is evidenced by the increase of the elongation of the extensometer observed in Figure 5-29c and Figure 5-30c after the end of the loading. Upon the unloading, the sample tested at 40°C starts cooling down at  $\sim 1\text{mm}$  outside the mid cross-section (Figure 5-29b). The temperature drop produces a significant shift in the stress needed for the reverse transformation in the mid cross-section, which could not even be completed after unloading the sample. It was only upon the return to thermal equilibrium stage that the transformation strain could finally be recovered. At 80°C, a similar phenomenon is observed (Figure 5-30b). This time the sample starts cooling at  $\sim 600\mu\text{m}$  from the mid cross-section and the reverse transformation onset decreased from 600MPa (see quasi-static response in Figure 5-30c) down to  $\sim 300\text{MPa}$ .

In conclusion, the characteristic latent heats of first order phase transformations as the ones occurring in NiTi generate significant gradients of temperature elevation, much higher than the ones induced by thermoelasticity. In the case of B2 $\rightarrow$ R phase transformation, temperature elevation differences of more than 1°C in a zone of 0.5mm long away from the mid cross-section were recorded. The temperature distribution turns much more

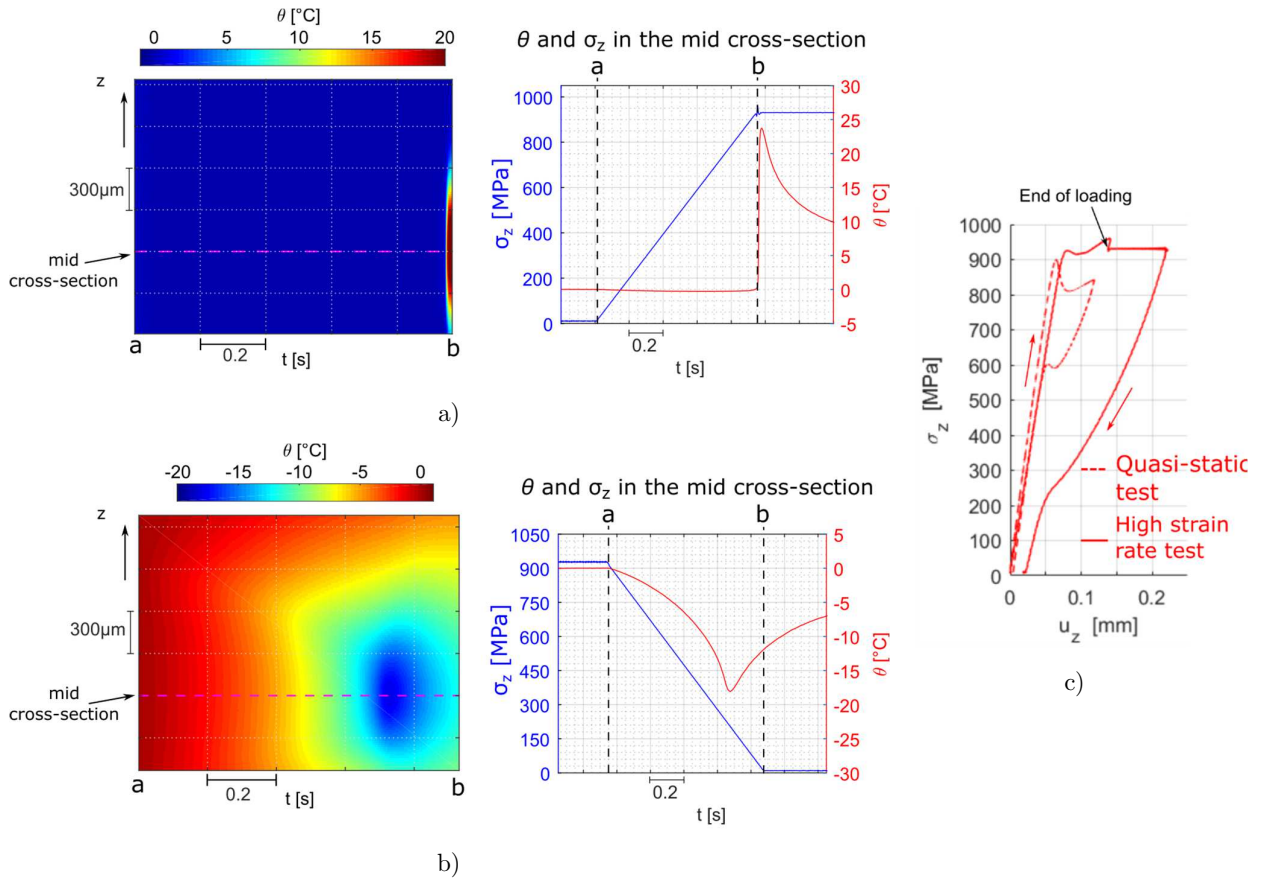


Figure 5-30 Temperature elevations upon high strain rate tests in the B2/R $\leftrightarrow$ B19' loading regime at 80°C. a) Load up to 930 MPa. b) Unloading down to 10 MPa. c) Nominal stress vs extensometer elongation response.

heterogeneous when the B19' transformation is induced. It even affects significantly the mechanical response of the material by shifting the transformation stresses.

In the following section, we propose a numerical tool to assess the interaction between phase transformations, heat and temperature taking into account the hourglass shape of our samples.

## 5.4. Modeling of the thermomechanical behavior of NiTi

### 5.4.1. 1D diffusion problem in hourglass-shaped samples

To begin with, we integrate the local form of the heat equation in the entire sample volume within the testing machine clamps:

$$\int_V \rho C_p \dot{T}(z, t) dV + \int_V \text{div}(\vec{q}(z, t)) dV = \int_V \rho C_p s_t(z, t) dV, \quad (5.24)$$

where the second term is computed using the theorem of the divergence:

$$\int_V \text{div}(\vec{q}(z, t)) dV = \int_{\partial V} \vec{q} \cdot \vec{n} dS. \quad (5.25)$$

As in the constant cross-section one-dimensional diffusion problem in section 5.1.2.2, the heat flux is defined by the Fourier's law

$$\bar{q}(z, t) = -\lambda \overline{\text{grad}}(T(z, t)); \quad (5.26)$$

therefore the heat conduction term (5.25) becomes

$$\int_V \text{div}(\bar{q}(z, t)) dV = \left( -\lambda \frac{\partial^2 T}{\partial z^2} + \frac{h_e S_{lat}(z)}{V(z)} \theta(z, t) \right) S_{cs}(z) dz. \quad (5.27)$$

Unlike the 1D diffusion problem described in section 5.1.2.2, the heat conduction term in this case considers the changing cross section  $S_{cs}$  in the  $z$  direction. As a result the volume

$$V(z) = \pi r(z)^2 dz \quad (5.28)$$

and the lateral area of the sample

$$S_{lat}(z) = 2\pi r(z) dz \quad (5.29)$$

are also functions of  $z$ . In (5.27),  $\lambda$  denotes the heat conductivity of the material and  $h_e$  the heat exchange coefficient of the sample with the surroundings. The temperature elevation  $\theta$  is defined this time as a function of  $z$  and the time  $t$ ,

$$\theta(z, t) = T(z, t) - T_{ref}(z, t), \quad (5.30)$$

where the reference temperature  $T_{ref}$  is the temperature distribution in the sample in the equilibrium state.

Rewriting the heat equation in terms of  $\theta(z, t)$  results in the following expression:

$$\frac{\partial \theta(z, t)}{\partial t} - \frac{-\lambda}{\rho C_p} \frac{\partial^2 \theta(z, t)}{\partial z^2} + \frac{\theta(z, t)}{\tau_{eq}(z)} = \frac{s_l(z, t)}{\rho C_p}, \quad (5.31)$$

where the characteristic time  $\tau_{eq}$  is a function of  $z$  defined as

$$\tau_{eq} = \frac{\rho C_p V(z)}{h_e S_{ext}(z)}. \quad (5.32)$$

The computation of the heat equation (5.31) was carried out using the Crank-Nicolson implicit finite difference method. It approximates the values  $\theta$  at the intermediate step time  $t+dt/2$  by averaging the values of  $\theta$  at the instants  $t$  and  $t+dt$ :

$$\theta\left(z, t + \frac{dt}{2}\right) \approx \frac{\theta(z, t) + \theta(z, t + dt)}{2} \quad (5.33)$$

The time derivative of  $\theta(z, t + dt/2)$  is approximated using a centered differences scheme, hence,

$$\frac{\partial \theta(z, t + \frac{dt}{2})}{\partial t} \approx \frac{\theta(z, t + dt) - \theta(z, t)}{dt} + O(dt), \quad (5.34)$$

whereas the first order spatial derivative at  $t+dt/2$  is approximated using the average of the first order centered differences for  $\theta_z(z, t)$  and  $\theta_z(z, t + dt)$ , i.e.:

$$\frac{\partial \theta(z, t + \frac{dt}{2})}{\partial z} = \frac{1}{2} \left( \frac{\theta(z + dz, t) - \theta(z - dz, t)}{2dz} + \frac{\theta(z + dz, t + dt) - \theta(z - dz, t + dt)}{2dz} \right) + O(dz). \quad (5.35)$$

Similarly, the second order spatial derivative at  $t+dt/2$  is computed by averaging the second order centered differences for  $\theta_{zz}(z, t)$  and  $\theta_{zz}(z, t + dt)$ , which results in

$$\begin{aligned} \frac{\partial^2 \theta(z, t + \frac{dt}{2})}{\partial z^2} = & \frac{1}{2} \left( \frac{\theta(z + dz, t) - 2\theta(z, t) + \theta(z - dz, t)}{\partial z^2} \right. \\ & \left. + \frac{\theta(z + dz, t + dt) - 2\theta(z, t + dt) + \theta(z - dz, t + dt)}{\partial z^2} \right) + O(dz^2). \end{aligned} \quad (5.36)$$

Assuming that the heat sources term  $s_t$  is time independent, the heat equation becomes

$$\begin{aligned} \frac{\partial \theta(z, t + dt) + \theta(z, t)}{\partial t} - \frac{\lambda}{2\rho C_p} \left( \frac{\theta(z + dz, t) - 2\theta(z, t) + \theta(z - dz, t)}{\partial z^2} \right. \\ \left. + \frac{\theta(z + dz, t + dt) - 2\theta(z, t + dt) + \theta(z - dz, t + dt)}{\partial z^2} \right) + \frac{\theta(z, t) + \theta(z, t + dt)}{2\tau_{eq}(z)} = \frac{s_t(z)}{\rho C_p}. \end{aligned} \quad (5.37)$$

Ordering the ,

$$\begin{aligned} \left( \frac{1}{dt} + \frac{\lambda}{2\rho C_p dz^2} + \frac{1}{2\tau_{eq}(z)} \right) \theta(z, t + dt) + \left( -\frac{1}{dt} + \frac{\lambda}{2\rho C_p dz^2} + \frac{1}{2\tau_{eq}(z)} \right) \theta(z, t) \\ - \frac{\lambda}{2\rho C_p dz^2} (\theta(z + dz, t + dt) + \theta(z - dz, t + dt) + \theta(z + dz, t) + \theta(z - dz, t + t)) = \frac{s_t(z)}{\rho C_p} \end{aligned} \quad (5.38)$$

with the initial condition

$$\theta(z, 0) = 0 \quad (5.39)$$

and the Robin boundary condition in  $z \in \{L, -L\}$ :

$$\frac{\partial \theta(z, t)}{\partial z} = -\frac{z}{L} \frac{h_c}{\lambda} \theta(z, t) \quad (5.40)$$

where  $h_c$  is the heat exchange coefficient between the sample and the testing machine clamps. Resolving the boundary condition (5.40) using the Crank-Nicolson scheme (equation (5.35)) results in

$$\frac{\theta(dz - L, t) - \theta(-L, t)}{\partial z} = \frac{h_c}{\lambda} \theta(-L, t) \quad (5.41)$$

and

$$\frac{\theta(L, t) - \theta(L - dz, t)}{\partial z} = -\frac{h_c}{\lambda} \theta(L, t). \quad (5.42)$$

The equation (5.38) can be reduced to a matrix form problem such as:

$$\mathbf{A}(z)\vec{\theta}(t + dt) + \mathbf{B}(z)\vec{\theta}(t) = \vec{S}_t(z, t) \quad (5.43)$$

with

$$\vec{\theta}(z, t) = \begin{pmatrix} \theta(-L, t) \\ \theta(dz - L, t) \\ \vdots \\ \theta(L - dz, t) \\ \theta(L, t) \end{pmatrix} \quad \text{and} \quad \vec{S}_t(z, t) = \frac{1}{\rho C_p} \begin{pmatrix} 0 \\ s_t(dz - L, t) \\ \vdots \\ s_t(L - dz, t) \\ 0 \end{pmatrix} \quad (5.44)$$

and

$$A(z) = \begin{pmatrix} a & -1 & 0 & 0 & \dots & 0 \\ b & c(z) & b & 0 & \dots & 0 \\ 0 & b & c(z) & b & \dots & 0 \\ \vdots & \vdots & \vdots & \vdots & \vdots & \vdots \\ 0 & \dots & 0 & b & c(z) & b \\ 0 & \dots & 0 & 0 & -1 & a \end{pmatrix} \quad \text{and} \quad B(z) = \begin{pmatrix} 0 & 0 & 0 & 0 & \dots & 0 \\ b & d(z) & b & 0 & \dots & 0 \\ 0 & b & d(z) & b & \dots & 0 \\ \vdots & \vdots & \vdots & \vdots & \vdots & \vdots \\ 0 & \dots & 0 & b & d(z) & b \\ 0 & \dots & 0 & 0 & 0 & 0 \end{pmatrix}. \quad (5.45)$$

$$\text{where} \quad \begin{cases} a = 1 + \frac{h_{clamps} dz}{\lambda} \\ b = -\frac{\lambda}{2\rho C_p dz^2} \\ c(z) = \frac{1}{dt} + \frac{\lambda}{2\rho C_p dz^2} + \frac{1}{2\tau_{eq}(z)} \\ d(z) = -\frac{1}{dt} + \frac{\lambda}{2\rho C_p dz^2} + \frac{1}{2\tau_{eq}(z)} \end{cases} \quad (5.46)$$

The Crank-Nicolson scheme is widely used for solving diffusion problems as it provides a second order accurate implicit finite-difference procedure in both time and space. Moreover, note that the matrix  $\mathbf{A}$  is tridiagonal and symmetric positive definite, which facilitates the calculation of its inverse when solving the system of linear equations (5.43). It worth mentioning that neither  $\mathbf{A}$  nor  $\mathbf{B}$  change in time as they are defined considering a constant time step  $dt$ . Similarly, their sizes are defined by the spatial discretization of the problem, assuming it is done at a fixed step equal to  $dz$ .

#### 5.4.1.1. Thermoelastic coupling

The thermoelastic coupling ( $s_{th}$ ) is one of the heat sources term previously introduced in the energy conservation equation (5.3). It defines the interaction between the volumetric strains and the temperature:

$$s_{th} = \rho T \frac{\partial^2 \Psi}{\partial T \partial \boldsymbol{\varepsilon}} : \dot{\boldsymbol{\varepsilon}}, \quad (5.47)$$

which allows us to describe the thermal expansion phenomenon and inversely, the adiabatic cooling effect produced upon pressure increase.

With respect to the volume specific Helmholtz free energy potential  $\rho\Psi$ , we adopted the same form as the potential  $\mathbf{F}$  introduced in the Sedláč model in Chapter 3:

$$\begin{aligned} \rho\Psi = \mathbf{F} = & \frac{1}{2} K tr(\boldsymbol{\varepsilon} - \alpha\theta\mathbf{I})^2 + G(\xi, \eta) \left\| dev(\boldsymbol{\varepsilon}) - \xi \boldsymbol{\varepsilon}^{tr} \right\|^2 \\ & + u_0^A - s_0^A T + c^A \left[ (T - T_0) - T \ln \left( \frac{T}{T_0} \right) \right] + \xi \Delta s^{AM} (T - T_0) + \eta \Delta s^{AR} (T - T_0^R). \end{aligned} \quad (5.48)$$

Note that we modified the definition of the strain tensor form proposed by Sedláč et al. in order to introduce the thermal expansion. As a result the strain tensor now reads

$$\boldsymbol{\varepsilon} = \boldsymbol{\varepsilon}^{el} + \boldsymbol{\varepsilon}^{in} + \alpha\theta\mathbf{I} \quad (5.49)$$

where  $\alpha$  is the isotropic thermal expansion coefficient and  $\mathbf{I}$  denotes the second order identity tensor. Let us recall the thermodynamic forces associated with the internal variables  $\boldsymbol{\varepsilon}$ ,  $\xi$  (volume fraction of B19' martensite),  $\boldsymbol{\varepsilon}^{tr}$  (transformation strain tensor), and  $\eta$  (volume fraction of R-phase) of the Sedláč model:

$$\boldsymbol{\sigma} = \rho \frac{\partial \Psi}{\partial \boldsymbol{\varepsilon}} = K tr(\boldsymbol{\varepsilon} - \alpha\theta\mathbf{I})\mathbf{I} + 2G(\xi, \eta) \left[ dev(\boldsymbol{\varepsilon}) - \xi \boldsymbol{\varepsilon}^{tr} \right], \quad (5.50)$$

$$\mathbf{X} = -\rho \frac{\partial \Psi}{\partial \boldsymbol{\varepsilon}^{tr}} = 2G(\xi, \eta) \left[ dev(\boldsymbol{\varepsilon}) - \xi \boldsymbol{\varepsilon}^{tr} \right], \quad (5.51)$$

$$\begin{aligned} \pi = -\rho \frac{\partial \Psi}{\partial \xi} = & -\frac{\partial G(\xi, \eta)}{\partial \xi} \left\| dev(\boldsymbol{\varepsilon}) - \xi \boldsymbol{\varepsilon}^{tr} \right\|^2 + 2G(\xi, \eta) \left( dev(\boldsymbol{\varepsilon}) - \xi \boldsymbol{\varepsilon}^{tr} \right) : \boldsymbol{\varepsilon}^{tr} \\ & - \Delta s^{AM} (T - T_0) + \eta \Delta s^{AR} \frac{\partial T_0^R(\xi, \eta)}{\partial \xi} \end{aligned} \quad (5.52)$$

$$\tau = -\rho \frac{\partial \Psi}{\partial \eta} = -\frac{\partial G(\xi, \eta)}{\partial \eta} \left\| dev(\boldsymbol{\varepsilon}) - \xi \boldsymbol{\varepsilon}^{tr} \right\|^2 - \Delta s^{AR} (T - T_0^R(\xi, \eta)) + \eta \Delta s^{AR} \frac{\partial T_0^R(\xi, \eta)}{\partial \eta}. \quad (5.53)$$

Now that we have introduced the thermal deformations, the thermoelastic coupling becomes

$$\rho T \frac{\partial^2 \Psi}{\partial T \partial \boldsymbol{\varepsilon}} : \dot{\boldsymbol{\varepsilon}} = -3K\alpha T \mathbf{I} : \dot{\boldsymbol{\varepsilon}} \quad (5.54)$$

with  $:$  as the double dot tensor product and the strain rate tensor as

$$\dot{\boldsymbol{\varepsilon}} = \dot{\boldsymbol{\varepsilon}}^{el} + \dot{\xi} \boldsymbol{\varepsilon}^{tr} + \xi \dot{\boldsymbol{\varepsilon}}^{tr} + \alpha \dot{\theta} \mathbf{I}. \quad (5.55)$$

In order to define the elastic strain rate tensor, let us rewrite the stress and elastic strain tensors in terms of the fourth order isotropic stiffness tensor  $\bar{\mathbf{C}}$ :

$$\boldsymbol{\sigma} = \bar{\mathbf{C}} : \boldsymbol{\varepsilon}^{el} \quad \text{and} \quad \boldsymbol{\varepsilon}^{el} = \bar{\mathbf{C}}^{-1} : \boldsymbol{\sigma}; \quad (5.56)$$

therefore the stress and strain rate tensors read

$$\dot{\boldsymbol{\sigma}} = \bar{\mathbf{C}} : \dot{\boldsymbol{\varepsilon}}^{el} \quad \text{and} \quad \dot{\boldsymbol{\varepsilon}}^{el} = \bar{\mathbf{C}}^{-1} : \dot{\boldsymbol{\sigma}}. \quad (5.57)$$

Moreover, in a uniaxial stress state, the stress tensor  $\boldsymbol{\sigma}$  can be defined as

$$\boldsymbol{\sigma} = \tilde{f}(t)\mathbf{N} \quad (5.58)$$

with

$$\mathbf{N} = \begin{bmatrix} 0 & 0 & 0 \\ & 1 & 0 \\ sym & & 0 \end{bmatrix}_{rz\theta} \quad (5.59)$$

as the normalized directional tensor and  $\tilde{f}(t)$  as the magnitude of the stress. Consequently the stress rate tensor reads

$$\dot{\boldsymbol{\sigma}} = \dot{\tilde{f}}(t)\mathbf{N}, \quad (5.60)$$

which lead us to the following expression for the strain rate tensor:

$$\dot{\boldsymbol{\varepsilon}} = \bar{\mathbf{C}}^{-1} : \dot{\boldsymbol{\sigma}} + k\dot{\xi}\mathbf{N}' + \alpha\dot{\theta}\mathbf{I}, \quad (5.61)$$

where we considered  $\boldsymbol{\varepsilon}^{tr} = k\mathbf{N}'$  (valid only in a uniaxial superelastic configuration), with  $k$  as the transformation strain magnitude and

$$\mathbf{N}' = \mathbf{N} - \frac{1}{3}tr(\mathbf{N})\mathbf{I}. \quad (5.62)$$

As a result, the expression  $\mathbf{I} : \dot{\boldsymbol{\varepsilon}}$  in (5.54) can be defined as

$$\mathbf{I} : \dot{\boldsymbol{\varepsilon}} = \dot{\tilde{f}}(t)\mathbf{I} : \bar{\mathbf{C}}^{-1} : \mathbf{N} + k\dot{\xi}\mathbf{I} : \mathbf{N}' + \alpha\dot{\theta}\mathbf{I} : \mathbf{I}, \quad (5.63)$$

where  $\mathbf{I} : \bar{\mathbf{C}}^{-1} = \frac{1}{3K}\mathbf{I}$ ,  $\mathbf{I} : \mathbf{N} = 1$ ,  $\mathbf{I} : \mathbf{N}' = 0$ , and  $\mathbf{I} : \mathbf{I} = 3$ . Finally, the thermoelastic coupling reads

$$\rho T \frac{\partial^2 \Psi}{\partial T \partial \boldsymbol{\varepsilon}} : \dot{\boldsymbol{\varepsilon}} = -\alpha \dot{\tilde{f}}(t) T - 9KT\alpha^2 \dot{\theta}. \quad (5.64)$$

Considering that the temperature elevations are small, we can assume  $T \approx T_{ref}$ . To implement the thermoelastic coupling in the 1D heat diffusion solution of a tensile loaded hourglass-shaped sample, we resolve  $\dot{\theta}$  using the Crank-Nicolson scheme. As a result, the components  $c(z)$  and  $d(z)$  of matrices  $\mathbf{A}$  and  $\mathbf{B}$  in (5.45) become

$$\begin{cases} c(z) = \frac{1}{dt} + \frac{\lambda}{2\rho C_p dz^2} + \frac{1}{2\tau_{eq}(z)} + \frac{9KT_{ref}\alpha^2}{\rho C_p dt} \\ d(z) = -\frac{1}{dt} + \frac{\lambda}{2\rho C_p dz^2} + \frac{1}{2\tau_{eq}(z)} - \frac{9KT_{ref}\alpha^2}{\rho C_p dt}, \end{cases} \quad (5.65)$$

and the thermoelastic component of the heat source term in (5.44) is now defined as:

$$s_{th}(z, t) = -\alpha \dot{f}(t) T_{ref}. \quad (5.66)$$

#### 5.4.1.2. Phase transformation thermomechanical coupling

The other thermomechanical couplings, associated to the internal variables  $\xi$ ,  $\boldsymbol{\varepsilon}^{tr}$ , and  $\eta$ , are defined as follows:

$$s_{\xi} = \rho T \frac{\partial^2 \Psi}{\partial T \partial \xi} \dot{\xi} = T_{ref} \Delta s^{AM} \dot{\xi} \quad (5.67)$$

$$s_{\boldsymbol{\varepsilon}^{tr}} = \rho T \frac{\partial^2 \Psi}{\partial T \partial \boldsymbol{\varepsilon}^{tr}} : \dot{\boldsymbol{\varepsilon}}^{tr} = 0 \quad (5.68)$$

$$s_{\eta} = \rho T \frac{\partial^2 \Psi}{\partial T \partial \eta} \dot{\eta} = T_{ref} \Delta s^{AR} \dot{\eta}. \quad (5.69)$$

As a result the total heat source term in (5.44) becomes

$$s_t(z, t) = s_{th}(z, t) + s_{\xi}(z, t) + s_{\eta}(z, t). \quad (5.70)$$

### 5.4.2. Identification of the heat exchange coefficients

In addition to the parameters of the Sedlák model identified in Chapter 3, the computation of the 1D diffusional problem of tensile loaded NiTi hourglass-shaped samples requires the identification of the heat conductivity  $\lambda$ , the thermal expansion coefficient  $\alpha$ , the specific heat capacity  $C_p$ , the volumetric mass  $\rho$  and the heat exchange parameters  $h_c$  and  $h_e$ . The first three quantities are material parameters, while the latest two are dependent on the boundary conditions of the problem.

For the purpose of simulations, we define the specific heat capacity  $C_p$  by averaging the values measured upon DSC experiments presented in Chapter 3. It resulted in a value of  $412 \text{J}(\text{kgK})^{-1}$ . The density mass was set equal to  $6400 \text{kgm}^{-3}$  as in other works [148][149], the thermal expansion coefficient equal to  $11 \times 10^{-6} \text{K}^{-1}$ , and the thermal conductivity set equal to  $5.5 \text{Wm}^{-1}\text{K}^{-1}$ , neglecting possible changes due to phase transformations. It worth mentioning that the thermal conductivity of NiTi shows large scatter among reported works in the literature. For instance, values as low as  $4.8 \text{Wm}^{-1}\text{K}^{-1}$  have been reported in thin NiTi films [150], and as high as  $18 \text{Wm}^{-1}\text{K}^{-1}$  in NiTi rods [151].

In order to estimate the heat exchange coefficients  $h_c$  and  $h_e$ , a commonly used practice consists in using the thermal model to predict the temperature evolution of a sample during its return to thermal equilibrium in the absence of heat sources (i.e. the right hand of the

heat equation (5.31) becomes 0). We carried out this procedure using the thermal data collected upon the return to thermal equilibrium of high strain rate tensile tests performed at 40°C (Figure 5-27). We focused on the loading and unloading tests in the B2→R loading regime since they showed temperature elevations well above the thermal resolution of the IR detector. Moreover, we avoided using the heat exchange coefficients estimate procedure in tests exhibiting stress-induced B19' transformation because we detected continuous phase transformation processes during the return to thermal equilibrium stage (see Figure 5-29c

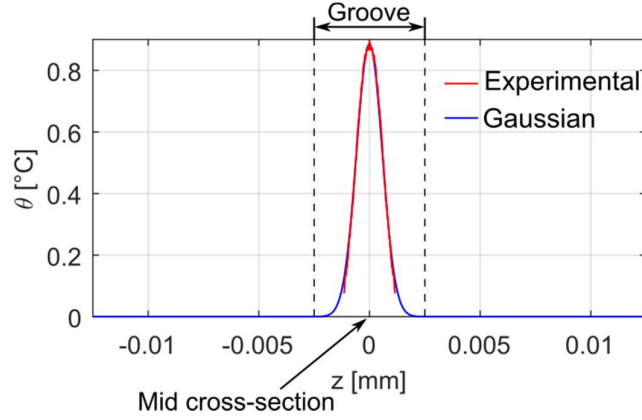


Figure 5-31 Fitting of a Gaussian function to the temperature profile obtained at the end of the high strain loading test presented in Figure 5-27a.

and Figure 5-30c). This, evidently, violates the zero-heat source assumption of the estimate procedure.

For estimating the heat exchange coefficients using the 1D heat equation model for hourglass-shaped samples, we require to know the axial temperature distribution of the whole sample volume within the tensile machine clamps at the beginning of the return to equilibrium stage. Since the tensile loading was applied at high strain rate, we might consider that negligible temperature evolutions occurred in the zones of the samples near the clamps (distanced ~12.5mm from the mid cross-section). This allowed us to approximate the full axial temperature distribution of the sample at the end of the loading by the following Gaussian function:

$$f(z) = Ce^{\frac{-z^2}{2b^2}} \quad (5.71)$$

where  $C$  is the local temperature in the mid-cross section and  $b$  is a parameter to fit. Figure 5-31 shows the estimate of the temperature profile in the 25mm length of the hourglass

Parameter	Value	Unit
$\lambda$	5.5	W(mK) <sup>-1</sup>
$C_p$	412	J(kgK) <sup>-1</sup>
$\rho$	4600	Kgm <sup>-3</sup>
$\alpha$	11x10-6	K <sup>-1</sup>
$h_e$	270	WK <sup>-1</sup> m <sup>-2</sup>
$h_c$	neglected	WK <sup>-1</sup> m <sup>-2</sup>

Table 5-2 Thermal material parameters for simulations of tensile loadings on NiTi hourglass-shaped samples

shaped sample tested at high strain rate in Figure 5-27a. The estimated profile was discretized in steps of  $15\mu\text{m}$ , then, used as an initial temperature profile to carry out the identification of the heat exchange coefficients.

The identification of the heat exchange coefficients was carried out by the least square error (LSE) fitting method. For that, we used the 128px-length 1D temperature data acquired during the return to thermal equilibrium stage after the loading and the unloading tests previously presented in Figure 5-27a and Figure 5-27b respectively.

The resulting values of the heat exchange coefficient with the surrounding air ( $h_e$ ) was calculated equal to  $152 \text{ WK}^{-1}\text{m}^{-2}$  in the case of LSE fitting to the return to thermal equilibrium after the loading test in Figure 5-27a, and equal to  $270 \text{ WK}^{-1}\text{m}^{-2}$  in the case of the unloading test in Figure 5-27b. In contrast, the heat exchange coefficient with the clamps ( $h_c$ ) did not show any effect on the simulated return to thermal equilibrium stages. We attribute this to the localized nature of the temperature elevation in the mid cross-section of the sample. Recall that

in the constant cross-section parts of the sample, the material sees almost 2.5 times less stress than in the mid cross-section; therefore, in principle, the heat sources there must be

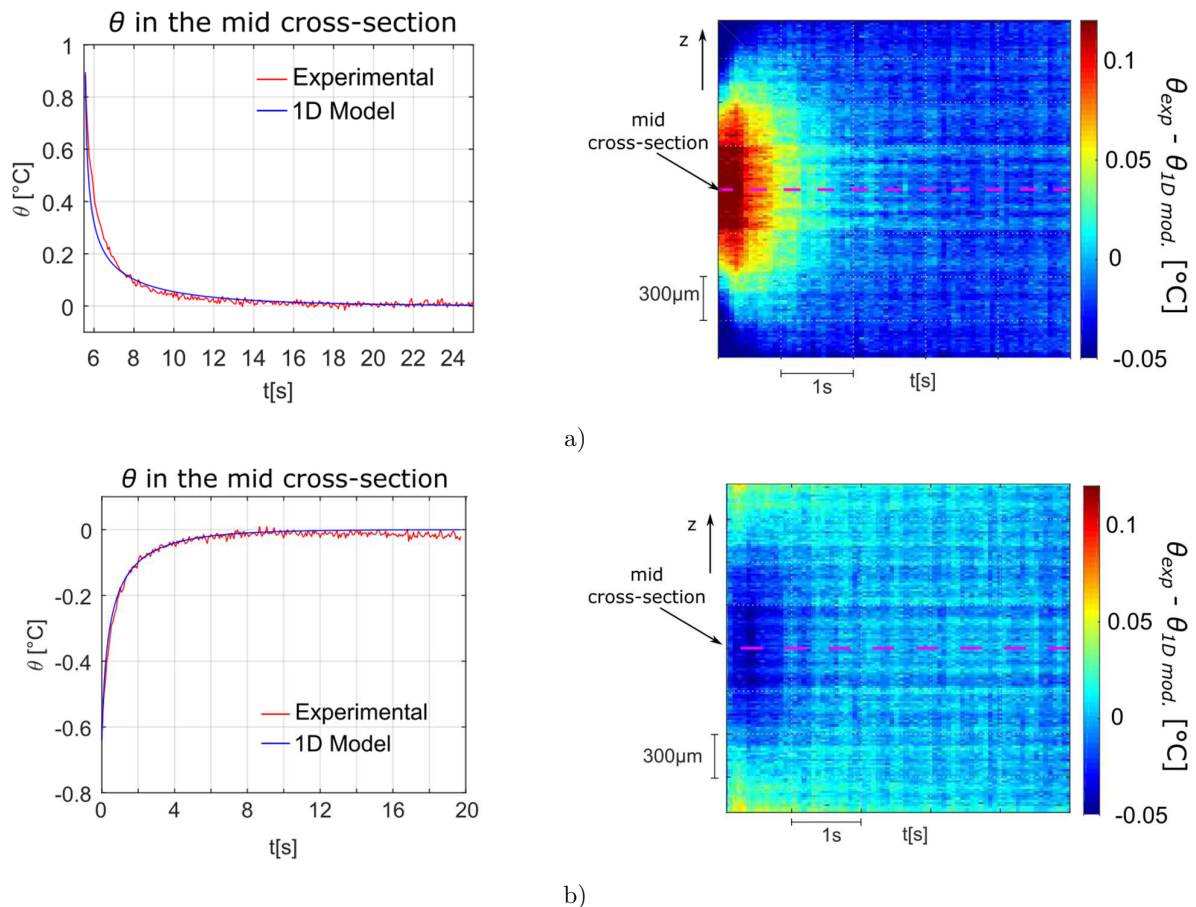


Figure 5-32 Results of simulations of the natural cooling/heating after high strain rate tests presented in Figure 5-27a (a) and Figure 5-27b (b). In addition the differences between the experimental temperature elevations and the modeled ones are presented in the form of height-time-temperature diagrams.

at least 2.5 times lower, which makes the temperature elevations in these parts very low. Since the temperature of the grips was stabilized for long time before running the tests, and considering that the length of the sample is much larger than the zone of concentrated temperature increase, we might change the Robin-type boundary conditions established in (5.40) by Neumann-type ones, i.e.:

$$\frac{\partial \theta(z,t)}{\partial z} = 0. \quad (5.72)$$

The predicted temperature evolutions in the mid cross-section after the high strain loading and unloading tests are shown in Figure 5-32. In addition, we show the temporal axial distribution of the error between the experimental data and the model. Note that the fitting procedure resulted in lower error magnitudes in the case of natural heating after the fast unloading test (Figure 5-32b) than in the case of natural cooling after the fast loading test (Figure 5-32a).

### 5.4.3. Cyclic thermoelastic effect

We simulated the thermal response of an isotropic elastic hourglass-shaped sample subjected to repetitive pull-pull tensile loading. For these simulations, we use the thermal parameters presented in Table 5-2 and the same bulk modulus as the one identified for NiTi in Chapter 3 (150GPa). The time discretization step was set equal to  $8 \times 10^{-4}$ s and the axial dimension of the sample discretized into steps of  $150 \mu\text{m}$ . Cyclic sinusoidal tests were simulated under force-control conditions at 25Hz with a stress ratio of 0.1 and a maximal stress of 490MPa. The simulation was started at the mean stress of the cyclic loading and conducted until completing 100 cycles. The reference temperature was kept constant at  $40^\circ\text{C}$ .

The simulated temperature evolution of an elastic hourglass-shaped sample is shown in Figure 5-33. As observed in the mid cross-section response (Figure 5-33b), the mean temperature stabilizes after the first couple of stress cycles. The cyclic component of the temperature, on the other hand, resulted  $90^\circ$  out-of-phase with respect to the cyclic applied

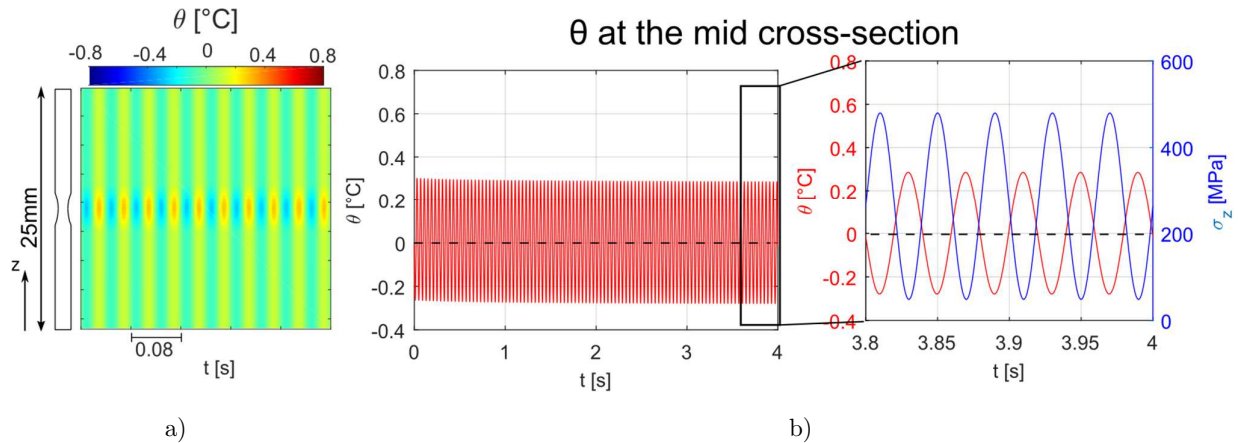


Figure 5-33 Simulated temperature response of an isotropic elastic hourglass-shaped sample under cyclic tensile stress. a) Height-time-temperature diagram showing the axial temperature distribution of the total length of the sample in the last 10 cycles of the simulation. b) Temperature elevation evolution in the mid cross-section.

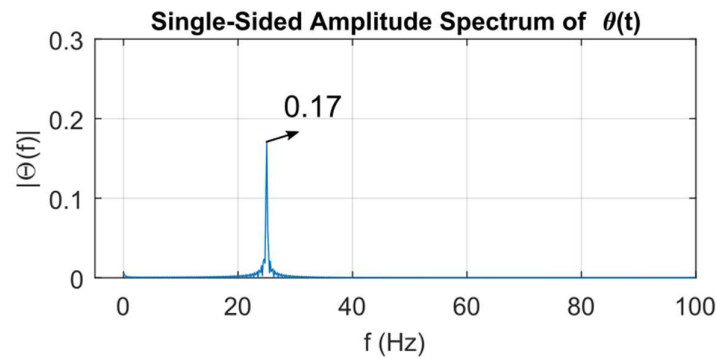


Figure 5-34 Frequency spectrum of the temperature elevation response in the mid cross-section of an elastic hourglass-shaped sample under cyclic tensile loading

stress. The amplitude of the temperature evolution was  $0.29^{\circ}\text{C}$ , which is about the same values found in experiments on NiTi samples in Figure 5-27 and Figure 5-28.

When looking at the frequency spectrum of the simulated signal in the mid-cross section (Figure 5-34), we notice the dominance of the first harmonic component and the absence of second order and third order harmonics.

From these numerical results, we may conclude that the cross section reduction, and therefore the stress gradient along the sample does not have an impact on the mean temperature elevation of the material in the mid-cross section.

#### 5.4.4. Cyclic phase transformation latent heat

We coupled the 1D heat equation solution of hourglass shaped samples with the 1D version of the thermomechanical model of Sedlák et al. As introduced in Chapter 3, the Sedlák model defines the temperature as a prescribed parameter. Therefore, to simulate the coupled behavior of NiTi under tensile stress, we develop a loop-based routine in which the mechanical and the microstructure material state are first calculated by Sedlák's model. Then, the heat sources related to phase changes are calculated and passed to the 1D heat equation model, which computes the temperature elevation along the axis of the sample. The procedure is repeated with a fixed simulation step time of  $8 \times 10^{-4}\text{s}$ . The spatial distribution was the same as the one used for the elastic simulations ( $150\mu\text{m}$ ).

In a first simulation, we considered the transformation thermomechanical coupling of the  $\text{B2} \leftrightarrow \text{R}$  transformation only; hence, we neglected the thermoelastic effect. The applied loading was the same as the one presented for the elastic simulations in Figure 5-33. The nominal

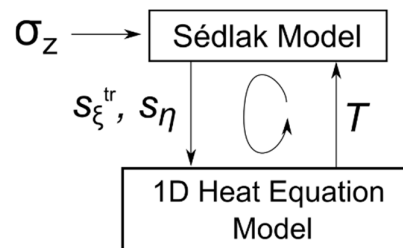


Figure 5-35 Schematic representation of the loop routine used for simulating the thermomechanical response of cyclic loaded hourglass-shaped NiTi samples.

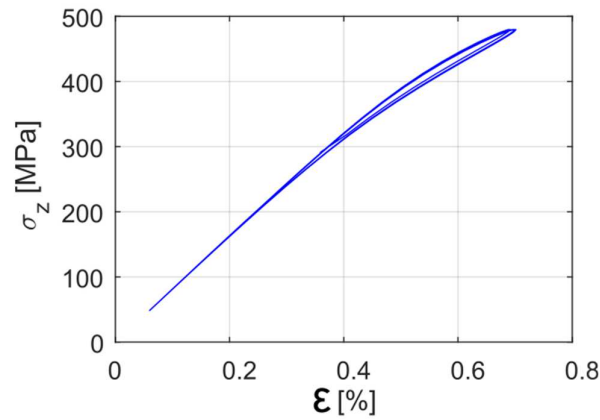


Figure 5-36 Simulated stress-strain response of an hourglass-shaped NiTi sample under cyclic tensile stresses, where the thermoelastic effect has been neglected.

material response at the mid cross-section of the sample is illustrated in Figure 5-36. In spite of the diffusionless definition of the B2→R transformation in Sedláč's model, the stress-strain response of the material exhibits hysteresis. This is caused exclusively by the cyclic temperature changes induced by the cyclic phase transformations latent heat, which modifies continuously the stress needed for initiating the transformation.

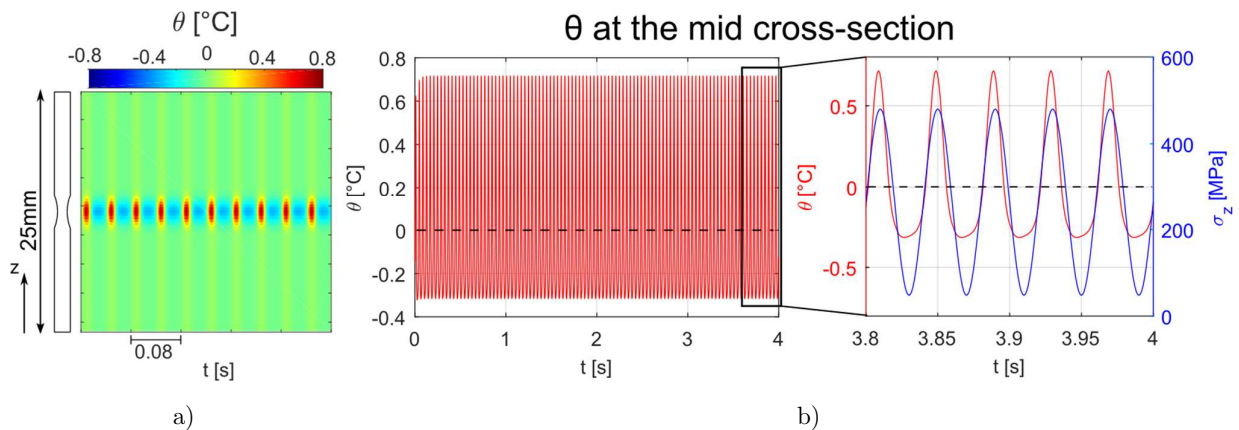


Figure 5-37 Simulated temperature response of NiTi hourglass-shaped sample under cyclic tensile stress neglecting the thermoelastic contributions. a) Height-time-temperature diagram showing the axial temperature distribution of the total length of the sample in the last 10 cycles of the simulation. b) Temperature elevation evolution in the mid cross-section.

By neglecting the thermoelasticity, the maximum local temperature in the mid-cross section gets in-phase with the maximum applied loading (Figure 5-37b). However, the temperature cycles are dissymmetric, showing more intense heating than cooling stages. The resulting steady state-temperature elevation, as in the elastic case, is zero, verifying that both the latent heat and the sample shape do not contribute to the self-heating behavior of the material. We observe as well that the temperature elevation keeps concentrated within the groove zone of the sample (Figure 5-37a); therefore, the temperature of the the constant cross-section parts of the sample oscillates homogeneously at low amplitudes.

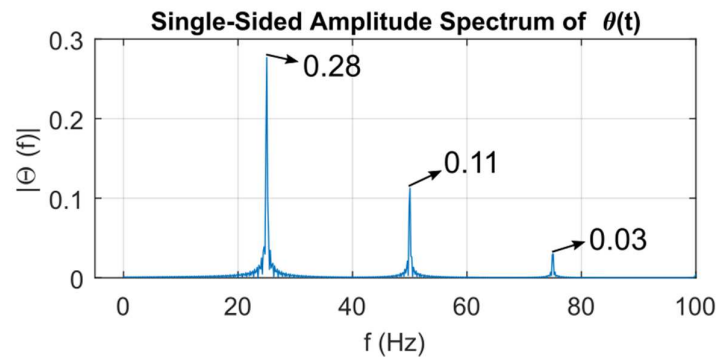


Figure 5-38 Frequency spectrum of the temperature elevation response in the mid cross-section of NiTi hourglass-shaped sample under cyclic tensile loading, where the thermoelastic effect has been neglected.

The distortion of the temperature cycles is reflected in the Fourier spectrum in Figure 5-38 by the appearance of second and third harmonic peaks, similar as the experimental results obtained upon self-heating measurements on NiTi.

#### 5.4.5. Interaction between the thermoelastic effect and the transformation latent heats

A third simulation was performed to evaluate the interaction between the thermoelasticity and the latent heat absorption/release during cyclic B2 $\leftrightarrow$ R transformations. The simulation was carried out under the same conditions like in the latest two cases.

The introduction of the thermoelastic effect makes the amplitude of the temperature response lower. As a result, the fundamental harmonic peak in the spectrum in Figure 5-41 sees a decrease of 0.17°C (same amplitude as in the thermoelastic spectrum in Figure 5-34). On the other hand, the amplitudes of the second and third order harmonics remain constant. In consequence of the decrease of temperature amplitude, the stress-strain response in the mid-cross section of the sample (Figure 5-39) shows this time a smaller hysteresis compared to the stress-strain curve presented in Figure 5-36.

The temperature elevations in the mid cross-section of the sample in Figure 5-40b shows a double peak response, similar to the one presented in experiments at 80°C in Figure 5-16c. The in-phase peak of temperature in Figure 5-40b appears between the B2 $\rightarrow$ R onset stress ( $\sim$ 220MPa) and the maximum applied stress. As in the two cases presented before, the interaction between thermoelasticity and transformation latent heats resulted in a mean steady-state temperature elevation equal to zero; thus confirming once again that the combination of hourglass geometry and multiplicity of reversible heat sources do not contribute to the self-heating of the material.

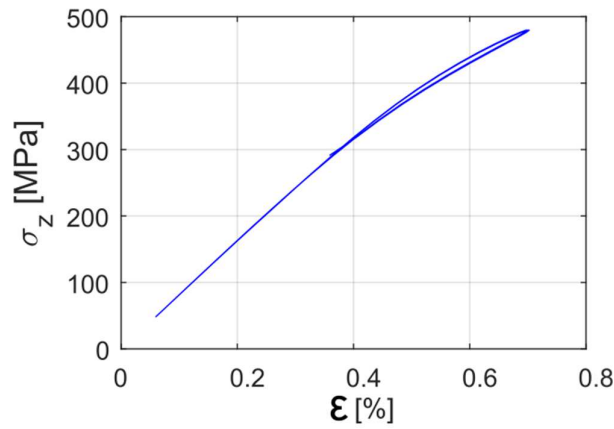


Figure 5-39 Simulated stress-strain response of an hourglass-shaped NiTi sample under cyclic tensile stresses considering both the thermoelastic effect and the transformation latent heats.

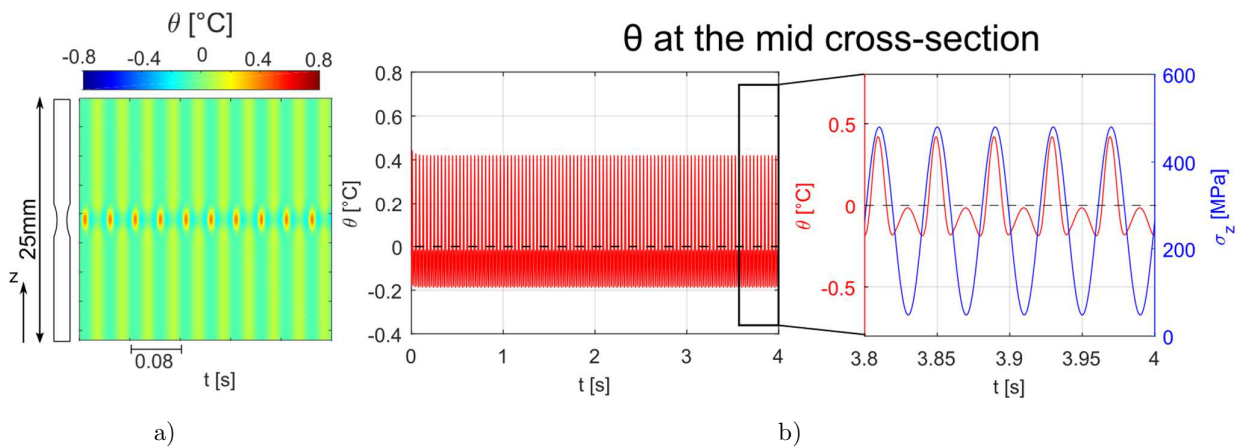


Figure 5-40 Simulated temperature response of NiTi hourglass-shaped sample under cyclic tensile stress considering both the transformation latent and the thermoelasticity. a) Height-time-temperature diagram showing the axial temperature distribution of the total length of the sample in the last 10 cycles of the simulation. b) Temperature elevation evolution in the mid cross-section.

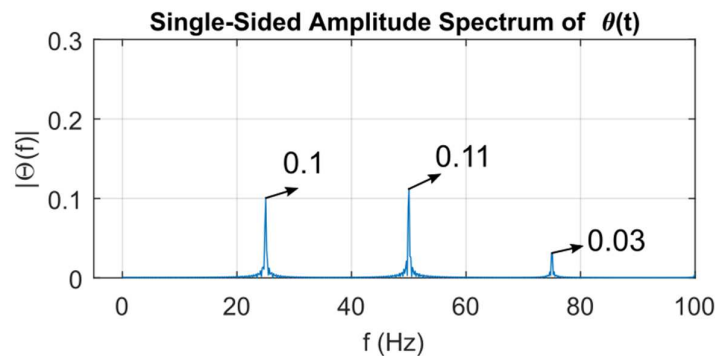


Figure 5-41 Frequency spectrum of the temperature elevation response in the mid cross-section of NiTi hourglass-shaped sample under cyclic tensile loading, considering both the thermoelastic effect and the transformation latent heats.

## 5.5. Summary

The self-heating method results in a very attractive option for assessing dissipative mechanisms on material samples subjected to cyclic stresses. The method was established with the aim of providing a fast prediction tool of lifetimes of materials in the HCF regime. It allows constituting fatigue models based on energy dissipation criteria, even for loadings that from a macroscopic point of view exhibit linear elasticity. These models are based on the knowledge of the heat sources and their relationship with fatigue damage upon repetitive loading. In SMA alloys, since most of the fatigue works reported in the literature tackled the Low Cycle Fatigue, there is a big gap of knowledge respecting the source of structural fatigue under stresses lower than the onset of B19' martensitic transformation. With the aim of providing further information about the mechanisms leading to fatigue failure in the HCF of NiTi alloys, we performed a series of self-heating measurements on hourglass-shaped samples at 25°C, 40°C, and 80°C.

The resulting self-heating curves obtained at 40°C and 80°C showed practically no mean temperature elevations under stresses lower than the B19' martensitic transformation onset. At 25°C, on the other hand, the mean temperature grows almost linearly with increasing the maximum load. From the characteristic transformation temperatures of the material, we deduced that the early self-heating of the sample tested at 25°C was related to low-stress B2→R transformation. Moreover, the characteristic elbow of self-heating curves, which allows the empiric assessment of the endurance limit of the material, was observed for all three tested temperatures only once the material attained the stress needed for b19' transformation (i.e. beyond the HCF scope).

Attempting to boost the self-heating responses of the material at 40°C and 80°C, we carried out self-heating measurements at higher loading frequencies. However, no significant improvements were obtained after these tests. Only the material tested at 25°C exhibited an increase of its self-heating response by increasing the loading frequency.

Since the temperature signal recorded at 40°C and 80°C were low, we decided to evaluate the harmonic components of the stabilized temperature signal for each block of cycles performed during self-heating measurements. Such an analysis is in principle more resilient to noise. The harmonic amplitudes evolution with the maximum applied stress shows interesting behaviors. For example, second order harmonic component evolution at 40°C denotes an inflection point that coincides with the endurance limit of the material at this temperature (~410MPa in Figure 5-21b). At 80°C, on the other hand, noise-free temperature harmonic curves are obtained.

We tried to identify the origin of the observed phenomena by performing thermomechanical simulations of NiTi hourglass-shaped samples. For this, we use the Sedlák model presented in Chapter 3 together with an implicit finite difference solution of the heat equation. The simulations allowed us to identify the impact of the B2→R transformation latent heat and the thermoelastic coupling on the harmonic component amplitudes. We evidenced that second and third harmonics appeared whenever the B2→R phase

transformation regime is entered. However, further simulations are needed in order to determine if the kinetics of the harmonic with applied stress is caused by a homogeneous material response or by localized dissipative phenomena, which would justify the use of multiscale modeling approaches.





# Conclusions

In this dissertation, we tackled the structural fatigue performance of superelastic NiTi wires. We focused on the High Cycle Fatigue regime, which involves cyclic elastic loading of austenite and stress-induced phase transformation into R-phase. We addressed this matter using hourglass-shaped samples manufactured from commercial NiTi wires. This particular approach, although very common among fatigue studies, has not been common to fatigue studies of NiTi because it is difficult to machine the hourglass-shaped samples from small NiTi components, as the ones used in biomedical applications. The smooth hourglass cross-section reduction allows confining all transformation, deformation and fatigue processes into a small volume in their mid-cross-section. Consequently, the shape of the samples prevents the random transformation deformation localization occurring in polycrystalline NiTi wires, which makes it difficult to interpret fatigue results gathered into S-N and Strain-N curves. Therefore, the hourglass shape was thought to help perform more accurate fatigue tests and provide an easier-to-interpret fatigue tests in the transition regime where the High Cycle Fatigue drifts into Low Cycle Fatigue. Besides the shape of tested samples, a special attention was paid to distinguish all possible transformation paths that usually occur in commercially used NiTi wires depending on the stress and temperature. Namely, we considered  $B2 \rightarrow R$ -phase,  $B2 \rightarrow B19'$ , and  $B2 \rightarrow R$ -phase  $\rightarrow B19'$  transformation paths that we were selected by test temperature and maximum loading amplitude while the microstructure was kept constant through a well-defined heat treatment of hourglass shaped samples. Note that the heat treatment was selected so that the material preserved a high degree of cold work hardening providing a stable superelastic response.

In the first part of this document, we analyzed the mechanical response of hourglass-shaped samples through finite element simulations assuming elastic, plastic and superelastic behaviors. This analysis was a key to an accurate interpretation of fatigue tests performed on the hourglass-shaped samples. We concluded from the simulations results that upon the  $B2 \rightarrow R$  transformation, the stress state of the material in the mid cross-section of hourglass shaped samples remains in almost pure uniaxiality. In fact, when the  $B2 \rightarrow R$  phase transformation is induced, the transformation acts as a stress reliever mechanism, which causes a decrease in the stress concentration in the surface of the sample. In contrast, when  $B2R \rightarrow B19'$  transformation is induced, the material in the mid cross-section experiences a complex stress state, in part due to the significant cross-section reduction entailed by the axial transformation strain. From X-ray diffraction analysis, we observe that the

transformation occurs instantaneously within a finite minimum volume right after the nominal stress approaches the critical stress level. Interestingly, although the transformation volumes spread out upon further loading, a significant volume fraction of austenite was detected in the transformed volume. A working hypothesis is that this might be an effect of the high hydrostatic pressure zone observed in the axis of the sample upon FEA simulations of tensile loaded hourglass-shaped samples.

The fatigue study presented in Chapter 4, shed light on the role of the intermediate phase transformation B2→R in the structural fatigue behavior of NiTi alloys. In this study, instead of testing samples prepared through different heat treatments, we decided to control the stress-induced microstructural processes in the material by modifying the temperature of the tests. As a result, we could evaluate the role of the R-phase for a fixed microstructure. From classic S-N curves, we observed that NiTi samples exhibiting R-phase transformation failed sooner than NiTi subjected to elastic loading in austenite elastic state. The R-phase transformation, on the other hand, shows a lower decrease in its fatigue endurance with increasing mean stress compared to the austenite elasticity regime. In order to verify this behavior, further fatigue testing at different stress ratios might be required. Note that it is important to determine the effects of the mean stress in the structural fatigue of superelastic NiTi, in order to construct reliable constant life diagrams.

From the fatigue fracture surface observations, we deduced that the very early stage of crack propagation gives rise to a cleavage like mode of rupture, most probably occurring in the austenite phase. Moreover, from high-resolution x-ray experiments, it was concluded that even harsh fatigue cycling (1000 cycle at 80 °C, and max. stress of 880 MPa) in austenite elasticity regime leads to no substantial changes in microstructure. Therefore, the failure seems to proceed in a very localized manner. It seems to nucleate in localized sites near the surface of the sample caused by the presence of surface defects and inclusions. Multiple crack initiation sites merge after some cycles giving rise to a well-defined crack front, which acts as a stress riser inducing B19' martensitic transformation and plastic deformation as evidenced through infrared thermography and the identification of fatigue striations in fracture surfaces. During the propagation of the fatigue crack front, when the B19' phase transformation occurs in a significant volume around the crack tip, crack opening is promoted, hence accelerating the fatigue failure of the material. In conclusion, the failure of NiTi in the austenite elasticity regime is assisted and accelerated by the martensitic transformation that is triggered at the crack front.

Finally, in the last Chapter of this document, we attempted to apply the self-heating method for a rapid characterization the fatigue behavior of our NiTi samples. However, the very low intensity of the temperature signals acquired by infrared means made it difficult to construct suitable self-heating curves. As a result, we proposed an alternative methodology based on the evaluation the fatigue limit by analyzing cyclic temperature signals in the frequency domain and the evolution of amplitudes of higher harmonics. The method is also supported by simulation of the thermomechanical coupling in a discrete SMA model. Further research is, however, necessary to approve the suggested links between the higher harmonics

of the temperature signal and dissipated energy that is considered as responsible for fatigue failure.

# References

- [1] C. Maletta and M. L. Young, "Stress-induced martensite in front of crack tips in niti shape memory alloys: Modeling versus experiments," *J. Mater. Eng. Perform.*, vol. 20, no. 4–5, pp. 597–604, 2011.
- [2] P. Wollants, M. Bonte, and J. R. Roos, "A Thermodynamic Analysis of the Stress-Induced Martensitic Transformation in a Single Crystal," *Z. Metallk.*, vol. 70, no. 1979, pp. 113–117, 1979.
- [3] A. Olander, "An Electrochemical Investigation of Solid Cadmium-Gold Alloys," *J. Am. Chem. Soc.*, vol. 54, 1932.
- [4] L. Chang and T. Read, "Plastic Deformation and Diffusionless Phase Changes in Metals —the Gold-Cadmium Beta-phase.," *Trans. Am. Institute of Mining Metall. Eng.*, vol. 191, pp. 47–52, 1951.
- [5] J. E. Reynolds and M. B. Bever, "On the Reversal of the Strain-Induced Martensitic Transformation in the Copper- Zinc System," *J. Met.*, 1952.
- [6] W. A. Rachinger, "A 'super-elastic' single crystal calibration bar," *Br. J. Appl. Phys.*, vol. 9, no. 6, pp. 250–252, Jun. 1958.
- [7] M. S. Wechsler, D. . Lieberman, and T. . Read, "On the Theory of the Formation of Martensite," *J. Met. (Trans AIME)*, vol. 197, pp. 1503–1515, 1953.
- [8] J. . Bowles and J. . Mackenzie, "The crystallography of martensite transformations I," *Acta Metall.*, vol. 2, no. 1, pp. 129–137, Jan. 1954.
- [9] J. M. Ball and R. D. James, "Fine phase mixtures as minimizers of energy," *Arch. Ration. Mech. Anal.*, vol. 100, no. 1, pp. 13–52, 1987.
- [10] W. J. Buehler, J. V. Gilfrich, and R. C. Wiley, "Effect of low-temperature phase changes on the mechanical properties of alloys near composition TiNi," *J. Appl. Phys.*, vol. 34, no. 5, pp. 1475–1477, 1963.
- [11] R. J. Wasilewski, "The effects of applied stress on the martensitic transformation in TiNi," *Metall. Mater. Trans. B*, vol. 2, no. 11, pp. 2973–2981, Nov. 1971.
- [12] F. Miura, M. Mogi, Y. Ohura, and M. Karibe, "The super-elastic Japanese NiTi alloy wire for use in orthodontics. Part III. Studies on the Japanese NiTi alloy coil springs.," *Am. J. Orthod. Dentofacial Orthop.*, vol. 94, no. 2, pp. 89–96, Aug. 1988.
- [13] F. Baumgart, G. Bensmann, J. Haasters, A. Nolker, and K. F. Schlegel, "Zur dwyerschen skoliosenoperation mittels drähten aus memory-legierungen - Eine experimentelle studie," *Arch. Orthop. Trauma. Surg.*, vol. 91, no. 1, pp. 67–75, 1978.
- [14] T. Duerig, a Pelton, and D. Stöckel, "An overview of nitinol medical applications," *Mater. Sci. Eng. A*, vol. 273–275, pp. 149–160, 1999.
- [15] Confluent Medical Technologies, "A Historical Perspective - Confluent Medical." [Online]. Available: <https://nitinol.com/reference/a-historical-perspective/>. [Accessed: 28-Jun-2017].
- [16] T. B. Massalski, H. (Hiroaki) Okamoto, and ASM International., *Binary alloy phase diagrams*. ASM

- International, 1990.
- [17] M. Nishida, C. M. Wayman, and T. Honma, "Precipitation processes in near-equiatomic TiNi shape memory alloys," *Metall. Trans. A*, vol. 17, no. 9, pp. 1505–1515, Sep. 1986.
- [18] K. F. Hane and T. W. Shield, "Microstructure in the cubic to monoclinic transition in titanium-nickel shape memory alloys," *Acta mater.*, vol. 47, no. 9, pp. 2603–2617, 1999.
- [19] X. Zhang and H. Sehitoglu, "Crystallography of the B2  $\rightarrow$  R  $\rightarrow$  B19' phase transformations in NiTi," *Mater. Sci. Eng. A*, vol. 374, no. 1–2, pp. 292–302, 2004.
- [20] K. Otsuka and X. Ren, "Physical metallurgy of Ti-Ni-based shape memory alloys," *Prog. Mater. Sci.*, vol. 50, no. 5, pp. 511–678, 2005.
- [21] T. Duerig, K. Melton, D. Stockel, and C. Wayman, *Engineering aspects of shape memory alloys*. 1990.
- [22] T. Yoneyama and S. Miyazaki, *Shape memory alloys for biomedical applications*. .
- [23] G. Eggeler, E. Hornbogen, a Yawny, a Heckmann, and M. Wagner, "Structural and functional fatigue of NiTi shape memory alloys," *Mater. Sci. Eng. A*, vol. 378, no. 1–2, pp. 24–33, Jul. 2004.
- [24] K. . Melton and O. Mercier, "The Effect of the Martensitic Phase Transformation on the Low Cycle Fatigue Behaviour of Polycrystalline Ni-Ti and Cu-Zn-Al Alloys," vol. 40, pp. 59–71, 1979.
- [25] J. Frenzel, E. P. George, A. Dlouhy, C. Somsen, M. F. X. Wagner, and G. Eggeler, "Influence of Ni on martensitic phase transformations in NiTi shape memory alloys," *Acta Mater.*, vol. 58, no. 9, pp. 3444–3458, 2010.
- [26] M. B. Salamon, M. E. Meichle, and C. M. Wayman, "Premartensitic phases of Ti<sub>50</sub> Ni<sub>47</sub> Fe<sub>3</sub>," *Phys. Rev. B*, vol. 31, no. 11, pp. 7306–7315, Jun. 1985.
- [27] P. Šittner, M. Landa, P. Lukáš, and V. Novák, "R-phase transformation phenomena in thermomechanically loaded NiTi polycrystals," *Mech. Mater.*, vol. 38, no. 5–6, pp. 475–492, 2006.
- [28] O. Matsumoto, S. Miyazaki, K. Otsuka, and H. Tamura, "Crystallography of martensitic transformation in TiNi single crystals," *Acta Metall.*, vol. 35, no. 8, pp. 2137–2144, 1987.
- [29] K. M. Knowles and D. A. Smith, "The crystallography of the martensitic transformation in equiatomic nickel-titanium," *Acta Metall.*, vol. 29, no. 1, pp. 101–110, 1981.
- [30] C. P. Frick *et al.*, "Thermal processing of polycrystalline NiTi shape memory alloys," *Mater. Sci. Eng. A*, vol. 405, no. 1–2, pp. 34–49, Sep. 2005.
- [31] P. G. McCormick, Y. Liu, X. Chena, and D. Favier, "Multistage transformation behaviour in NiTi," in *Ecomaterials*, Elsevier, 1994, pp. 1105–1108.
- [32] Z. Zhang, R. D. James, and S. Müller, "Energy barriers and hysteresis in martensitic phase transformations," *Acta Mater.*, vol. 57, no. 15, pp. 4332–4352, 2009.
- [33] Y. Liu, "Thermodynamics of the shape memory effect in Ti-Ni alloys," in *Shape Memory Alloys for Biomedical Applications*, Woodhead Publishing, 2009, pp. 37–68.
- [34] G. B. Stachowiak and P. G. McCormick, "Two stage yielding in a NiTi alloy," *Scr. Metall.*, vol. 21, no. 3, pp. 403–406, 1987.
- [35] S. Miyazaki, K. Otsuka, and Y. Suzuki, "Transformation pseudoelasticity and deformation behavior in a Ti-50.6at%Ni alloy," *Scr. Met.*, vol. 17, no. 2, pp. 385–388, 1983.
- [36] S. Miyazaki, S. Kimura, and K. Otsuka, "Shape-memory effect and pseudoelasticity associated with the R-phase transition in Ti-50 · 5 at.% Ni single crystals," *Philos. Mag. A*, vol. 57, no. 3, pp. 467–478, 1988.
- [37] P. Sittner, L. Heller, J. Pilch, C. Curfs, T. Alonso, and D. Favier, "Young's modulus of austenite and

- martensite phases in superelastic NiTi wires,” *J. Mater. Eng. Perform.*, vol. 23, no. 7, pp. 2303–2314, 2014.
- [38] J. Olbricht, A. Yawny, J. L. Pelegrina, G. Eggeler, and V. A. Yardley, “Characteristics of the stress-induced formation of R-phase in ultrafine-grained NiTi shape memory wire,” *J. Alloys Compd.*, vol. 579, pp. 249–252, 2013.
- [39] G. Helbert *et al.*, “Experimental characterisation of three-phase NiTi wires under tension,” *Mech. Mater.*, vol. 79, pp. 85–101, 2014.
- [40] T. W. Duerig and K. Bhattacharya, “The Influence of the R-Phase on the Superelastic Behavior of NiTi,” *Shape Mem. Superelasticity*, vol. 1, no. 2, pp. 153–161, 2015.
- [41] P. Sedlák, M. Frost, B. Benešová, T. Ben Zineb, and P. Šittner, “Thermomechanical model for NiTi-based shape memory alloys including R-phase and material anisotropy under multi-axial loadings,” *Int. J. Plast.*, vol. 39, pp. 132–151, 2012.
- [42] P. Sedmák *et al.*, “Grain-resolved analysis of localized deformation in nickel-titanium wire under tensile load,” *Science (80-. )*, vol. 353, no. 6299, 2016.
- [43] D. Jiang, S. Kyriakides, C. M. Landis, and K. Kazinakis, “Modeling of propagation of phase transformation fronts in NiTi under uniaxial,” *Eur. J. Mech. - A/Solids*, 2017.
- [44] N. J. Bechle and S. Kyriakides, “Localization in NiTi tubes under bending,” *Int. J. Solids Struct.*, vol. 51, no. 5, pp. 967–980, Mar. 2014.
- [45] G. Laplanche, T. Birk, S. Schneider, J. Frenzel, and G. Eggeler, “Effect of temperature and texture on the reorientation of martensite variants in NiTi shape memory alloys,” *Acta Mater.*, vol. 127, pp. 143–152, 2017.
- [46] X. Zhang, P. Feng, Y. He, T. Yu, and Q. Sun, “Experimental study on rate dependence of macroscopic domain and stress hysteresis in NiTi shape memory alloy strips,” *Int. J. Mech. Sci.*, vol. 52, no. 12, pp. 1660–1670, 2010.
- [47] Q. P. Sun and Z. Q. Li, “Phase transformation in superelastic NiTi polycrystalline micro-tubes under tension and torsion - From localization to homogeneous deformation,” *Int. J. Solids Struct.*, vol. 39, no. 13–14, pp. 3797–3809, 2002.
- [48] J. Pfetzinger-Micklich, R. Ghisleni, T. Simon, C. Somsen, J. Michler, and G. Eggeler, “Orientation dependence of stress-induced phase transformation and dislocation plasticity in NiTi shape memory alloys on the micro scale,” *Mater. Sci. Eng. A*, vol. 538, pp. 265–271, 2012.
- [49] R. Delville, B. Malard, J. Pilch, P. Sittner, and D. Schryvers, “Transmission electron microscopy investigation of dislocation slip during superelastic cycling of Ni–Ti wires,” *Int. J. Plast.*, vol. 27, no. 2, pp. 282–297, Feb. 2011.
- [50] R. F. Hamilton, H. Sehitoglu, Y. Chumlyakov, and H. J. Maier, “Stress dependence of the hysteresis in single crystal NiTi alloys,” *Acta Mater.*, vol. 52, no. 11, pp. 3383–3402, 2004.
- [51] A. R. Pelton, G. H. Huang, P. Moine, and R. Sinclair, “Effects of thermal cycling on microstructure and properties in Nitinol,” *Mater. Sci. Eng. A*, vol. 532, pp. 130–138, 2012.
- [52] D. M. Norfleet *et al.*, “Transformation-induced plasticity during pseudoelastic deformation in Ni-Ti microcrystals,” *Acta Mater.*, vol. 57, no. 12, pp. 3549–3561, 2009.
- [53] S. Nemat-Nasser, J. Y. Choi, W. G. Guo, and J. B. Isaacs, “Very high strain-rate response of a NiTi shape-memory alloy,” *Mech. Mater.*, vol. 37, no. 2–3 SPEC. ISS., pp. 287–298, 2005.
- [54] Y. Liu, Z. Xie, J. Van Humbeeck, and L. Delaey, “Asymmetry of stress-strain curves under tension and compression for NiTi shape memory alloys,” *Acta Mater.*, vol. 46, no. 12, pp. 4325–4338, 1998.

- [55] Y. Chumlyakov, I. Kireeva, E. Panchenko, I. Karaman, H. J. Maier, and E. Timofeeva, "Shape memory effect and high-temperature superelasticity in high-strength single crystals," *J. Alloys Compd.*, vol. 577, no. SUPPL. 1, pp. S393–S398, 2013.
- [56] P. Chowdhury and H. Sehitoglu, "A revisit to atomistic rationale for slip in shape memory alloys," *Prog. Mater. Sci.*, vol. 85, pp. 1–42, 2017.
- [57] T. Ezaz, J. Wang, H. Sehitoglu, and H. J. Maier, "Plastic deformation of NiTi shape memory alloys," *Acta Mater.*, vol. 61, no. 1, pp. 67–78, 2013.
- [58] Aerofit, "Couplings - CRYOFIT." [Online]. Available: <http://www.aerofit.com/sma-cryofit-couplings/>.
- [59] J. Van Humbeeck, "Non-medical applications of shape memory alloys," *Mater. Sci. Eng. A*, vol. 273–275, pp. 134–148, 1999.
- [60] Synoste, "Bone lengthening devices." [Online]. Available: <http://synoste.com/>.
- [61] S. Seok, C. D. Onal, K. J. Cho, R. J. Wood, D. Rus, and S. Kim, "Meshworm: A peristaltic soft robot with antagonistic nickel titanium coil actuators," *IEEE/ASME Trans. Mechatronics*, vol. 18, no. 5, pp. 1485–1497, 2013.
- [62] E. H. Schiller, "Heat Engine Driven by Shape Memory Alloys: Prototyping and Design Heat Engine Driven by Shape Memory Alloys: Prototyping and Design," pp. 1–80, 2002.
- [63] C. Bonsignore, "Present and future approaches to lifetime prediction of superelastic nitinol," *Theor. Appl. Fract. Mech.*, 2017.
- [64] O. A. Peters, M. Guiomar, and D. A. Bahia, "Contemporary Root Canal Preparation Innovations in Biomechanics," vol. 61, pp. 37–58, 2017.
- [65] M. Peignet, E. Merliot, and M. Dieng, "Amortisseur avec composant en alliage a memoire de forme et limiteur de temperature ; dispositif de maintien comprenant cet amortisseur," WO2011064507 A1, 2012.
- [66] R. Arbab-Chirani, V. Chevalier, S. Arbab-Chirani, and S. Calloch, "Comparative analysis of torsional and bending behavior through finite-element models of 5 Ni–Ti endodontic instruments," *Oral Surgery, Oral Med. Oral Pathol. Oral Radiol. Endodontology*, vol. 111, no. 1, pp. 115–121, 2011.
- [67] F. Lo Savio, E. Pedullà, E. Rapisarda, and G. La Rosa, "Influence of heat-treatment on torsional resistance to fracture of nickel-titanium endodontic instruments," *Procedia Struct. Integr.*, vol. 2, pp. 1311–1318, 2016.
- [68] P. Parashos and H. H. Messer, "Rotary NiTi Instrument Fracture and its Consequences," *J. Endod.*, vol. 32, no. 11, pp. 1031–1043, 2006.
- [69] E. Pedullà *et al.*, "Torsional and Cyclic Fatigue Resistance of a New Nickel-Titanium Instrument Manufactured by Electrical Discharge Machining," *J. Endod.*, vol. 42, no. 1, pp. 156–159, 2016.
- [70] M. B. McGuigan, C. Louca, and H. F. Duncan, "Endodontic instrument fracture: causes and prevention.," *Br. Dent. J.*, vol. 214, no. 7, pp. 341–8, 2013.
- [71] E. Alarcon *et al.*, "Fatigue performance of superelastic NiTi near stress-induced martensitic transformation," *Int. J. Fatigue*, vol. 95, pp. 76–89, 2017.
- [72] J. Tušek *et al.*, "The Elastocaloric Effect: A Way to Cool Efficiently," *Adv. Energy Mater.*, vol. 5, no. 13, p. 1500361, Jul. 2015.
- [73] B. Kockar, I. Karaman, J. I. Kim, Y. I. Chumlyakov, J. Sharp, and C.-J. (Mike) Yu, "Thermomechanical cyclic response of an ultrafine-grained NiTi shape memory alloy," *Acta Mater.*, vol. 56, no. 14, pp. 3630–3646, 2008.
- [74] D. A. Miller and D. C. Lagoudas, "Influence of cold work and heat treatment on the shape memory effect and plastic strain development of NiTi," *Mater. Sci. Eng. A*, vol. 308, no. 1–2, pp. 161–175, 2001.

- [75] K. C. Atli, I. Karaman, R. D. Noebe, G. Bigelow, and D. Gaydos, "Work production using the two-way shape memory effect in NiTi and a Ni-rich NiTiHf high-temperature shape memory alloy," *Smart Mater. Struct.*, vol. 24, no. 12, p. 125023, 2015.
- [76] L. J. Chiang, C. H. Li, Y. F. Hsu, and W. H. Wang, "Effects of thermal cycling on multiple-stage transformation in Ti<sub>49.3</sub>Ni<sub>50.7</sub> shape memory alloy," *J. Alloys Compd.*, vol. 462, no. 1–2, pp. 47–51, 2008.
- [77] P. Sedmák, P. Šittner, J. Pilch, and C. Curfs, "Instability of cyclic superelastic deformation of NiTi investigated by synchrotron X-ray diffraction," *Acta Mater.*, vol. 94, pp. 257–270, 2015.
- [78] S. Miyazaki, T. Imai, Y. Igo, and K. Otsuka, "Effect of cyclic deformation on the pseudoelasticity characteristics of Ti-Ni alloys," *Metall. Trans. A*, vol. 17, no. 1, pp. 115–120, 1986.
- [79] R. Delville, B. Malard, J. Pilch, P. Sittner, and D. Schryvers, "Microstructure changes during non-conventional heat treatment of thin Ni-Ti wires by pulsed electric current studied by transmission electron microscopy," *Acta Mater.*, vol. 58, no. 13, pp. 4503–4515, 2010.
- [80] P. Sedmák, P. Šittner, J. Pilch, and C. Curfs, "Instability of cyclic superelastic deformation of NiTi investigated by synchrotron X-ray diffraction," *Acta Mater.*, vol. 94, pp. 257–270, 2015.
- [81] A. R. Pelton, V. Schroeder, M. R. Mitchell, X. Y. Gong, M. Barney, and S. W. Robertson, "Fatigue and Durability of Nitinol Stents," *J. Mech. Behav. Biomed. Mater.*, vol. 1, pp. 153–164, 2008.
- [82] S. M. Jaureguizar, M. D. Chapetti, and A. A. Yawny, "Fatigue of NiTi shape memory wires," *Procedia Struct. Integr.*, vol. 2, pp. 1427–1434, 2016.
- [83] A. Carvalho, D. Montalvo, M. Freitas, L. Reis, and M. Fonte, "Determination of the rotary fatigue life of NiTi alloy wires," *Theor. Appl. Fract. Mech.*, vol. 85, pp. 37–44, 2016.
- [84] A. R. Pelton *et al.*, "Rotary-bending fatigue characteristics of medical-grade Nitinol wire.," *J. Mech. Behav. Biomed. Mater.*, vol. 27, pp. 19–32, Nov. 2013.
- [85] S. Miyazaki, K. Mizukoshi, T. Ueki, T. Sakuma, and Y. Liu, "Fatigue life of Ti–50 at.% Ni and Ti–40Ni–10Cu (at.%) shape memory alloy wires," *Mater. Sci. Eng. A*, vol. 273–275, pp. 658–663, Dec. 1999.
- [86] S. Miyazaki, K. Mizukoshi, T. Ueki, T. Sakuma, and Y. Liu, "Fatigue life of Ti–50 at.% Ni and Ti–40Ni–10Cu (at.%) shape memory alloy wires," *Mater. Sci. Eng. A*, vol. 273–275, pp. 658–663, 1999.
- [87] E. Johnson, A. Lloyd, S. Kuttler, and K. Namerow, "Comparison between a Novel Nickel-Titanium Alloy and 508 Nitinol on the Cyclic Fatigue Life of ProFile 25/.04 Rotary Instruments," *J. Endod.*, vol. 34, no. 11, pp. 1406–1409, 2008.
- [88] Y. Kim, "Fatigue Properties of the Ti-Ni Base Shape Memory Alloy Wire.," *Mater. Trans.*, vol. 43, no. 7, pp. 1703–1706, 2002.
- [89] Y. Kim and S. Miyazaki, "Fatigue properties of Ti–50.9at%Ni shape memory wires," 1997.
- [90] J. Racek, M. Stora, P. Šittner, L. Heller, J. Kopeček, and M. Petrenek, "Monitoring Tensile Fatigue of Superelastic NiTi Wire in Liquids by Electrochemical Potential," *Shape Mem. Superelasticity*, vol. 1, no. 2, pp. 1–27, 2015.
- [91] "Standard Test Method for Strain-Controlled Fatigue Testing." Active Standard ASTM E606 / E606M.
- [92] K. . Melton and O. Mercier, "Fatigue of NITI thermoelastic martensites," *Acta Metall.*, vol. 27, no. 1, pp. 137–144, 1979.
- [93] M. J. Mahtabi, N. Shamsaei, and B. Rutherford, "Mean Strain Effects on the Fatigue Behavior of Superelastic Nitinol Alloys: An Experimental Investigation," *Procedia Eng.*, vol. 133, pp. 646–654, 2015.

- [94] N. Morgan, J. Painter, and a. Moffat, "Mean strain effects and microstructural observations during in vitro fatigue testing of NiTi," *SMST-2003. Proc. ...*, no. 1, pp. 303–310, 2004.
- [95] C. Maletta, E. Sgambitterra, F. Furgiuele, R. Casati, and a. Tuissi, "Fatigue properties of a pseudoelastic NiTi alloy: Strain ratcheting and hysteresis under cyclic tensile loading," *Int. J. Fatigue*, vol. 66, pp. 78–85, 2014.
- [96] D. Tolomeo, S. Davidson, and M. Santinoranont, "Cyclic Properties of Superelastic Nitinol: Design Implications," in *Proceedings of the International Conference on Shape Memory and Superelastic Technologies, SMST-2000*, 2001, pp. 471–476.
- [97] L. Zheng, Y. He, and Z. Moumni, "Luders-like band front motion and fatigue life of pseudoelastic polycrystalline NiTi shape memory alloy," *Scr. Mater.*, vol. 123, pp. 46–50, 2016.
- [98] A. M. Figueiredo, P. Modenesi, and V. Buono, "Low-cycle fatigue life of superelastic NiTi wires," *Int. J. Fatigue*, vol. 31, no. 4, pp. 751–758, 2009.
- [99] J. F. Luo, S. C. Mao, X. D. Han, C. Cheng, Z. Zhang, and M. H. Wu, "High-cycle Fatigue Mechanisms of a NiTi Shape Memory Alloy under Different Mean Strains," *Mater. Sci. Forum*, vol. 610–613, pp. 1120–1127, 2002.
- [100] W. D. Pilkey, *PETERSON'S STRESS CONCENTRATION Second Edition*. 1997.
- [101] "Nitinol #1 - Fort Wayne Metals." [Online]. Available: <http://www.fwmetals.com/services/resource-library/nitinol-1/>.
- [102] B. Malard, J. Pilch, P. Sittner, R. Delville, and C. Curfs, "In situ investigation of the fast microstructure evolution during electropulse treatment of cold drawn NiTi wires," *Acta Mater.*, vol. 59, pp. 1542–1556, 2011.
- [103] D. Velten, V. Biehl, F. Aubertin, B. Valeske, W. Possart, and J. Breme, "Preparation of TiO<sub>2</sub> layers on cp-Ti and Ti6Al4V by thermal and anodic oxidation and by sol-gel coating techniques and their characterization," *J. Biomed. Mater. Res.*, vol. 59, no. 1, pp. 18–28, 2002.
- [104] M. V. Diamanti, B. Del Curto, and M. Pedferri, "Interference colors of thin oxide layers on titanium," *Color Res. Appl.*, vol. 33, no. 3, pp. 221–228, Jun. 2008.
- [105] M. V. Diamanti, S. Aliverti, and M. P. Pedferri, "Decoupling the dual source of colour alteration of architectural titanium: Soiling or oxidation?," *Corros. Sci.*, vol. 72, pp. 125–132, Jul. 2013.
- [106] L. Zhu, C. Trépanier, and A. R. Pelton, "Oxidation of Nitinol and its Effect on Corrosion Resistance," Jan. 2004.
- [107] ASTM International, *Standard Terminology for Nickel-Titanium Shape Memory Alloys*. 2015.
- [108] J. Kieffer *et al.*, "The fast azimuthal integration Python library: PyFAI," *J. Appl. Crystallogr.*, vol. 48, no. 2, pp. 510–519, 2015.
- [109] L. L. Meisner, V. P. Rotshtein, A. B. Markov, S. N. Meisner, E. V. Yakovlev, and F. D'yachenko, "Effect of nonmetallic and intermetallic inclusions on crater formation on the surface of TiNi alloys under the electron-beam impact," *Procedia Struct. Integr.*, vol. 2, pp. 1465–1472, 2016.
- [110] A. Coda, S. Zilio, D. Norwich, and F. Sczerzenie, "Characterization of inclusions in VIM/VAR NiTi alloys," *J. Mater. Eng. Perform.*, vol. 21, no. 12, pp. 2572–2577, 2012.
- [111] J. Blaber, B. Adair, and A. Antoniou, "Ncorr: Open-Source 2D Digital Image Correlation Matlab Software," *Exp. Mech.*, vol. 55, no. 6, pp. 1105–1122, 2015.
- [112] "pyFAI." [Online]. Available: <http://pyfai.readthedocs.io/en/latest/pyFAI.html>.
- [113] "GSAS II." [Online]. Available: <https://subversion.xray.aps.anl.gov/trac/pyGSAS>.

- [114] P. Lu Aš, P. Sittner, D. Lugovoy, D. Neov, and M. Ceretti, “In situ neutron diffraction studies of the R-phase transformation in the NiTi shape memory alloy,” vol. 1123, pp. 1121–1123, 2002.
- [115] H. J. Bunge, “Texture Analysis in Materials Science: Mathematical Methods.” p. 593, 1993.
- [116] M. F.-X. Wagner and W. Windl, “Lattice stability, elastic constants and macroscopic moduli of NiTi martensites from first principles,” *Acta Mater.*, vol. 56, no. 20, pp. 6232–6245, Dec. 2008.
- [117] J. A. Nelder and R. Mead, “A Simplex Method for Function Minimization,” *Comput. J.*, vol. 7, no. 4, pp. 308–313, Jan. 1965.
- [118] M. Frost, “Modeling of phase transformations in shape memory materials.,” Doctoral Thesis. Charles University in Prague. Faculty of Mathematics and Physics, 2012.
- [119] W. J. Dixon and A. M. Mood, “A Method for Obtaining and Analyzing Sensitivity Data,” *J. Am. Stat. Assoc.*, vol. 43, no. 241, pp. 109–126, Mar. 1948.
- [120] S. Subresh, *Fatigue of Materials*. 2004.
- [121] S. Suresh, *Fatigue of Materials (Cambridge Solid State Science Series) Second Edition*, 2 edition. Cambridge; New York: Cambridge University Press, 1998.
- [122] J. CM, W. HJ, and W. RJ, *The alloy with a memory, 55-Nitinol: Its physical metallurgy, properties, and applications*. Battelle Memorial Institute, 1972.
- [123] J. Racek, P. Sittner, L. Heller, J. Pilch, M. Petrevec, and P. Sedlak, “Corrosion of NiTi wires with cracked oxide layer,” *J. Mater. Eng. Perform.*, vol. 23, no. 7, pp. 2659–2668, 2014.
- [124] Y. Nancy, G. Ken, S. Huseyin, C. Yuriy, and L. S. National, “FRACTURE MECHANISMS IN B2 NiTi,” *ICF10, Honolulu, Hawaii - 2001*, 2001.
- [125] S. W. Robertson and R. O. Ritchie, “In vitro fatigue-crack growth and fracture toughness behavior of thin-walled superelastic Nitinol tube for endovascular stents: A basis for defining the effect of crack-like defects.,” *Biomaterials*, vol. 28, no. 4, pp. 700–9, Feb. 2007.
- [126] M. Rahim *et al.*, “Impurity levels and fatigue lives of pseudoelastic NiTi shape memory alloys,” *Acta Mater.*, vol. 61, no. 10, pp. 3667–3686, Jun. 2013.
- [127] M. J. Mahtabi, N. Shamsaei, and M. R. Mitchell, “Fatigue of Nitinol: The state-of-the-art and ongoing challenges,” *J. Mech. Behav. Biomed. Mater.*, vol. 50, pp. 228–254, Oct. 2015.
- [128] S. Gollerthan, M. L. Young, K. Neuking, U. Ramamurty, and G. Eggeler, “Direct physical evidence for the back-transformation of stress-induced martensite in the vicinity of cracks in pseudoelastic NiTi shape memory alloys,” *Acta Mater.*, vol. 57, no. 19, pp. 5892–5897, Nov. 2009.
- [129] J. Cui *et al.*, “Demonstration of high efficiency elastocaloric cooling with large  $\Delta T$  using NiTi wires,” *Appl. Phys. Lett.*, vol. 101, no. 7, p. 73904, Aug. 2012.
- [130] R. Munier, C. Doudard, S. Calloch, and B. Weber, “Determination of high cycle fatigue properties of a wide range of steel sheet grades from self-heating measurements,” *Int. J. Fatigue*, vol. 63, pp. 46–61, Jun. 2014.
- [131] C. E. Stromeyer, “The determination of fatigue limits under alternating stress conditions,” *Proc. R. Soc. A Math. Phys. Eng. Sci.*, vol. 90, no. 620, pp. 411–425, 1914.
- [132] W. J. Putman and J. W. Harsch, “‘Rise of Temperature’ method of determining endurance limit,” in *An investigation of the fatigue of metals*, University of Illinois Bulletin, 1921, pp. 119–127.
- [133] R. Cazaud, *La fatigue de métaux*. 1969.
- [134] M. P. Luong, “Infrared thermographic scanning of fatigue in metals,” *Nucl. Eng. Des.*, vol. 158, no. 2–3, pp. 363–376, 1995.

- 
- [135] J. Krapez, D. Pacou, and G. Gardette, “Lock-in thermography and fatigue limit of metals,” *Off. Natl. D Etudes ...*, pp. 3–8, 2000.
- [136] B. Yang, “Thermography detection on the fatigue damage,” p. 248, 2003.
- [137] J. Krapez and D. Pacou, “Thermography detection of early thermal effects during fatigue tests of steel and aluminium samples,” *Brunswick, MN, US*, vol. AIP, pp. 1545–1552, 2001.
- [138] A. Ezanno, C. Doudard, S. Calloch, and J.-L. Heuzé, “A new approach to characterizing and modeling the high cycle fatigue properties of cast materials based on self-heating measurements under cyclic loadings,” *Int. J. Fatigue*, vol. 47, pp. 232–243, Feb. 2013.
- [139] C. Doudard and S. Calloch, “Influence of hardening type on self-heating of metallic materials under cyclic loadings at low amplitude,” *Eur. J. Mech. A/Solids*, vol. 28, no. 2, pp. 233–240, 2009.
- [140] L. Jegou, Y. Marco, V. Le Saux, and S. Calloch, “Fast prediction of the Wohler curve from heat build-up measurements on Short Fiber Reinforced Plastic,” *Int. J. Fatigue*, vol. 47, pp. 259–267, 2013.
- [141] V. Le Saux, Y. Marco, S. Calloch, C. Doudard, and P. Charrier, “Fast evaluation of the fatigue lifetime of rubber-like materials based on a heat build-up protocol and micro-tomography measurements,” *Int. J. Fatigue*, vol. 32, no. 10, pp. 1582–1590, 2010.
- [142] G. La Rosa and A. Risitano, “Thermographic methodology for rapid determination of the fatigue limit of materials and mechanical components,” *Int. J. Fatigue*, vol. 22, no. 1, pp. 65–73, 2000.
- [143] C. Doudard *et al.*, “A PROBABILISTIC TWO-SCALE MODEL FOR HIGH CYCLE FATIGUE LIFE PREDICTIONS To cite this version : HAL Id : hal-00322496,” 2008.
- [144] C. Doudard, S. Calloch, F. Hild, P. Cugy, and A. Galtier, “Identification of the scatter in high cycle fatigue from temperature measurements,” *Comptes Rendus Mécanique*, vol. 332, no. 10, pp. 795–801, 2004.
- [145] C. Mareau, V. Favier, B. Weber, A. Galtier, and M. Berveiller, “Micromechanical modeling of the interactions between the microstructure and the dissipative deformation mechanisms in steels under cyclic loading,” *Int. J. Plast.*, vol. 32–33, pp. 106–120, 2012.
- [146] A. Chrysochoos and H. Louche, “An infrared image processing to analyse the calorific effects accompanying strain localisation,” *Int. J. Eng. Sci.*, vol. 38, no. 16, pp. 1759–1788, 2000.
- [147] P. Vázquez *et al.*, “Infrared thermography monitoring of the NaCl crystallisation process,” *Infrared Phys. Technol.*, vol. 71, pp. 198–207, 2015.
- [148] Y. Terada, K. Ohkubo, K. Nakagawa, T. Mohri, and T. Suzuki, “Thermal conductivity of B2-type aluminides and titanides,” *Intermetallics*, vol. 3, no. 5, pp. 347–355, 1995.
- [149] C. Zanotti, P. Giuliani, P. Bassani, Z. Zhang, and A. Chrysanthou, “Comparison between the thermal properties of fully dense and porous NiTi SMAs,” *Intermetallics*, vol. 18, no. 1, pp. 14–21, 2010.
- [150] A. Jain and K. E. Goodson, “Measurement of the Thermal Conductivity and Heat Capacity of Freestanding Shape Memory Thin Films Using the  $3\omega$  Method,” *J. Heat Transfer*, vol. 130, no. 10, p. 102402, 2008.
- [151] Goff J.F., “Thermal conductivity, thermoelectric power, and the electrical resistivity of stoichiometric TiNi in the 3–300 K temperature range,” *J. Appl. Phys*, vol. 35, pp. 2919–2927, 1964.



# Fatigue Structurale de Fils Superélastiques de NiTi

## Résumé

Ce travail de thèse aborde les conditions et les mécanismes qui conduisent des fils superélastiques de NiTi à la rupture sous chargement mécanique cyclique. Les alliages à mémoire de forme du type NiTi présentent des propriétés thermomécaniques fonctionnelles comme la superélasticité et l'effet de mémoire de forme simple et double, lesquels sont générées grâce aux transformations de phase martensitiques provoquées soit par un changement de la contrainte ou de la température. Ces transformations de phase sont en principe des processus totalement réversibles et sans endommagement. Cependant, lorsque le NiTi est soumis à des transformations de phase induites par des contraintes cycliques, la performance en fatigue de l'alliage chute considérablement par rapport au NiTi non-transformant. La plupart des courbes S-N de fatigue rapportant cette chute ont été mesurées sur des fils NiTi à section constante dans lesquels les transformations martensitiques se développent de façon hétérogène par nucléation et propagation de bandes de cisaillement. De plus, d'après notre expérience, des essais de fatigue sur des échantillons de fils à section constante entraînent la rupture à l'intérieur des mors de la machine d'essai. Par conséquent, les valeurs de contrainte-déformation rapportées dans les courbes S-N ne sont pas nécessairement représentatives des conditions mécaniques critiques qui conduisent le matériau à la rupture. Dans le but de mieux caractériser les performances en fatigue des fils NiTi, nous avons effectué une série de tests de fatigue en traction-traction, tout en utilisant des échantillons sous forme « diabolo ». La géométrie de ces échantillons nous a permis de confiner tous les processus de transformation martensitique et de fatigue dans une volume utile bien définie. La caractérisation du comportement thermomécanique de ces échantillons a été réalisée en combinant plusieurs techniques expérimentales et d'analyse telles que la corrélation d'image numérique (DIC), la thermographie infrarouge, la diffraction des rayons X à source synchrotron, la microscopie optique, la microscopie électronique à balayage et l'analyse par éléments finis. Une attention particulière a été portée à la performance de NiTi dans le régime à grande nombre de cycles (HCF) dans laquelle le matériau présente un comportement élastique ou une transformation de phase intermédiaire (appelée R-phase). Les résultats des tests de fatigue nous ont permis de distinguer les étapes de nucléation et de propagation des fissures pendant la durée de vie totale de nos échantillons. Afin de mieux comprendre les mécanismes qui conduisent à la nucléation des fissures, nous avons appliqué la méthode de l'auto-échauffement, qui a démontré son efficacité dans la prédiction de fatigue dans les cas des alliages d'aluminium et des alliages d'acier. Cette méthode corréle l'élévation de température d'un échantillon soumis à différentes amplitudes de charge cyclique avec des mécanismes de dissipation d'énergie. Ces mécanismes dissipatifs sont après associés à l'accumulation d'endommagement locale dans le matériau. La méthode d'auto-échauffement a été réalisée en utilisant des mesures de champs thermiques des d'échantillons de NiTi sous forme diabolo pendant de chargement cyclique.

**Mot clés :** NiTi, Alliages à Mémoire de Forme, Fatigue à Grande Nombre de Cycles (HCF), Fatigue Structurale, Auto-échauffement, Thermographie Infrarouge, R-phase



# Structural Fatigue of Superelastic NiTi Wires

## Abstract

This Ph.D. dissertation thesis addresses the conditions and mechanisms that lead superelastic NiTi wires to fail under cyclic mechanical loads. NiTi shape memory alloys exhibit functional thermomechanical properties (superelasticity, shape memory effect, thermal actuation) due to martensitic phase transformations caused by a change of the applied stress and temperature. These phase transformations are though as fully reversible damage-free processes, however, when NiTi is subjected to repetitive stress-induced phase transformations its fatigue performance drops drastically in comparison to non-transforming NiTi. Most of fatigue S-N curves reporting this drop were measured on straight NiTi wires in which martensitic transformations proceed heterogeneously through nucleation and propagation of shear bands. Moreover, from our experience fatigue testing straight wire samples results in undesired failure inside the testing machine clamps. Hence, the reported stress-strain values in S-N curves are not necessarily representative of the critical mechanical conditions that lead the material to failure. With the aim of better characterize the fatigue performance of NiTi wires, we started by carrying out a series of pull-pull fatigue tests using hourglass-shaped samples. This sample geometry allowed us to confine all martensitic transformation and related material fatigue processes into a well-defined gauge volume. The samples' characterization was performed by combining several experimental and analysis techniques such as Digital Image Correlation, Infrared Thermography, Synchrotron-source X-ray diffraction, Optical Microscopy, Scanning Electron Microscopy and Finite Element Analysis. A special attention was paid to the High Cycle Fatigue (HCF) performance of NiTi in which the material shows elastic behavior and/or an intermediate phase transformation (so-called R-phase). The results from HCF tests allowed us to distinguish crack nucleation and crack propagation stages during the total life of our NiTi samples. In order to get a better understanding of the mechanisms that lead to crack nucleation, we applied the non-conventional Self-Heating fatigue assessment method, which has shown efficiency in the case of aluminum and steel alloys. This method correlates the temperature elevation of a sample subjected to different cyclic load amplitudes with energy dissipating mechanisms that contribute to accumulating local damage in the material. The Self-Heating method was performed using full-field thermal measurements of cyclically loaded NiTi hourglass-shaped samples.

**Keywords:** NiTi, Shape Memory Alloys, High Cycle Fatigue, Structural Fatigue, Self-heating, Infrared Thermography, R-phase.